

Dissertation

submitted to the
Combined Faculties for the Natural Sciences and for Mathematics
of the Ruperto-Carola University of Heidelberg
for the degree of
Doctor of Natural Sciences

Put forward by
Johannes Tadeo Lumma
born in Huelva, Spain
Oral examination: November 25th, 2020

New physics in and with Gravity

Referees:

Prof. Dr. Astrid Eichhorn

Prof. Dr. Björn Malte Schäfer

Abstract:

Im Zentrum von schwarzen Löchern bricht die allgemeine Relativitätstheorie zusammen. Diese Singularitäten könnten durch eine Theorie der Quantengravitation aufgelöst werden. In dieser Arbeit untersuchen wir Tensormodelle für Quantengravitation und beleuchten mögliche Gemeinsamkeiten mit anderen Theorien der Quantengravitation, zum Beispiel mit der asymptotisch sicheren Quantengravitation. Von besonderer Bedeutung in diesem Zusammenhang ist die Existenz eines universellen Kontinuumslikes. Auch wenn die allgemeine Relativitätstheorie bei kleinen Längenskalen nicht konsistent ist, so ist sie auf makroskopischen Skalen äußerst erfolgreich. Wir werden untersuchen wie eine der Vorhersagen der allgemeinen Relativitätstheorie, Gravitationswellen, neue Physik implizieren kann.

Abstrakt:

At the center of black holes, the theory of general relativity breaks down. The resolution of such singularities could require a theory of quantum gravity which describes the fundamental nature of space-time at shortest distances. In this thesis, we explore the tensor model approach to quantum gravity and inspect its relation to other theories of quantum gravity, such as, e.g., asymptotic safety, through a universal continuum limit. Even though at microscopic distances, general relativity breaks down, at large distances this theory is highly successful. We will inspect how one of the predictions of general relativity, gravitational waves, can help us to learn more about new physics beyond the Standard Model.

Contents

I	New Physics in and with Gravity	9
1	Introduction	11
2	The Philosophy of Coarse-Graining	13
2.1	Generating Functionals	14
2.2	Universality	16
2.3	The FRG	24
3	The continuum limit in Quantum Gravity	29
3.1	A general overview	29
3.2	Background Independence and the Renormalization Group	31
3.3	The path integral and sum over histories	32
3.4	Asymptotically Safe Quantum Gravity	33
3.5	Euclidean Dynamical Triangulations	35
3.6	Causal Dynamical Triangulations	38
3.7	Matrix & Tensor Models	40
3.8	Causal Sets Quantum Gravity	42
3.9	Spin Foams	44
3.10	Group Field Theory	46
4	Tensor Models	47
4.1	Tensor Models	68
4.2	RG flows for Matrix and Tensor Models	71
4.2.1	FRG for Matrix and Tensor Models	73
4.2.2	An algorithm for Tensor Models	75
4.3	Understanding 3D	83
4.4	Towards four-dimensional Quantum Gravity	110
5	Gravitational Waves from an Electroweak Phase Transition	117
5.1	Phase Transitions in the Standard Model and Beyond	118
5.2	Dynamics of Phase Transitions	124
5.2.1	Gravitational Waves from a Phase Transition	134
5.3	Results	139
6	Conclusion & Outlook	147

II Appendix	153
A Liouville	155
B Computations with the FRG	159
C Mathematica for Models	163
D β-functions of the real rank-3 tensor model	165
E Bubble Nucleation	171
F Hydrodynamics of expanding bubbles for fast PTs	175
G Gravitational Waves - A primer	181
H Efficiencies of gravitational wave production processes	185
I Result tables for the gravitational wave spectra	189
J Lists	193
J.1 List of Figures	193
J.2 List of Tables	195
K Own publications	197
L Bibliography	199
Acknowledgements	225

Part I

New Physics in and with Gravity

1 Introduction

Gravity is a topic that has fascinated humankind for centuries. Our current insight into the gravitational force is summarized by the theory of general relativity (GR), where space-time is dynamical and the interaction between masses leads to a curving of space-time: Matter dictates how space-time is bent while space-time describes how matter moves. This intuitive understanding of gravity brings an incredibly rich set of consequences with it. Examples are the prediction of the existence of gravitational waves, detected by LIGO [4], or the appearance of a black hole shadow, which has been recently observed by the EHT Collaboration [5, 6, 7]. These two predictions are just the most recently verified ones in a long history of testing observational consequences of GR. Exploring further implications of the theory of general relativity and its interplay with matter might help us to not only better understand the gravitational force, but also learn more about the fundamental properties of matter and the matter content of our universe.

The detection of a stochastic background of gravitational waves in the frequency range of future space-based interferometers LISA and DECIGO, for instance, can result from a first-order phase transition in the early universe. While phase transitions in the Standard Model are only cross-overs, a first order phase transition is a prediction of many beyond the Standard Model scenarios, e.g., in order to attempt to provide a mechanism to generate the observed matter-antimatter asymmetry. To realize such an asymmetry, a deviation from thermal equilibrium is required. A possible way to achieve a departure from thermal equilibrium is by means of a first-order phase transition at the electroweak scale at around 10^2 GeV, where the Higgs particle acquires an expectation value, thus giving mass to particles.

Gravitational waves offer not only a way to probe new physics in the matter sector, but also allow to constrain the theory of general relativity. The detection of gravitational waves in 2015 by the LIGO collaboration has cemented GR as the theory of gravity, putting tight constraints on any modifications. An analysis of the first measurement showed that the merger of two black holes with masses $M_1 = (36 \pm 6)M_\odot$ and $M_2 = (29 \pm 4)M_\odot$ had been the source of the signal. While the detection of gravitational waves is fully consistent with Einsteins theory of general relativity, the astrophysical objects producing them are not fully described by GR: The center of a black hole cannot be described by general relativity, as the theory breaks down due to a singularity. Hence, even though GR in the classical regime is well-understood with a plethora of exciting repercussions that will allow us to learn more about the matter content of our universe, gravity itself features internal inconsistencies at shortest distances. The resolution of these inconsistencies could require a theory of quantum gravity that will offer fascinating insight into the fundamental nature of

space-time in the quantum regime.

A predictive theory of Quantum Gravity is not yet formulated as the naive way to quantize gravity, which was so successful to quantize all other forces in nature, fails. Part of the challenge of establishing a theory of quantum gravity is also due to the fact that the Planck scale m_p at which quantum gravity effects are expected to become important is $m_p \approx 10^{19}$ GeV, which makes it very challenging to design experimental tests. The LHC, for instance, was operating at 1.3×10^4 GeV before its operation was stopped in order to set-up the next high luminosity run, expected to launch in 2027. Hence, it is important to explore a diverse number of quantum gravity approaches, which feature different strengths and weaknesses. Exploring distinct approaches to quantum gravity can contribute to the development of new ideas and viewpoints.

What a number of quantum gravity approaches have in common is that discreteness is introduced in order to make sense of the path-integral for quantum gravity. The spirit is very similar to lattice gauge theories, where discreteness allows to truncate the number of degrees of freedom and serves as a regularization of the theory.

Continuum space-time is then discretized by little building blocks. In the continuum limit, which corresponds to a second-order phase transition, the effects of the discretization can be removed in order to recover a continuum space-time. Universality, which is a key property of second-order phase transitions, guarantees that the physics that emerges in the continuum is independent of the exact shape of the building blocks. In a broader sense, universality also has powerful implications, as it potentially allows to relate microscopic descriptions which lead to the same continuum limit. It may thus be that seemingly different theories of quantum gravity turn out to be related when taking the continuum limit.

While exploring some very fascinating questions related to new physics with and in gravity we will be covering a wide range of fields of physics spanning from mathematical physics to phenomenology.

Our journey through these different fields begins in Ch. 2, where we introduce the necessary technical tools that will allow us to study the continuum limit in quantum gravity. This will be the topic of Ch. 3, where we will review the status of the continuum limit in different approaches to quantum gravity and highlight potential relationships between some of those approaches and Ch. 4, where we will inspect the continuum limit in tensors models, one approach to quantum gravity, in more detail. Finally, Ch. 5 will be devoted to the study of how gravity, in particular the production of gravitational waves in the early universe, can help us to learn more about the fundamental properties of matter.

2 The Philosophy of Coarse-Graining

In order to discuss the relevance and subtleties of the continuum limit in quantum gravity, it is necessary to equip the reader with the necessary concepts and tools. The renormalization group offers a framework to study the continuum limit. We will introduce the idea of the renormalization group by providing an intuitive understanding through the so-called block spin approach. From there, we will discuss a more modern understanding of renormalization by introducing the functional renormalization group, which will allow us to study the continuum limit in the tensor-model approach to quantum gravity.

As a physicist one is always eager to make things as simple yet precise as possible. While it should certainly be possible to derive the physical properties of a water molecule from some fundamental action of our universe, such an approach would be very cumbersome. It would be equally cumbersome to derive the flow of a river from the microscopic interactions of each individual water molecule. The clever physicist will therefore try to find some effective degrees of freedom appropriate to study the problem at hand. The flow of a river, for instance, is well-described by its velocity, its pressure, its density and its dynamic viscosity, variables whose dynamics are described by the Navier Stokes equations.

Nonetheless, one would expect that the different effective degrees of freedom that are useful to study each phenomenon mentioned above are related in some way. The concept behind the idea that a system with many degrees of freedom, such as the river that consists of many water molecules, can also be expressed in terms of fewer, more suited variables, is called coarse-graining. It is not only of relevance in physics but also, e.g., in the social sciences. Economists for instance use aggregate variables like the unemployment rate or the gross domestic product (GDP) to describe the state of an economy rather than analyzing the complicated individual interactions of all parties making up that economy. Coarse-graining describes a way to relate the different variables at each scale.

One of the very first historical examples of coarse-graining is the block spin approach originally introduced by Leo Kadanoff in the 1950's in order to study the Ising model [8]. Kadanoff considered a two-dimensional lattice of spins pointing either up ($s = 1$) or down ($s = -1$). The original idea of coarse-graining consists in choosing a *local* patch of spins and average over them. This is precisely what is called a block spin transformation. For instance, one could compare the number of up-spins in a patch to the number of down-spins and assign a collective spin $s' = +1$ or $s' = -1$ depending on which configuration is more prevalent. Finally, the lattice spacing is rescaled to its initial size. This will result in a lattice made up of the effective spins assigned to the different patches in the original set-up. The current

discussion on coarse-graining is very qualitative but it sets the conceptual basis for the further discussions on the renormalization group. In order to equip the reader with the technical knowledge to follow the discussion on a the renormalization group, we will briefly review the relevant field-theoretical concepts.

2.1 Generating Functionals

The central object in field theory is the generating functional that allows for the derivation of all correlation functions of all degrees of freedom to all orders. Having total knowledge of the correlation functions of a system is equivalent to knowing the exact form of the generating functional and implies that the underlying theory is fully understood. One such generating functional is the partition function Z defined as

$$Z = \int \mathcal{D}\varphi e^{-S[\varphi] + \int d^D x J(x)\varphi(x)}, \quad (2.1)$$

where J is a source-term. The real-time, Minkowski version of the above path-integral is assumed to be defined through a Wick-rotation of its Euclidean avatar given by Eq. 2.1. In particular, it is assumed that Euclidean correlation functions can be analytically continued back to real time, while preserving their pole structure in order to get Minkowski correlation functions¹. In this sense, quantum and statistical mechanics can be regarded as very closely related.

It is straightforward to check that correlations functions are obtained as follows

$$\langle \varphi(x_1) \dots \varphi(x_n) \rangle = \frac{1}{Z[0]} \frac{\partial^n Z[J]}{\partial J(x_1) \dots \partial J(x_n)} = \frac{\int \mathcal{D}\varphi \varphi(x_1) \dots \varphi(x_n) e^{-S[\varphi] + J\varphi}}{Z[0]}. \quad (2.2)$$

The above generating functional $Z[J]$ allows to obtain all correlation functions, however, it is not very effective as both connected and non-connected correlation functions are generated even though we are mostly interested in connected correlation functions for physical processes. One example is the derivation of scattering amplitudes through the LSZ formalism, which only requires connected correlation functions. A more efficient generating functional from which only connected correlation functions are derived is the Schwinger functional $W[J] = -i\hbar \ln Z[J]$. This generating functional is also closely related to the free energy F , well-known from statistical mechanics with the difference that the free energy F corresponds to a thermodynamic potential which is also reflected in its definition, $F = k_B T \ln Z[T]$, where k_B is the Boltzmann factor and T the temperature. This slight difference in prefactors, i.e. $-i\hbar$ vs. $k_B T$, reflects the different underlying physical systems described by $W[J]$ and $F[T]$ and also relates to the previous point that a Minkowski theory can be defined through its Euclidean version by means of a Wick-rotation.

¹Technically, this can for instance be done by means of a Padé approximation [9].

In quantum gravity, Wick rotation is non-trivial. We will therefore neglect these aspects for now and comment on them later on. Probabilities of expectation values on the statistical mechanics side correspond to amplitudes on the quantum mechanical side.

Connected correlation functions are obtained by differentiating $W[J]$ with respect to the source J . For instance, applying functional derivatives twice gives

$$\frac{\delta^2 W[J]}{\delta J(x) \delta J(y)} = \langle \varphi(x) \varphi(y) \rangle_c = \langle \varphi(x) \varphi(y) \rangle - \phi(x) \phi(y), \quad (2.3)$$

where we introduced the notation $\phi(x) \equiv \langle \varphi(x) \rangle$. For most practical purposes, it will, however, turn out to be beneficial to introduce yet another generating function $\Gamma[\phi]$, which stores the same physical information as $W[J]$ in a yet more efficient way and is also more accessible from a physical point of view due to its exactness at tree level. Tree-level exactness implies that the effective action allows one to derive full quantum corrected propagators and vertices which in turn allow to determine physical parameters like masses. As a matter of fact, the masses and interaction terms appearing in the effective action Γ are also those that are measured in experiment. The effective action $\Gamma[\phi]$ is defined via a Legendre transform of $W[J]$,

$$\Gamma[\phi] = \sup_J \left(\int d^D x J(x) \phi(x) - W[J] \right), \quad (2.4)$$

and physically corresponds to the full quantum action which takes into account all quantum corrections of a given theory. This becomes apparent as the definition of Γ entails the following quantum equation of motion

$$\frac{\delta \Gamma[\phi(x)]}{\delta \phi(y)} = J(y), \quad (2.5)$$

which is analogous to the classical equation of motion

$$\frac{\delta S[\varphi(x)]}{\delta \varphi(y)} = 0. \quad (2.6)$$

Since ϕ accounts for all fluctuations φ , it becomes evident that the above equation of motion is truly a full quantum one. When no quantum fluctuations are considered, the effective action Γ is just the microscopic action S . As useful as it is to have full knowledge of the effective action Γ , it is hard to access in practice. This can be seen by considering the definition of Γ via the Legendre transform of the Schwinger functional $W[J]$ provided by Eq. 2.4 and plugging in the explicit form of $W[J]$ given by $W[J] = -i\hbar \ln Z[J]$. The resulting expression

$$e^{-\Gamma[\phi]} = \int_{\Lambda} \mathcal{D}\varphi \exp \left(-S[\phi + \varphi] + \int \frac{\delta \Gamma[\phi]}{\delta \phi} \varphi \right), \quad (2.7)$$

is a complicated integro-differential equation for ϕ that is difficult to solve exactly. In the above expression Λ is an ultraviolet cut-off that regularizes the measure and φ can be regarded as a quantum mechanical fluctuation around some background field ϕ .

2.2 Universality

Universality is a key concept that is associated to second and higher-order phase transitions. In the 50's and 60's, second order phase transitions in gas-liquid systems and magnets were studied in great detail. Researchers observed that the scale-dependence of certain observables followed a power-law, when approaching a continuous phase transition. Intriguingly, the scaling exponents of these operators are *universal*, meaning that they are independent of the exact nature of the material undergoing the phase transition. The spontaneous magnetization for instance was found to have the following scaling

$$M(T) \propto (T - T_c)^\beta, \quad (2.8)$$

where T is the temperature, T_c the critical temperature at which the phase transition takes place and β is a universal quantity. A *universality class* is characterized by a set of universal critical exponents that describe the scaling of observables near a critical point. Seemingly unrelated physical systems belonging to the same universality class feature quantitatively similar large-scale behavior characterized by the same set of critical exponents. An example of a well-studied universality class is the $3d$ Ising universality class, which describes both the liquid-gas phase transition as well as the ferromagnetic-paramagnetic phase transition. This highlights, that systems that may be completely different in terms of chemical and physical properties may feature similar behavior close to a critical point at which a second-order phase transition takes place. Phrased differently, universality corresponds to the statement that in order to describe the large-scale physics of a continuous phase transition only a few number of parameters are relevant. In particular, the microscopic details, such as the exact chemical composition of a system, are washed out.

In a field theoretical language, the concept of universality was put on firm ground by Wilson in the 1970's [10, 11]. Most QFTs of physical interest lead to unphysical UV divergences that have to be properly tamed. This can be achieved by the introduction of a cut-off Λ , which can be thought of as introducing a minimal length $1/\Lambda$ or an energy scale Λ up to which the theory is well-defined. Since physics should not be affected by the length scale at which this unphysical cut-off is introduced, the physics at different cut-off scales Λ should be related in some way. Building on the previous discussion on generating functionals, which are the standard way to define physical theories, this implies the following relationship between two generating functionals Z describing the same theory defined up to different cut-offs Λ and Λ' ,

$$\int_0^\Lambda \mathcal{D}\phi e^{-S_0[\phi]} = \int_0^{\Lambda'} \mathcal{D}\phi' e^{-S'_{\text{eff}}[\phi]}, \quad (2.9)$$

which exactly expresses the fact that low-energy physics should remain independent of the scale at which the cut-off is introduced. Remember that physical observables are derived as derivatives from either the right or left hand side of the above equation. The fact that both expressions are identical, implies that gauge-invariant quantities

derived from either one of the expressions will be the same. The fact that physics at different cut-offs has to be related implies the existence of an RG-scale Λ' , which allows one to interpolate between physics at different cut-offs Λ . We will refer to Λ' as either the RG scale or the 'floating' cut-off. The basis of the interpolation consists in splitting the degrees of freedom ϕ of the theory into 'low-energy' (or low-momentum) and 'high-energy' (or high-momentum) degrees of freedom, ϕ_ℓ and ϕ_h as follows

$$\phi_\ell(p) = \begin{cases} \phi(p), & \text{if } p < \Lambda' \\ 0, & \text{otherwise,} \end{cases} \quad (2.10)$$

and

$$\phi_h(p) = \begin{cases} \phi(p), & \text{if } \Lambda' < p \leq \Lambda \\ 0, & \text{otherwise,} \end{cases} \quad (2.11)$$

where p corresponds to the momentum of the mode ϕ . The above definition guarantees that $\phi(p) = \phi_\ell(p) + \phi_h(p)$. The key to relate the same physics defined at two different cut-off scales Λ and Λ' is to integrate out the high-momentum modes ϕ_h as follows

$$Z_\Lambda \equiv \int_0^{\Lambda'} \mathcal{D}\phi_\ell \int_{\Lambda'}^\Lambda \mathcal{D}\phi_h e^{-S_0[\phi_\ell + \phi_h]} = Z_{\Lambda'} \int_0^{\Lambda'} \mathcal{D}\phi' e^{-S'_{\text{eff}}[\phi']}, \quad (2.12)$$

where we have relabeled ϕ_ℓ as ϕ' in order to make contact with the right hand side of Eq. (2.9). In order to compensate for the fact that the high-momentum degrees of freedom have been integrated out, the couplings have to be rescaled. The rescaling of couplings reflects the coarse-graining nature of Wilson's approach. Similar to the Block-spin approach, where the variables need to be rescaled according to new scale of the lattice after a block spin transformation has been performed, the action in the path-integral S_{eff} is now expressed in terms of effective couplings.

The mode ϕ' may also be split once again into low- and high-momentum modes in order to relate $Z_{\Lambda'}$ to some $Z_{\Lambda''}$ in a similar way as we just related Z_Λ to $Z_{\Lambda'}$. Successively integrating out the high-energy modes leads to a constant change or flow of the action $S_{\text{eff}}[\phi]$ as a function of the RG-scale in order to satisfy the condition $Z_\Lambda = Z'_\Lambda$ for any Λ and Λ' . The re-scaling dependence of the action S on the RG-scale is typically characterized in terms of β functions of the dimensionless couplings. Beta functions describe the scale dependence of the individual couplings, referred to as the running of couplings. They are defined as

$$\beta_{g_i} \equiv k \partial_k g_i, \quad (2.13)$$

where k denotes the RG scale and have the following generic form

$$\beta_{g_i} = -\Delta_i g_i + \text{quantum corrections}, \quad (2.14)$$

where Δ_i is the canonical scaling² of the coupling g_i . The dependence of the couplings on the 'floating' cut-off scale k as well as the generic form of the beta functions follows from the assumption that the action S may be expanded in terms of all field monomials \mathcal{O} that respect the underlying symmetry of the theory such that

$$S_k = \sum_i \bar{g}_i(k) \mathcal{O}_i(\partial, \varphi), \quad (2.15)$$

where the dimensionful coupling constants \bar{g}_i with mass dimension Δ_i can be expressed in terms of dimensionless couplings³ g_i as

$$g_i \equiv \bar{g}_i k^{-\Delta_i}. \quad (2.17)$$

The so-called theory space is spanned by all essential couplings⁴ g that are compatible with the symmetries of the theory and is typically infinite-dimensional. The running of couplings can be shown to lead to divergences of physical observables unless it is possible to identify fixed points g_{i*} of the renormalization group flow at which either the IR or the UV limit can be taken. A fixed point has the defining property that all couplings in theory space lose their scale-dependence, i.e.,

$$\beta_{g_i}(g_j = g_{j*}) = 0 \quad \forall i, j. \quad (2.18)$$

Thus, the requirement posed on any fundamental theory is that the renormalization group trajectory emanate from a UV fixed point at which the dimensionless couplings do not change under infinitesimal changes of the RG scale k . This allows to take the limit $k^2 \rightarrow \Lambda \rightarrow \infty$, as we will discuss in a brief moment. It is possible to distinguish between two types of fixed points. The Gaussian fixed point, which always exists, where all couplings vanish trivially at the fixed point and non-Gaussian fixed points where some couplings take fixed point values different from zero. If the theory departs from a Gaussian fixed point at high energies, this scenario is called asymptotic freedom. On the other hand, if the theory starts at an interacting fixed

²The canonical dimension or scaling of a coupling characterizes the rescaling properties of that coupling under space-time dilations $x \rightarrow \lambda x$, where λ is a constant. The canonical dimension of the mass for instance is one.

³Dimensionless coupling constants are used because physical observables such as cross sections can be rewritten in terms of dimensionless couplings. Any dimensionful observable $\langle \bar{O} \rangle$ can be expressed as

$$\langle O(\bar{g}_i) \rangle = f(g_i(k), X) E^\Delta, \quad (2.16)$$

where f is a function of the dimensionless couplings g_i and X , which describes any other possible dimensionless dependencies of $\langle \bar{O}(\bar{g}_i) \rangle$. Δ is the canonical dimensionality of O and E the energy scale at which the observable is measured. Since E is finite, O will not diverge as long as its dimensionless version is finite at any finite E . In turn, this poses a requirement on the dimensionless couplings to not diverge.

⁴Essential couplings are those that cannot be removed by a field redefinition. The wave function renormalization Z_k for instance is an inessential parameter, as it can be removed by a field re-definition.

point at high energies, it is referred to as asymptotic safety.

A fixed point can further be characterized in terms of the behavior close to the fixed point of the couplings spanning the infinite-dimensional theory space. It is therefore instructive to linearize the flow close to some fixed point g_* ,

$$g_i = g_{i*} + \delta g_i, \quad (2.19)$$

where δg_i corresponds to a small perturbation away from the fixed point. The scale-dependence of the perturbed couplings g_i close to the fixed point are described by the following series-expansion of the beta functions

$$\beta_i(g) = \beta_i(g_*) - \sum_j M_{ij}(g_*) \delta g_j + \mathcal{O}((\delta g)^2), \quad (2.20)$$

where M_{ij} denotes the entries of the typically non-diagonal stability matrix M defined as

$$M_{ij} = -\frac{\partial \beta_i}{\partial g_j} \quad (2.21)$$

Here, we are interested in the physics close to the fixed point and therefore the linearized behavior of the flow is sufficient for our analysis. Since the fixed point criterion is precisely that $\beta_i(g_*) = 0$, the first term vanishes and to linear order the flow close to the fixed point g_* is completely described by the stability matrix M , since

$$\beta_i(g) = -\sum_j M_{ij}(g_*) \delta g_j + \mathcal{O}(\delta g^2). \quad (2.22)$$

The above equation can be solved by rotating into a basis of theory space in which the stability matrix is diagonal. In that case the linearized solution reads

$$g_i(k) \approx g_i^* + \sum_I C_I V_i^I \left(\frac{k}{k_0} \right)^{-\theta_I}, \quad (2.23)$$

where θ_I are the critical exponents corresponding to the eigenvalues of the stability matrix M . The index I labels the couplings $g' = S^{-1}g$ in a basis that diagonalizes the stability matrix, the C_I are constants of integration and are free parameters of the theory, the V^I are the eigendirections corresponding to the different critical exponents and k_0 is a reference scale. Lowering k/k_0 corresponds to flowing towards the IR. The above equation Eq. 2.23 describes the RG trajectory of a theory in coupling space, once the linearized regime, where Eq. 2.23 holds, is entered. In principle, one has to determine all free parameters C_I in order to fully fix the RG trajectory. However, the critical exponents θ_I allow for the notion of relevant and irrelevant directions in theory space. If the real part $\Re(\theta_I)$ of the critical exponent θ_I satisfies $\Re(\theta_I) > 0$, then the corresponding eigendirection is repulsed from the fixed

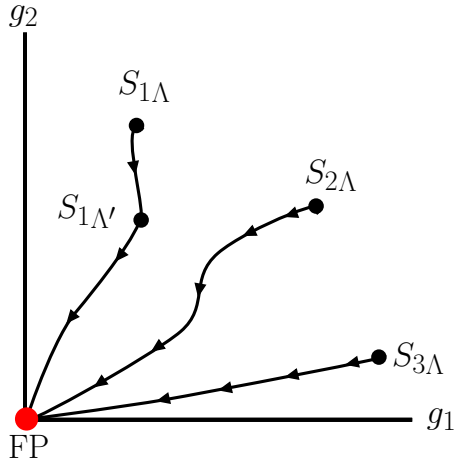


Figure 2.1: The above figure illustrates the concept of universality. Different actions S_1 , S_2 and S_3 serve as initial conditions of renormalization group trajectories that reach the same fixed point FP for $\Lambda \rightarrow 0$ with the arrows pointing towards the IR. The different physically realized renormalization group trajectories are functions of the relevant couplings g_1 and g_2 . Moreover, we also depict the concept of Wilsonian renormalization by explicitly showing that one given renormalization group trajectory connects an action S_1 defined at different cut-offs Λ .

point towards the IR. The coupling⁵ $g'_i(k)$ will grow towards the IR and consequently the IR values of relevant couplings will depend on the constants C_I . Eigendirections along which the flow emanates from a fixed point towards the IR are therefore called relevant directions because they are directions, the value of which is relevant for the IR. On the other hand $\Re(\theta_I) < 0$ will drive the flow towards the fixed point in the limit $k/k_0 \rightarrow 0$. Hence, the value of C_I will not be relevant for the IR value of the coupling associated to the irrelevant eigendirection. Hence, a multitude of different initial conditions will lead to that fixed point. This corresponds to the idea of universality in field theory, where the same IR fixed point can be reached by different microscopic actions S_i . This is depicted in Fig. 2.1. Moreover, one may also ask whether an RG trajectory is UV complete, i.e. whether it starts at $k \rightarrow \infty$. In order for an RG trajectory to be UV-complete, the constant C_I has to be set to zero for the irrelevant directions such that there is only one allowed RG trajectory for an irrelevant direction, which in turn implies that the value of the corresponding coupling is fixed by the fixed point requirement. If the stability matrix also features zero eigenvalues, $\Re(\theta_i) = 0$, the behavior of these marginally (ir)relevant directions is determined by the next order in the linearized flow. An eigendirection

⁵Note that strictly speaking g'_i no longer has to correspond to the original set of couplings introduced to describe the effective action since in order to solve the linearized flow equation we rotated to a basis in coupling space that diagonalizes the stability matrix M . Hence, the coupling g'_i could well be a linear combination of the original couplings.

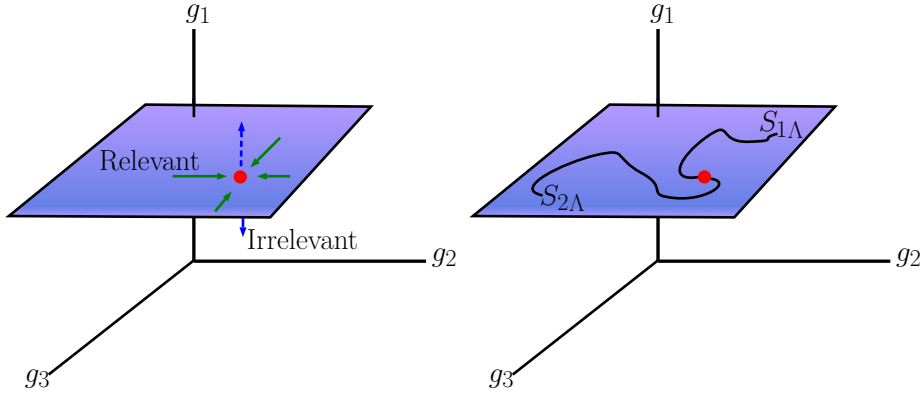


Figure 2.2: The left panel of the above figure depicts a truncated theory space with two relevant couplings which span a two-dimensional critical hypersurface, which contains all RG trajectories that emanate in the fixed point, illustrated in red. The coupling g_1 corresponds to an irrelevant direction, illustrated by the blue dashed line and is therefore fixed by the fixed point condition. The relevant directions sketched in green are attracted. The right panel of the figure depicts a truncated theory space with two relevant couplings which span a two-dimensional critical hypersurface. The hypersurface contains all trajectories that emanate in the fixed point FP. The coupling g_3 is irrelevant and is therefore fixed by the fixed point condition.

is truly marginal if it is marginal to all orders⁶. The classification of the flow of S_k in terms of relevant and irrelevant directions leads to the concept of the UV critical hypersurface, which can be associated to a fixed point in the ultraviolet. The UV critical hypersurface is spanned by all trajectories that emanate from a fixed point towards the IR. Since irrelevant directions are driven towards the fixed point, the critical hypersurface will have the dimensionality of the number of eigendirections with positive critical exponents $\Re(\theta_i > 0)$. A sketch of the critical hypersurface is shown in Fig. 2.2.

In the previous section we have introduced the effective action Γ as a convenient way to store physical information. Here, universality follows from a fixed point of a renormalization group trajectory. At a fixed point, the details of the microscopic physics have been integrated out with the macroscopic physics being described by only a small number of relevant parameters or fully fixed if there are no free parameters.

As a little toy example to illustrate the concepts related to the characterization of

⁶An example of a theory that is truly marginal to all orders is the non-commutative ϕ^4 model [12, 13].

fixed points, we may consider the following dynamical system

$$\begin{aligned}\partial_t x &= \alpha x - \beta xy \\ \partial_t y &= \delta xy - \gamma y.\end{aligned}\tag{2.24}$$

One may think of $\partial_t x$ and $\partial_t y$ as corresponding to a system of β functions but it does not have to. As a matter of fact the above toy-model is also known as the predator-prey or Lotka-Volterra model [14] and describes the dynamics of two population groups, predators and their prey that 'interact' with each other. The Lotka-Volterra model features a Gaussian fixed point with one relevant and one irrelevant direction, see Fig. 2.3, which can be understood as follows: The above set of coupled non-linear differential equations describe how the predator population y increases if there is enough prey x . In the absence of prey, i.e., $x = 0$, the time evolution of the predator population is dominated by an exponential decay term. On the other hand, the prey population of course decreases if there are a lot of predators around. This is reflected by the $-\beta xy$ term. In the absence of predators, the prey population increases exponentially. Note have that in the predator-prey example the notion of IR or UV fixed point does not exist. This way of classifying dynamical systems goes back to Liapunov [15].

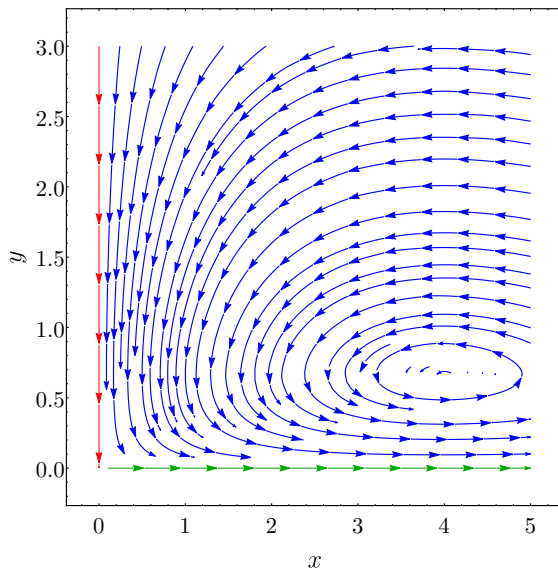


Figure 2.3: Phase diagram of a particular Lotka-Volterra model with parameters $\alpha = 2$, $\beta = 3$, $\gamma = 4$ and $\delta = 1$. The model exhibits a Gaussian fixed point corresponding to an equilibrium state with a stable and an unstable direction. This is physically very intuitive. The time evolution of the predator population consists of two competing terms. On the one hand, there is a term δxy , which accounts for the fact that the predator populations rises if there is enough prey. On the other hand, there is an exponential decay term $-\gamma y$, which is related to the fact that predators die if there is no prey to eat. Conversely, the prey population experiences an exponential growth in the absence of predators. The assumption is that the prey has an infinite food supply (they may be for instance herbivores). The observation that in the absence of prey the predator population extinguishes is also illustrated in the above figure: If we are placed at $x = 0$, i.e., there is no prey around, the 'time-flow' naturally brings us to the Gaussian fixed point ($x = 0, y = 0$) where the predators have died out due to a lack of food supply. The critical exponent associated to that eigendirection is consequently negative. Alternatively, assuming that for some reason there are no predators around (i.e., $y = 0$), the prey population starts to increase in an unconstrained way. This example also illustrates nicely that a fixed is a priori not a UV or an IR fixed point, but that this distinction depends on the choice of trajectory. To make contact with our discussion about UV and IR fixed points, one can think of the time t as being related to the RG scale k : $t = 0$ corresponds to $k \rightarrow \infty$, while $t \gg 1$ is related to $k \rightarrow 0$. Moreover, the figure also displays a so-called *limiting cycle*, indicating a recurrent pattern, where the predator and prey population increases and decreases in time-periods: If there is enough prey available, the predator population will increase, consequently leading to a more substantial decrease of prey population, which in turn will also affect the predator population. With less predators around, the prey population can grow again and the cycle restarts. In the context of QFTs limiting cycles are more exotic.

2.3 The FRG

In short, the functional renormalization group acts like a mathematical microscope that allows one to zoom into the microscopic properties of a theory.

This is achieved by interpolating between the bare action S_0 in the UV and the effective action Γ , as defined in Eq. 2.4, in the IR, which, as we have explained before in Sec. 2.1, includes all quantum corrections. The interpolation is realized with a scale-dependent action Γ_k , which can be shown to satisfy the following interpolation equation [16, 17, 18]

$$k\partial_k\Gamma_k[\phi] = \frac{1}{2}\text{Tr} \left(\left(\Gamma_k^{(2)}[\phi] + R_k(p) \right)^{-1} k\partial_k R_k(p) \right), \quad (2.25)$$

where k denotes the RG-scale and R_k acts as both, an infrared and a UV regulator satisfying a set of conditions that we will discuss below. The first term in the brackets $\left(\Gamma_k^{(2)}[\phi] + R_k(p) \right)^{-1}$ corresponds to the field-dependant *non-perturbative* regularized propagator, where $\Gamma_k^{(2)}[\phi]$ is defined as the second functional derivative with respect to the field ϕ . The above equation is also known as the functional renormalization group equation and its conceptual idea is depicted in Fig. 2.4. The derivation of Γ_k follows along similar lines as the derivation of the full quantum effective action Γ with the sole difference that the action S which is used to define the generating functional Z in Eq. (2.1) now includes an additional regulator term ΔS_k , which is given as

$$\Delta S_k = \frac{1}{2} \int \frac{d^d p}{(2\pi)^d} \phi(p) R_k(p^2) \phi(-p). \quad (2.26)$$

This term is chosen such that modes with momentum $p < k$ are suppressed at the level of the path-integral and only those with $p > k$ can be integrated out. The derivation of Γ_k and the functional renormalization group are provided in the appendix. Since the FRG involves the trace of a propagator, it has a one-loop structure and therefore can also be written in the following diagrammatic form

$$\partial_t \Gamma_k[\phi] = \frac{1}{2} \text{Tr} \left(\text{Diagram} \right), \quad (2.27)$$


where the crossed circle corresponds to the regulator insertion $k\partial_k R_k$, while the closed loop corresponds to the traced propagator with the regulator insertion. Let us now comment on the so far unspecified regulator term $R_k(p)$. The regulator term has to be chosen such that on the one hand it acts as an IR regulator by providing a mass term to the low-energy and massless modes with $p < k$. This implies the following condition

$$\lim_{p^2/k^2 \rightarrow 0} R_k(p^2) > 0. \quad (2.28)$$

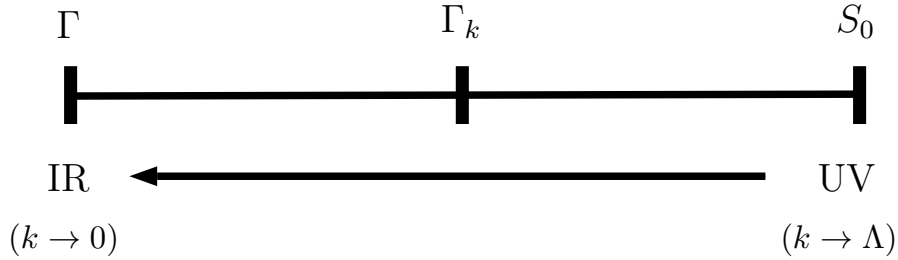


Figure 2.4: Graphical depiction of the philosophy behind the FRG. The scale-dependent effective action Γ_k interpolates between the microscopic action S in the UV and the full quantum-effective action Γ in the IR as the RG scale goes to zero.

Moreover, we want the FRG to interpolate between the microscopic action S , when $k^2 \rightarrow \Lambda \rightarrow \infty$ and the quantum effective action Γ , defined by Eq. 2.4, when $k \rightarrow 0$. See Fig. 2.4 for a graphical depiction of the general idea. This property is only guaranteed if on the one hand

$$R_k(p^2) \rightarrow 0 \quad \text{for} \quad k^2 \rightarrow 0, \quad (2.29)$$

which implies that Γ_k approaches Γ as k goes to zero and

$$R_k(p^2) \rightarrow \infty \quad \text{for} \quad k^2 \rightarrow \Lambda, \quad (2.30)$$

which ensures that the microscopic action S is recovered⁷ in the limit $k^2 \rightarrow \Lambda \rightarrow \infty$, limit in which the path-integral is dominated by the stationary point of the action Γ_k in that limit. This permits to use a saddle-point approximation which selects the classical field configuration and the bare action $\Gamma_{k^2 \rightarrow \Lambda} = S + \text{const.}$ A regulator, often employed in the FRG literature, is the Litim regulator [21, 22]

$$R_k(p) = (k^2 - p^2)\theta(k^2 - p^2). \quad (2.31)$$

There exist also other possible choices of regulators. We refer to [23] for a discussion on possible choices of regulators. Solving the FRG in Eq. 2.25 would yield an expression for the full effective action, which alternatively could also be derived from the path-integral formalism. Note, however, that the definition of Γ_k provided by the FRG does not make any reference to a path-integral even if its derivation involved one. Hence, the FRG can be viewed as an alternative way to define a QFT. As an example that the two definitions of the effective action agree, it is possible to

⁷Reconstructing the correct bare action S from the effective action Γ_k , at some finite k , is challenging as the RG procedure is only defined for flows to lower values of k . This is because lowering k is related to having integrated out massive degrees of freedom. Increasing k is therefore non-trivial as one does not have knowledge about the degrees of freedom that could have been integrated out. Obtaining the microscopic action S from the effective action Γ_k is known as the reconstruction problem and has been addressed in [19, 20].

derive the perturbative one-loop effective action from the functional RG. Assuming that the full effective action admits the following perturbative expansion

$$\Gamma_k[\phi] = S[\phi] + \sum_{n=1}^{\infty} \Gamma_{n,k}[\phi], \quad (2.32)$$

it is possible to identify

$$\partial_t \Gamma_{1,k} = \frac{1}{2} \text{Tr} \left(\frac{\partial_t R_k}{S^{(2)} + R_k} \right) = \frac{1}{2} \partial_t \text{Tr} \ln (S^{(2)} + R_k), \quad (2.33)$$

due to the one-loop character of the effective action. Solving this equation and taking the $k \rightarrow 0$ limit gives the well-known perturbative one-loop result for the effective action

$$\Gamma^{\text{1-loop}}[\phi] = S[\phi] + \frac{1}{2} \text{Tr} \ln (S^{(2)}[\phi]) + \text{const}, \quad (2.34)$$

where const is a constant of integration that follows from Eq. 2.33. Accessing the full non-perturbative Γ in the $k \rightarrow 0$ limit requires solving Eq. 2.25. Since the FRG is a partial differential equation, solving it requires the specification of an initial boundary condition at some scale $k^2 = \Lambda$. In practice, the FRG cannot be solved exactly. Gaining insight about non-perturbative physics by solving the flow equation therefore requires an approximation scheme. A standard approximation scheme involves expanding Γ_k in a basis of local field monomials \mathcal{O}_i allowed by symmetries such that

$$\Gamma_k = \sum_i g_i(k) \mathcal{O}_i, \quad (2.35)$$

where the couplings g_i span the full infinite-dimensional theory space. To perform practical computations with the FRG, the infinite-dimensional theory space is truncated to a finite number of couplings and corresponding field monomials. This implies that the flow of Γ_k can be written as

$$\partial_t \Gamma_k = \sum_{i=1}^n \beta_{g_i} \mathcal{O}_i, \quad (2.36)$$

where β_{g_i} is just the beta function of the coupling g_i . The sum over operators $g_i \mathcal{O}_i$ is truncated at some finite n . The only two ingredients required to perform practical computations with the FRG are thus the regulator R_k that has to be chosen such that it satisfies the three criteria mentioned above and a truncation of the effective action Γ_k . The beta functions of the individual couplings are isolated by employing some projection scheme such as $\partial/\partial \mathcal{O}_i$. The projection scheme is also applied to the right hand side of the FRG in Eq. (2.25), which can be expanded in a basis of field monomials \mathcal{O}_i , as can be for instance seen by expanding the field-dependent

propagator term $\left(\Gamma_k^{(2)}[\phi] + R_k(p)\right)$ in powers of the fields.

Approximating the full Γ_k by a finite set of local field monomials introduces spurious truncation artifacts. Consequently, one has to be careful when searching for fixed points where $\beta_{g_i} = 0$. Not all zeros of the beta functions will also be physical fixed points. In order to distinguish between physical fixed points, which imply universality and a set of critical exponents, and truncation artifacts, a set of necessary but not sufficient criteria can be put in place. For instance, the critical exponents associated to a physical fixed point should display apparent convergence when expanding the truncation. Enlarging the truncation should, thus, not induce new relevant directions.

We will discuss these details more carefully when applying the FRG in practice in a later section. Note also that the renormalization techniques developed in this section heavily relied on the existence of a background with respect to which it was possible to define a scale. In the case of quantum gravity, which is supposed to be a theory of space-time the notion of a background has to be absent. This makes the application of renormalization group techniques highly non-trivial as we will also discuss later on. In case the reader is interested in further details on the FRG, he or she may consult [24, 25, 26, 23, 27, 28, 29]

3 The continuum limit in Quantum Gravity

A theory of quantum gravity is expected to resolve the inconsistencies of GR such as the existence of black hole singularities or the big bang singularity. The naive way to quantize gravity fails, however. In order to tame the divergences that result from the naive quantization, a number of quantum gravity approaches introduce a discreteness scale, which is either fundamental or merely introduced as a technical way to deal with the divergent path-integral. The path-integral then simplifies to a sum over discrete configurations. In the following we are going to sharpen these general points by providing an overview of the standard problems encountered when quantizing gravity and argue that discreteness at the level of configurations that are summed over in the path-integral does not necessarily imply discreteness at the level of the resulting geometry. We are going to provide a brief summary of some of the arguments put forward to motivate a fundamentally discrete quantum space-time.

3.1 A general overview

The Standard Model of particle physics offers a very successful framework to unify three of the four fundamental forces in nature, the weak force, the strong force and the electromagnetic force. The quantum formulation of the fourth known force, gravity, has so far stayed elusive. While there is no proof that the gravitational force is indeed quantized at very short distances, there exist a number of heuristic arguments as to why this has to be the case. The appearance of singularities inside of black holes as well as the big bang singularity are often named as standard examples to motivate the need for a theory of quantum gravity, that can ultimately resolve these shortcomings of classical General Relativity. First attempts to formulate a theory of quantum gravity using the same strategies that were so successful when formulating the Standard Model failed. Mainly, this is due to the fact that Einstein gravity is perturbatively non-renormalizable and hence the introduction of new counterterms at every loop order in order to remove divergences renders the theory unpredictable. Indeed, while 't Hooft and Veltman were able to show that gravity coupled to scalar matter already features divergences at one-loop, in the pure gravity case some miraculous cancellations led to an on-shell one-loop finiteness of Einstein quantum gravity [30]. Ultimately, Goroff and Sagnotti showed that pure gravity is two-loop divergent [31]¹. The quest for a predictive theory of Quantum

¹In principle some miraculous cancellations can still occur at higher-loop orders. A full proof that infinitely many counterterms are required to cancel divergences is still missing.

Gravity has sparked a very intense research program focusing on different attempts to make sense of the quantization of the gravitational field. The different potential theories for Quantum Gravity can be partitioned into two sets. On the one hand there are those theories that assume that gravity at shortest scales is fundamentally discrete and on the other hand there are those that assume a continuum space-time at shortest distance scales.

It is possible to identify two main motivations as to why space-time at very short distances might be fundamentally discrete. One argument is of technical nature and is related to the fact that the absence of a UV cut-off in a path-integral approach to Quantum Gravity leads to divergences. Introducing a scale at which space-time is fundamentally discrete, is one possibility to get rid of the usual divergences appearing in local QFTs. Another motivation to consider a fundamentally discrete theory comes from black-hole entropy arguments. Since works by Bekenstein and Hawking in the 70's sparked the field of black-hole thermodynamics [32, 33, 34, 35], it is known that it is possible to associate an entropy to a black hole by dividing the area of a black hole horizon by the Planck length squared, i.e.,

$$S_{BH} = \frac{A}{\ell_p^2} = \frac{c^3 A}{4G\hbar}, \quad (3.1)$$

where the subscript is due to the fact that this entropy has been labeled Bekenstein-Hawking entropy. At first, the above relation was only interpreted as an analogy to the concept of entropy appearing in classical thermodynamics, even though intuitively it makes sense to assign an entropy to black holes. Typically entropy refers to the lack of information one has about a system, which is indeed of relevance to black holes, where information inside the black hole is screened to external observers by the horizon. With the discovery by Hawking that black holes radiate and it is possible to assign a temperature to these systems [36], black-hole thermodynamics was finally put on a firm ground [37]. Since then, a plethora of different interpretations of black-hole entropy have been investigated. One interpretation is to understand the Bekenstein-Hawking entropy in terms of small bits of information carried by Planck-sized patches of the horizon. For a black hole with a horizon of size A there are consequently $2^{A/\ell_p^2}$ microstate configurations. The associated entropy is then expressed as $S = \log_2(2^{A/\ell_p^2}) = A/\ell_p^2$. From the fact that the horizon area is discrete one also is led to the conclusion that space-time itself is discrete. Alternatively, it also possible to understand black-hole entropy in terms of so-called entanglement entropy. See [38] for a review. The idea behind associating the Bekenstein-Hawking entropy with entanglement entropy is that since a black hole is created by the collapse of some form of matter, the degrees of freedom within the black-hole horizon must be correlated with the degrees of freedom outside the horizon. An observer, however, can only access information about the degrees of freedom *outside* the horizon. The entanglement entropy is obtained by tracing out the internal degrees of freedom of a black hole, which are not accessible to an external observer. It turns out that the entanglement entropy is proportional to the area of the black-hole horizon with a coefficient that is UV-divergent if no appropriate UV-cutoff is introduced.

This divergence can either be absorbed in the Newton coupling G [39] or tamed by introducing a space-time that is fundamentally discrete.

Nonetheless, fundamentally discrete theories face a series of challenges. One consists in recovering diffeomorphism invariance at low energies. Another one lies in the fact that from an EFT point of view, close to the cut-off scale one would expect a loss of predictivity: Physics in the IR is described by only a few interactions, as most interactions are suppressed by the cut-off scale. In the UV, however, all infinitely many couplings allowed by symmetries contribute to the dynamics [40]. As a consequence, some mechanism is required in order to relate these couplings to render the theory predictive by only having a finite number of free parameters left to fix. These aspects can be remedied if discreteness is merely introduced as a technical tool. In that case the physics results from taking the continuum limit. Building on the notions introduced in the previous section, the continuum limit corresponds to a fixed point of a renormalization group flow. Not only may diffeomorphism invariance be recovered² by the fact that the cut-off is removed, but an RG fixed point also features universality, thus introducing infinitely many relations between the couplings and leaving only a finite number of relevant parameters to be measured. The question of whether the continuum limit in quantum gravity is of relevance or not is a highly-debated one.

3.2 Background Independence and the Renormalization Group

One of the great difficulties associated to a continuum limit in Quantum Gravity is the fact that unlike the gauge forces described by the Standard Model, gravity is a force describing the dynamics of space-time *itself*. Hence, background-independence should be a crucial ingredient of any theory of quantum gravity. This requirement comes with a baggage of difficulties. In the absence of a background, setting up a renormalization group flow becomes very challenging, as the absence of a background also implies the lack of scales. The notion of scales and being able to hierarchically organize degrees of freedom in terms of these scales is, however, at the heart of the renormalization-group approach. Setting up a renormalization group flow, which allows one to connect a given UV theory to the IR, becomes difficult. When discussing the continuum limit in different theories of quantum gravity in the following, we will discuss different strategies to circumvent these issues.

²Note that this does not necessarily have to be the case. The continuum limit could for instance also correspond to Horava-Lifshitz gravity, a continuum theory of quantum gravity which explicitly breaks diffeomorphism invariance in the UV.

3.3 The path integral and sum over histories

So far we have discussed that the standard way to quantize gravity fails and an appropriate regulator that tames the divergences has to be introduced. Let us now shortly review the expression that several theories of quantum gravity attempt to make sense of.

A number of approaches to Quantum Gravity build on the path-integral formalism corresponding to a *sum over histories*. The quantum gravitational path-integral is schematically given as

$$Z_{\text{QG}} = \sum_{\text{topologies}} \int \mathcal{D}g e^{iS_{\text{Gravity}}}, \quad (3.2)$$

where the topologies might or might not fluctuate and the integration is performed over all physical four-geometries³. S_{Gravity} is supposed to be the fundamental action of space-time and could denote the Einstein-Hilbert action S_{EH} but doesn't have to. In principle one could replace the Einstein-Hilbert action by a different action possibly even including gravitational degrees of freedom different from the metric, as long as the low-energy effective theory is given by the Einstein-Hilbert action⁴. The debate of what exactly fluctuates due to gravitational fluctuations is still ongoing, for instance there is also no clear reason as to why the deep-UV dimension of space-time should be fixed to four. The transition amplitude from a state s characterizing a space-time manifold \mathcal{M} equipped with a metric g to a state s' describing a space-time manifold \mathcal{M}' with metric g' is then computed in standard fashion as

$$\langle s|s' \rangle = \sum_{\text{topologies}} \int_{g(\mathcal{M})}^{g'(\mathcal{M}')} \mathcal{D}g e^{iS_{\text{Gravity}}}, \quad (3.3)$$

where the integral is performed over all four-geometries connecting the two boundary manifolds \mathcal{M} and \mathcal{M}' , making the sum-over-histories interpretation more evident. While the path-integral approach to quantum gravity is conceptually intriguing since it allows for a clear interpretation of gravitational fluctuations as a sum-over-all histories, it is an ill-defined expression when using standard perturbative techniques. One of the reasons is that the measure term is an ill-defined quantity leading to the standard UV divergences of QFT. A number of different approaches to quantum gravity provide different solutions to remedy the problems related to the naive path-integral approach to Quantum Gravity, relying on a non-perturbative treatment

³One could argue, however, that the path-integral should be performed over all four-geometries, or maybe even over all geometries of any dimension and that the gravitational action should be such that these unphysical geometries interfere destructively with each other. This is exactly the stand-point taken by causal set theory, as we will see later on.

⁴In that regard, it is important to mention that even if Z_{QG} is not UV-complete, one can still make sense of it from an EFT point of view. For a review on general relativity as an effective field theory the reader may consult [41, 42]. One notable prediction is the derivation of quantum gravity corrections to the Newtonian potential [43].

of the Einstein-Hilbert action. Ultimately, a consistency test that any theory of quantum gravity has to pass is that it has to feature a continuum limit that allows one to recover the well known IR physics described by the Einstein Hilbert action. In the following, we will introduce the continuum limit and the associated challenges in obtaining it in a number of different quantum gravity approaches. This discussion will also allow to highlight the difference between discreteness at the kinematical level of configurations that enter the path-integral

3.4 Asymptotically Safe Quantum Gravity

Arguably, the most conservative approach to quantize gravity is provided by the asymptotic safety scenario of quantum gravity, as it does not require the inclusion of new degrees of freedom or the introduction of physical discreteness at short distance scales. Here, the underlying assumption is that, even though quantum gravity is perturbatively non-renormalizable it might be non-perturbatively renormalizable. As such, asymptotic safety is a generalization of asymptotic freedom, where couplings attain a vanishing fixed point value at high-energies. The concept of asymptotic safety is, therefore, not only limited to quantum gravity but is much more general⁵. Asymptotic safety corresponds to a realization of quantum scale symmetry at the Planck scale, where quantum gravity effects are expected to become relevant [45, 46]. Quantum scale symmetry is realized if the canonical scaling and the quantum scaling of couplings are evened out. This implies that at least one of the couplings of the theory attains a finite fixed point value such that gravity could be non-perturbatively renormalizable.

Physically, asymptotic safety predicts that beyond the Planck scale the equations governing the fundamental nature of space-time remain the same at energy scales beyond the Planck scale. Another way to interpret the scale invariance entailed by asymptotic safety is that space-time at shortest distance scales becomes fractal-like since couplings become independent of the scale at which they are probed as they reach their fixed point values. Zooming in on space-time thus no longer changes its fundamental description giving rise to a fractal-like space-time. In relation to this point, it is also possible to argue that asymptotic safety features a minimal length scale [47, 48]. Length scales below this scale cannot be probed as space-times 'looks' the same. Thus, asymptotic safety can be regarded as a continuum theory that nonetheless features elements of discreteness.

One of the key consequences of quantum scale symmetry is the enhanced predictivity it entails for the underlying theory. Quantum scale symmetry can be regarded as an additional imposed symmetry that restricts the number of free parameters to a finite one. This is related to the discussion on relevant and irrelevant parameters in the previous chapter: The critical hypersurface introduced in Sec. 2 is finite-dimensional such that only a finite number of parameters have to be fixed by experiment. Tech-

⁵As an example, in $2 < d < 4$, $O(N)$ models have a non-trivial fixed point known as the Wilson-Fisher fixed point [44].

nically, evidence for the existence of a non-trivial UV fixed point at which quantum scale invariance is realized is gathered with the FRG, also introduced in the previous section and has been initiated with the seminal paper [49]. Here, a UV fixed point has been found in the so-called Einstein-Hilbert truncation that only includes two couplings, the Newton constant G_N and the cosmological constant Λ . Studies with the FRG have collected evidence point towards the existence of a gravitational universality class, which has been dubbed Reuter universality class, within different truncations of the full theory space [50, 51, 52, 53, 54, 55, 56, 57, 58, 59, 60]. There exists now an increasing consensus in the literature that the Reuter universality class is characterized by three relevant directions, even though recently there has it has also been claimed that the dimension of the critical hypersurface of asymptotically safe quantum gravity could be four [61]. Another key challenge of Asymptotic Safety concerns the unitarity of the theory at the fixed point. General relativity can be shown to be renormalizable if an R^2 term, where R is the Ricci scalar, is introduced. However, the inclusion of such a term introduces a so-called *ghost* which renders the theory non-unitary, violating a basic axiom of quantum mechanics, whereas probabilities are conserved.

In Asymptotic Safety it is expected that higher-order curvature terms are turned on, i.e., contribute to the dynamics of the theory at the fixed point. The appearance of ghosts, which is related to the existence of additional poles, besides the pole located at zero momentum corresponding to the massless graviton mode, in the graviton propagator could, however, be avoided if the momentum-dependent interactions causing the additional poles can be resummed to yield a non-local function. Challenges related to unitarity can be addressed the study of so-called form factors, which not only depend on the coarse-graining scale k but also on the momenta of the fields. For studies in this direction consider [62].

One of the strengths of the asymptotic safety program for quantum gravity is that it is straightforwardly possible to study the interplay of gravity and matter [63, 64, 65, 66] and derive potential phenomenological implications [67, 68, 69, 70, 71, 72, 73, 74, 75, 76]. Studying gravity-matter systems is also of interest as it allows to put bounds on the matter content by demanding that the fixed point be not destroyed by the inclusion of matter [63, 65]. As an example, in QCD, asymptotic freedom is destroyed when too many quarks flavors are added. Studies of gravity-matter systems have been performed in For a more detailed account of Asymptotic Safety we advise the reader to consult the textbooks [77, 78] and the reviews [79, 80, 81, 82, 66, 83, 84, 85, 86, 87, 88].

For the discussion on the relevance of the continuum limit in different quantum gravity approaches, the crucial take-away message for the reader is that even though the configurations that enter the path-integral of asymptotically safe quantum gravity are continuous four-geometries, the quantum scale invariance entailed by asymptotic safety introduces a minimal length.

3.5 Euclidean Dynamical Triangulations

The EDT program of Quantum Gravity falls into the family of theories of Quantum Gravity that aim to quantize the Einstein-Hilbert action non-perturbatively by introducing a lattice, i.e., a minimal length scale which takes the role of a regulator term. Thus the physical content of the theory is obtained by removing the regulator by sending the lattice cut-off to zero. The basic idea of EDT is that continuum GR can be discretized in terms of equilateral four-simplices⁶ that are glued together in order to form four-dimensional manifolds. As such it can be regarded as an attempt to formulate a lattice version of quantum gravity, allowing for a full non-perturbative treatment of the theory. As usual for theories defined on a lattice, the actual physics emerges when taking a proper continuum limit, as the effects of the discretization are washed out. The hope of this program is that the continuum limit corresponds to a theory of continuum quantum gravity, which could well be Asymptotic Safety. In two dimensions this program is fully successful [89, 90, 91, 92, 93, 94], reproducing results that are compatible with ones obtained via the quantization of gravity in the continuum by means of the Liouville formalism, which will be presented in a forthcoming section. The reason that gravity is solvable in two dimensions lies in its topological nature in two dimensions. There are no local fluctuating degrees of freedom.

The idea of triangulating space-time manifolds is borrowed from Regge calculus [95]. In contrast to Regge calculus, however, where the edge lengths of the triangles are allowed to fluctuate, EDT posits equilateral triangles of edge length a , in the case of two-dimensional quantum gravity. We refer to [96, 97] for an introduction to Regge calculus.

A triangulation consisting of N_4 four-simplices⁷ that are glued together in such a way that said triangulation consists of N_0 vertices, is weighted with the exponential of the following action

$$S[T] = -\kappa_0 N_0(T) + \kappa_4 N_4(T), \quad (3.4)$$

where κ_0 is related to the inverse bare Newton coupling while κ_4 is a function of both, the bare cosmological constant and the continuum Newton coupling. Vertices correspond to 'meeting points' of four-simplices. Intuitively, a triangulation T_1 with a given number of four-simplices N_4' and vertices N_0' will have a larger overall degree of local curvature than a triangulation T_2 with the same number of four-simplices N_4' but with a larger number of vertices $N_0'' > N_0'$. This intuition is made clear by introducing the so-called deficit angle. In the absence of matter, we would thus expect the former triangulation T_1 to be less favorable than the latter configuration T_2 , as T_2 is closer to the classical solution corresponding to a flat space-time. This expectation is indeed reflected by the above action, where a triangulation with a large

⁶A four-simplex can be thought of as being a four-dimensional triangle. A three-simplex for instance corresponds to a tetrahedron, while a two-simplex is a triangle.

⁷A four-simplex can be regarded as a four-dimensional generalization of a triangle.

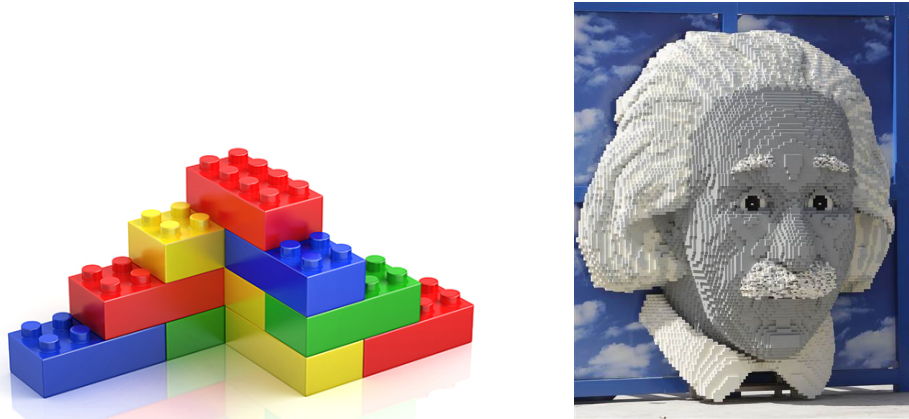


Figure 3.1: The principle behind the continuum limit in dynamical triangulations: In the figure above, a three-volume is approximated by building blocks with a certain edge length a . The edge length of the buildings is continuously taken to be smaller, while demanding that the overall volume remains invariant under these rescalings. In particular, the continuum limit allows to completely remove the discretization effects by rescaling the building blocks to have vanishing edge length. The picture of Einstein's head on the right, for instance, already resembles that of a continuum head. The figure on the left is credited to Getty Images. The Einstein head on the right can be found at Legoland Florida.

number of vertices will be ultimately favored in the path integral since triangulations are weighted as follows

$$Z = \sum_{\text{random triangulations}} \frac{1}{s(T)} \exp \{ - (-\kappa_0 N_0(T) + \kappa_4 N_4(T)) \}, \quad (3.5)$$

where $s(T)$ is a symmetry factor accounting for the fact that there are distinct ways of gluing four-simplices while obtaining the same triangulation T . In other words, one can relabel the simplices and still end up with the same triangulation. The fact that configurations with larger overall curvature tend to be suppressed in the path-integral is also analogous to what happens in the continuum path-integral formulation of Euclidean Quantum Gravity.

Having argued [95, 98] that the action $S[T]$ in Eq. (3.4) is indeed a discretized version of the Einstein-Hilbert action, it is important to stress once again that the discretization introduced by the lattice is of a merely technical nature as, ultimately, one is interested in the continuum limit, where the lattice spacing can be removed, as is usual for lattice theories in general. Concretely, the continuum limit is of interest because it allows to rescale the four-simplices to have infinitesimally small edge length such that the discretization effects can be fully removed. To make this point clear consider Fig. 3.1 which schematically shows how the continuum limit allows to remove the discretization effects.

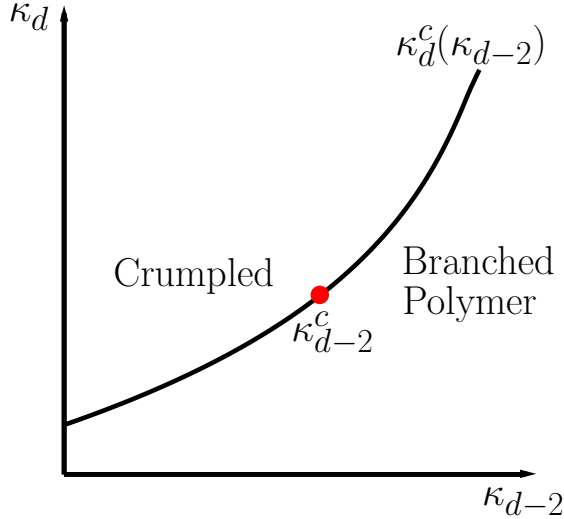


Figure 3.2: Phase diagram of DT uncovered from Monte Carlo simulations. The parameter κ_4 needs to be tuned to a critical value in order find the continuum limit.

In EDT the infinite volume limit is obtained by tuning κ_4 to the critical line $\kappa_4^c(\kappa_2)$ ⁸. When κ_4 approaches the critical line from above it can be shown that the discrete four-volume grows as [99]

$$\langle V \rangle \sim \frac{a^d}{\kappa_4 - \kappa_4^c}, \quad (3.6)$$

diverging at exactly the critical line. In order to keep the physical four-volume $\langle V \rangle$ fixed, the cut-off a has to be removed. We will discuss dynamical triangulations in more detail in an upcoming section, where we will also illustrate why tuning κ_4 to the critical line $\kappa_4^c(\kappa_2)$ gives access to the continuum limit. For now it is sufficient to just note that κ_4 is send to a critical line leaving κ_2 as the only tuneable parameter to find an interesting continuum phase resembling Einstein-Hilbert gravity. The phase space of euclidean dynamical triangulations has been explored in [100, 101] and the phase diagram depicted in Fig. 3.2 has emerged from these studies, where a critical point (κ_2^c, κ_4^c) separates two phases by means of a first order phase transition. The different phases can be quantified in terms of different observables that allow for comparisons with the continuum. One such observable is the Hausdorff dimension d_H . The Hausdorff dimension defines how the volume of a sphere r scales with the volume V . In the case of a four-dimensional continuum space-time the Hausdorff dimension agrees with the topological dimension. Hence, a good indication for a continuum phase of gravity is to find $d_H = 4$. However, none of the two phases identified by euclidean dynamical triangulations have turned out to be related to

⁸ $\kappa_4^c(\kappa_2)$ corresponds to a critical line as κ_2 is a free parameter that can be tuned freely. The infinite volume limit is independent of the value that κ_2 takes.

a four-dimensional continuum gravity phase [102, 103, 104, 105]. At small values of $\kappa_2 < \kappa_2^c$ the lattice continuum limit corresponds to a so-called crumpled phase with no extended space, characterized by an infinitely large Hausdorff dimension, while at large values of $\kappa_2 > \kappa_2^c$, the continuum phase resembles branched polymers with an associated Hausdorff dimension of $d_H = 2$. Moreover, the phase transition between the two phases was found to be first-order [106, 107] making the existence of a continuum limit improbable. The failure to find an interesting continuum limit from the discretized Einstein-Hilbert action Eq. (3.4) has given rise to the causal dynamical triangulations program, which we will introduce in a brief moment.

Nonetheless, some recent studies suggest that an appropriate measure term needs to be taken into account to compensate for the breaking of diffeomorphism invariance due to the discretization introduced by the lattice [108, 109, 110, 111]. This then results in a critical surface $\kappa_4^c(\kappa_2, \beta)$ with two tuneable parameters β and κ_2 , where β is the additional measure term that is introduced.

Dynamical triangulations is an approach to quantum gravity that tries to make sense of the path-integral of quantum gravity by following a discrete strategy. Ultimately, however, one is interested in the continuum limit, where the discretization effects can be removed.

3.6 Causal Dynamical Triangulations

The failure to find evidence for a second order phase transition in four dimensions in (Euclidean) dynamical triangulations has given rise to the causal dynamical triangulations program [112, 113, 114, 115, 116, 117]. For reviews on CDT we refer to [118, 119, 120]. The causal dynamical triangulation approach continues to follow the same methodological line as the dynamical triangulations framework in the sense that one is still interested in a UV fixed point where the lattice cut-off a can be removed giving rise to a continuum theory. As an update to the dynamical triangulations program, a global time foliation is introduced, which can be viewed as a lattice version of global hyperbolicity in general relativity, which allows to uniquely evolve a spatial hypersurface in time⁹. In particular, unlike in EDT, simplices are no longer equilateral, but are characterized in terms of space-like edge lengths, $\ell_p^2 = a_p^2$, and time-like edge lengths with $\ell_p^2 = -\alpha a_p^2$. This distinction allows to construct two different types of four-simplices, which we will denote $(4, 1)$ and $(3, 2)$. The former contains four vertices in a time slice t and one vertex in the neighboring time slice $t - 1$ or $t + 1$, while the latter contains three vertices in a time slice t and two in the time slice $t - 1$ or $t + 1$. Thus, CDT can be viewed as a theory of triangulations of Lorentzian geometries. As such, it is possible to analytically continue CDT triangulations to Euclidean signature and the discretized action of CDT satisfies $iS[LG] = -S[EG]$, where $'LG'$ denotes triangulations of Lorentzian geometries and $'EG'$ corresponds to triangulations of the rotated Euclidean geometries. The action for causal dynamical triangulations is more involved than the one for dynamical

⁹This is closely related to the ADM decomposition of GR.

triangulations introduced before. It is given by [118]

$$S[T] = -(\kappa_0 + 6\Delta)N_0(T) + \kappa_4(N_{4,1}(T) + N_{3,2}(T)) + \Delta N_{4,1}(T) \quad (3.7)$$

and introduces an additional coupling parameter Δ related to the anisotropy parameter α . As a reminder, just as in EDT, κ_0 is related to the bare Newton coupling and κ_4 corresponds to the bare cosmological constant. The coupling space of CDT is therefore larger than the one of EDT and correspondingly also offers a richer phase diagram. The original DT action is recovered for $\Delta = 0$. It is, however, worth emphasizing that the configuration space is still different, so the phase diagrams of EDT and CDT will differ even though the actions agree. The key characteristics of the CDT parameter space have by now been largely revealed [117, 116, 121, 122, 123, 124, 125, 126], showing a phase diagram with four phases depicted in Fig. 3.3. Phase A is the oscillating phase, where the universe fluctuates quickly and adjacent slices are not correlated. Phase B is characterized by the CDT 'building blocks' being concentrated into a minimal number of time slices. Neither phase A nor phase B correspond to our universe. The phase C_{dS} is of most interest, as it exhibits a semi-classical geometry that resembles Euclidean de Sitter space in four dimensions [116, 117, 122]. For larger κ_0 , one observes a first-order phase transition from C_{dS} to A, while for lower values of the asymmetry parameter Δ , a second- or higher-order phase transition to the bifurcation phase C_b , which is characterized by the emergence of local geometry around some vertices of the triangulation, is observed [127, 128, 125]. Moreover, for even lower values of Δ , the bifurcation phase C_b and the phase B are also separated by second- or higher-order phase transition [129]. Of particular interest is the behavior of the model close to the phase boundary of continuous phase transitions, as it is of direct relevance for the definition of a physical large-volume limit. In this limit, the lattice volume diverges such that the discretization effects of the simplices can be removed¹⁰.

Hence, the current goal of the CDT program is to have a renormalization group flow via the de Sitter phase C_{dS} in the space of bare couplings towards an UV fixed point, which characterizes a second-order phase transition, while keeping observable quantities fixed. The existence of such a UV fixed point allows for the edge-length of the simplices to be sent to zero such that the discretization effects can be removed,

¹⁰This applies to lattice theories in general. For instance, in lattice field theory, the 'physical', renormalized mass m_R is extracted from the decay of the two-point function

$$\langle \phi(x)\phi(y) \rangle \propto \exp(-m_R|x-y|) = \exp\left(-\frac{|x-y|}{\xi}\right), \quad (3.8)$$

where ξ is the correlation length. On the lattice, it is only possible to measure dimensionless quantities such that one can only measure the dimensionless combination $am_R = \frac{1}{\xi a}$, whereas the distance $|x-y|$ can only be measured in lattice units. Taking the continuum limit $a \rightarrow 0$, while keeping m_R constant, drives the correlation length measured in lattice units ξ/a to diverge. This is only the case if the phase transition is of second order or higher. To make contact with the discussion above, the correlation length measured in lattice units in our example corresponds to the lattice volume N_4 .

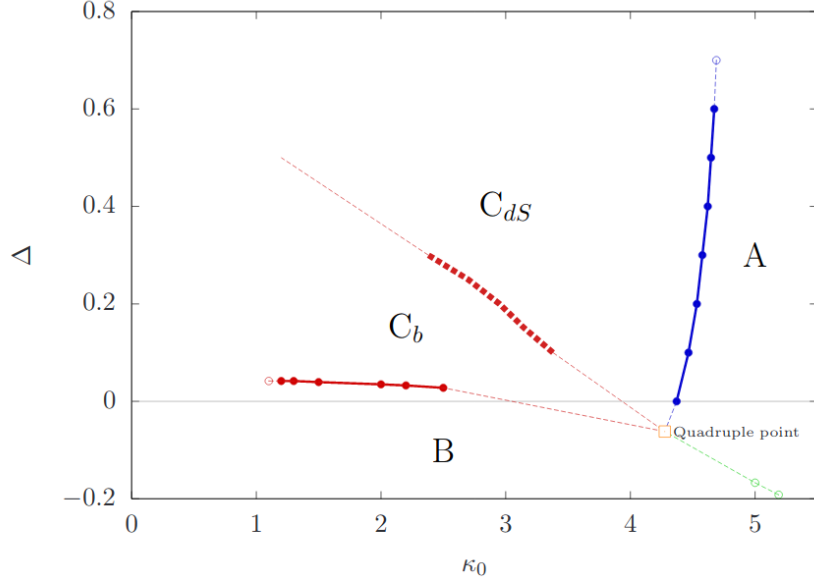


Figure 3.3: Phase diagram of CDT uncovered from Monte Carlo simulations. The parameter κ_4 needs to be tuned to a critical value in order find the infinite volume limit, which allows the edge lengths to be sent to zero, while physical quantities remain finite. This leaves a two-dimensional parameter space, that allows for the phase diagram depicted above. Four phases A, B, C_{ds} and C_b have been identified. Phase A is the oscillating phase, the three volume of the universe fluctuates quickly and adjacent slices are not correlated. In Phase B the simplices are all concentrated at one time slice, in which the Hausdorff dimension is large. This is similar to the crumpled phase in DT. The most interesting of the three phases is phase C. Phase C can be split into two subphases. In phase C, the average three-volume of the universe can be described by an effective minisuperspace action. This minisuperspace action describes a Euclidean de Sitter cosmology. The Hausdorff dimension of this geometry is 4. Figure taken from [130].

while demanding that physical observables, such as $N_4^{1/4}a$, stay finite. Evidence for a second-order phase transition has been found and the current studies focus on exploring the geometry underlying that phase transition.

3.7 Matrix & Tensor Models

The philosophy of the tensor-model approach [131, 132, 133, 134] to Quantum Gravity coincides with the one of dynamical triangulations. Discretization of a continuum space-time is imposed as a technical way to introduce a regularization, which allows

to treat the UV-divergences that appear in a continuum path-integral approach to Quantum Gravity. The key of tensor models is that they generate Feynman diagrams which are dual to random triangulations of space-time, see Fig. 3.4. In order to triangulate a four-dimensional surface a tensor with four indices having certain symmetry properties, which we will not specify at this point, is assumed, where, in simplified words, each index corresponds to one dimension. Uncovering a continuum limit corresponding to a phase of quantum gravity phase in tensor models is still ongoing research. The key, however, is that there exists a relationship between the continuum path-integral of Quantum Gravity and a, yet unknown, path-integral of tensor models

$$\sum_{\text{topologies}} \int Dg e^{-S_{\text{Gravity}}[g]-S_{\text{Matter}}[\phi]} \sim \ln \left(\int DT e^{-S_{\text{tensor}}[T]} \right), \quad (3.9)$$

where $S_{\text{Gravity}}[g]$ corresponds to a fundamental gravitational action, which does not have to be the Einstein-Hilbert action and S_{matter} encodes the matter degrees of freedom of our universe. The question of whether topological fluctuations are actually allowed is still an ongoing research question. The motivation to study tensor models to solve the four-dimensional path-integral for gravity follows from the success of matrix models in two dimensions. In matrix models, which generate Feynman diagrams that are dual to triangulations of two-dimensional manifolds, the question of the continuum limit has already been answered by explicitly comparing for instance critical exponents characterizing the singular behavior of observables that have also been obtained by continuum methods. The generating functional for matrix models is given as

$$F_{\text{MM}}[M] = \ln \left(\int DM e^{-\text{tr}(M^2)+g\text{tr}(M^3)} \right). \quad (3.10)$$

In matrix models the continuum limit corresponds to the so-called double-scaling limit, which we will also explore in more detail in a later section. In short, the double-scaling limit is taken by sending the matrix coupling g to some critical value g_c , while simultaneously assuming the matrix size N to be very large, i.e., $N \rightarrow \infty$. The success of matrix models in recovering two-dimensional Quantum Gravity therefore also provides the motivation to study tensor models in the first place. Indeed, matrix and tensor models generate Feynman diagrams that are dual to two-dimensional and higher-dimensional random triangulations of space-time, respectively. Therefore, matrix and tensor models can be seen as an alternative formulation of Euclidean Dynamical Triangulations. For a review of the connection between matrix models and two-dimensional quantum gravity we advise the reader to consult [135].

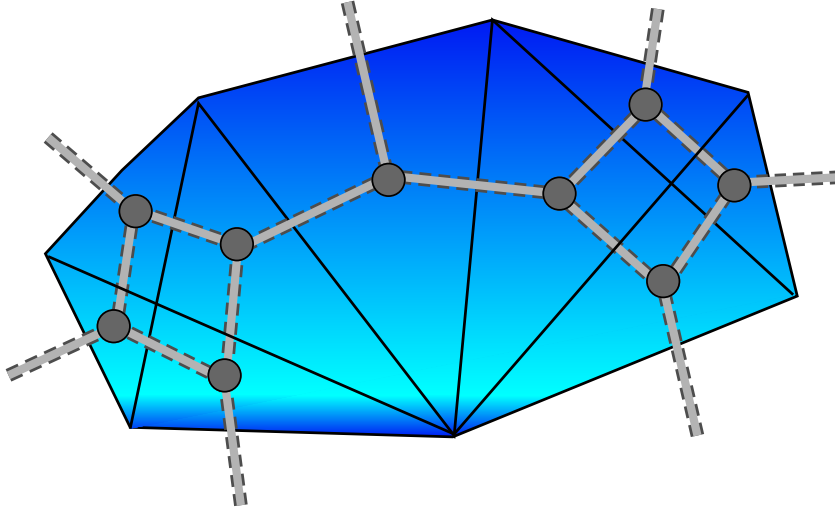


Figure 3.4: Depiction of the duality between the Feynman graph expansion of the free energy of a matrix model and a random triangulation. The vertices in the matrix model correspond to triangles and the propagators to edges of the triangles. The thickened structure of the lines is due to the fact that matrices carry two indices.

3.8 Causal Sets Quantum Gravity

The Causal Sets approach to Quantum Gravity posits the causal nature of space-time as fundamental [136]. For a more detailed account of causal sets quantum gravity, the reader is advised to consult [137, 138, 139, 140, 141, 142, 143]. The minimalistic idea is that space-time geometry can be fully described in terms of the causal structure of a manifold and the specification of a local volume element, known as the conformal mode [136]. As such the assumption is that the space-time structure is described by a partially order, locally finite set of events. The causal structure of a manifold is realized by introducing a partial order relation \prec , which implies the following two conditions

$$\text{Transitivity : } (\forall x, y, z \in \mathcal{C})(x \prec y \prec z \implies x \prec z) \quad (3.11)$$

$$\text{Acylicity : } (\forall x \in \mathcal{C})(x \not\prec x). \quad (3.12)$$

The transitivity condition enforces the usual continuum idea of causal relation, while the acyclicity condition forbids causal loops, which would allow travelling back in 'time'¹¹ These two conditions are intrinsically Lorentzian given that in a Euclidean setting there exists no notion of causal order as space-time points are only space-like separated. The above conditions are not enough to completely fix the causal structure of space-time. It is still necessary to introduce a scale. Otherwise, it is just

¹¹An example of a causal loop would be $x \prec y \prec z \prec x$.

possible to make relative statements about lengths and volumes but to definite ones. For that reason it is also necessary to set a unit-volume and associate a scale to the theory¹². Hence the causal structure is not enough to fully specify the metric degrees of freedom but it is necessary to provide a notion of scale or volume information. This is done by introducing the local finiteness condition:

$$\text{Local finiteness : } (x, z \in \mathcal{C})(\mathbf{card}\{x \prec y \prec z | y \in \mathcal{C}\} < \infty). \quad (3.15)$$

The finiteness condition implies that there is only a finite number of causal points between any two elements of a casual set. It thus introduces a notion of discreteness. There exist two philosophies to interpret the discreteness condition: One is to assume that the discreteness is merely a tool to regularize the continuum path integral of quantum gravity, just as was the case for dynamical triangulations and tensor models, while the other interpretation is to postulate that space-time at the Planck scale is fundamentally discrete¹³. Following the latter line of interpretation, which is the most prevalent in the causal sets community, the Planck length is postulated as the fundamental length scale and continuum physics is emergent in a coarse-graining sense, where the metric is just an effective degree of freedom at scales below the Planck scale. The number of elements of a causal set then corresponds to the space-time volume. Broadly speaking the following interpretation of causal set is set to hold

$$\text{Order + Number = Geometry.} \quad (3.16)$$

This slogan was originally coined by Rafael Sorkin.

Going back to the interpretation of the discreteness condition in Causal Sets, depending on which point of view is taken, one is interested in the continuum limit or not. If the discreteness is seen as a technical tool to regularize the path integral for gravity, like a type of random lattice, physics only appears in the continuum limit. Here, we will be mostly concerned with this interpretation. There are several challenges associated to the continuum limit in causal sets quantum gravity. Schematically, the continuum limit implies the following relation

$$\sum \mathcal{D}C e^{iS[C]} \rightarrow \int \mathcal{D}g_{\mu\nu} e^{iS[g_{\mu\nu}]}, \quad (3.17)$$

¹²A metric g can be rescaled in the following way

$$g_{\mu\nu}(x) \rightarrow \tilde{g}_{\mu\nu}(x) = \Omega(x)^2 g_{\mu\nu}(x) \quad (3.13)$$

such that the line element is given by

$$ds^2 \rightarrow d\tilde{s}^2 = \Omega(x)^2 ds^2. \quad (3.14)$$

Such a rescaling leaves the causal structure invariant ($ds^2 = 0$), independently of $\Omega(x)$.

¹³Note that the fact that space-time at the Planck scale is fundamentally discrete is an additional assumption which does not just follow from local finiteness.

where the causal set path integral is performed over all causal sets C that satisfy the transitivity, acyclicity and finiteness condition. This already brings us to the first challenge: What is the configuration space of Causal Sets? That is, what are the causal sets C that enter the path-integral? It turns out that most causal sets are actually *not* manifoldlike. A manifoldlike causal set, is defined as causal set that could have arisen through a random selection of a set of point from a manifold. This selection process should be such that the volume is locally conserved under Lorentz transformations. This selection process is referred to as sprinkling in the causal set literature and space-time points are selected using a Poisson distribution. Given that most causal sets are not manifoldlike the hope is that the manifoldlike causal sets interfere destructively. Alternatively, the configuration space could also be restricted to just the causal sets that follow from a sprinkling process.

As an additional challenge, the causal set approach of quantum gravity also only allows to make statements about the kinematics, dictated by the three conditions Eq. (3.11), Eq. (3.12) and Eq. (3.15). It could therefore well be that non-manifoldlike causal sets are kinematically allowed but dynamically forbidden. This raises the question on the dynamics of causal sets: What exactly is the action $S[C]$? Assuming that regularization is a technical tool, the action $S[C]$ is ultimately determined by the continuum physics, for instance by the Asymptotic Safety conjecture. Following that line of thought, the schematic continuum limit introduced in Eq. (3.17) could take the following form

$$\sum \mathcal{D}C_{\text{sp}} e^{iS[C_{\text{sp}}]} \rightarrow \int \mathcal{D}g_{\mu\nu} e^{iS_{\text{AS}}[g_{\mu\nu}]}, \quad (3.18)$$

where S_{AS} corresponds to the microscopic asymptotic safety action. There exist two possibilities to search for a continuum limit: Either by Monte-Carlo simulations or using the functional renormalization group introduced in the previous section [143]. Both methods are not suited for Lorentzian studies and hence an additional parameter that allows for an analytical continuation has to be introduced. We refer to [143] for technical details.

3.9 Spin Foams

The spin foam approach to Quantum Gravity aims to provide a framework that is intrinsically background-independent and non-perturbative with no reference to a background geometry at all. The idea is to interpret the sum over all space-time histories as a sum over all boundary configurations obtained in terms of so-called spin networks. Spin networks are kinematical states describing the discrete quantum geometry of space in terms of combinatorial and group-theoretical data and are derived in loop quantum gravity. Spin foams provide a framework to study the dynamical evolution of spin networks with the spin foam amplitudes describing the transition probability between two given spin network states s and s' . For a more detailed account of spin foams, we refer the reader to [144, 145, 146] More generally,

spin foams can be regarded as a lattice gauge theory: Space-time is described as a quantum superposition of geometries weighted by some appropriate amplitude. Hereby, a lattice is introduced in order to deal with the infinite number of degrees of freedom that describe the evolution of a spin network¹⁴ by truncating them using the discretization provided by the lattice. The sum over geometries and topologies then consists in summing over discrete building blocks of space-time. This is very similar to the tensor model approach to quantum gravity, in the sense that spin foams are defined as graphs carrying vertices, edges and faces. The difference, however, is that in spin foams the building blocks also carry group-theoretical data related to the Lorentz group by carrying spins of the unitary irreducible representation of $SU(2)$, which can intuitively be thought of as being related to the area of a building block and intertwiners assigned to the edges and nodes of a spin foam respectively, which carry information about the shape of the building block. Hence, compared to tensor models the building blocks already carry some amount information about the continuum space-time. The question of the continuum limit is highly debated in the spin foams community. One of the early successes of spin foams is the derivation of a semi-classical limit for one spin foam building block corresponding to the Regge action, a discretized version of the Einstein-Hilbert action. The question of how to take the continuum limit in order to recover four-dimensional manifolds, however, is still open for debate. There exist different proposals as to how to make sense of a spin foam path-integral. One possibility would be to sum over all possible foams, that is over all allowed dynamics of spin networks. This way of interpreting the path-integral is the philosophy adopted by the group field theory approach that is discussed below.

Alternatively, a spin foam can be regarded as a regulator. The continuum limit can then be established in the following way: A truncation of fine hypercuboids is considered. Similar to a coarse-graining procedure, the fine hypercuboids are replaced by fewer more coarse and effective ones. The non-trivial aspect of this coarse-graining procedure concerns the mapping of the boundary data, i.e., the spins and intertwiners, to the fine building blocks. This relation is provided by so-called embedding maps, mapping states on the coarse boundary to states on the fine boundary. The exact choice of an embedding map is highly non-trivial [147, 148, 149, 150]. Evidence for a phase transition in spin foams has been reported in [151]. Nonetheless, given the conceptual points mentioned above, we would like to reemphasize, The continuum limit in spin foams is one of the open challenges: While it is possible to obtain discrete GR as a semi-classical limit for large quantum numbers, it is not clear how to obtain a continuum geometry in limit of large lattices. See [152] a recent review on coarse-graining and renormalization in spin foam models.

¹⁴The degrees of freedom in spin-foams are spins and intertwiners.

3.10 Group Field Theory

Group field theories (GFTs) are closely related to tensor models, spin foams and the simplicial quantum gravity models like EDT and CDT. The idea behind GFTs is that a continuum geometry can be recovered from physically discrete atoms of space. Space-time is ultimately recovered by considering large collections of building blocks. In simple words, the picture that GFT proposes is that the universe can be regarded as a quantum fluid, where the microscopic building blocks form a condensate [153], analogous to Bose-Einstein condensation. That is, a continuum space is recovered for a very large number of very small quanta of space-time close to equilibrium, where the equilibrium state corresponds to a yet to be determined many-particles vacuum state. Recovering continuum spaces of physical relevance is still one of the challenges of GFTs. However, using a certain set of simplifications a Friedmann equation with quantum gravity corrections can be recovered from the hydrodynamics of a GFT condensate [154], which replaces the classical cosmological singularity with a quantum bounce. In more technical words GFT is motivated as follows: In the Loop Quantum Gravity formalism space at the quantum level is described by combinatorial graphs, equipped with algebraic data related to the group representation, which for four dimensional quantum gravity models is typically $SO(3,1)$ (or $SL(2, \mathcal{C})$) in the Lorentzian case and $SO(4)$ in the Riemannian case. The graphs carrying algebraic and combinatorial data are called spin networks. Spin networks states can be shown to correspond to many-body states in a second-quantized Fock space, where the quanta making up this Fock space correspond to building blocks of spacetime. The Fock space made up by the discrete building blocks of space is the Hilbert space that underlies GFTs [155]. For a more detailed account of GFTs and its relation to other approaches of quantum gravity, we advise the reader to consult [156].

4 Tensor Models

In the previous section, we have discussed the relevance of the continuum limit as well as its challenges for different approaches to quantum gravity. We have argued that there exists a difference between discreteness at the kinematical level, before the continuum is taken, and discreteness at the dynamical level, after the continuum limit has been taken. Crucially these two realizations of discreteness do not have to imply each other. The path-integral may consist in summing over discrete configurations but the emerging geometry might be continuous

Dynamical triangulations and the tensor model approach to quantum gravity, for instance, exploit the discretization of space-time as a technical way to regularize the divergent path-integral of quantum gravity where the actual physics is found by taking the continuum limit. In that regard, we have also discussed some key points related to the continuum limit in asymptotic safety, dynamical triangulations and tensor models, and how these three approaches are or might be related to each other. Here, we will attempt to make these points more precise and clear, paying particular attention to the tensor model approach to quantum gravity. We will start by discussing the conceptual commonalities of dynamical triangulations, matrix models¹ and continuum quantum gravity in two dimensions. Their relationship is displayed in Fig. 4.1. The idea of the relationships depicted in Fig. 4.1 is the following: A continuum surface can be discretized in terms of small polygons, whose exact shape does not matter. For instance, the surface can be triangulated or discretized in terms of squares. The continuum limit, where the effects of the polygonization can be removed, then corresponds to two dimensional quantum gravity. The dynamical triangulations approach hinges mostly on numerical methods as computations are performed on the lattice. The matrix model formulation of quantum gravity offers analytical insights into the theory of random triangulations as its Feynman diagram expansion can be shown to be dual to polygonizations of two-dimensional surfaces. Matrix models, hence, provide an analytical way to access the continuum limit. Understanding the relationships depicted in Fig. 4.1 will set the stage to discuss higher space-time dimensions, in particular four. Whether the relationships depicted in Fig. 4.1 actually also hold in higher dimensions is still an open research question. Gravity in two dimensions is special, as we will see below, and therefore it is highly non-trivial that a relationship between tensor models, dynamical triangulations and continuum gravity could also persist in higher dimensions. In any case, the discussion on two-dimensional quantum gravity will provide us with a toolbox to discuss higher-dimensions, also shining light on possible subtleties related to the inclusion of topological fluctuations in the path-integral of quantum gravity. Equipped with

¹Here, matrices can just be regarded as tensors with two indices.

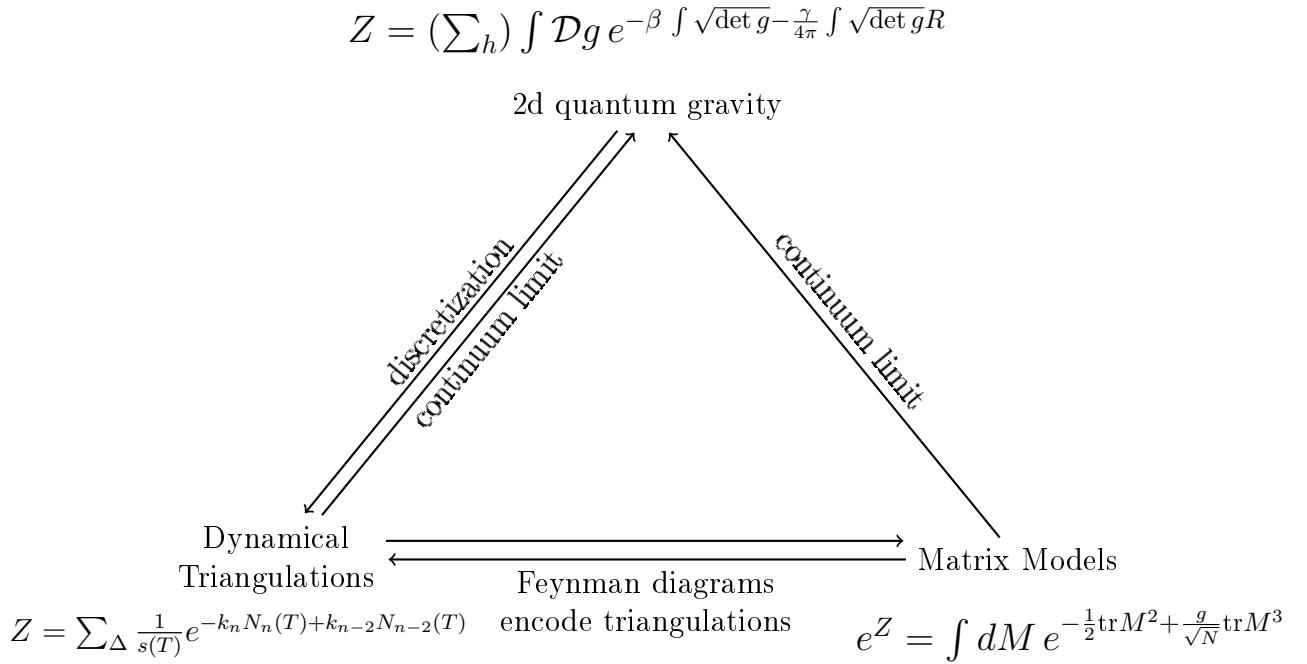


Figure 4.1: General idea of how matrix models relate to Dynamical Triangulations and 2d Quantum Gravity.

the toolbox that we acquired from studying two-dimensional quantum gravity, we will explore the possibility of a continuum limit in tensor models in three and four dimensions that might provide insight into a phase of quantum gravity, potentially corresponding to Asymptotic Safety. The technical tool that we will employ to explore this possibility will be the functional renormalization group introduced in Ch. 2. As already discussed in the previous chapter, the fact that a theory of quantum gravity has to be a theory *of* space-time rather than a theory *on* space-time implies the absence of a notion of a background, which is a crucial ingredient in the usual Wilsonian RG approach introduced in Ch. 2. We will overcome these conceptual difficulties by setting up a renormalization group flow in terms of the tensor size N , which counts the number of degrees of freedom. While the tensor size N no longer corresponds to a local scale, taking N to be the RG scale makes contact with the coarse-graining approach, where the philosophy is to replace many fundamental variables by a few more effective ones. Equivalently, taking the tensor size N as a scale, we will replace large tensors with many entries by more effective tensors with fewer degrees of freedom.

We will, thus, pay particular attention to these conceptual points in the following when discussing the continuum limit in tensor models.

2D Quantum Gravity in the continuum

Our quest to explore tensor models for four-dimensional quantum gravity begins in two dimensions, where gravity is special, allowing us to introduce a set of tools that will be also of relevance for higher-dimensions.

The fact that two-dimensional gravity is special, is already apparent at the classical level, as the classical equations of motion are trivially satisfied. As a consequence, gravity is, on the one hand, purely topological and on the other hand not only diffeomorphism-invariant but also Weyl-invariant, which greatly restricts the physical metric degrees of freedom. This can be seen by considering the Riemann curvature tensor $R_{\mu\nu\rho\sigma}$, which respects the following set of symmetries

$$R_{\mu\nu\rho\sigma} = -R_{\nu\mu\rho\sigma} = -R_{\mu\nu\sigma\rho}, \quad (4.1)$$

$$R_{\mu\nu\rho\sigma} = R_{\rho\sigma\mu\nu}, \quad (4.2)$$

$$R_{\mu\nu\rho\sigma} + R_{\mu\sigma\nu\rho} + R_{\mu\rho\sigma\nu} = 0. \quad (4.3)$$

In any space-time dimension d , the Riemann tensor can be shown to have

$$C = \frac{1}{12}d^2(d^2 - 1) \quad (4.4)$$

independent components. This implies in particular, that in two dimensions the Riemann tensor only admits $C = 1$ independent components.

Gaining a deeper understanding about the Einstein equations in two dimensions allows to better understand why two-dimensional gravity is special. It is therefore of interest to have knowledge not only about the number of independent components of the Riemann tensor but also about its exact form. For this reason, it is instructive to consider a maximally symmetric space-time, that is a space-time that is both homogeneous and isotropic. For such a space-time, it is possible to show that the Riemann tensor only admits one independent component, corresponding to the Ricci scalar R . Indeed it can be shown that $R_{\mu\nu\rho\sigma}$ can be written as

$$R_{\mu\nu\rho\sigma} = \frac{R}{d(d-1)} (g_{\mu\rho}g_{\nu\sigma} - g_{\mu\sigma}g_{\nu\rho}), \quad (4.5)$$

which after contraction with $g_{\rho\sigma}$ also yields the Ricci tensor

$$R_{\mu\nu} = \frac{R}{d}g_{\mu\nu} \quad (4.6)$$

for a maximally symmetric space-time. Similarly, as already pointed out, in two dimensions the Riemann tensor admits $C = 1$ independent components. Therefore, the Ricci tensor of two-dimensional gravity will have the same form as Eq. 4.6, with the exception that in two dimensions R can depend on the space-time position unlike in the maximally symmetric case where R is constant. Since now, in two dimensions

$$R_{\mu\nu} = \frac{R}{2}g_{\mu\nu} \quad (4.7)$$

it follows that the Einstein tensor

$$G_{\mu\nu} = R_{\mu\nu} - \frac{1}{2}g_{\mu\nu}R = 0 \quad (4.8)$$

vanishes trivially, independent of the space-time considered. This is a consequence of the fact that two-dimensional gravity is topological, i.e.,

$$\int d^2x \sqrt{g} R = \chi, \quad (4.9)$$

where χ is the Euler character. In two dimensions the Euler character can be expressed in terms of the number of handles h of the underlying space-time, i.e. $\chi = 2 - 2h$. Hence, there are no local but only topological degrees of freedom in two-dimensional classical gravity.

The fact that the Einstein tensor vanishes identically implies that the two-dimensional cosmological constant also has to vanish in the case of pure gravity. As a result, the classical theory is not only invariant under diffeomorphisms but also possesses an additional conformal symmetry since the classical action is invariant under

$$g_{\mu\nu} = e^{2\omega(x^\mu)} g'_{\mu\nu}, \quad (4.10)$$

where $\omega(x)$ is a space-time dependent parameter. The fact that two dimensional gravity possesses an additional symmetry besides coordinate reparametrization invariance will turn out to have interesting far reaching implications for the quantum theory.

Liouville Gravity

In two dimensions, classical gravity is not only diffeomorphism invariant but also classically conformal. At the quantum level, however, conformal invariance is broken due to the path-integral measure term not being invariant under conformal transformations. In order to restore conformal invariance, one is led to introduce the so-called Liouville action, which renders two-dimensional quantum gravity coupled to conformal matter non-trivial by introducing an additional gravitational interaction on top of the ones included by the Einstein-Hilbert action. The conformal anomaly introduces an additional interaction that has the structure of the Liouville action

$$S_L(\sigma) = \int d^2\xi \sqrt{g} \left(\frac{1}{2} g^{\mu\nu} \partial_\mu \sigma \partial_\nu \sigma + R\sigma + \gamma e^\sigma \right), \quad (4.11)$$

up to some different prefactors. The above action introduces an interaction term $R\sigma$, rendering the quantum theory of two-dimensional gravity non-trivial. Here, σ is the Liouville field corresponding to the conformal mode.

A standard quantity that allows to compare Liouville gravity to dynamical triangulations and matrix models is the so-called *string susceptibility*, which describes how

the partition function scales for fixed large areas. The area can be fixed by including a delta constraint in the path-integral such that

$$Z(A) = \int \mathcal{D}\chi \mathcal{D}g e^{-S} \delta \left(\int d^2\xi \sqrt{\hat{g}} e^{\alpha\phi} - A \right), \quad (4.12)$$

where the measure $\mathcal{D}\chi$ describes the integration over matter fields and $\mathcal{D}g$ the integration over conformal metrics. Here, \hat{g} denotes the background metric in the conformal gauge $g_{ab} = e^{\phi} \hat{g}_{ab}$. For large areas, the scaling of the partition function can be expressed as

$$\lim_{A \rightarrow \infty} Z(A) \sim A^{(\gamma-2)\frac{\chi}{2}-1}, \quad (4.13)$$

which also serves as a definition for the string susceptibility γ . The string susceptibility γ can be determined by a scaling argument presented in the appendix. From that scaling argument it follows that γ is given as

$$\gamma = \frac{1}{12} \left((D-1) - \sqrt{(D-25)(D-1)} \right). \quad (4.14)$$

Here, D corresponds to the so-called *central charge* which can be expressed as $D = 1 - 6/m(m+1)$, where m is an integer $m \geq 2$ indexing the unitary discrete series of conformal field theories. D has been normalized such that the theory with one free boson has central charge $D = 1$. Pure gravity then corresponds to a theory with central charge $D = 0$. To make contact with matrix models, we replace the central charge D by m such that the string susceptibility is given as

$$\gamma = -\frac{1}{m}. \quad (4.15)$$

For pure gravity, $D = 0$ such that $m = 2$. In that case the string susceptibility corresponds to $\gamma = -1/2$. A theory coupled to a conformal 1/2-boson or a fermion can be shown to have a central charge of $D = 1/2$ such that $m = 3$. Such a theory is known as the two-dimensional critical Ising model and has a string susceptibility of $\gamma = -1/3$. The string susceptibility is historically the first indication for a correspondence between matrix models, dynamical triangulations and two-dimensional continuum gravity. Further evidence in favour of this correspondence has been gathered by studying the scaling of observables close to the critical point that is approached in order to take the continuum limit.

Let us finally close the discussion on Liouville gravity by pointing out that it only allows to derive the area scaling for fixed topology given by Eq. (4.13). As an outlook, matrix models for two-dimensional gravity can be solved for both fixed and fluctuating topologies. When the topology is held fixed, the string susceptibility will agree with the one of Liouville gravity. Two-dimensional quantum gravity with fluctuating topology is defined through the matrix model formulation. It is, however, still an open research question whether topological fluctuations actually have

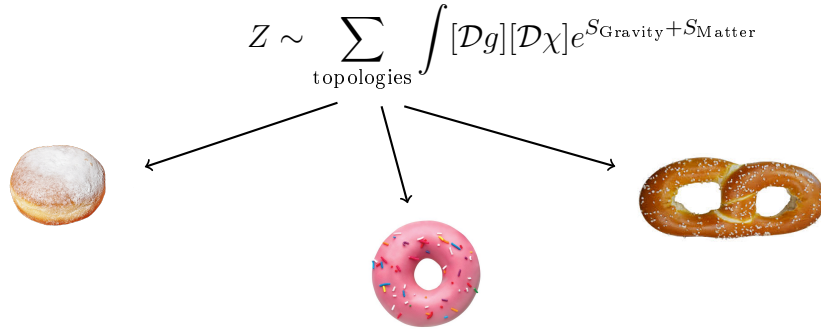


Figure 4.2: The gravitational path-integral including gravitational, matter and topological fluctuations.

to be taken into account. If topological fluctuations are considered, one then finds the following schematic description in two dimensions

$$Z \sim \sum_{\text{topologies}} \int \mathcal{D}g e^{-S_{EH}[g]} = \sum_h \int \mathcal{D}g e^{-\beta A - \gamma \chi}, \quad (4.16)$$

where β is the two-dimensional cosmological constant which is coupled to the area $A = \int \sqrt{\det g}$ and γ is related to the two-dimensional Newton coupling and linked to the Euler character which is given by

$$\chi = \frac{1}{4\pi} \int \sqrt{\det g} R = 2 - 2h, \quad (4.17)$$

where we made use of the Gauss-Bonnet theorem, which states that in two dimensions $\int \sqrt{\det g} R$ is topological and replaced the sum over topologies by a sum over handles h , which in two dimensions denotes the number of holes of a given topology as depicted in Fig. 4.2

Dynamical Triangulations and Quantum Gravity

So far, we have remained in the realm of continuum gravity. We have shown that classical two-dimensional gravity is trivial. At the classical level, 2d gravity is not only diffeomorphism invariant but also Weyl invariant. The latter symmetry is broken at the quantum level and the restoration of the symmetry, by including a Liouville-like action, renders the theory non-trivial. We showed that for fixed topology it is derive a set of critical exponents that describe how the partition function of Liouville gravity scales for fixed large areas. In the following, we will be also interested in considering topological fluctuations. This challenge can be addressed in the matrix model framework. We will see that for fixed topologies, the string susceptibility derived for Liouville gravity can also be recovered in matrix models

Matrix models offer an alternative formulation of two-dimensional quantum gravity². In an attempt to make the relationship between matrix models and quantum gravity clear we will first understand how two-dimensional space-times can be discretized in order to deal with the usual divergences appearing in quantum field theory. This is the cornerstone of not only dynamical triangulations but also Regge calculus, an alternative, and historically, the first way to discretize the path-integral of quantum gravity. The second step will consist in understanding how these discretized surfaces can be naturally generated via a certain family of matrix models. Finally, we will show how to remove the effects of the discretization and take the continuum limit, which encodes all the physical content and argue why the continuum limit corresponds to two-dimensional quantum gravity. *En route* we will highlight the power of matrix models, which are easier to access analytically compared to dynamical triangulations. As a reminder for the reader to not get lost at this stage, the big picture of how all these aspects are related is encoded in Fig. 4.1. The following subsections will be devoted to understanding the different relationships depicted in Fig. 4.1.

Discretizing 2d Quantum Gravity

It is an open question, whether topological fluctuations have to be taken into account in the gravitational path-integral³. If topological fluctuations are considered, the path-integral in two dimensions also contains a sum over h , where h denotes the number of handles. Liouville gravity with fluctuating topology has not been solved as we discussed in the previous section. A framework that allows to study the two-dimensional gravitational path-integral with fluctuating topology is, however, provided by the theory of dynamical triangulations and matrix models, which we will inspect in more detail, foreseeing the relevance of these two frameworks for further discussions on higher dimensions.

The main obstacle in order to solve the path-integral for quantum gravity is that $\int \mathcal{D}g$ is not clearly defined and leads to divergences. One strategy to overcome this obstacle is to *discretize* the path-integral by replacing the sum over topologies and space-times by a sum over random discrete triangulations. Ultimately, the physics content of the theory is accessed in the continuum limit, where the effects of the discretization are removed. In a field theoretical language this suggests the following replacement

$$\sum_h \int \mathcal{D}g \rightarrow \sum_{\text{random triangulations}} . \quad (4.18)$$

²In the context of quantum gravity, matrix models have actually emerged in two distinct ways: On the one hand matrix models were successful as a way to solve two dimensional Liouville Quantum Gravity. On the other hand matrix models also found use in 0-dimensional String Theory, which can be regarded as a theory of surfaces with no coupling to matter.

³Note that even though topological fluctuations might be allowed kinematically at the level of configurations that are summed over in the path-integral it is not clear whether they can appear from a dynamical point of view.

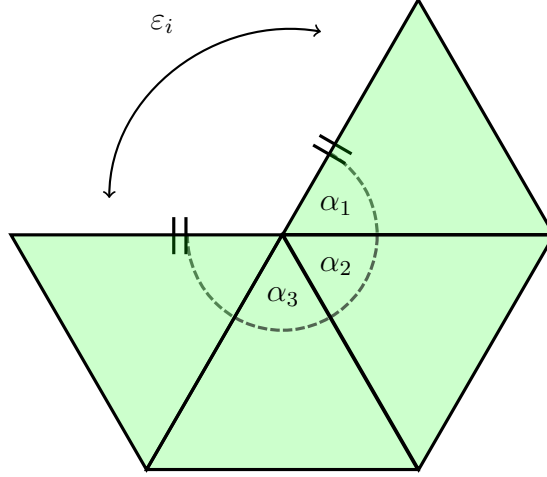


Figure 4.3: Graphical depiction of the deficit angle ϵ_i , which is a way to quantify local curvature in a discrete setting. If $\epsilon_i = 0$, six equilateral triangles meet a vertex. This corresponds to a locally flat triangulation. In the above figure $\epsilon_i > 0$, which implies that in order to connect the triangles at the two extremes, it is necessary to 'cut the page' and the local curvature will be positive. Conversely, $\epsilon_i < 0$ describes negative curvature.

In this context the use of matrix models as a tool to solve two-dimensional quantum gravity will also become more apparent. In order to justify the line of argument proposed by Eq. 4.18, where the gravitational path-integral is discretized, we will first convince ourselves that is indeed possible to rewrite geometric continuum quantities in a discrete way. This will provide some heuristic evidence that random triangulations and matrix models are indeed a way to describe two-dimensional quantum gravity and that Eq. 4.18 is a valid way to tackle the challenges associated to the path-integral of quantum gravity. In that spirit, to support our line of argument that dynamical triangulations provides a way to solve two-dimensional quantum gravity, we will understand how the Ricci scalar can be rewritten in a discrete form in a dynamical triangulations setting. While showing that such an equivalence holds is not sufficient in order to prove that dynamical triangulations in 2D corresponds to two-dimensional quantum gravity as we remain agnostic to the dynamics of dynamical triangulations and quantum fluctuations might spoil this duality, it will provide some motivation in favor of Eq. 4.18. We will address these issues later on.

The space-time volume term in two dimensions can be shown to be discretized as

$$\int_{\mathcal{M}} \sqrt{\det g} \longleftrightarrow \frac{1}{3} \sum_i N_i \frac{\sqrt{3}a^2}{4}, \quad (4.19)$$

where N_i denotes the number of triangles at each vertex i and $\sqrt{3}a^2/4$ is the area of an equilateral triangle of edge length a and is typically set to one by convention

such that the area element in a discrete setting reads

$$\sigma_i = \frac{1}{3} \sum_i N_i. \quad (4.20)$$

In simple words, the quantity on the right hand side represents the total number of triangles. The factor $1/3$ accounts for the fact that we are overcounting the number of triangles as we are summing over all vertices i and each triangle is part of three vertices, as each triangle has three corners.

In order to rewrite the curvature term in a discrete setting it is necessary to introduce a notion of local curvature. One way to do so is via the so-called deficit angle, which intuitively measures the departure from flatness, see Fig. 4.3, and is given by

$$\varepsilon_i = 2\pi - \sum_{t \in i} \alpha_i(t), \quad (4.21)$$

where $\alpha_i(t)$ is the angle of a triangle at a vertex i . In a flat triangulation, the angles of all triangles meeting at a vertex i will add up to 2π , such that $\varepsilon_i = 0$. If $\varepsilon_i < 0$ ($\varepsilon_i > 0$), the curvature will be negative (positive). Assuming equilateral triangles, this expression can be rewritten as

$$\varepsilon_i = 2\pi - N_i \frac{\pi}{3}, \quad (4.22)$$

where $\pi/3$, the angle of an equilateral triangle, is multiplied with the number of incident triangles at a vertex i . The curvature can then be discretized in terms of the deficit angle as

$$\int_{\mathcal{M}} \sqrt{\det g} R \longleftrightarrow 2 \sum_i \text{Vol}(i^{\text{th}} - \text{vertex}) \varepsilon_i \equiv 2 \sum_i \varepsilon_i, \quad (4.23)$$

where $\text{Vol}(i^{\text{th}} - \text{vertex})$ is the volume of a vertex and is set to one by convention, such that the total curvature can be expressed as a sum over deficit angles. Note that the above relationship only holds in two dimensions, where $\int \sqrt{\det g} R$ is a topological invariant. Indeed, the above equality is fixed by demanding that both, the discrete as well as the continuum version give the Euler character, as we will show in a moment.

Plugging ε_i given by Eq. (4.22) into the above expression we obtain

$$\int \sqrt{\det g} R \longleftrightarrow \sum_i 4\pi \left(1 - \frac{N_i}{6}\right), \quad (4.24)$$

such that the generating functional Z is given by

$$Z \sim \sum_{\text{oriented triangulations}} \exp \left(-1/3 \sum_i N_i - \sum_i 4\pi \left(1 - \frac{N_i}{6}\right) \right). \quad (4.25)$$

Let us recall that the discrete version of the area element $\sqrt{\det g}$ is expressed as the total number of triangles which can be written in terms of Eq. (4.19). Combining this with the above equation, it is evident that the Ricci scalar admits the following discrete formulation

$$R_i = \frac{2\pi(6 - N_i)}{N_i}, \quad (4.26)$$

where N_i denotes the number of incident triangles at a vertex i . The reader can indeed check that $\sigma_i R_i$ yields Eq. (4.24). The dependence of the discrete Ricci scalar on the number of incident triangles captures its local nature. For $N_i = 6$ the triangulation is locally flat at the vertex i , while for $N_i > 6$ ($N_i < 6$) the curvature is negative (positive). Using some identities relating the total number of vertices, edges and faces, which are non-local quantities to the number of incident triangles at each vertex i it is possible to rewrite the discrete Einstein-Hilbert action in a more convenient form. Rewriting the discretized Einstein-Hilbert action in terms of vertices, edges and faces has the benefit that they can be related to the topological Euler character, something which is not evident from the current form, where we have expressed the Einstein-Hilbert action in terms of local properties at the incident vertices.

The first step in the derivation consists in realizing that each edge is shared by two triangles such that we can relate the total number of edges to the number of incident triangles in the following way

$$2E = \sum_i N_i. \quad (4.27)$$

Another way to understand the above expression is by multiplying the total number of triangles by three, which is the number of edges of each triangle. As argued above the total number of triangles is given by $1/3 \sum_i N_i$.

Discrete Quantum Gravity

Having hopefully convinced the reader that it is possible to rewrite geometrical quantities in the continuum in a local setting, we will now explore the relationship between dynamical triangulations and two-dimensional quantum gravity. The generating functional for dynamical triangulations takes the following form [157]

$$Z = \sum_{\text{oriented triangulations}} \frac{1}{s(T)} e^{a_0 N_0 + a_- N_- + a_\Delta N_\Delta}, \quad (4.28)$$

where N_0, N_- and N_Δ are respectively the number of vertices, links and triangles and a_0, a_-, a_Δ are free parameters and $s(T)$ is a symmetry factor, which follows from the fact that there are several ways to obtain the same triangulation, just by permuting the vertices, edges and faces of the triangles. The vertices v , edges e and faces f used to built the surface are taken from the labeled sets

$v = \{v_1, \dots, v_{N_0}\}$, $e = \{e_1, \dots, e_{N_-}\}$ and $f = \{f_1, \dots, f_{N_\Delta}\}$; for this reason the symmetry factor is given by $s(T) = N_0!N_-!N_\Delta!$. Relabeling of the triangulation can be seen as a discrete version of diffeomorphism-invariance in the continuum. The configuration space over which one is summing contains only oriented triangulations in order to forbid non-Riemannian manifolds such as the Möbius strip. Moreover, the edge length is kept fixed, in contrast to Regge calculus, where the edge length is allowed to fluctuate [97]. The above path-integral can be understood intuitively as one adds all the ingredients required to build a triangulation with a discrete notion of local curvature. It is, however, clear that these ingredients (the vertices, links and triangles) cannot be independent from each other as a triangle is constructed from vertices, links and edges. This is also what one expects from trying to make contact with the continuum formulation of the Einstein-Hilbert theory of quantum gravity, which only contains two free parameters, the Newton coupling and the cosmological constant. Indeed, the following identity relates the number of links to the number of triangles

$$3N_\Delta = 2N_-, \quad (4.29)$$

which can be understood from the observation that each face of a triangle contains three edges that are each shared by two triangles. Taking also into account the discrete version of the Euler character $\chi = N_0 - N_- + N_\Delta$, one can recast the generating functional of dynamical triangulations into the following form

$$Z = \sum_{\text{oriented triangulations}} \frac{1}{s(T)} e^{-\lambda N_\Delta + \gamma \chi}, \quad (4.30)$$

with λ and γ being given as

$$\lambda = - \left(\frac{a_0}{2} + \frac{3a_-}{2} + a_\Delta \right) \quad (4.31)$$

and

$$\gamma = a_0. \quad (4.32)$$

It is straightforward to see that λ and γ are related to the cosmological constant and the Newton coupling, respectively. The exact relation between λ and γ on the one hand and the Newton coupling and the cosmological constant on the other hand is given as

$$\lambda = \Lambda + \frac{1}{16G} \quad (4.33)$$

and

$$\gamma = \frac{1}{8G}, \quad (4.34)$$

where we set the area of an equilateral triangle to be one. Note that even though λ does depend on the Newton coupling G it is often somewhat inaccurately also just referred to as the cosmological constant in the literature. From the generating functional Eq. (4.30) it is possible to generate dynamical triangulations via a Feynman graph expansion. Note that the previous conceptual discussion on the discretization of continuum quantum gravity does not require triangulations. We could equally well have considered any type of polygonizations. The discreteness is merely a technical tool and the dependence on the form of discretization should disappear when taking the continuum limit.

The remaining question is now how to obtain the continuum formulation. This question can be approached following two related lines of thoughts.

The first one being that from an intuitive point of view, we expect the continuum limit to be the limit where the average number of triangles diverges, while physical quantities such as the total space-time volume or the renormalized cosmological constant are kept fixed as shown in Fig. 4.4. Following this line of argument we would see (as we will also discuss in the following), that the size of the triangles would have to go to zero. Alternatively, one could also reverse the order of the previous argument and demand that the continuum limit must correspond to the limit where the size of the triangles a , which acts as a cut-off, is sent to zero. Indeed, in the continuum limit all information on the discretization should be lost, as the discretization is assumed to be merely technical rather than a physical feature of the theory. A continuum limit at a finite a , however, suggests that the shape of the polygon that is used to discretize the surface is actually relevant. This feature is only avoided in the limit $a \rightarrow 0$. Again, just as in the former line of argument, physical quantities should be finite in order to be observable. Paired with the fact that we sent $a \rightarrow 0$, this implies that the average number of triangles $\langle N_\Delta \rangle$ has to diverge⁴. In short, the continuum limit corresponds to the limit where $a \rightarrow 0$ and $\langle N_\Delta \rangle \rightarrow \infty$, while physical quantities are kept constant. Let us fix for now the topology. In order to have the average number of triangles diverge, the partition function Z needs to be singular. This can be easily understood as correlation functions are computed by taking derivatives of the partition function with respect to the discrete avatar of the cosmological constant, λ , as

$$\langle N_\Delta^n \rangle_h = (-1)^n \frac{\partial^n}{\partial \lambda^n} \ln Z_h. \quad (4.35)$$

and only diverge if Z_h is singular. Typically, these divergences occur in a power-law fashion. Given also that the two-dimensional theory depends only on one parameter λ , it is therefore safe to assume the following singular behavior, where we fix the

⁴Note that even though $\langle N_\Delta \rangle$ and is therefore strictly speaking an observable it does not correspond to a physical quantity. The average number of triangles is a mere artifact of the discretization. The unphysical nature of the average number of triangles becomes very obvious if one thinks about discretizing a given surface. Depending on the size of the triangles the average number will differ even though the physical quantity, the area of the surface, remains constant.

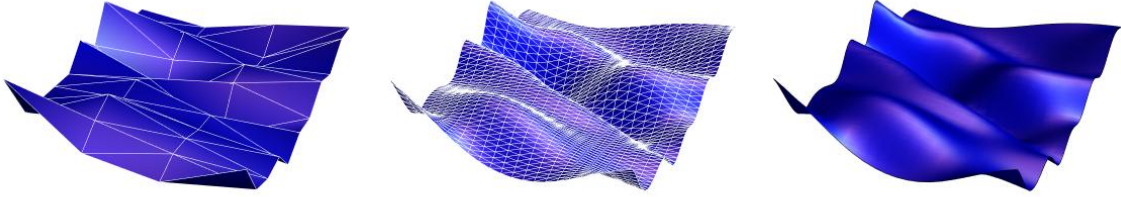


Figure 4.4: Continuum Limit in the dynamical triangulations approach. The average number of triangles is increased while the volume of the triangulation is kept finite. The continuum limit corresponds to the limit where the average number of triangles diverges.

topology

$$Z_0[g] \propto (\lambda - \lambda_c)^{-\alpha} + \text{less singular terms.} \quad (4.36)$$

The coefficient α captures the way in which the singularity is approached and is related to the critical exponent at the fixed point. The average number of triangles is then given as

$$\langle N_\Delta \rangle_h = -\frac{\partial}{\partial \lambda} \ln Z_h = \frac{\alpha}{\lambda - \lambda_c} + \text{less singular terms.} \quad (4.37)$$

One observes that the limit where $\langle N_\Delta \rangle$ tends to infinity implies that λ is sent to some critical value λ_c . All higher-order moments, such as e.g. $\langle N_\Delta N_\Delta \rangle$, can be also shown to diverge. Physically, this means that the system no longer has a characteristic scale. Indeed, an alternative way of phrasing the continuum limit is that one is interested in a critical point where scale invariance is observed⁵. As discussed in Ch. 2 scale invariance implies a second order phase-transition, which is characterized by diverging observables. The diverging behavior allows one to remove the cut-off.

Let us stress once again that the continuum limit corresponds to the limit, where the average number of triangles diverges while the size of the triangles a , which acts as a cut-off, is sent to zero in such a way that physical quantities such as the volume or the dimensionful cosmological constant are kept fixed and finite. Note however, that the cosmological constant or the space-time volume of individual configurations can differ and are therefore fluctuating. It is only the volume and the cosmological constant averaged over all space-time configurations that are kept fixed. The dimensionful cosmological constant in two dimensions is given as

$$\Lambda = \lambda/a^2. \quad (4.38)$$

⁵In two dimensions it can be shown that scale invariance also implies conformal invariance, which puts even more constraints on the theory. Whether this also extends to higher dimensions is a current research topic.

It is then possible to define a renormalized cosmological constant as

$$\Lambda_R = (\lambda - \lambda_c)/a^2, \quad (4.39)$$

such that the unphysical cut-off a can be removed if λ is tuned to some critical value λ_c in such a way that Λ_R is kept fixed and finite.

As a consistency check to see that all physical quantities do indeed remain finite if Λ_R is kept finite, it is worthwhile to have a closer look at the physical volume. In two dimensions this simply corresponds to the total average area, which is given via

$$\begin{aligned} \langle A \rangle &= a^2 \langle N_\Delta \rangle \\ &= \alpha \frac{a^2}{\lambda - \lambda_c} \propto \frac{1}{\Lambda_R}. \end{aligned} \quad (4.40)$$

We see that the requirement that Λ_R be finite also implies finiteness of the physical area. It is straightforward to check that also the higher moments $\langle A^n \rangle$ are finite.

Let us remark that this previous analysis is not a proof that the continuum limit actually is equivalent to the continuum theory defined according to Eq. (4.16). In the previous analysis we have assumed fixed topology. The question on the existence of a continuum limit when topological fluctuations are allowed can also be asked and is best addressed in the framework of random matrices. The surfaces of different topology that one is summing over can be approximated by unphysical discrete polygonizations. It turns out that these polygonizations can be generated by matrix models by making use of a duality between the Feynman graphs of the following matrix model with an n -valent interaction term g and the polygonized surfaces. The benefit of using matrix models rather than staying in the framework of triangulations is that matrix models can be tackled analytically as we will also see in some later section.

2D Gravity from matrix models

As already touched upon, matrix models are dual to dynamical triangulations and therefore offer an alternative road to solving two-dimensional Quantum Gravity. The benefit of matrix models is that they can be accessed in an analytical way. The generating functional for matrix models is

$$e^Z = \int dM e^{-\frac{1}{2} \text{tr} M^2 + \frac{g}{N^{k/2-1}} \text{tr} M^k}, \quad (4.41)$$

where M is a hermitian matrix and N is the size of the matrix. The logarithm of the above expression corresponds to the free energy of the theory. The particular scaling in N is required in order to relate matrix models to dynamical triangulations as in that case each Feynman diagram is weighted by a factor N^χ , where χ denotes the Euler character. This allows to recast the sum over Feynman diagrams in a matrix model in terms of a sum over topologies. The above expression generates

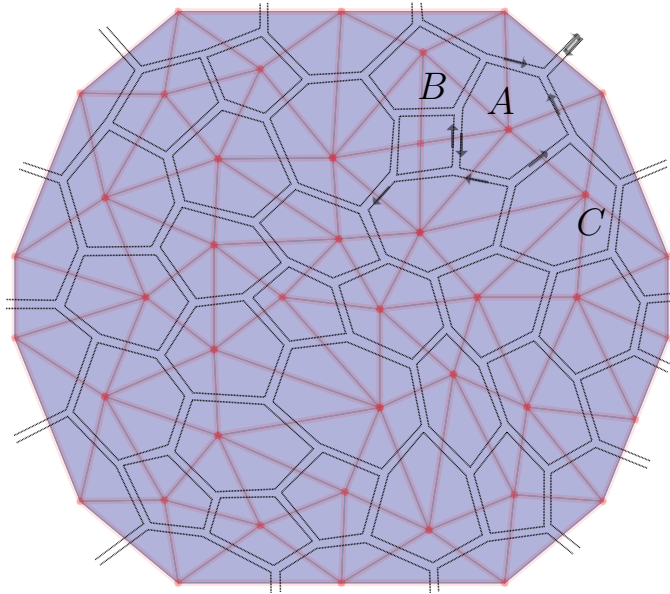


Figure 4.5: Part of a random triangulation. At A and C the triangulation is locally flat as six equilateral triangles are meeting at one vertex. At B the triangulation is curved, as there are less than six triangles meeting at one vertex.

both connected as well as non-connected correlation functions, which is the reason why the logarithm of the above expression, which is the free energy, will correspond to the path integral of two-dimensional quantum gravity in the continuum limit. In that case the non-connected diagrams, which are dual to non-connected patches of space-time, are removed. A more naive approach to generate 2d surfaces would involve a scalar ϕ^n theory. However, the generated Feynman diagrams will not have enough structure to only reproduce Riemann surfaces. This is remedied by Hermitian matrix models, which generate so-called ribbon graphs with orientable loops, thus avoiding non-orientable surfaces like the Möbius strip.

Using a tri-valent interaction term, i.e. $k = 3$, will lead to Feynman diagrams that are dual to triangulations of the surface. It is, however, important to stress that the way in which the surface is tessellated plays no role, as the discretization is just a tool to make sense of the path-integral and one is ultimately interested in the continuum limit, where the effects of the discretization will disappear. The key concept here is universality, which wipes off any details of the discretization. Having motivated why it is interesting to consider matrix models to solve 2d Quantum Gravity, we will now explain in more detail how matrix Models connect to 2d gravity. The key is to relate the inverse Newton coupling γ and the cosmological constant β to the characteristic quantities of the matrix model, namely the coupling g and the size of the matrix N . We will leave the technical details of the exact identification for the

appendix. For now it will suffice to note that the above-mentioned quantities are related in the following way

$$g \sim e^{c_1\beta/\gamma} \quad \& \quad N \sim e^{c_2\gamma}, \quad (4.42)$$

where c_1 and c_2 are constants larger than zero. These relations can be understood through a series expansion of the path integral.

The continuum limit in matrix models

In order to learn about the continuum limit in the matrix model scenario, it is useful to perform the following rescaling of the matrix M

$$M \rightarrow M\sqrt{N}, \quad (4.43)$$

where N denotes the size of the matrix, which allows one to pull out an overall factor of N in the matrix model action, such that one gets

$$e^Z = \int dM e^{N(-\frac{1}{2}\text{tr}M^2 + g\text{tr}M^k)}. \quad (4.44)$$

The benefit of this rescaling is that it is easier to keep track of the powers of N appearing in the amplitudes of a Feynman expansion: Each propagator will contribute with a power of N^{-1} , each vertex with a power of N and each loop will also contribute with a power of N , due to the contraction of delta functions coming from the propagators. The series expansion of e^Z can be reorganized in a $1/N$ expansion in the following way

$$e^Z = \sum_h N^{2-2h} Z_h, \quad (4.45)$$

where h is the number of handles reflecting the underlying topology. Taking the naive large- N limit leads to a domination of planar topologies ($h = 0$). On the other hand, it is possible to rewrite the 2d continuum action in a similar way as

$$Z = \sum_h \int \mathcal{D}g e^{-\beta A + \gamma \chi} = \sum_h (e^\gamma)^{2-2h} Z_h, \quad (4.46)$$

where the series expansion is indexed in terms of the number of handles of a given Feynman diagram which allows to immediately identify $N \sim e^\gamma$. The perturbative series Z_h in the coupling g can be shown to, asymptotically for large number of vertices n , behave as

$$Z_h[g] \approx \sum_n a_h n^{(2-\gamma_{\text{str}})\chi/2-1} \left(\frac{g}{g_c}\right)^n \approx a_h (g_c - g)^{(2-\gamma_{\text{str}})(1-h)}, \quad (4.47)$$

where we replaced χ by $\chi = 2 - 2h$, which holds in two dimensions and a_h is a constant.

In order to compare with continuum results we need to identify a notion of 'area' in matrix models. This can be done as follows: If we restrict ourselves to spherical topology, $h = 0$ and express Z_h in terms of a perturbative series in the coupling g , we find that

$$Z_h \sim \sum_n n^{\gamma-3} \left(\frac{g}{g_c} \right)^n. \quad (4.48)$$

The average area of all triangulations $\langle A \rangle = \langle n \rangle$ corresponds to

$$\langle A \rangle = \langle n \rangle \sim \frac{1}{g_c - g} = \frac{\partial}{\partial g} \ln Z_h. \quad (4.49)$$

The critical exponent γ_{str} is called the string susceptibility for historical reasons and $\gamma_{\text{str}} = -1/2$ for pure gravity and $\gamma_{\text{str}} = -1/3$ for gravity coupled to the Ising model. Assuming a matrix model potential such as the one introduced in the free energy Eq. (4.44) with one interaction parameter, it is possible to show that there exists a critical point at which the continuum limit can be taken for which $\gamma_{\text{str}} = -1/2$. Assuming a more complicated potential with additional couplings to tune, it is possible to recover so-called multi-critical points. These multi-critical points can be shown to be characterized by the critical exponents of gravity plus conformal matter [158, 159, 160, 161, 162, 163, 164, 165, 166, 167, 168, 169], as derived from Liouville gravity coupled to conformal matter. One can think of the new parameters as being related to additional degrees of freedom, as now, additional distinct geometrical forms are introduced in the dual picture. For instance a potential of the form

$$V(M) = \frac{1}{2} \text{tr}(M^2) + \text{tr}(M^3) + \text{tr}(M^4), \quad (4.50)$$

will lead to Feynman graph expansion which in the dual picture mixes triangles and squares. Again, the exact geometrical form does not matter, as it is a mere technical tool to discretize the continuum path integral. What matters is the property of having two distinct interactions that can be understood as being related to two distinct degrees of freedom. For $\gamma_{\text{str}} < 2$ topological fluctuations are enhanced as g approaches the critical value g_c . This raises the question whether it is possible to compensate the suppression of topological fluctuations in the large- N limit by an enhancement of them as g approaches g_c . As we will see in a forthcoming section, it turns out that it is indeed possible to consider all topologies when taking the so-called *double-scaling limit*.

Analytical Results of matrix models

One of the main advantages of matrix models compared to dynamical triangulations is that it is easier to get an analytical handle of matrix models.

The first indications pointing at the equivalence of 2d quantum gravity and matrix models in the continuum limit relied on comparing critical exponents on both sides. The critical exponents of matrix models in the simple large- N limit can be derived analytically using standard matrix-model techniques.

Saddle Point Approximation

One of the main advantages of matrix models compared to dynamical triangulations is that it is easier to get an analytical handle of matrix models.

The first indications pointing at the equivalence of 2d quantum gravity and matrix models in the continuum limit relied on comparing critical exponents on both sides. The critical exponents of matrix models in the simple large- N limit can be derived analytically using standard matrix model techniques. The key is to rewrite the hermitian matrix model in Eq. (4.44) in terms of an integration over eigenvalues and it is therefore crucial that the matrix be a square matrix. Decomposing the matrix in Eq. (4.44) in terms of its eigenvalues gives

$$e^Z = \int dM e^{-(N/g)\text{tr}V(M)} = \int \prod_{i=1}^N d\lambda_i \Delta^2(\lambda) e^{-(N/g)\sum V(\lambda_i)}, \quad (4.51)$$

where we renormalized the potential in order to pull out the coupling constant g and $\Delta(\lambda)$ is the Vandermonde determinant corresponding to the jacobian that follows from reducing the measure dM to an integration over eigenvalues. The Vandermonde determinant is defined as

$$\Delta(\lambda) = \prod_{i<j} (\lambda_j - \lambda_i) \quad (4.52)$$

and can be interpreted as a repulsive force pushing the eigenvalues away from each other. This effect competes with the potential V that acts as an attractive force which in itself would be minimized if all the eigenvalues lied together at some constant value. For the potential we are considering here this constant value would be zero. Interestingly, this mechanism of balancing the repulsive nature of the Vandermonde determinant and the attractive nature of the potential allows to model a number of phenomena in nature, e.g., the distance between cars parked in a street or birds perching on an electric wire [170, 171]. This can be understood in the following way: On the one hand, the wire is limited in its size and hence acts as a constraining potential. On the other hand the birds cannot occupy the same space, pushing their neighbors mildly to the sides. This leads to a repulsion that can be modeled by the Vandermonde determinant. The reader may consult [170] to see that the gap distribution of eigenvalues of a Gaussian matrix model at large- N indeed fits the distribution of spacing between perched birds or parked cars.

In the large- N limit, it is possible to perform a saddle-point expansion in order to solve the path integral. The saddle point equation is then derived from

$$\frac{\partial}{\partial \lambda_k} \left(e^{\ln(\Delta^2(\lambda)) - (N/g)\sum V(\lambda_i)} \right) = 0, \quad (4.53)$$

where we exponentiated the Vandermonde determinant in order to make its contribution to the total potential more apparent. Performing the derivative leads to

$$\frac{2}{N} \sum_{j \neq i} \frac{1}{\lambda_i - \lambda_j} = \frac{1}{g} V'(\lambda_i), \quad (4.54)$$

where the effect of the Vandermonde determinant is illustrated very clearly as the minimum of the total potential is shifted by a contribution proportional to $-1/\sum_{j \neq i}(\lambda_i - \lambda_j)$. Solving the above equation is quite cumbersome and we refer the reader to [172]. Having found a solution to the classical equations of motion, one then proceeds to evaluate the partition function in the saddle-point approximation approaching some critical point where the continuum limit can be taken and the partition function becomes singular. It turns out that near the singular point g_c the partition functions behaves as

$$Z(g) \sim -\frac{4}{15} \frac{N^2}{g^{5/2}} (g_c - g)^{5/2}. \quad (4.55)$$

The singular behaviour of Z near its critical point is then compared to the singular behaviour in the Liouville case which is given by

$$Z(A) \sim A^{(\gamma_{\text{str}}-2)\frac{X}{2}-1} \quad (4.56)$$

and may be compared to the scaling of $Z(g)$.

Orthogonal Polynomial Method

The saddle point method introduced in the previous section was historically the first approach to solve matrix models. It is however limited to fixed genus g . A more powerful method that also allows to solve the partition function of matrix models of relevance for quantum gravity with fluctuating genus is the orthogonal polynomial method. We will illustrate the conceptual steps and refer to [172] for the details. The starting point is again the decomposition of the matrix in terms of its Eigenvalues such that

$$e^Z = \int dM e^{-\text{tr}V(M)} = \int \prod_{i=1}^N d\lambda_i \Delta^2(\lambda) e^{-\sum_i V(\lambda_i)}. \quad (4.57)$$

The orthogonal polynomial method now consists in introducing a set of polynomials that are orthogonal with respect to the measure of the matrix model such that

$$\int_{-\infty}^{\infty} d\lambda e^{-V(\lambda)} P_n(\lambda) P_m(\lambda) = s_n \delta_{nm}, \quad (4.58)$$

where s_n are normalization coefficients that are fixed such that the polynomial P_n has the form $P_n = \lambda^n + \dots$, which explains the appearance of the constant s_n on the right-hand side of the above equation.

The free energy of the matrix model can then be rewritten as

$$F = e^Z = N! \prod_{i=0}^{N-1} s_i = N! \prod_{k=0}^{N-1} f_k^{N-k}, \quad (4.59)$$

where $f_k \equiv s_k/s_{k-1}$. Solving the matrix model therefore comes back to finding the normalizations s_n or equivalently their ratios. We refer the reader to [172] for details on how this is done.

The Double-Scaling Limit

In the previous section we have discussed how to take the continuum limit at fixed topology h . This led to a domination of planar diagrams which tessellate the two-dimensional sphere \mathcal{S}^2 . In the following, we will also consider topological fluctuations, which in the so-called double-scaling limit are enhanced such that manifolds of all topologies contribute in the continuum limit. In the large- N limit, where N denotes the size of the matrix, and for large number of vertices n in the Feynman graph expansion, it is straightforward to rewrite the free energy of a Hermitian matrix model with a tri-valent interaction as

$$e^Z \sim \sum_h \left(N (g_c - g)^{(2-\gamma_{\text{str}})/2} \right)^{2-2h} a_h \quad (4.60)$$

using the findings of the previous section. Topological fluctuations will only be retained, if the expression inside the brackets approaches a finite value. That is N approaches infinity, while g is tuned to its critical value g_c in such a way that

$$N (g_c - g)^{(\gamma_{\text{str}}-2)/2} = \text{cst}, \quad (4.61)$$

is kept fixed at some constant. This is exactly the double-scaling limit. We will come back to this limit later on when thinking about how to set up a renormalization group flow for matrix and tensor models.

What about higher dimensions?

In higher dimensions the argument to write down the path-integral and search for a continuum limit would go along similar lines. That is once again we can keep Fig. 4.1 in the back of our mind. The generating functional for higher-dimensional dynamical triangulations will now take the more general form

$$Z = \sum_{\text{oriented triangulations}} \frac{1}{s(T)} \exp \left(a_0 N_0 + a_{\square} N_{\square} + a_{\Delta} N_{\Delta} + \sum_{i=3}^D a_i N_i \right), \quad (4.62)$$

where the N_i are i -simplices. We include all i -simplices up to the space-time dimension D . Just like in the two-dimensional case the different i -simplices are not independent from each other. The constraints given through the Euler character and the relation between edges and faces in the previously discussed two-dimensional case are updated by higher-dimensional versions [173]. These higher-dimensional constraints are the so-called Dehn-Sommerville relations [174, 175]. To construct a simplicial manifold \mathcal{T} one must therefore satisfy

$$\chi(T) = \sum_{i=0}^D (-1)^i N_i(T), \quad (4.63)$$

where $\chi(T)$ is the Euler character and

$$\sum_{i=2k-1}^D (-1)^i \frac{(i+1)!}{(i-2k+2)!(2k-1)!} N_i(T) = 0 \quad (4.64)$$

where k is an integer satisfying $1 \leq k \leq D/2$ if D is even or

$$\sum_{i=2k}^D (-1)^i \frac{(i+1)!}{(i-2k+1)!(2k)!} N_i(T) = 0 \quad (4.65)$$

where k is an integer ranges from $1 \leq k \leq (D-1)/2$ if D is odd.

Let us take a closer look at the four-dimensional case where the Dehn-Sommerville conditions imply the following set of constraints:

$$N_0 - N_1 + N_2 - N_3 + N_4 = \chi, \quad (4.66)$$

$$2N_1 - 3N_2 + 4N_3 - 5N_4 = 0, \quad (4.67)$$

$$5N_4 = 2N_3. \quad (4.68)$$

Combining the above expressions with Eq. 4.62 leads to a path-integral formulation with two independent couplings, which in turn means that the theory space of couplings consists of two tuneable parameters to identify an interesting continuum limit. In particular, the partition function is given by

$$Z = \sum_{\text{oriented triangulations}} \frac{1}{s(T)} e^{-k_n N_n(T) + k_{n-2} N_{n-2}(T)}, \quad (4.69)$$

where the couplings k_n and k_{n-2} can be associated with the Newton coupling G and the cosmological constant Λ as follows

$$k_n = \Lambda \text{vol}(\sigma^n) + \frac{1}{2} (n+1) n \frac{\arccos(\frac{1}{n})}{16\pi G} \text{vol}(\sigma^{n-2}) \quad (4.70)$$

and

$$k_{n-2} = \frac{\text{vol}(\sigma^{n-2})}{8G}, \quad (4.71)$$

where the former is a linear combination of the cosmological constant Λ and $1/16\pi G$, while the latter is inversely proportional to $1/16\pi G$.

It is possible to explore the continuum limit following the same line of argument as in the previously discussed two-dimensional case. Physical quantities are demanded to remain finite, while the lattice cut-off a is removed.

What about higher-curvature terms

The Asymptotic Safety scenario of quantum gravity suggests that it might be interesting to also consider discrete versions of higher-order curvature terms. In particular, there are hints that some linear combination of R^2 and $R_{\mu\nu}R^{\mu\nu}$ might be a relevant direction [55, 56, 57, 58, 59, 60]. This would imply that one would have to tune an additional parameter in the discrete setting in order to find a physically interesting continuum limit. From the previous discussion we know that we can identify

$$R_i = \frac{2\pi(6 - N_i)}{N_i} \quad (4.72)$$

which in turn implies that we can generalize this to obtain a discrete expression for R^2 by simply squaring the previous expression [176]

$$R_i^2 = \left(\frac{2\pi(6 - N_i)}{N_i} \right)^2. \quad (4.73)$$

A much less obvious question, which is still an open research question is how to discretize $R_{\mu\nu}R^{\mu\nu}$. Proposals in that direction have been put forward in [177, 178, 179].

4.1 Tensor Models

The previous sections were devoted to gain an understanding of how matrix models, dynamical triangulations and two-dimensional quantum gravity are related. In particular, we showed that a Feynman graph expansion of the free energy is dual to dynamical triangulations. The power of matrix models is that they can be accessed analytically which allowed us to study their relationship to two-dimensional Quantum Gravity. The success of matrix models as a way to solve two-dimensional Quantum Gravity, naturally motivated physicists in the 90's to consider a generalization of matrix models to higher-dimensions, in particular to three and four dimensions [180, 181, 182, 183]. This led to the consideration of tensor models. The simple idea behind studying tensor models is that it is possible to construct dual building blocks of space-time from a tensor interaction such that a Feynman expansion of the free energy of a tensor model corresponds to a gluing of these building blocks.

In two dimensions, the duality between matrix models and dynamical triangulation hinged on the fact that vertices corresponded to two-simplices while propagators were associated to edge pairings. Tensor models allow to extend this duality to higher dimensions d by relating vertices to d -simplices and propagators to gluings of faces of co-dimension 1. Each index of a rank- D tensor can be associated with the $D - 1$ face of a D dimensional polyhedron. The rank of a tensor which corresponds to the number of indices of a tensor is then related to the space-time dimension d .

The standard techniques that allowed to solve matrix models, such as for instance the orthogonal polynomial method that we discussed previously, were, however, not available for tensor models. Ultimately, the first tensor models were discarded because they did not admit a $1/N$ expansion of the free energy as matrix models did, where the $1/N$ expansion could be recast into a topological expansion, indexed by the genus.

In 2009 and thereafter, the so-called (un)colored tensor models [184, 185, 186, 187], were introduced and shown to admit a $1/N$ -expansion of the free energy labeled by the so-called *Gurau degree* [188, 189, 190]. This non-negative integer, unlike the genus is, not a topological quantity, but depends on both the topology and the details of the triangulation. This new class of colored tensor models was characterized by more constraining symmetries, making the diagrammatics of the Feynman graph expansion more tractable compared to the original tensor models studied in the 90's, which were taken to be completely symmetric under permutation of indices. In two dimensions, the leading diagrams in the $1/N$ expansion of the free energy are the planar ones, which correspond to triangulations of the sphere. Hence, taking the continuum limit (without enhancing topological fluctuations) was shown to lead to planar diagrams. The equivalent of planar diagrams in tensor models are the so-called melonic diagrams which are characterized by a Gurau degree $\omega = 0$ and dominate the $1/N$ expansion of the free energy.

While tensor models were introduced as a way to generalize the success of matrix models in solving two-dimensional quantum gravity to higher-dimensions, they have also found applications in a wide range of different fields. It is possible to devise two lines of thoughts where tensor models have found applications. One line of research attempts to explore the relationship between tensor models and random surfaces [191], which is the line of research followed in this thesis, while the other line of thought is dedicated to the study of strongly-coupled QFTs.

For theories with a large number of fields N , a perturbative series in terms of $1/N$ exists that allows to treat the couplings non-perturbatively. This is of interest in the study of holographic dualities, where, recently, tensor models have been considered in the context of the AdS/CFT conjecture after a reformulation of the Sachdev-Ye-Kitaev (SYK) model [192, 193]. The SYK model is a toy model that allows to study the AdS/CFT conjecture, employing real fermionic tensor fields without quenched disorder and was put forward in [194, 195, 196, 197]. In contrast to the tensor models that are of interest to quantum gravity, the tensor models that are studied in the context of the SYK model are space-time dependent. The link between the SYK model and tensor models has, thus, sparked intense research of so-called tensor field theories in one or more dimensions [198, 199, 200, 201, 202, 203, 204, 205, 206, 207, 208, 209, 210, 211, 212, 213, 214, 215]. More generally, tensor field theories are also of interest due to their generic properties in the melonic large- N limit⁶. For instance, in [195, 201] a non-trivial conformal field theory (CFT) has been found in

⁶As a reminder, the large- N limit of tensor field theories is dominated by so-called melonic diagrams.

the infrared. The motivation behind studying such CFTs is on the one hand to improve the theoretical understanding of CFTs in higher dimensions and on the other the potential relation to the AdS/CFT conjecture. For a review on melonic CFTs we refer the reader to [216]. As a side remark, it is worth mentioning that more recently, tensor models have also been studied in the context of machine learning [217, 218].

Complex tensor models

The first uncolored tensor models studied in the tensor model literature were the complex tensor models.

A complex rank- D tensor model is a model that is invariant under independent rotations of each tensor index under the unitary group $U(N)$, where N denotes the size of the tensor, that is

$$T_{b_1 b_2 \dots b_D} \Rightarrow T'_{a_1 a_2 \dots a_D} = \sum_{b_1, b_2, \dots, b_D} U_{a_1 b_1}^{(1)} U_{a_2 b_2}^{(2)} \dots U_{a_D b_D}^{(D)} T_{b_1 b_2 \dots b_D}, \quad (4.74)$$

where the matrix U is unitary. As a consequence, tensor invariants, invariant under U , are always built from complex conjugate pairs of tensors where the first index of one tensor T is contracted with the first index of another complex conjugate tensor \bar{T} . Finding tensor invariants at a given interaction order therefore amounts to a combinatorial problem.

A valid tensor invariant could for instance take the following form

$$f(T) = \sum_{a_i, b_i} T_{a_1 a_2 a_3} \bar{T}_{a_1 a_2 b_3} T_{b_1 b_2 a_3} \bar{T}_{b_1 b_2 b_3}, \quad (4.75)$$

It is straightforward to show that the above expression is invariant under actions of the $U(N)$ group on each tensor index.

In the following we will drop the sum and summation over indices will always be implied.

It is standard in the literature to associate colors to the distinct indices in order to keep track of the contraction pattern. These colors however are not related to colored tensor models introduced before.

The tensor invariants of a complex tensor model admit a graphic representation in terms of edge-colored bipartite graphs.

Real tensor models

Real rank- D tensor models were shown to also admit a large- N limit [219]. They are defined as being invariant under independent actions of the $O(N)$ group on each tensor index. More explicitly, one has

$$T_{b_1, b_2, \dots, b_D} \Rightarrow T'_{a_1, a_2, \dots, a_D} = \sum_{b_1, b_2, \dots, b_D} O_{a_1 b_1}^{(1)} O_{a_2 b_2}^{(2)} \dots O_{a_D b_D}^{(D)} T_{b_1, b_2, \dots, b_D}. \quad (4.76)$$

The property of O entails that invariants are built from pairs of real tensors, where just like in the complex case, the index of some tensor at some position i is contracted with the i^{th} index of some other tensor. The interactions of the complex model also exist in the real model in the sense that in the real model $\bar{T} = T$. However, compared to the complex tensor model, the real tensor model has an extended and therefore richer set of interactions. Of particular importance is the so-called cross interaction of a rank-3 real tensor model

$$C(T) = T_{a_1 a_2 a_3} T_{a_1 b_2 b_3} T_{b_1 a_2 b_3} T_{b_1 b_2 a_3}, \quad (4.77)$$

where each tensor is contacted to all the other tensors in the invariant. The name of this interaction stems from the fact that tensor invariants can also be represented as edge-colored graphs. In order to do so, indices of a tensor are associated to edges of a graph and tensors are represented by vertices. The contraction pattern of a given tensor invariant is then captured in the specific way that vertices are connected by edges. As an example, the above introduced interaction admits the following graphical representation.

$$C(T) = T_{a_1 a_2 a_3} T_{a_1 b_2 b_3} T_{b_1 a_2 b_3} T_{b_1 b_2 a_3} = \begin{array}{c} \bullet \text{---} \text{---} \bullet \\ \diagup \quad \diagdown \\ \bullet \text{---} \text{---} \bullet \\ \diagdown \quad \diagup \end{array}, \quad (4.78)$$

where the edges correspond to indices and lines correspond to contractions between them. The colouring of the line indicates the position of the index in the tensor. In the graphical representation Fig. 4.78 it becomes evident why $C(T)$ is referred to as the cross interaction.

Multi-orientable models

It is also possible to consider invariants constructed from both real and complex tensor. Such models are called multi-orientable models and were introduced in [220, 221, 222, 223]. See [224] for a review. They were originally introduced as an update to colored tensor models by allowing for a larger class of invariants, while still admitting a large-N expansion.

4.2 RG flows for Matrix and Tensor Models

Let us summarize our discussion on tensor models so far. In two dimensions there exists a relationship between continuum quantum gravity and matrix models. This relationship provides the motivation to study tensor models as a way to discretize higher-dimensional gravity. First attempts to bridge the gap between tensor models and continuum quantum gravity were already undertaken in the 90's. Unlike matrix models, where the Feynman diagram expansion of the free energy could be organized in a $1/N$ expansion in terms of the genus, the tensor models considered at that time

were not $1/N$ -expandable. Almost 20 years later a new class of colored tensor models was proposed, which was shown to admit a $1/N$ expansion of the free energy indexed by the so-called Gurau degree. This resparked the original idea of tensor models to provide a way to analytically access a discretized path-integral for four dimensional quantum gravity. The physics emerges when taking the continuum limit. In the following we are going to discuss how the continuum limit can be studied in the context of tensor models and highlight how a renormalization group flow can be set up for tensor models. The continuum limit then corresponds to a fixed point of this RG flow.

Typically one is used to thinking about the RG in terms of a shell-wise integration of momenta. This approach allows one to clearly define the UV and the IR in terms of high and low momenta, respectively. The existence of a UV and an IR regime requires the existence of a background, which describes the underlying space-time. In a theory of Quantum Gravity, however, space-time itself is also fluctuating. As a consequence, a theory of Quantum Gravity is expected to be background independent as the singling out of a special background would contradict our intuition about GR. The absence of a fixed background geometry in turn implies the absence of any characteristic length or scale in general, which is a crucial ingredient in the Wilsonian renormalization group approach. It is therefore a highly non-trivial question how one can set up an RG flow to search for fixed points of that flow.

It is, however, possible to circumvent these issues by setting up an RG flow in such a way that the outermost layers of indices are integrated out. The size of the matrix or the tensor can then be interpreted as the RG scale. This way to set up an RG flow is actually very intuitive as it is very much related to the fundamental philosophy of coarse-graining as a way to describe a system with many degrees of freedom in terms of fewer, more effective, degrees of freedom, where one thinks of the matrix or tensor size N as counting the number of degrees of freedom of a matrix or tensor model. Successively integrating out rows and columns in a matrix model for instance corresponds to decreasing the matrix size N and reducing the number of degrees of freedom [135]. To make this analogy more solid, it is necessary to recall the discussion on the continuum limit in matrix models for two-dimensional quantum gravity, where it was shown that the so-called double-scaling limit can be taken in order to recover a two-dimensional quantum gravity phase characterized by an associated critical exponent. As a reminder, the double-scaling limit is characterized by the coupling g in Eq. (4.41) approaching its critical value g_c , while the matrix size N tends to infinity in such a way that the expression

$$(g - g_c)^{\frac{1}{\theta}} N = N_0 \tag{4.79}$$

is kept at a constant value N_0 . It is possible to rewrite this expression in a more familiar way, where

$$g = g_c + \left(\frac{N}{N_0} \right)^{-\theta} . \tag{4.80}$$

Rewritten in this way, the above equation resembles the linearization of the flow around a fixed point, as discussed in Ch.2 at g_c where θ denotes the critical exponent and N sets the RG-scale. The existence of a double-scaling limit in matrix models can therefore be shown to be analogous to the existence of a fixed point characterized by one relevant direction.

4.2.1 FRG for Matrix and Tensor Models

Given that the double-scaling limit of matrix models can be interpreted as an RG flow in terms of the matrix size N , it is possible to also set up a functional RG to study non-perturbative phenomena along the lines of the derivation presented in section Ch.2. Given a matrix model or a tensor model it is possible to derive a flow equation for the effective action Γ_N , given as

$$\partial_t \Gamma_N = \frac{1}{2} \text{Tr} \left(\left(\Gamma_N^{(2)} + R_N \right)^{-1} \partial_t R_N \right), \quad (4.81)$$

where R_N is a regulator that satisfies the criteria mentioned in Ch.2 such that it acts as both an IR and a UV regulator. The FRG for matrix and tensor models was first derived in [225, 226]. Since the FRG cannot be solved exactly and one has to rely on a truncation of the effective action Γ_N . In a local QFT, a truncation is typically set-up in terms of local operators and the notion of a background allows one to define a canonical mass dimension for these operators, which then implies a canonical scaling dimension which is a crucial ingredient when building truncations, as otherwise the canonical guiding principle, discussed in Ch.2 becomes nonsensical. The absence of a background in matrix and tensor models, however, makes the scaling properties of operators with the RG scale N a non-trivial question. We will show that it is, nonetheless, possible to give matrix and tensor operators a canonical scaling dimension without making reference to a background.

Large- N scaling for Tensor Models with the FRG

The definition of units of length or energy (GeV) only make sense when specified in reference to a background, as one can for instance see from the standard definition of the line element $ds^2 = g_{\mu\nu} dx^\mu dx^\nu$, which requires the specification of a background geometry equipped with a metric g . The existence of a background and the possibility to define units imply the notion of a canonical *mass* dimension. The canonical *scaling* dimension is then derived from the assumption that a re-scaling of units, such as $\text{GeV} \rightarrow \lambda \text{GeV}$, where λ is an arbitrary constant, should be unphysical and therefore not affect the theory. In a local coarse-graining procedure the scaling dimension thus accounts for the response of operators to a re-scaling of lengths and momenta and the canonical *mass* dimension therefore implies the canonical *scaling* dimension. In order for the re-scaling of units to not affect the theory, the action has to remain dimensionless and the *dimensionful* operators need to be rescaled

accordingly. A simple example to determine the scaling dimension of an operator can be given in the framework of a free scalar field theory with the action

$$S[\phi] = \int d^4x m^2 \phi^2. \quad (4.82)$$

Rescaling the units of energy as $\text{GeV} \rightarrow \lambda \text{GeV}$ and performing a dimensional analysis, requires to redefine $\phi \rightarrow \lambda \phi$, which implies that the operator $\int d^4x \phi^2$ has canonical scaling dimension -2 . Contrary to standard QFT, tensor models, however, do not make any reference to a background and therefore it is no longer possible to define a notion of length or momentum. The definition of a canonical dimension seems to be therefore, a priori, not possible or an ill-defined problem, and it is therefore also no longer possible to analyze the response of a tensor operator to a rescaling of some fundamental length scale. There exists, however, an alternative way to define the canonical scaling dimension in a local QFT, which relies on the beta functions becoming autonomous, i.e., independent of the RG scale. This method allows one to recover a scaling dimension that still agrees with the mass dimension, as one would expect for a local and therefore background-dependent theory. This second way of determining the scaling dimension, by requiring the beta function to become autonomous is also more suited for tensor models, where we will require the beta functions to lose their explicit dependence on N in the large- N limit. Phrased differently, the beta functions have to admit a $1/N$ -expansion with non-trivial $1/N^0$ terms. This requirement will be shown to set upper bounds on the scaling dimension of couplings. If the upper bound is satisfied the scaling dimension of the couplings is called enhanced [227, 228, 229, 230, 231].

Ultimately, the scaling has to be fixed uniquely by making contact with the geometric interpretation of matrix or tensor models. We already discussed that in two dimensions matrix models can be shown to be dual to dynamical triangulations. This observation relied on the fact that it is possible to identify the free energy of a matrix model with the partition function of dynamical triangulations. Demanding this identification allowed us to relate the two different approaches. In tensor models the sum over Feynman diagrams are weighted by the Gurau index ω in contrast to the Euler character χ in two dimensions [188]. While there is so far no analogue of the Gurau index in higher-dimensional dynamical triangulations, one would expect that for the duality between tensor models and dynamical triangulations to make sense, it should be possible to also introduce a Gurau index in dynamical triangulations and to perform a similar analysis to the one done in order to show that matrix models and dynamical triangulations in two dimensions are dual.

Benchmarking FRG results

The FRG for matrix models was first derived in [225]. Here, the FRG was applied to both a truncation of single-trace matrix operators as well as one with both single-trace and double-trace operators. The double-scaling limit of matrix models was shown to imply the interpretation of a renormalization group flow in the couplings

in terms of the matrix size N in [135]. Since the FRG for discrete models has been derived in [225, 232], different continuum limits have been charted with these tools, not only in tensor models but also in the closely related group field theories [233, 234, 235, 236, 237, 238, 239, 240, 241, 242, 243, 244, 245, 246, 1, 247].

4.2.2 An algorithm for Tensor Models

In the last sections, we have been showing how it is possible to set up an RG flow for tensor models in terms of the tensor size N , which allows to search for continuum limits that are of possible interest for quantum gravity. Crucially, the absence of a background implied that it is not possible to assign a canonical mass dimension to operators and couplings in order to study their behavior under rescalings of the mass dimension. This posed some additional complications in setting up an RG flow. We circumvented these issues by arguing that an alternative way to assign a notion of canonical scaling dimension is by insisting that the beta functions do not explicitly depend on the RG scale N . For local QFTs, this way of fixing the scaling exactly yielded the canonical mass dimension. The reader is now equipped with the necessary tools and aware of the subtleties related to a renormalization group flow in tensor models.

Deriving the running in the tensor size N for all couplings up to interaction order T^8 is no longer feasible by hand within the lifetime of a PhD. For that purpose it is unavoidable to rely on a computer code which is able to derive all beta functions with as little input as possible. In the following we will present an algorithm which only requires the T^4 interactions of a given tensor model as initial input in order to derive the beta functions of any rank at any interaction order in principle. The practical implementation is done in Mathematica and requires the xAct and xTensor packages [248]. In practice, however, computing higher-order beta functions becomes very expensive with increasing order of the truncation.

The derivation of beta functions with the FRG requires in practice the specification of a truncation of the effective action. In order to set up a momentum-independent truncation it is therefore necessary to construct and identify all invariants at a given interaction order. A bottom up approach to construct all possible invariant of an arbitrary tensor model is the following

- Provide all T^4 interactions. This is the only input needed.
- Compute the two-point functions of all T^4 interactions. Derivatives are defined in accordance with the symmetry of the underlying model. As an example, tensor derivatives in the $O(N)^3$ model are defined as

$$\frac{\partial T_{a_1 a_2 a_3}}{\partial T_{b_1 b_2 b_3}} = \delta_{a_1 b_1} \delta_{a_2 b_2} \delta_{a_3 b_3}, \quad (4.83)$$

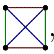
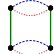
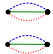
while a symmetric tensor model, where tensors are invariant under permuta-

tions of all their indices, has the property that

$$\frac{\partial T_{a_1 a_2 a_3}}{\partial T_{b_1 b_2 b_3}} = \frac{1}{3!} (\delta_{a_1 b_1} \delta_{a_2 b_2} \delta_{a_3 b_3} + \delta_{a_1 b_2} \delta_{a_2 b_1} \delta_{a_3 b_3} + \delta_{a_1 b_3} \delta_{a_2 b_2} \delta_{a_3 b_1} + \delta_{a_1 b_1} \delta_{a_2 b_3} \delta_{a_3 b_2} + \delta_{a_1 b_2} \delta_{a_2 b_3} \delta_{a_3 b_2} + \delta_{a_1 b_3} \delta_{a_2 b_1} \delta_{a_3 b_2}). \quad (4.84)$$

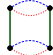
- From the T^4 two-point functions we can construct all T^{2n} interactions, with $n \in \mathbb{N}$ and $n \geq 2$ by simply contracting the different two-point functions with delta functions.

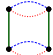
The method will be illustrated with the real rank-3 tensor model, although it is important to stress that the algorithm is model independent and therefore the method will go through for any tensor model, independently of the symmetry.

Let us consider one representative of each color-symmetric family, which we define to be the class of interactions that are invariant under color permutation. We therefore consider ,  and . The two-point function of the so-called *melon* interaction⁷, for instance, can be written diagrammatically as

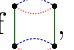
$$\frac{\partial^2}{\partial T_{\{\alpha_i\}} \partial T_{\{\beta_i\}}} \text{[diagram of pillow interaction]} = 4 \text{[diagram 1]} + 4 \text{[diagram 2]} + 4 \text{[diagram 3]}, \quad (4.85)$$

where we introduced the notation $\{\alpha_i\}$ to represent the three indices α_1 , α_2 and α_3 . Using the graphical notation introduced previously in Eq. (4.78), vertices correspond to tensors, edges between vertices are linked to contracted indices and open lines going out of a vertex represent uncontracted, open indices. Single lines are delta functions.

The above graphical expression for the two-point function can be then understood as follows: Acting with the second derivative on a tensor invariant is equivalent to opening up a graph by removing two vertices. There are distinct ways of removing two vertices which in the case above results in three different tensorial building blocks. The prefactors in front of the distinct tensorial pieces of the two-point function are of combinatorial nature and count the number of possibilities one has to remove two vertices while generating the same opened graph. In the above example the prefactor of four can be understood as $4 = 2 \times 2$; The two-point function is symmetric under permutation of the order of derivation. This accounts for an overall factor of two. The other factor of two in front of each of the pieces of the two-point function accounts for the symmetries of the invariant when represented as a graph. Note that it is a peculiarity of T^4 that this symmetry factor is the same for all contributions to the two-point function. At higher orders in T this is no longer the case. Each of the three pieces in the above two-point function of  represents

⁷Alternatively, we will also call refer to  as pillow interaction, as is also common in the literature.

a building block to construct higher-order tensor invariants.

The remaining building blocks are obtained from the color-symmetric siblings of , as well as from the cross interaction and the multi-trace invariant. The two-point function of the cross-interaction reads

$$\frac{\partial^2}{\partial T_{\{\alpha_i\}} \partial T_{\{\beta_i\}}} \text{Diagram} = 4 \text{Diagram}_1 + 4 \text{Diagram}_2 + 4 \text{Diagram}_3, \quad (4.86)$$

while the two-point function of the multi-trace interaction is given by

$$\frac{\partial^2}{\partial T_{\{\alpha_i\}} \partial T_{\{\beta_i\}}} \text{Diagram} = 4 \text{Diagram}_1 + 4 \text{Diagram}_2. \quad (4.87)$$

Interactions of a given order are built by combining all building blocks obtained from the two-point functions of the T^4 interactions in all possible ways and tracing over them. Up to degeneracies, this procedure allows to generate all interactions of a given order. As an example, a T^6 interaction of a rank-3 $O(N)$ model can be built from combining the following three building blocks

$$\text{Tr} \left(\text{Diagram}_1 \text{Diagram}_2 \text{Diagram}_3 \right) = N \cdot \text{Diagram}_4, \quad (4.88)$$

where the prefactor of N follows from contracting the delta functions associated to the red indices. In order to determine all possible invariants we do not care about this prefactor and therefore drop it, only keeping the tensor invariant. The above generated T^6 interactions corresponds to $T_{a_1 a_2 a_3} T_{a_1 a_2 b_3} T_{b_1 b_2 b_3} T_{b_1 b_2 c_3} T_{c_1 c_2 c_3} T_{c_1 c_2 a_3}$ in the Einstein convention. Since distinct building blocks can generate the same invariants, one has to get rid of such degeneracies. In *Mathematica*, this can be practically done with the *ToCanonical* function of the *xTensor* package. Implementing the described algorithm and removing degenerate invariants we find the following number of interactions for the $O(N)^3$ model at interaction order T^2, T^4, T^6, T^8 and T^{10} respectively

$$1, 5, 16, 86, 448. \quad (4.89)$$

while we find the following number of rank-4 $O(N)$ interactions at interaction order T^2, T^4, T^6 and T^8 , respectively

$$1, 14, 132, 4154. \quad (4.90)$$

As a cross-check of our method we find that these numbers are in exact agreement with those found by the authors of [249, 250]. Similarly, we also recover the same number of invariants for the rank-3 $U(N)$ model as the authors of [251]. Having identified all possible invariants of a given model up to a certain order, there are two possible ways to continue to set up the truncation:

- 1 The most general theory space is considered by assigning a coupling to every tensor interaction.
- 2 A color-symmetric theory space is set-up, which collects the different tensor interactions in terms of combinatorial families. Each interaction belonging to the same color symmetric equivalence class gets assigned the same coupling.

Possibility (1), where a distinct coupling is assigned to every interaction, is significantly easier to deal with than alternative (2) as one does not have to find a feasible prescription to collect interactions belonging to the same combinatorial family. On the other hand the theory space in option (1) will be significantly larger, consequently leading to a larger number of beta functions to be derived.

Let us analyze scenario (2) and explain how one can collect all tensor interactions belonging to the same combinatorial family. More explicitly we are interested in setting up a truncation of the following kind

$$\Gamma_N \sim g \left(\begin{array}{c} \text{Diagram 1} \\ + \\ \text{Diagram 2} \\ + \\ \text{Diagram 3} \end{array} \right). \quad (4.91)$$

This is a non-trivial question as *Mathematica* generates output in the Einstein notation, that is, e.g., as $T_{a_1 a_2 a_3} T_{a_1 a_2 b_3} T_{b_1 b_2 b_3} T_{b_1 b_2 a_3}$. To deal with this challenge, a novel combinatorial object, which we shall call the *indicator*, that allows to assign interactions to a unique combinatorial family is introduced. The indicator of depth k can be defined as follows

Definition 4.1. Let $T_{i_1 i_2 \dots i_d} \equiv T_I$ be a tensor of rank d transforming under some arbitrary symmetry. Let $O_n(T) = \sum_{\ell, I_\ell} T_{I_1} T_{I_2} \dots T_{I_n} K(I_1, I_2, \dots, I_n)$ be a tensor observable, where the kernel K is a product of Kroneckers implementing the contraction of indices in a particular pattern. The indicator of depth k of a tensor observable of tensors of rank $d \geq 2$ is a set of pairs of numbers derived from $\text{Tr}(\frac{\delta^k}{\delta T_{a_1, \dots, a_d} \dots \delta T_{a_1, \dots, a_d}} \text{Tr}(T^n))$. To determine the indicator of depth k , with $k \leq n$, the combinatorial prefactors resulting from the derivatives acting on the tensor observable as well as the power in the tensor size N multiplying each newly generated tensor invariant are collected to form a couple.

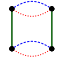
In the following we will refer to the indicator of depth $k = 2$ as simply the indicator given that this will be the quantity that we will be using in order to identify color-symmetric families. An example of how to derive the indicator of a given tensor invariant will be provided below. In simple words the indicator of depth $k = 2$ of any interaction is computed as follows:

S.1 Compute the second variation of a tensor invariant, respecting its symmetries.

S.2 Take the trace of the obtained object. This will result in a sum of terms involving a product between a tensor interaction, a prefactor $p \in \mathbb{N}$ and the tensor size N to some power x , where $0 \leq x \leq d$ and d is the rank of the

tensor. The number of elements in the sum is a way to measure the amount of symmetry of a given interaction. Broadly speaking: The more symmetry a given tensor interaction has, the less terms there are in the sum.

S.3 We collect all the prefactors p as well as the powers in N , that we denote by x . This gives a list of pairs of numbers (p and x) whose length equals the number of terms in the sum that one obtained in the previous step. We call this object the *indicator*.

As an illustrative example, let us consider again the real rank-3 tensor model and compute the indicator for the pillow interaction . Invoking the definition of the indicator, the computational steps are the following

$$\begin{aligned}
\text{Tr} \frac{\partial^2}{\partial T_{\{\alpha_i\}} \partial T_{\{\beta_i\}}} \text{pillow} &= \text{Tr} \left(4 \begin{array}{c} \text{---} \bullet \text{---} \\ \text{---} \bullet \text{---} \\ \text{---} \bullet \text{---} \\ \text{---} \bullet \text{---} \end{array} + 4 \begin{array}{c} \text{---} \bullet \text{---} \\ \text{---} \bullet \text{---} \\ \text{---} \bullet \text{---} \\ \text{---} \bullet \text{---} \end{array} + 4 \begin{array}{c} \text{---} \bullet \text{---} \\ \text{---} \bullet \text{---} \\ \text{---} \bullet \text{---} \\ \text{---} \bullet \text{---} \end{array} \right) \\
&= 4 \begin{array}{c} \text{---} \bullet \text{---} \\ \text{---} \bullet \text{---} \\ \text{---} \bullet \text{---} \\ \text{---} \bullet \text{---} \end{array} + 4 \begin{array}{c} \text{---} \bullet \text{---} \\ \text{---} \bullet \text{---} \\ \text{---} \bullet \text{---} \\ \text{---} \bullet \text{---} \end{array} + 4 \begin{array}{c} \text{---} \bullet \text{---} \\ \text{---} \bullet \text{---} \\ \text{---} \bullet \text{---} \\ \text{---} \bullet \text{---} \end{array} \\
&\Rightarrow \{(4, 2), (4, 1), (4, 0)\} \tag{4.92}
\end{aligned}$$

The idea is to compute the indicator for every interaction in order to finally compare the indicators of the different invariants to each other. Using the fact that interactions belonging to the same combinatorial family have the same indicator, we can then assign a single coupling to all interactions belonging to the same family. This step completes the construction of the truncated effective action in the case that the same coupling is assigned to all interactions of a given-symmetric family. Crucially, we have assumed that the following conjecture holds:

Conjecture 1. There is a one-to-one correspondence between a given indicator and a tensor invariant.

If the above conjecture did not hold, it could be that invariants belonging to different color-symmetric families could share the same indicator. We have not found any evidence that the conjecture does not hold. Having set up a truncated effective action in the case where the same coupling is assigned to all interactions of a given color-symmetric family, it is possible to proceed with the derivation of the beta functions using the functional RG. The following steps apply again to both, scenario (1) and (2). In order to evaluate the flow of the truncated effective action Γ_N it is necessary to evaluate the right hand side of the FRG equation Eq. (4.81). One option to proceed with the practical computations is to use the so-called $\mathcal{P}^{-1}\mathcal{F}$ expansion. The flow equation can then be expressed as

$$\partial_t \Gamma_N = \frac{1}{2} \text{Tr} [(\partial_t R_N) \mathcal{P}^{-1}] + \frac{1}{2} \sum_{n=1}^{\infty} (-1)^n \text{Tr} [(\partial_t R_N) \mathcal{P}^{-1} (\mathcal{P}^{-1} \mathcal{F})^n] \tag{4.93}$$

with

$$\mathcal{P} = \Gamma_N^{(2)}|_{T=0} + R_N \quad (4.94)$$

and

$$\mathcal{F} = \Gamma_N^{(2)} - \Gamma_N^{(2)}|_{T=0}. \quad (4.95)$$

The $\mathcal{P}^{-1}\mathcal{F}$ expansion is an expansion in powers of tensors. The trace in equation Eq. (4.93) involves summing over all indices and fields. Tracing over the contraction of delta functions appearing in \mathcal{P} due to the field-independent part of the second variation of the effective action Γ_N with the open indices arising from the field-dependent part of the second variation (e.g. as illustrated in Eq. (4.87), where the second variation of the multi-trace melonic invariant opens up indices by "removing" two vertices), generates new interactions. Hereby, the mechanism is very similar to the one illustrated in Eq. (4.88), where we were setting up the truncation by tracing over contractions of different building blocks of the two-point functions of the T^4 invariants. In contrast to this procedure, however, it is now also necessary to take into account the presence of the regulator R_N in the definition of the inverse propagator \mathcal{P} and its scale-derivative $\partial_t R_N$. The combinatorics of a particular invariant resulting at order $n = 3$ constructed through the $\mathcal{P}^{-1}\mathcal{F}$ expansion can therefore be illustrated pedagogically using the following diagrammatic notation

$$\begin{aligned} \text{Tr} \left[(\partial_t R_N) \mathcal{P}^{-1} (\mathcal{P}^{-1} \mathcal{F})^3 \right] &= \text{Tr} \left((\partial_t R_N) \begin{array}{c} \text{---} \text{---} \text{---} \\ \text{---} \text{---} \text{---} \\ \text{---} \text{---} \text{---} \end{array} \right) \\ &\equiv \begin{array}{c} \text{---} \text{---} \text{---} \\ \text{---} \text{---} \text{---} \\ \text{---} \text{---} \text{---} \end{array} \otimes \begin{array}{c} \text{---} \text{---} \text{---} \\ \text{---} \text{---} \text{---} \\ \text{---} \text{---} \text{---} \end{array} \sim \begin{array}{c} \text{---} \text{---} \text{---} \\ \text{---} \text{---} \text{---} \\ \text{---} \text{---} \text{---} \end{array} \end{aligned} \quad (4.96)$$

where the single lines represent delta functions and the scale derivative of the regulator R_N was replaced by a cross. Lines of same color running through the regulator are contracted. This allows to identify the generated invariant. Note that the above expression only describes the combinatorics as we dropped for instance the couplings and prefactors.

We will discuss the details of the $\mathcal{P}^{-1}\mathcal{F}$ expansion when studying the real rank-3 tensor model and in Appendix B. For now it is sufficient to bear in mind that the flow generates symmetry-breaking (index-dependent) terms of the following form through the $\mathcal{P}^{-1}\mathcal{F}$ expansion

$$\begin{aligned} \sum_n \text{Tr} (\mathcal{P}^{-1} (\partial_t R_N) (\mathcal{P}^{-1} \mathcal{F})^n) &= \\ &= \sum_{I, a_i, b_i} H(a_i, b_i; g_j) \times \text{Invariant}^{(I)}(T^k; a_i, b_j), \end{aligned} \quad (4.97)$$

where k counts the number of tensors that constitute the invariant and H is a threshold function that includes index-dependent terms coming from the presence of the regulator multiplied with the couplings associated to the invariants entering a given term of the $\mathcal{P}^{-1}\mathcal{F}$ expansion. In general H will have the following generic form

$$\begin{aligned}
H(a_i, b_i; g_j) &= \\
&= f_g(g_j) \times F(a_i, b_i) \times \\
&\quad \times \text{Degeneracy of couplings} \times \text{Prefactors of two-point function}, \tag{4.98}
\end{aligned}$$

where $f_g(g_j)$ is a function that depends on the couplings only and $F(a_i, b_i)$ is a function that depends on the indices. The degeneracy of couplings follows from the fact that the $\mathcal{P}^{-1}\mathcal{F}$ expansion at order n generates $n!/\text{deg}(g_i)!$ terms, where $\text{deg}(g_i)$ counts the degeneracy of the coupling g_i , as one can see more clearly using a little example. For that purpose, we consider the following explicit form of a part of the $\mathcal{P}^{-1}\mathcal{F}$ expansion

$$(\mathcal{P}^{-1}\mathcal{F})^n = \mathcal{P}^{-1}\mathcal{F} \cdot \dots \cdot \mathcal{P}^{-1}\mathcal{F}. \tag{4.99}$$

Invoking the definition of \mathcal{F} in Eq. 4.95, it is clear that there exist $n!/\text{deg}(g_i)!$ ways to generate the same invariant as each individual \mathcal{F} will be a function of the form

$$\mathcal{F} = \sum_i g_i O_i^{(2)}(T^k, k > 2). \tag{4.100}$$

For instance, we may consider again the example provided in Eq. (4.96), this time making the dependence on the couplings explicit. In that case

$$\begin{aligned}
(\mathcal{P}^{-1}\mathcal{F})^3 &= \left(g_{4,1}^0 \cdot \text{diag}_1 \times g_{4,1}^{2,1} \cdot \text{diag}_2 \times g_{4,1}^{2,1} \cdot \text{diag}_3 \right) \\
&= \left(g_{4,1}^{2,1} \cdot \text{diag}_4 \times g_{4,1}^0 \cdot \text{diag}_1 \times g_{4,1}^{2,1} \cdot \text{diag}_5 \right) \\
&= \left(g_{4,1}^{2,1} \cdot \text{diag}_6 \times g_{4,1}^{2,1} \cdot \text{diag}_7 \times g_{4,1}^0 \cdot \text{diag}_8 \right) \\
&\sim \text{diag}_9. \tag{4.101}
\end{aligned}$$

A proper treatment of the symmetry-breaking due to the regulator requires to consider modified Ward Identities. This in turn necessitates to extend the theory space by terms that explicitly break the symmetry of the model. The truncated theory

spaces that we consider in this work will not include index-dependent terms and therefore we will set indices that appear simultaneously in the function F and as a contraction in the invariant $\text{Invariant}^I(T^k; a_l, b_j)$ to zero as they are not part of the truncations that we will consider here. Ward identities in the context of the FRG applied to tensor models have been considered in [252, 253, 254, 255]. See [256] for a review on the current status. Setting the indices that appear in both the threshold function F and the tensor invariant to zero allows one to perform the threshold sums

$$I_n^m = \sum_{a_m} F(a_m), \quad (4.102)$$

that appear in the computation of the flow of Γ_N , for instance in Eq. 4.97. Here, a_m denotes the $m \leq D$, where D is the rank of the tensor model, indices that are non-zero and n labels the order of the $\mathcal{P}^{-1}\mathcal{F}$ expansion. Hereby, I_n^m is a function of the anomalous dimension η , the parameter r introduced in the Litim-regulator and the scale N introduced by the regulator. The threshold functions for the real rank-3 tensor model assuming a Litim-type regulator are provided in Eq (B.19) in Appendix B. We will leave the technical details for a forthcoming section on the real rank-3 tensor model.

The steps *S.1-S.3* of the algorithm have allowed us to derive the function $f_g(g_j)$, the threshold function F_{a_i, b_i} and the prefactors of the two-point function which enter the function H in Eq. 4.97. In order to read off the beta functions of the individual *dimensionful* couplings, the expressions resulting from the evaluation of the right hand side of the FRGE, structurally given by Eq. (4.97), need to be compared with the expressions resulting from the right hand side, which have the following structure

$$\sum_I (\partial_t g_I) \times \text{Invariant}^I(T^k) \quad (4.103)$$

The beta functions can therefore be read off by comparing the invariants appearing in the terms given by Eq. (4.97), that have been generated on the right hand side of Eq. (4.93) through the $\mathcal{P}^{-1}\mathcal{F}$ expansion with those coming from $\partial_t \Gamma_N$ given by Eq. (4.103). In *Mathematica* the comparison between the invariants generated through the $\mathcal{P}^{-1}\mathcal{F}$ expansion with those in $\partial_t \Gamma_N$ involves the following steps *S*:

- S.4* The previous steps *S.1-S.3* yield terms that involve numerical prefactors, couplings and tensor invariants.
- S.5* Compute the difference between an invariant T_g generated through the $\mathcal{P}^{-1}\mathcal{F}$ expansion and an invariant T_i appearing in the effective action. If this difference is equal to zero then the prefunction F associated to the generated interaction T_g contribute to the beta function of the coupling linked to T_i .
- S.6* Do this comparison between all interactions of a given interaction order $2n$ that can be generated through a $\mathcal{P}^{-1}\mathcal{F}$ expansion and all interactions of order $2n$ defining our effective action. As before, whenever this difference is zero, an

$\mathcal{P}^{-1}\mathcal{F}$ -generated interaction contributes to the beta function of the interaction we are comparing to. If a coupling is assigned to every invariant the speed of this comparison can be accelerated.

S.7 Keep track of the symmetry factors appearing due to the degeneracies of couplings, as well as the 1/2 prefactors coming from the flow equation.

S.8 Add the contributions from the threshold functions.

S.9 Add the contribution from the canonical scaling dimension.

This allows us to find the dimensionful beta functions. The dimensionless beta functions are determined by insisting on a well defined large- N limit where the beta functions become autonomous. They will in general have the following generic form The beta functions that one derives for tensor models will always the following generic form

$$\beta_{g_k} = (-[g_k] + 2\eta) g_k + \sum_j N^n i_n^m f_{j,m,n} \left(\prod_C g_C \right) N^{-[g]_k + \sum_C [\bar{g}_C]}, \quad (4.104)$$

where the functions f_j are functions of (products of) couplings g_C , where C indexes the couplings associated to interactions that generate the invariant linked to g_k by means of the $\mathcal{P}^{-1}\mathcal{F}$ expansion. The i_n^m are the threshold functions introduced in Eq. (B.19), where the power in N has been factored out. They depend on the anomalous dimension η and the parameter r introduced in the definition of the modified Litim-regulator in Eq. (4.111). Herein, m counts the order at which the $\mathcal{P}^{-1}\mathcal{F}$ expansion has been performed in order to generate the invariant linked to g_k and n counts the number indices running freely through the regulator as delta functions.

Let us summarize this rather technical part of the thesis. Our goal is to study the continuum limit of tensor models for four-dimensional quantum gravity. The tool that we are using in order to search for fixed points of a renormalization group flow in the tensor size N is the FRG. The benefit of the FRG is that it allows to perform practical computations and is thus a very convenient way to explore new universality classes. The FRG cannot be solved exactly and therefore we have to rely on truncations of a scale-dependent effective action Γ_N . We then search for fixed points within these truncations. To do so, we have to derive the running of the couplings that span the truncation. The number of tensor invariants at each interaction order grows very quickly and hence a derivation of the beta functions by hand becomes unfeasible.

4.3 Understanding 3D

As a first stepping stone towards four-dimensional Quantum Gravity we are going to study three dimensions.

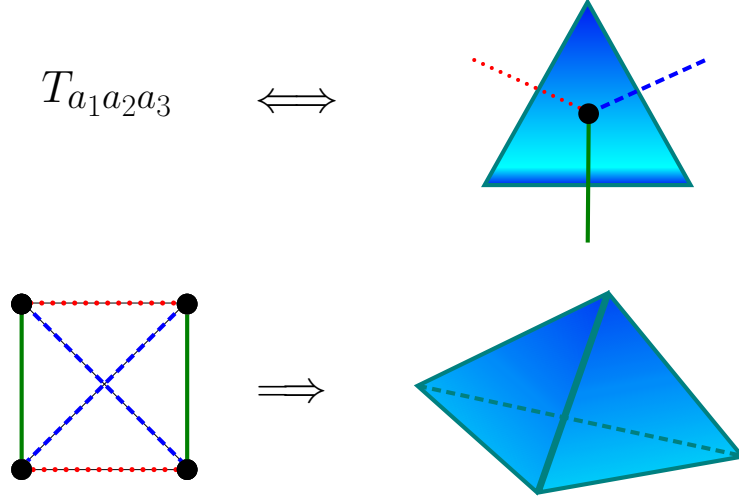


Figure 4.6: Geometrical interpretation of the cross-interaction: The tensor is replaced by the face of a triangle, while its indices are represented by the edges of that triangle. With this identification in mind, the cross interaction $T_{a_1 a_2 a_3} T_{a_1 b_2 b_3} T_{b_1 b_2 a_3} T_{b_1 a_2 b_3}$, which can be diagrammatically represented as shown in Eq. 4.78, is dual to a tetrahedron. One therefore expects that such an invariant might be of relevance for a possible three-dimensional quantum gravity phase.

Even though ultimately one is interested in 3+1 dimensions, in this work we will only focus on purely Euclidean models since the implementation of causality conditions is not yet understood in higher-dimensional quantum gravity. For this purpose we will consider a tensor model of rank-3.

In particular, we will study a real tensor model featuring an $O(N) \times O(N) \times O(N)$ symmetry such that a tensor transforms under three distinct copies of the $O(N)$ group as

$$T_{a_1 a_2 a_3} = O_{a_1 b_1}^{(1)} O_{a_2 b_2}^{(2)} O_{a_3 b_3}^{(3)} T_{b_1 b_2 b_3} \quad (4.105)$$

leaving the action invariant. The three-dimensional case will also allow us to illustrate the intricacies of the FRG applied to tensor models that we discussed previously. We look for a continuum limit using the FRG. The Feynman diagrams generated by tensor models are dual to dynamical triangulations and therefore studying tensor models in three dimensions is an alternative to probing the continuum limit in three dimensional dynamical triangulations. The benefit of the FRG is that it is computationally less costly than the computer simulations that are run in order to find a tentative continuum limit in the dynamical triangulations setting. Rank-3 Tensor Models have been studied before using Large- N techniques as well as the FRG [233, 235, 238, 239]. Compared to previous tensor models studied within the FRG, the real tensor model provides an extended theory space and therefore a potentially interesting continuum limit. In particular, the $O(N)^3$ model allows for a

so-called tetrahedral invariant, $T_{a_1 a_2 a_3} T_{a_1 b_2 b_3} T_{b_1 a_2 b_3} T_{b_1 b_2 a_3}$, which is forbidden in the complex tensor model case. On the one hand such a type of interaction extends the theory space and therefore offers a richer set of possibility of potential continuum limits. On the other hand one can associate a dual geometrical meaning if one associates to each tensor a triangle, with the edges denoting the indices of said tensor and then glues the edges of the triangle together following the contraction pattern of the interaction, as depicted in Fig. 4.6. As a matter of fact, using this prescription it is possible to construct a geometric dual for all allowed tensor interactions. Naively, one can then think of the Feynman expansion of a tensor model as gluing together these microscopic geometric entities, such as the tetrahedra depicted in Fig. 4.6. It is, however, important to stress again that ultimately the physics in the continuum limit should be independent of the way that the space-time is discretized and one should therefore not associate any physical meaning to the shape of these microscopic building blocks and only think about them in an intuitive way. The key notion is universality, which implies the independence of the emergent physics from the microscopic details. We will search for candidate fixed points for the flowing effective action Γ_N , which allows for a universal continuum limit, using the FRG

$$\partial_t \Gamma_N [T] = N \partial_N \Gamma_N [T] = \frac{1}{2} \text{Tr} \left[\left(\Gamma_N^{(2)} + R_N \right)^{-1} \partial_t R_N \right], \quad (4.106)$$

where, for now, we leave the regulator R_N unspecified. As we have discussed in previous chapters, the flow equation cannot be solved exactly and we therefore need to specify a truncation of the flowing effective action $\Gamma_N [N]$. In continuum FRG computations truncations are typically set up following the assumption that the canonical dimension is a reliable estimate to tell whether a coupling is relevant or irrelevant. This so-called canonical guiding principle therefore implies that increasing a truncation should not induce new relevant directions. In the tensor model language there is however no notion of background and therefore one can also not associate a canonical dimension to a coupling. We have discussed in the previous section how it is nonetheless possible to associate a scaling in the tensor size N to a tensor model coupling by insisting on the large- N limit. We will assume that increasing the order of interaction leads to lower scaling dimensions and is therefore an appropriate way to increase a truncation, just like in standard local quantum field theory. In the following, we will therefore study a truncation of the average effective action Γ_N up to order T^6 , i.e.,

$$\Gamma_N = \Gamma_{N,2} + \Gamma_{N,4} + \Gamma_{N,6}, \quad (4.107)$$

with

$$\Gamma_{N,2} = \frac{Z_N}{2} T_{a_1 a_2 a_3} T_{a_1 a_2 a_3}, \quad (4.108)$$

where Z_N denotes the wave function renormalization,

$$\begin{aligned}
\Gamma_{N,4} &= \bar{g}_{4,1}^{-2,1} T_{a_1 a_2 a_3} T_{b_1 a_2 a_3} T_{b_1 b_2 b_3} T_{a_1 b_2 b_3} \\
&+ \bar{g}_{4,1}^{-2,2} T_{a_1 a_2 a_3} T_{a_1 b_2 a_3} T_{b_1 b_2 b_3} T_{b_1 a_2 b_3} \\
&+ \bar{g}_{4,1}^{-2,3} T_{a_1 a_2 a_3} T_{a_1 a_2 b_3} T_{b_1 b_2 b_3} T_{b_1 b_2 a_3} \\
&+ \bar{g}_{4,1}^{-0} T_{a_1 a_2 a_3} T_{b_1 a_2 b_3} T_{b_1 b_2 a_3} T_{a_1 b_2 b_3} \\
&+ \bar{g}_{4,2}^{-2} T_{a_1 a_2 a_3} T_{a_1 a_2 a_3} T_{b_1 b_2 b_3} T_{b_1 b_2 b_3} ,
\end{aligned} \tag{4.109}$$

and

$$\begin{aligned}
\Gamma_{N,6} &= \bar{g}_{6,1}^{-3,1} T_{a_1 a_2 a_3} T_{b_1 a_2 a_3} T_{b_1 b_2 b_3} T_{c_1 b_2 b_3} T_{c_1 c_2 c_3} T_{a_1 c_2 c_3} \\
&+ \bar{g}_{6,1}^{-3,2} T_{a_1 a_2 a_3} T_{a_1 b_2 a_3} T_{b_1 b_2 b_3} T_{b_1 c_2 b_3} T_{c_1 c_2 c_3} T_{c_1 a_2 c_3} \\
&+ \bar{g}_{6,1}^{-3,3} T_{a_1 a_2 a_3} T_{a_1 a_2 b_3} T_{b_1 b_2 b_3} T_{b_1 b_2 c_3} T_{c_1 c_2 c_3} T_{c_1 c_2 a_3} \\
&+ \bar{g}_{6,1}^{-2,1} T_{a_1 a_2 a_3} T_{a_1 b_2 a_3} T_{b_1 b_2 b_3} T_{c_1 c_2 b_3} T_{c_1 c_2 c_3} T_{b_1 a_2 c_3} \\
&+ \bar{g}_{6,1}^{-2,2} T_{a_1 a_2 a_3} T_{b_1 a_2 a_3} T_{b_1 b_2 b_3} T_{c_1 c_2 b_3} T_{c_1 c_2 c_3} T_{a_1 b_2 c_3} \\
&+ \bar{g}_{6,1}^{-2,3} T_{a_1 a_2 a_3} T_{b_1 a_2 a_3} T_{b_1 b_2 b_3} T_{c_1 b_2 c_3} T_{c_1 c_2 c_3} T_{a_1 c_2 b_3} \\
&+ \bar{g}_{6,1}^{-1,1} T_{a_1 a_2 a_3} T_{a_1 b_2 b_3} T_{b_1 b_2 a_3} T_{b_1 c_2 c_3} T_{c_1 c_2 c_3} T_{c_1 a_2 b_3} \\
&+ \bar{g}_{6,1}^{-1,2} T_{a_1 a_2 a_3} T_{b_1 a_2 b_3} T_{b_1 b_2 a_3} T_{c_1 b_2 c_3} T_{c_1 c_2 c_3} T_{a_1 c_2 b_3} \\
&+ \bar{g}_{6,1}^{-1,3} T_{a_1 a_2 a_3} T_{b_1 b_2 a_3} T_{a_1 b_2 b_3} T_{c_1 c_2 b_3} T_{c_1 c_2 c_3} T_{b_1 a_2 c_3} \\
&+ \bar{g}_{6,1}^{-0,np} T_{a_1 a_2 a_3} T_{b_1 a_2 b_3} T_{b_1 c_2 c_3} T_{c_1 c_2 a_3} T_{c_1 b_2 b_3} T_{a_1 b_2 c_3} \\
&+ \bar{g}_{6,1}^{-0,p} T_{a_1 a_2 a_3} T_{b_1 a_2 b_3} T_{b_1 b_2 c_3} T_{c_1 b_2 b_3} T_{c_1 c_2 a_3} T_{a_1 c_2 c_3} \\
&+ \bar{g}_{6,2}^{-3,1} T_{a_1 a_2 a_3} T_{b_1 a_2 a_3} T_{b_1 b_2 b_3} T_{a_1 b_2 b_3} T_{c_1 c_2 c_3} T_{c_1 c_2 c_3} \\
&+ \bar{g}_{6,2}^{-3,2} T_{a_1 a_2 a_3} T_{a_1 b_2 a_3} T_{b_1 b_2 b_3} T_{b_1 a_2 b_3} T_{c_1 c_2 c_3} T_{c_1 c_2 c_3} \\
&+ \bar{g}_{6,2}^{-3,3} T_{a_1 a_2 a_3} T_{a_1 a_2 b_3} T_{b_1 b_2 b_3} T_{b_1 b_2 a_3} T_{c_1 c_2 c_3} T_{c_1 c_2 c_3} \\
&+ \bar{g}_{6,2}^{-1} T_{a_1 a_2 a_3} T_{b_1 a_2 b_3} T_{b_1 b_2 a_3} T_{a_1 b_2 b_3} T_{c_1 c_2 c_3} T_{c_1 c_2 c_3} \\
&+ \bar{g}_{6,2}^{-3} T_{a_1 a_2 a_3} T_{a_1 a_2 a_3} T_{b_1 b_2 b_3} T_{b_1 b_2 b_3} T_{c_1 c_2 c_3} T_{c_1 c_2 c_3} .
\end{aligned} \tag{4.110}$$

The studied truncation in the graphical representation for the different interactions is depicted in Fig. 4.7. Herein, the subscripts associated to the different couplings $g_{k,l}^{i,j}$ have to be understood as follows: i denotes the number of sub-melons, i.e. the number of times pairs of indices of two tensors are contracted; j denotes the position of a distinct index of a tensor invariant; k denotes the order of the interaction and l denotes the number of connected tensor components. Additionally, we also introduced the superscripts p and np which indicate whether the graph associated to that interaction is planar or non-planar. It is worthwhile to discuss the appearance of invariants with more than one connected components, i.e. $l > 1$. These invariants can be represented as disconnected graphs and the analogous versions of these terms in background-dependent QFT, $(\int d^4 x_1 L_1(x_1)) \dots (\int d^4 x_n L_n(x_n))$, are typically not

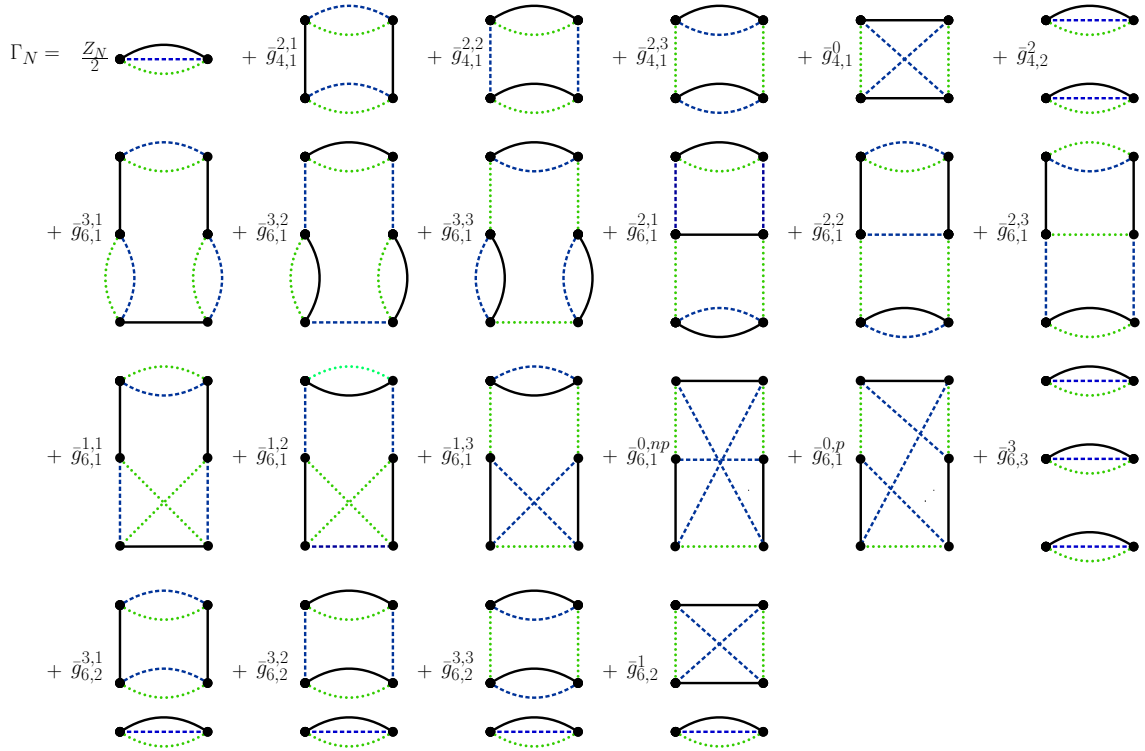


Figure 4.7: Depicted above is the truncation of Γ_N for the real rank-3 model studied in this work using the graphical representation introduced in Eq. (4.78) for the invariants.

considered as they are suppressed with the space-time volume. Physically, such interactions also seem weird in a local setting as they necessitate the notion of a disconnected space-time and would violate the notion of causality as fields in different disconnected space-times could interact with each other. In a background independent setting, however, where the notion of space-time does not appear, these disconnected interactions are not associated to disconnected space-times but are typically obtained as disconnected boundaries of a connected space-time which are sometimes just referred to as baby universes. Unlike in the local case where non-local interactions of the form described above are space-time suppressed, the corresponding non-local interactions, such as $T_{\alpha_1\alpha_2\alpha_3}T_{\alpha_1\alpha_2\alpha_3}$, in tensor models are generated by the RG flow. We will show this explicitly when discussing the β functions of the real rank-3 tensor model. It is therefore not possible to discard these kind of interactions as they directly contribute to the anomalous dimension and the critical exponents characterizing the fixed point. It is also not possible to suppress these interactions through the assignment of an appropriate scaling. One route one might take, however, is to find mechanism that dynamically realizes a vanishing fixed point value $g_{4,2}^{2,*} = 0$ for $g_{4,2}^2$. We will show later on in the discussion of the beta functions that this can be realized if no symmetry between colors is assumed, that is if

$g_{4,1}^{2,1} = g_{4,1}^{2,2} = g_{4,1}^{2,3}$ is violated.

Compared to the $U(N)^3$ model which has previously been studied in the literature using the FRG up to a T^6 truncation, we have to consider the additional interactions, associated to the couplings $g_{4,1}^0$, $g_{6,1}^{3,i}$, $g_{6,1}^{0,p}$ and $g_{6,2}^1$.

Applying the FRG

In order to study the above truncation with the functional RG, we have to specify a regulator that fulfills the set of conditions given by Eq. 2.28, Eq. 2.29 and Eq. 2.30. Different choices of regulators exist and we will use the Litim regulator

$$R_N(\{a_i, b_i\}) = Z_N \delta_{a_1 b_1} \delta_{a_2 b_2} \delta_{a_3 b_3} \left(\frac{N^r}{a_1 + a_2 + a_3} - 1 \right) \theta \left(\frac{N^r}{a_1 + a_2 + a_3} - 1 \right), \quad (4.111)$$

where N refers to the size of the tensor and we have introduced the parameter r , which for the standard Litim regulator, commonly employed in local FRG computations, has to be one by arguments of dimensionality. To make this point clearer, let us discuss why $r = 1$ in local quantum field theory. Typically, in a Wilsonian RG setting in momentum space one splits the fields into light modes and heavy modes according $\phi = \phi_\ell(p) + \phi_h(p)$, where

$$\phi_\ell(p) = \begin{cases} \phi(p), & \text{if } p < k \\ 0, & \text{otherwise,} \end{cases} \quad (4.112)$$

and

$$\phi_h(p) = \begin{cases} \phi(p), & \text{if } k < p \leq \Lambda \\ 0, & \text{otherwise,} \end{cases} \quad (4.113)$$

A flow in the couplings follows from integrating out the heavy modes and demanding the path-integral to remain unchanged. The distinction between light modes and heavy modes is based on the existence of a notion of momentum scale, which necessitates a background in order to be defined, since $\sqrt{p^2} = \sqrt{g_{\mu\nu} p^\mu p^\nu}$. The existence of a background and the associated notion of momentum thus also fixes the ratio between the mass dimension of k and the mass dimension of p to be one in order for the distinction between light and heavy modes to make sense from a dimensional point of view, and therefore $r = 1$. In the tensor model RG language the distinction between what would be the analogue of the light and heavy modes in local quantum field theory is based on the number of tensor entries. The larger indices of a tensor are associated to the UV modes, while lower indices are related to the IR. More concretely, in a tensor model language one could make the following analogue distinction to the local QFT-on-a-background case

$$T_{a_i}^\ell = \begin{cases} T_{a_i}, & \text{if } \sum_i a_i < N \\ 0, & \text{otherwise,} \end{cases} \quad (4.114)$$

and

$$T_{a_i}^h = \begin{cases} T_{a_i}, & \text{if } N < \sum_i a_i \leq N' \\ 0, & \text{otherwise,} \end{cases} \quad (4.115)$$

where N' denotes the total number of tensor indices and is the analogue of the UV-cut-off Λ in the local QFT-on-a-background scenario. The crucial difference to a QFT defined on a background is now that the distinction between light and heavy modes is made in terms of the magnitude of the indices, which are numbers without any reference to a background and therefore it is also not possible to associate any notion of mass dimension to these tensor indices. In turn, this means that the power of the floating cut-off N can be chosen freely such that more generally one may make the following distinction

$$T_{a_i}^\ell = \begin{cases} T_{a_i}, & \text{if } \sum_i a_i < N^r \\ 0, & \text{otherwise,} \end{cases} \quad (4.116)$$

and

$$T_{a_i}^h = \begin{cases} T_{a_i}, & \text{if } N^r < \sum_i a_i \leq N' \\ 0, & \text{otherwise,} \end{cases} \quad (4.117)$$

which explains why the appearance of the parameter r in the Litim regulator defined previously is an allowed peculiarity of background-independent models. Nonetheless, r cannot be chosen at random but has to be larger than zero: In the limit $N \rightarrow N' \rightarrow \infty$ no 'heavy' modes should have been integrated out. In that case Eq. 4.116 should always be satisfied. If $r < 0$, however, the role of N is reversed. The limit $N \rightarrow 0$ corresponds to the UV limit where no modes have been integrated out, while $N \rightarrow \infty$ corresponds to the IR. The case $r = 0$ is also forbidden because in that case the 'floating' cut-off N completely disappears by becoming constant and continuously integrating out heavy modes of freedom is no longer possible because N cannot be varied. In the following search for fixed points that allow for a potentially interesting continuum limit that leads to a three-dimensional quantum gravity phase, we are, however, going to restrain ourselves to the $r = 1$ case, although ultimately r is fixed by trying to make contact with the actual physics that one is interested in. Choosing a different r has an immediate influence on the scaling dimension of the individual couplings. We will discuss this point in more detail later on. The $r \neq 1$ case has been discussed in [257].

Derivation of beta functions

Beta functions can be obtained from the Wetterich equation. The $\mathcal{P}^{-1}\mathcal{F}$ expansion allows one to then carry out practical computations with the FRG and to derive beta functions. We will now build on the previous discussion on the derivation of beta functions and try to make the technical steps avoided in the previous discussion on

the $\mathcal{P}^{-1}\mathcal{F}$ expansion clearer and more concrete. The reader who is more interested in the physics of tensor models rather than in the technical details may therefore skip this section.

Practical computations with the FRG require two ingredients. First a truncation, that we already specified in Eq. (4.107) and second a regulator R_N , which is given by Eq. (4.111). For $r = 1$ this regulator entails that its scale-derivative is given by

$$\partial_t R_N = Z_N \prod_{i=1}^3 \delta_{a_i b_i} \theta \left(\frac{N}{a_1 + a_2 + a_3} - 1 \right) \left((1 - \eta) \frac{N}{a_1 + a_2 + a_3} + \eta \right), \quad (4.118)$$

where the anomalous dimension η is defined as $\eta = -\partial_t Z_N / Z_N$. Hence, the truncation and the regulator R_N are all the ingredients that are needed in order to perform practical computations with the $\mathcal{P}^{-1}\mathcal{F}$ expansion of the FRG introduced in Eq. (4.93). As already discussed, the regulator introduces an index-dependence that only vanishes in the limit $N \rightarrow 0$ and which breaks the original $O(N') \times O(N') \times O(N')$ symmetry of the model. Accordingly, it is necessary to introduce a projection prescription that differentiates between symmetric and symmetry-breaking terms. This is done by setting indices that appear simultaneously in the regulator and as indices in tensors to zero. A simple example that arises in the computations is the following

$$\begin{aligned} & \text{Tr} \left(\partial_t R_N \mathcal{P}^{-1} (\mathcal{P}^{-1}\mathcal{F})^3 \right) \\ & \sim \sum_{I_i} \frac{1}{2} \times \frac{3!}{2!} \bar{g}_{4,1}^0 (\bar{g}_{4,1}^{2,1})^2 N \frac{1}{Z_N^3} \left(\frac{a_1 + a_2 + a_3}{N} \right)^2 \left((1 - \eta) \frac{N}{a_1 + a_2 + a_3} + \eta \right) \\ & \times \frac{1}{1 - \left(\frac{N}{e_1 + a_2 + a_3} - 1 \right) \Theta(e_1, a_2, a_3)} \frac{1}{1 - \left(\frac{N}{g_1 + a_2 + a_3} - 1 \right) \Theta(g_1, a_2, a_3)} \\ & \times T_{a_1 a_2 a_3} T_{e_1 a_2 a_3} T_{e_1 \beta_2 \beta_3} T_{g_1 \beta_2 \beta_3} T_{g_1 \gamma_2 \gamma_3} T_{a_1 \gamma_2 \gamma_3}, \end{aligned} \quad (4.119)$$

where I_i denotes the set of indices $I_i = \{ \{a_i\}, e_1, g_1, \alpha_2, \alpha_3, \beta_2, \beta_3, \gamma_2, \gamma_3 \}$ and Θ is defined as $\Theta(i_1, i_2, i_3) \equiv \theta(N - i_1 - i_2 - i_3)$. The factor of $1/2$ is the prefactor that appears on the right hand side of the definition of the FRG. The factor $3!/2!$ is of combinatorial nature and counts the degeneracy of couplings. The factor of N arises from the contraction of free delta functions.

The above expression can be compared to the one given by Eq. (4.97). Hereby, the function F is given by $F = F(a_1, a_2, a_3, e_1, g_1)$. The indices e_1, a_1, g_1 and a_2 occur as both, overall prefactors and as tensor indices and need therefore to be set to zero in order to recover the original underlying symmetry of the model. The index a_3 does not appear as a tensor index and consequently also does not break the original symmetry of the real model. Thus, in order to project out non-symmetric terms one considers the function $F = F(0, 0, a_3, 0, 0)$. This allows for the calculation of the

spectral sums $\sum_{a_i} F(a_i)$ as the sum does no longer involve a summation over indices that appear simultaneously in the threshold function F and the tensor invariant. In the thermodynamic large- N limit the threshold sums become threshold integrals. The detailed computational steps are performed in Appendix B. Therefore without loss of generality we may write in the large- N limit

$$\begin{aligned} & \text{Tr} \left(\partial_t R_N \mathcal{P}^{-1} (\mathcal{P}^{-1} \mathcal{F})^3 \right) \\ &= 96 \frac{1}{Z_N^3} I_3^1 (\bar{g}_{4,1}^0) (\bar{g}_{4,1}^{2,1})^2 \end{aligned} \quad (4.120)$$

Note that at most R indices, where R is the rank of the tensor, can be non-zero. In that case the $\mathcal{P}^{-1} \mathcal{F}$ expansion involves only terms of the two-point function of multi-trace invariants of the type $T_{\alpha_1 \alpha_2 \alpha_3} T_{\alpha_1 \alpha_2 \alpha_3} \text{Tr}(T^n)$, where n is an even integer, that have no opened lines, e.g.

$$\frac{\partial^2}{\partial T_{\{\alpha_i\}} \partial T_{\{\beta_i\}}} \begin{array}{c} \text{---} \text{---} \\ \text{---} \text{---} \end{array} \sim 4 \begin{array}{c} \text{---} \text{---} \\ \text{---} \text{---} \end{array}. \quad (4.121)$$

The combinatorics of the resulting invariant constructed through the $\mathcal{P}^{-1} \mathcal{F}$ expansion in the above example in Eq. (4.119) can be illustrated pedagogically using the diagrammatic notation

$$\begin{aligned} \text{Tr} \left[(\partial_t R_N) \mathcal{P}^{-1} (\mathcal{P}^{-1} \mathcal{F})^3 \right] &= \text{Tr} \left((\partial_t R_N) \begin{array}{c} \text{---} \text{---} \\ \text{---} \text{---} \end{array} \begin{array}{c} \text{---} \text{---} \\ \text{---} \text{---} \end{array} \begin{array}{c} \text{---} \text{---} \\ \text{---} \text{---} \end{array} \right) \\ &\equiv \begin{array}{c} \text{---} \text{---} \\ \text{---} \text{---} \end{array} \begin{array}{c} \text{---} \text{---} \\ \text{---} \text{---} \end{array} \begin{array}{c} \text{---} \text{---} \\ \text{---} \text{---} \end{array} \begin{array}{c} \text{---} \text{---} \\ \text{---} \text{---} \end{array} \\ &\sim \begin{array}{c} \text{---} \text{---} \\ \text{---} \text{---} \end{array} \begin{array}{c} \text{---} \text{---} \\ \text{---} \text{---} \end{array} \end{aligned} \quad (4.122)$$

where the single lines represent delta functions and the scale derivative of the regulator R_N was replaced by a cross. Lines of same color running through the regulator are contracted. This allows to identify the generated invariant. Note that the above expression only keeps track of the combinatorics and not of the spectral sums that need to be performed.

Scaling Dimension in rank-3 Tensor Models

We have already discussed in detail that as a consequence of the background independence of tensor models the scaling dimension has to fixed *after* having derived the beta functions by demanding the beta functions to become autonomous, i.e. loose their explicit dependence on N , in the large- N limit. The beta functions that

one derives for tensor models will always the following generic form

$$\beta_{g_k} = (-[g_k] + 2\eta) g_k + \sum_j N^n i_n^m f_{j,m,n} \left(\prod_C g_C \right) N^{-[\bar{g}]_k + \sum_C [\bar{g}_C]}, \quad (4.123)$$

where the functions f_j are functions of (products of) couplings g_C , where C indexes the couplings associated to interactions that generate the invariant linked to g_k by means of the $\mathcal{P}^{-1}\mathcal{F}$ expansion. The i_n^m are the threshold functions introduced in Eq. (B.19), where the power in N has been factored out. They depend on the anomalous dimension η and the parameter r introduced in the definition of the modified Litim-regulator in Eq. (4.111). Herein, m counts the order at which the $\mathcal{P}^{-1}\mathcal{F}$ expansion has been performed in order to generate the invariant linked to g_k and n counts the number indices running freely through the regulator as delta functions. The requirement of having a well-defined large- N limit implies the following set of inequalities

$$n - [\bar{g}_k] + \sum_C [\bar{g}_C] \leq 0. \quad (4.124)$$

Sticking for instance to the example of Eq. (4.119), this entails the following inequality for $r = 1$

$$1 - 2[\bar{g}_{4,1}^{2,1}] - [\bar{g}_{4,1}^0] + [\bar{g}_{6,1}^{3,1}] \leq 0. \quad (4.125)$$

Every term contributing to every beta function will therefore entail an inequality such as the one above. These inequalities will, however, not be sufficient in order to uniquely fix the scaling. Ultimately, the scaling has to be fixed by comparing with the continuum side.

The derived beta functions are presented in the appendix.

Search for universality classes

We may now look for universality classes in the large- N limit. The theory spaces that we consider in this thesis are rather large and solving

$$\beta_{g_i} = 0 \quad (4.126)$$

will yield a zoo of zeros of the set of beta functions. This, however, does not mean that the solutions found to this set of equations are actual physical fixed points. In order to distinguish spurious zeros of the beta functions that arise as truncation artifacts from physical fixed points we consider the following set of criteria that need to be satisfied

C.1 Stability of results under successive extension of the truncation.

C.2 Regulator bound $\eta < r$.

C.3 Canonical guiding principle.

The first criterion implies that a fixed point should already be apparent at low order in the truncation. In detail this implies that we consider fixed points that already appear at T^4 for $\eta = 0$ or in special cases, as we will see later on for a perturbative approximation of the anomalous dimension. We track those fixed points through successive extensions of the truncation by considering different approximations of the anomalous dimension as well as increasing the order of the invariants taken into account. Therefore, the scheme where $\eta = 0$ and only T^4 interactions are taken into account is the simplest one. Next, a perturbative approximation of the anomalous dimension is considered. This implies that, whenever the anomalous dimension follows from the scale-derivative of the regulator it is set to zero. This way only the 'canonical' η 's that follow from the wave function renormalization of the couplings are taken into account. The name originates from the fact that the universal one-loop beta functions for the dimensionless couplings are derived within such an approximation from the FRG. Finally, taking into account the full non-polynomial form of the anomalous dimension corresponds to resumming higher-order couplings. This same scheme is then applied at the next higher interaction order. This allows us to track the fixed point going from $\eta = 0$ at T^4 to the full non-polynomial anomalous dimension at order T^6 . The change of the critical exponents should hereby not be larger than $\mathcal{O}(1)$. This implies that the number of relevant or conversely irrelevant directions should only change if $|\theta_i| < 1$. The second criterion follows from the consistency of the regulator. In the limit, where the 'floating' cut-off N tends towards the UV -cut-off N' which tends towards infinity the effective action Γ_N becomes the microscopic action S . For this to occur the regulator has to diverge, i.e.,⁸

$$\lim_{N \rightarrow N' \rightarrow \infty} R_N = \lim_{N \rightarrow N' \rightarrow \infty} Z_N \left(\frac{N^r}{\sum_{i=1}^D a_i} - 1 \right) \theta(N - \sum_{i=1}^D a_i) \rightarrow \infty. \quad (4.127)$$

Note that Z_N has an explicit dependence on N . In order to analyze the conditions that need to be satisfied for the regulator to diverge, we are therefore interested in the particular scaling in N of Z_N , which follows from solving the differential equation

$$-\frac{\partial_t Z_N}{Z_N} = \eta. \quad (4.128)$$

It follows that

$$Z_N \sim N^\eta. \quad (4.129)$$

⁸In the UV , where the regulator cut-off N tends towards the UV cut-off N' which itself is sent to infinity, one wants to recover the bare microscopic action S from the effective action Γ_N . The regulator term in the path-integral $\exp(-T_{\{\alpha_i\}} R_N(\{\alpha_i, \beta_i\}) T_{\{\beta_i\}})$ has to therefore decouple in that limit, which sets the requirement that R_N diverges in the limit, where $N' \rightarrow N \rightarrow \infty$. This also justifies the use of a saddle point approximation that singles out the microscopic action S .

In turn this implies that in the UV the Litim regulator has the following scaling in N

$$\begin{aligned} \lim_{N \rightarrow N' \rightarrow \infty} R_N &= \lim_{N \rightarrow N' \rightarrow \infty} N^\eta \left(\frac{N^r}{\sum_{i=1}^D a_i} - 1 \right) \theta(N - \sum_{i=1}^D a_i) \\ &\sim \lim_{N \rightarrow N' \rightarrow \infty} N^{\eta+r} \rightarrow \infty, \end{aligned} \quad (4.130)$$

where the regulator only diverges if $\eta < r$. This explains the regulator bound introduced as the second criterion C.2 that we require a fixed point to satisfy. Finally, the third criterion is the canonical guiding principle. It implies that enlarging a truncation should not induce new relevant directions. Phrased differently, it means that the fixed point should not be *too* non-perturbative such that the classical scaling of an operator is still a reliable estimate of whether that given operator is relevant or irrelevant at an interacting fixed point. In standard, local QFT, the canonical guiding principle implies that standard power counting of operators is a reliable way to set up truncations.

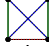
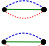
In more quantitative terms, the canonical guiding principle sets a bound on the largest allowed critical exponent by demanding that the inclusion of new operators in a truncation that has been set up through power counting of operators, should not induce new relevant directions once the new couplings that are added are sufficiently irrelevant in the canonical counting.. Therefore, the maximal shift between the largest critical exponent $\max(\theta)$ and the scaling dimension $\max(d_{[\bar{g}]})$ of the coupling with the largest canonical scaling should not exceed the value of the jump that is required to make the coupling with the largest scaling dimension outside of the truncation $\max(d_{[\bar{g}]_{\text{out}}})$ marginal. This sets the following bound

$$\max(\theta) - \max(d_{[\bar{g}]}) \leq 0 - \max(d_{[\bar{g}]_{\text{out}}}). \quad (4.131)$$

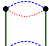
Note that not satisfying the above bound does not necessarily imply that the candidate fixed point does not exist. It rather means that larger truncations have to be studied in order to reliably establish its existence or a different way of setting-up the truncation than the near-canonical guiding principle has to be considered.

Universality classes in 3d tensor models


We find five candidate fixed points that can be separated into two different families of fixed points: The family of dimensionally-reduced fixed points and the family of fixed point candidates for three-dimensional quantum gravity. By dimensionally-reduced fixed points we mean fixed points at which all the invariants that have non-zero fixed points values exhibit an enhanced symmetry. These invariants are characterized by the fact that certain indices are always contracted in multiplets. As a consequence, these multiplets of indices can be 'merged' to form a super index. An example of dimensional reduction is illustrated in Fig. 4.8. On the other hand, the candidate fixed points for three-dimensional quantum gravity cannot be

dimensionally reduced by merging the *same* set of multiplets. An example of an invariant that cannot be dimensionally reduced is the cross interaction  where all indices are distinct. Indeed, the cross-diagram allows for a dual 'geometric' interpretation as a tetrahedron, as illustrated in Fig. 4.6. The three-dimensional character of the cross-interaction therefore suggests that it might be of relevance in describing a three-dimensional quantum gravity phase and one would therefore expect that a fixed point describing a continuum limit where one recovers three-dimensional quantum gravity features a non-zero value for the tetrahedral coupling. Let us analyze which generic types of fixed points may appear at a quartic truncation just from understanding the structure of the quartic beta functions. We will first focus on fixed points that can be dimensionally reduced and afterwards study the ones that might be of potential interest for a 3d quantum gravity phase. The quartic beta functions are given as follows. The running of the coupling associated to the invariant  has the following form

$$\begin{aligned} \beta_{g_{4,2}^2} &= (3 + 2\eta)g_{4,2}^2 + \frac{4}{5}(5 - \eta)g_{4,2}^2(g_{4,1}^{2,1} + g_{4,1}^{2,2} + g_{4,1}^{2,3}) \\ &+ \frac{4}{3}(4 - \eta)(g_{4,1}^{2,1}g_{4,1}^{2,2} + g_{4,1}^{2,1}g_{4,1}^{2,3} + g_{4,1}^{2,2}g_{4,1}^{2,3}) + \frac{2}{5}(6 - \eta)(g_{4,2}^2)^2 \end{aligned} \quad (4.132)$$

The beta functions up to order T^4 associated to  (and color-symmetric permutations thereof) are given via

$$\beta_{g_{4,1}^{2,i}} = (2 + 2\eta)g_{4,1}^{2,i} + \frac{2}{5}(5 - \eta)(g_{4,1}^{2,i})^2 + \frac{2}{3}(4 - \eta)(g_{4,1}^0)^2. \quad (4.133)$$

Note that the above beta functions are invariant under $g_{4,1}^{2,1} \leftrightarrow g_{4,1}^{2,2} \leftrightarrow g_{4,1}^{2,3}$. This simply reflects the fact that the pillow diagrams have the same combinatorial form and only differ through their preferred color. Finally, at quartic order, the running of the coupling of the cross-interaction  is captured via

$$\beta_{g_{4,1}^0} = \left(\frac{3}{2} + 2\eta\right)g_{4,1}^0, \quad (4.134)$$

where we have chosen the enhanced scaling, that is the upper bounds derived through the requirement of obtaining autonomous beta functions in the large- N limit are saturated. This implies that $g_{4,2}^2$ has scaling dimension -3 , the couplings of the pillow interactions $g_{4,1}^{2,i}$ have scaling dimension -2 and the coupling linked to the cross interaction has a scaling in N of $-3/2$. Let us analyze the type of fixed points that can be found.

The cross interaction coupling $g_{4,1}^0$ may be consistently set to zero. In that case its beta function vanishes identically. There now exist different mechanisms in order to also make the $\beta_{g_{4,2}^2}$ and $\beta_{g_{4,1}^{2,i}}$ vanish.

Let us focus on the case that is related to the original reason that we introduced different couplings for the different pillow interactions, namely the dynamical decoupling of $g_{4,2}^2$ which was argued to be related to the emergence of connected

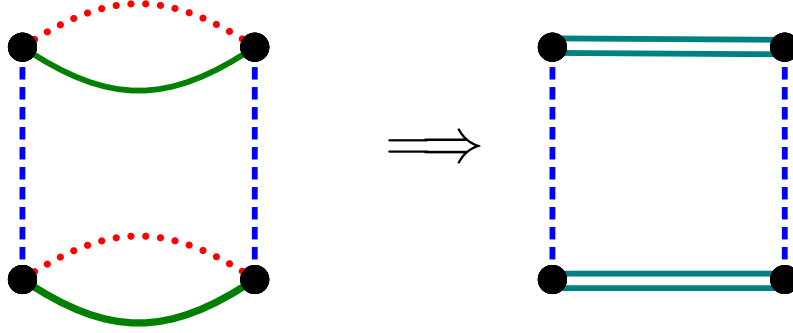
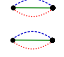


Figure 4.8: The 'pillow' invariant depicted above features an enhanced $O(N') \times O(N'^2)$ symmetry compared to the original $O(N') \times O(N') \times O(N')$ symmetry of the underlying model. This enhanced symmetry can be understood from the fact that two indices always appear in pairs. As a consequence it is possible to merge these pairs of indices to a super-index. The resulting invariant in its diagrammatic form is shown above on the right and represents the rank-2 tensor operator $M_{a_1 A_2} M_{a_1 B_2} M_{a_2 A_1} M_{a_2 B_2}$, where capital indices run from 1 to $(N')^2$. While rank-3 tensor models generate Feynman diagrams that are dual to triangulations of three-dimensional pseudo-manifolds, the Feynman diagrams of rank-2 tensor models (or simply matrix models) are dual to two-dimensional triangulations. This explains the term dimensional reduction when referring to fixed points where all invariants feature the same enhanced symmetry and pairs or triplets of indices can be 'collected' to form a super-index.

space-times with disconnected boundaries. Such kind of topological fluctuations are deemed unphysical as they are associated with an infinite burst of energy when the space-time splits into baby-universes. Setting the multi-trace interaction  to zero implies that its beta function takes the following preliminary form

$$\beta_{g_{4,2}^2} = \frac{4}{3} (4 - \eta) (g_{4,1}^{2,1} g_{4,1}^{2,2} + g_{4,1}^{2,1} g_{4,1}^{2,3} + g_{4,1}^{2,2} g_{4,1}^{2,3}). \quad (4.135)$$

The above part of the beta function vanishes if all pillow couplings vanish, this corresponds to the Gaussian fixed point, or if one pillow coupling is non-vanishing while two are. If all pillow couplings are zero than also their beta functions vanish identically. Let us analyze the case in which one of the pillow couplings is non-zero. In that case one of the pillow beta functions, say $\beta_{g_{4,1}^{2,1}}$ will have the following preliminary form, with $g_{4,1}^0 = g_{4,2}^2 = g_{4,1}^{2,2} = g_{4,1}^{2,3} = 0$, namely

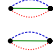
$$\beta_{g_{4,1}^{2,1}} = (2 + 2\eta) g_{4,1}^{2,1} + \frac{2}{5} (5 - \eta) (g_{4,1}^{2,1})^2. \quad (4.136)$$

A non-trivial zero is found if the canonical term $(2+2\eta)$ is balanced with $\frac{2}{5} (5 - \eta) g_{4,1}^{2,1}$. In particular this implies that $g_{4,1}^{2,1}$ has the following non-trivial fixed point solution

for a quartic truncation

$$g_{4,1}^{2,1*} = -\frac{5}{2} \cdot \frac{2+2\eta}{5-\eta}. \quad (4.137)$$

We call a fixed point where $g_{4,1}^{0,*} = g_{4,2}^{2,*} = g_{4,1}^{2,2*} = g_{4,1}^{2,3*} = 0$ while $g_{4,1}^{2,1*}$ are non-trivial (or permutations thereof) a *cyclic-melonic single trace* fixed point. We see that it is indeed possible to dynamically decouple the multi-trace interaction.

The second fixed point that we expect is one where only $g_{4,2}^2$ is turned on. One reason for this expectation is that the multi-trace invariant  exhibits an enhanced $O(N^3)$ symmetry and there is a folk theorem that the flow protects the symmetry. Alternatively, it is straightforward to see that $g_{4,1}^0 = g_{4,1}^{2,1} = g_{4,1}^{2,2} = g_{4,1}^{2,3} = 0$ implies vanishing beta functions for all those couplings, while the running of $g_{4,2}^2$ has the following remaining contribution

$$\beta_{g_{4,2}^2} = (3+2\eta)g_{4,2}^2 + \frac{2}{15}(6-\eta)(g_{4,2}^2)^2. \quad (4.138)$$

The beta function vanishes either trivially if $g_{4,2}^2 = 0$, which corresponds to the Gaussian fixed point or non-trivially if the two contributions to the running of $g_{4,2}^2$ are properly balanced such that

$$g_{4,2}^{2,*} = -\frac{15}{2} \cdot \frac{3+2\eta}{6-\eta}. \quad (4.139)$$

We call such a type of fixed point a *multi-trace melonic* fixed point.

Moreover, we expect fixed points where $g_{4,2}^2$ takes non-trivial values and either one, two or all pillow interactions are also turned on. The underlying reason for this is the fact that the different colours don't mix. That is the running of $g_{4,1}^{2,i}$ only features contributions from couplings that have no preferred colour or have preferred colour i . The only scenario out of these three featuring dimensional reduction is the one where $g_{4,2}^2 \neq 0$ and one of the pillow couplings is non-vanishing. Since $g_{4,2}^2$ does not contribute directly to the running of the cyclic-single trace couplings $g_{4,1}^{2,i}$, the balancing mechanism applicable to generate a non-trivial fixed point for $g_{4,1}^{2,i}$ that worked previously for the *cyclic-melonic single-trace* fixed point also applies here. The running of $g_{4,2}^2$ then takes the following form

$$\beta_{g_{4,2}^2} = (3+2\eta)g_{4,2}^2 + \frac{4}{5}g_{4,2}^2 \left(g_{4,1}^{2,k*}\right) + \frac{4}{3}(4-\eta) \left(g_{4,1}^{2,k*}\right), \quad (4.140)$$

This equation can then be solved for $g_{4,2}^2$ in order to have $\beta_{g_{4,2}^2} = 0$. We dub such a fixed point a *cyclic-melonic multitrace* fixed point. It is always possible to make any beta function of a pillow interaction with preferred color i vanish by having either $g_{4,1}^{0,*} = 0$ and $g_{4,1}^{2,i*} = 0$ or $g_{4,1}^{0,*} = 0$ and $g_{4,1}^{2,i*}$ given by Eq. (4.137) which follows from balancing the different remaining contributions after $g_{4,1}^0 = 0$ to the running of $g_{4,1}^{2,i}$. The fact that the pillows invariants are combinatorially identical, implies

that the beta functions of all pillow interactions have the same form and therefore if the balancing mechanism works for one pillow interaction it works for any. As a consequence, in the case where one pillow coupling vanishes while the fixed point values of the two others are given non-trivially by Eq. (4.137) the running of $g_{4,2}^2$ takes the following form

$$\beta_{g_{4,2}^2} = (3 + 2\eta)g_{4,2}^2 + \frac{4}{5}g_{4,2}^2 \left(g_{4,1}^{2,k*} + g_{4,1}^{2,j*} \right) + \frac{4}{3}(4 - \eta) \left(g_{4,1}^{2,j*} g_{4,1}^{2,k*} \right), \quad (4.141)$$

where $i \neq j \neq k$. The fixed point values of $g_{4,1}^{2,j}$ and $g_{4,1}^{2,k}$ are determined via the same balancing mechanism that already applied in Eq. 4.136, i.e.

$$g_{4,1}^{2,1*} = g_{4,1}^{2,2*} = -\frac{5}{2} \cdot \frac{2 + 2\eta}{5 - \eta}. \quad (4.142)$$

Plugging the fixed point value obtained via the balancing mechanism at quartic order given by Eq. 4.137 into Eq. 4.141 it is straightforward to find two possible fixed point values for $g_{4,2}^2$. Namely, they are given by solving the quadratic equation that follows from the fixed point requirement $\beta_{g_{4,2}^2} = 0$. The fixed point solutions for $g_{4,2}^2$ take a rather involved form. For $\eta = 0$, however, the fixed solutions found are complex and are given as

$$g_{4,2}^{2*} = \frac{1}{24} \left(25 \pm i\sqrt{655} \right) \quad (4.143)$$

This artifact also persists when the full anomalous dimension is taken into account at quartic order. The picture changes, however, for the hexic truncation, where all fixed point values are real. Interestingly, this fixed point features no dimensional reduction, that is it is not possible to 'merge' the same pairs of indices in order to obtain a single matrix model.

Yet another fixed point that we expect from the combinatorial structure of the beta functions which features no dimensional reduction involving multi-trace and single-trace melonic interactions is the so-called *isocolored melonic* fixed point. The *isocolored melonic* fixed point is characterized by $g_{4,2}^2$ and all single-trace couplings $g_{4,1}^{2,i}$ being non-zero. The fixed point mechanism is similar to the one that also applied for the *cyclic-melonic single-trace*, the *cyclic-melonic multitrace* and the *double cyclic-melonic multitrace* fixed points: Non-trivial fixed point values for the pillow couplings are generated via a balancing mechanism derived from Eq. (4.136) such that the pillow couplings $g_{4,1}^{2,i}$ are given by Eq. (4.137). This fixed point will turn out to have complex fixed point values at quartic and at hexic order in the truncation.

Lastly, while the running of the cross coupling $g_{4,1}^0$ seems rather trivial; it is given by

$$\beta_{g_{4,1}^0} = \left(\frac{3}{2} + 2\eta \right) g_{4,1}^0 \quad (4.144)$$

it is actually possible to generate a fixed point for $g_{4,1}^0$ within a quartic truncation by demanding that $\eta = -3/4$. In that case the canonical prefactor of $g_{4,1}^0$ vanishes identically and $g_{4,1}^0$ can take non-trivial fixed point values. The set of allowed fixed point values for $g_{4,1}^{2,i*}$ and $g_{4,2}^{2*}$ is thereby constrained by the beta functions vanishing and $\eta = -3/4$. This also sets a restriction on possible fixed point values that $g_{4,1}^0$ can take, even though its running is identically zero due to $\eta = -3/4$. As a consequence of the fact that $g_{4,1}^0$ has a quadratic contribution to the pillow couplings it turns out that there will be two possible fixed points resulting from the constraint $\eta = -3/4$.

Dimensionally reduced fixed points

This section reports on the dimensionally reduced fixed points that we find and expect from the previous discussion. They are not candidates for three-dimensional quantum gravity, but are related to either branched polymers or two-dimensional quantum gravity. As a reminder, from the structure of the quartic β functions we expect to find the following fixed point candidates

- A *cyclic-melonic single-trace* fixed point where only $g_{4,1}^{2,1}$ and $g_{6,1}^{3,1}$ as introduced in Fig. 4.7 are non-zero (and color permutations thereof).
- A *multi-trace bubble* fixed point, where only $g_{4,2}^2$ and $g_{6,3}^3$ are non-zero.
- A *cyclic-melonic multi-trace* fixed point, where $g_{4,1}^{2,1}$, $g_{6,1}^{3,1}$, $g_{6,2}^{3,1}$, $g_{4,2}^2$ and $g_{6,3}^3$ are non-zero (and color permutations thereof).

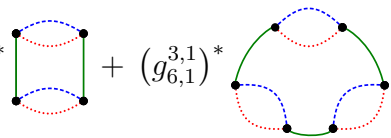
Let us discuss these fixed points in more detail and understand the mechanisms behind their 'generation', potentially also at hexic order.

Cyclic-Melonic Single-Trace fixed point

The fact that at the cyclic-melonic single-trace fixed point only the couplings $g_{4,1}^{2,1}$ and $g_{6,1}^{3,1}$ are non-trivial implies an enhanced symmetry. The values of the coupling constants at the fixed point as well as the associated critical exponents are reported in Tab. 4.1 for the quartic truncation and in Tab. 4.2 for the hexic truncation. At the fixed point, one has

$$S_{FP}^* = (g_{4,1}^{2,1})^* T_{a_1 a_2 a_3} T_{b_1 a_2 a_3} T_{a_1 b_2 b_3} T_{b_1 b_2 b_3} + (g_{6,1}^{3,1})^* T_{a_1 a_2 a_3} T_{b_1 a_2 a_3} T_{b_1 b_2 b_3} T_{c_1 b_2 b_3} T_{c_1 c_2 c_3} T_{a_1 c_2 c_3}, \quad (4.145)$$

or in the diagrammatic form

$$S_{FP}^* = (g_{4,1}^{2,1})^* \text{[diagram 1]} + (g_{6,1}^{3,1})^* \text{[diagram 2]} \quad (4.146)$$


that is the last two indices are always contracted in pairs. Therefore, as also illustrated in Fig. 4.8, we may merge these two indices to form a new 'super-index'. The resulting rewritten fixed point action is then

$$S_{FP}^* = (g_{4,1}^{2,1})^* T_{a_1 A_2} T_{b_1 A_2} T_{a_1 B_2} T_{b_1 B_2} + (g_{6,1}^{3,1})^* T_{a_1 A_2} T_{b_1 A_2} T_{b_1 B_2} T_{c_1 B_2} T_{c_1 C_2} T_{a_1 C_2} \quad (4.147)$$

or in the diagrammatic form

$$S_{FP}^* = (g_{4,1}^{2,1})^* \begin{array}{c} \bullet \\ \text{---} \\ \bullet \\ \text{---} \\ \bullet \\ \text{---} \\ \bullet \end{array} + (g_{6,1}^{3,1})^* \begin{array}{c} \bullet \\ \text{---} \\ \bullet \\ \text{---} \\ \bullet \\ \text{---} \\ \bullet \\ \text{---} \\ \bullet \end{array}. \quad (4.148)$$

The double lines indicate that this index runs from 1 to N'^2 . At quartic order in

scheme	$g_{4,1}^{0,*}$	$g_{4,1}^{2,1,*}$	$g_{4,1}^{2,2,*}$	$g_{4,1}^{2,3,*}$	$g_{4,2}^{2,*}$	
full	0	-0.38	0	0	0	
pert	0	-0.43	0	0	0	
$\eta = 0$	0	-1	0	0	0	
scheme	θ_1	θ_2	θ_3	θ_4	θ_5	η
full	2.27	-0.16	-0.34	-0.84	-0.84	-0.58
pert	2	-0.14	-0.36	-0.86	-0.86	-0.57
$\eta = 0$	2	1	-1.5	-2	-2	-

Table 4.1: The cyclic-melonic single-trace fixed point features one relevant direction in the quartic truncation.

the truncation we observe one relevant direction as the anomalous dimension η is taken into account in the perturbative scheme and in the full non-polynomial one. There exists a degeneracy between two critical exponents, which is a consequence of the existing symmetry of the system of β -functions under the exchange of $g_{4,1}^{2,2}$ and $g_{4,1}^{2,3}$. At order T^4 , the system of β -functions and the critical exponents can be solved exactly as the stability matrix takes a block diagonal form. The stability matrix reflects the fact that the β functions of $g_{4,1}^{2,2}$ and $g_{4,1}^{2,3}$ only have contributions through their canonical scaling term $(2 + 2\eta)g_{4,1}^{2,i}$ as all other contributions are quadratic in the couplings and all couplings except $g_{4,1}^{2,2}$ vanish at the fixed point. The fact that the β functions are invariant under the exchange of $g_{4,1}^{2,2}$ and $g_{4,1}^{2,3}$ and have at most a

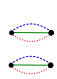

scheme	$g_{4,1}^{2,1*}$	$g_{6,1}^{3,1*}$						
full	-0.28	-0.15						
pert	-0.30	-0.18						
$\eta = 0$	-0.46	-0.50						
scheme	θ_1	θ_2	θ_3	$\theta_{4,5}$	θ_6	$\theta_{7,8}$	θ_9	θ_{10}
full	2.19	-0.03	-0.69	-1.19	-1.68	-1.78	-2.08	-2.15
pert	2	-0.03	-0.70	-1.20	-1.69	-1.79	-2.09	-2.17
$\eta = 0$	2	0.53	-1.5	-2	-2.58	-3	-2.66	-3.25
scheme	$\theta_{11,12}$	$\theta_{13,14}$	$\theta_{15,16,17}$	θ_{18}	θ_{19}	$\theta_{20,21}$	η	
full	-2.18	-2.28	-2.78	-2.94	-2.98	-3.18	-0.41	
pert	-2.19	-2.29	-2.79	-2.94	-2.98	-3.19	-0.40	
$\eta = 0$	-3.08	-3.5	-4	-3.41	-3.94	-4.08	-	

Table 4.2: The cyclic-melonic single-trace fixed point only features cyclic melonic couplings and one associated relevant direction in the truncation to sixth order. Given the systematic error of the truncation and the small value $\theta_2 = -0.03$, a second positive critical exponent might exist at higher orders in the truncation.

linear dependence in the coupling allows us to easily read off the critical exponents

$$\begin{aligned}
\theta_1 &= -(2 + 2\eta) - \frac{4}{5}(5 - \eta)(g_{4,1}^{2,1})^* \\
\theta_2 &= -\left(\frac{3}{2} + 2\eta\right) \\
\theta_3 &= -(3 + 2\eta) - \frac{4}{5}(5 - \eta)(g_{4,1}^{2,1})^* \\
\theta_{4,5} &= -(2 + 2\eta).
\end{aligned} \tag{4.149}$$

Multitrace bubble fixed point

The multitrace bubble fixed point is characterized by only the multitrace invariant with the most non-connected components being non-zero. That is $g_{n,n/2}^{n/2}$, where n is the order of the interaction is interacting at the fixed point. For a hexic truncation this implies that the couplings associated to  and  are non-trivial. This fixed point features an enhanced $O(N^3)$ symmetry, which follows from the fact that indices are always contracted as triplets. It is therefore possible to 'merge' this indices in order to a single one. The resulting model is a vector model. A peculiarity of the multitrace bubble fixed point is the simplicity of the involved combinatorics, which makes it very easy to include higher-order terms in the truncation and track it deep into theory space. At hexic order the only non-trivial beta functions, i.e., those that are not trivially vanishing after setting all couplings except $g_{4,2}^2$ and $g_{6,3}^3$

to zero are precisely those related to these two couplings, i.e.,

$$\beta_{g_{4,2}^2} = (3 + 2\eta)g_{4,2}^2 + 4 \cdot I_2^3 \cdot (g_{4,2}^2)^2 + 6 \cdot I_1^3 \cdot g_{6,3}^3 \quad (4.150)$$

and

$$\beta_{g_{6,3}^3} = (6 + 3\eta)g_{6,3}^3 + 4^3 \cdot I_3^3 \cdot (g_{4,2}^2)^3 + \frac{3!}{2!} \cdot (4 \cdot 6) \cdot I_2^3 \cdot (g_{6,3}^3) (g_{4,2}^2)^3. \quad (4.151)$$

Each term contributing to a tensor model beta function consists of a prefactor that follows from the permutativity of couplings, a prefactor that follows from the computation of the two-point function, a threshold function I and a product of couplings. In the case of multi-trace couplings of the form $g_{2n,n}^n$, where $2n$ denotes the order of the invariant, the prefactors that follow from the computation of the two-point function are straightforward to identify. Namely, they are exactly given by the numbers of tensors $2n$, which follows from the fact that each multitrace invariant related to couplings of the form $g_{2n,n}^n$ consists of n products of tensor contractions of the form $T_{\alpha_1\alpha_2\alpha_3}T_{\alpha_1\alpha_2\alpha_3}$. Since derivatives commute each such pair of tensor contractions gives an overall factor of two. Given that the invariant associated to $g_{2n,n}^n$ has n such pairs of tensor contractions this results in an overall factor of $2n$. This knowledge allows one to systematically write down the beta functions for higher-order invariants. Since at the multi-trace bubble fixed point all interactions except those of the type $g_{2n,n}^n$ are turned on, it is possible to extend the T^6 truncation by just including multi-trace interactions of the form $g_{2n,n}^n$ without generating terms outside the truncation, or more precisely the terms that are generated outside the truncation would be vanishing at this fixed point. This is a consequence of the enhanced $O(N^3)$ symmetry featured by the fixed point. Including for instance $g_{8,4}^4$ results in the following additional beta function

$$\begin{aligned} \beta_{g_{8,4}^4} = & (9 + 4\eta)g_{8,4}^4 + 4^4 \cdot I_4^3 \cdot (g_{4,2}^2)^4 + \frac{3!}{2!} \cdot (6 \cdot 4^2) \cdot I_3^3 \cdot (g_{6,3}^3) (g_{4,2}^2)^2 \\ & + 6^2 \cdot I_2^3 \cdot (g_{6,3}^3)^2 + \frac{3!}{2!} \cdot (8 \cdot 4) \cdot I_2^3 \cdot (g_{8,4}^4) (g_{4,2}^2) \end{aligned} \quad (4.152)$$

and having to take into account an additional contribution of $g_{8,4}^4$ to the running of $g_{6,3}^3$. The fixed point values and critical exponents that we find for each successive scheme are reported in Table 4.3 for the quartic truncation and Table 4.4 for the hexic truncation. The critical exponents associated to this fixed point are in agreement with the ones found in the complex model [226]. However, due to a larger theory space a second relevant direction is picked up in the quartic truncation. The systematic error associated to regulator and truncation dependence is expected to be larger than the second relevant critical exponent, which in the scheme where the full anomalous dimension is taken into account, is $\theta_2 = 0.18$. We therefore caution that the quartic truncation is not sufficient to make statements on the number of relevant directions associated to the *multitrace bubble* fixed point. As a matter of fact, the hexic truncation features only one relevant direction. In order to test, whether this

picture persists at higher truncations we extend our truncation by $g_{8,4}^4$ as discussed above. The additional beta function is given by Eq. (4.152). We observe that under an extension of the truncation in this form, the number of relevant directions remains stable. Indeed for $\eta = 0$ we find that $\theta_1 = 3$ while $\theta_2 = -1.5$. Enlarging the truncation with a perturbative approximation of the anomalous dimension yields $\theta_1 = 3$ and $\theta_2 = -0.65$. Finally, taking into account the full non-polynomial form of η results in $\theta_1 = 3.24$ and $\theta_2 = -0.64$, while $\eta_{\text{full}} = -0.43$.

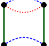
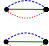
scheme	$g_{4,1}^{0*}$	$g_{4,1}^{2,1*}$	$g_{4,1}^{2,2*}$	$g_{4,1}^{2,3*}$	$g_{4,2}^{2*}$	
full	0	0	0	0	-1.44	
pert	0	0	0	0	-1.67	
$\eta = 0$	0	0	0	0	-3.75	
scheme	θ_1	θ_2	θ_3	θ_4	θ_5	η
full	3.47	0.18	-0.32	-0.32	-0.32	-0.84
pert	3	0.17	-0.33	-0.33	-0.33	-0.83
$(\eta = 0)$	3	-1.5	-2	-2	-2	-

Table 4.3: The multitrace-bubble fixed point features two relevant directions in the truncation to quartic order, with one of the positive critical exponents rather close to zero, calling for an extension of the truncation to confirm its relevance.

sch.	$g_{4,1}^{0*}$	$g_{4,1}^{2,i*}$	$g_{4,2}^{2*}$	$g_{6,1}^{0,np*}$	$g_{6,1}^{0,p*}$	$g_{6,1}^{1,i*}$	$g_{6,1}^{2,i*}$	$g_{6,1}^{3,i*}$	$g_{6,2}^{3,i*}$	$g_{6,2}^{1*}$	$g_{6,3}^{3*}$
full	0	0	-1.05	0	0	0	0	0	0	0	-2.27
pert	0	0	-1.16	0	0	0	0	0	0	0	-2.82
$\eta = 0$	0	0	-1.73	0	0	0	0	0	0	0	-7.45
sch.	θ_1	θ_2	$\theta_{3,4,5}$	$\theta_{6,7}$	$\theta_{8,9,10}$	θ_{11}	$\theta_{12,13,14,15,16,17}$	$\theta_{18,19,20}$	θ_{21}	η	
full	3.32	-0.33	-0.83	-1.24	-1.74	-1.82	-2.24	-2.32	-3.28	-0.59	
pert	3	-0.34	-0.84	-1.26	-1.76	-1.83	-2.26	-2.33	-3.30	-0.58	
$\eta = 0$	3	-1.5	-2	-3	-3.5	-3.12	-4	-3.62	-5.08	-	

Table 4.4: Results for the multitrace-bubble fixed point at order T^6 in the truncation. The leading critical exponent is close to our bound $\theta < 3.5$, yet the explicit extension to T^8 shows the fixed point persists.

Cyclic-melonic multitrace fixed point

The last fixed point belonging to the family of dimensionally reduced fixed points and expected from the combinatorial structure of the quartic beta functions is the *cyclic-melonic multitrace* fixed point. At quartic order this fixed point is characterized by one non-vanishing pillow interaction  with coupling $g_{4,1}^{2,i}$ and a non-vanishing multitrace interaction  with coupling $g_{4,2}^2$. This fixed point has also

been explored in the complex model, featuring two relevant directions in both, the real and the complex model. At quartic order, the critical exponents of the real and the complex model agree. At hexic order, however, the critical exponents reported in this work differ from those found in the complex model [226]. The reason for this deviation, which is 15% for the most relevant critical exponent in the full non-polynomial approximation, is that in the study of the complex model, the upper scaling bounds of $g_{6,1}^{2,i}$ were not satisfied. The fact that in this work the upper bounds are satisfied also explains the reported three-fold degeneracy in a subset of the critical exponents in Table. 4.6, which was not observed in the complex case. The degeneracy follows from the fact that if the upper bound is satisfied for $g_{6,1}^{2,i}$ is has the same scaling as the hexic cyclic single-trace melonic couplings $g_{6,1}^{3,i}$. In that case, the couplings $g_{6,1}^{2,1}$, $g_{6,1}^{3,2}$ and $g_{6,1}^{3,3}$ have the same diagonal contribution $-(4 + 3\eta)$ to the stability matrix, which turns out to then be block-diagonal in these entries. The three-degeneracy follows from there.

This fixed features an enhanced $O(N') \times O(N'^2)$ symmetry, just like the *cyclic-melonic single-trace* fixed point, whereby the fixed point action can be rewritten a single matrix model

$$\begin{aligned}
S_{FP}^* = & g_{4,1}^{2,1*} \text{[square]} + g_{4,2}^{2*} \text{[two arcs]} + g_{6,1}^{3,1*} \text{[hexagon]} \\
& + g_{6,3}^{3*} \text{[two arcs]} + g_{6,2}^{3,1*} \text{[square]}. \tag{4.153}
\end{aligned}$$

Note that in principle the indices of the multi-trace invariants could be merged even further, as the new 'super-index' and the 'green' index still appear in pairs. This would result in a matrix-vector model since the melonic interactions cannot be further dimensionally reduced. Consequently, one would still expect of such a fixed point to be associated to the triangulation of a two-dimensional surface. Interestingly, it has been observed that taking into account multi-trace invariants in matrix models allows one to correctly derive the precise critical exponents describing two-dimensional quantum gravity coupled to conformal matter. Intuitively, this could follow from the fact that the multi-trace In that context, one would expect that the cyclic-melonic multitrace invariant M of the form

$$M = T_{\alpha_1 \alpha_2 \alpha_3} T_{\alpha_1 \beta_2 \beta_3} T_{\beta_1 \beta_2 \beta_3} T_{\beta_1 \alpha_2 \alpha_3} T_{\gamma_1 \gamma_2 \gamma_3} T_{\gamma_1 \gamma_2 \gamma_3} = \text{[diagram]} \tag{4.154}$$

might be important, as it mixes vector and matrix degrees of freedom when dimensionally reduced as follows

$$M = (V_A V_A) \text{Tr} (M^4) = \begin{array}{c} \bullet \text{---} \bullet \\ \square \\ \bullet \text{---} \bullet \end{array}. \quad (4.155)$$

It is evident that the above invariant mixes vector and matrix degrees of freedom, which could tentatively be interpreted as an interaction between matter and two-dimensional gravitational degrees of freedom on the continuum side.

scheme	$g_{4,1}^{0*}$	$g_{4,1}^{2,1*}$	$g_{4,1}^{2,2*}$	$g_{4,1}^{2,3*}$	$g_{4,2}^{2*}$
full	0	-0.29	0	0	-0.38
pert.	0	-0.35	0	0	-0.38
$\eta=0$	0	-1	0	0	1.25
scheme	θ_1	θ_2	θ_3	$\theta_{4,5}$	η
full	2.57	0.11	-0.16	-0.66	-0.67
pert.	2.20	0.10	-0.19	-0.69	-0.65
$\eta=0$	2	-1	-1.5	-2	0

Table 4.5: At quartic order the fixed point possesses two relevant directions. Compared to the complex model, one finds a new irrelevant direction (θ_3) which is associated to the "tetrahedral" interaction. There is good agreement between the complex and the real model at quartic level.

sch.	$g_{4,1}^{2,1*}$	$g_{4,1}^{2,(2,3)*}$	$g_{4,2}^{2*}$	$g_{6,1}^{2,i*}$	$g_{6,1}^{3,1*}$	$g_{6,1}^{3,(2,3)*}$	$g_{6,2}^{3,1*}$	$g_{6,2}^{3,(2,3)*}$	$g_{6,3}^{3*}$
full	-0.27	0	-0.05	0	-0.13	0	-0.05	0	-0.01
pert	-0.30	0	-0.04	0	-0.17	0	-0.05	0	-0.01
$\eta = 0$	-0.46	0	0	0	-0.50	0	0	0	0
sch.	θ_1	θ_2	θ_3	$\theta_{4,5}$	θ_6	$\theta_{7,8}$	θ_9	θ_{10}	
full	2.23	0.03	-0.66	-1.16	-1.66	-1.74	-2.04	-2.12	
pert.	2.03	0.03	-0.67	-1.17	-1.67	-1.76	-2.05	-2.14	
$\eta = 0$	2	0.53	-1.5	-2	-2.58	-3	-2.66	-3.25	
-	$\theta_{11,12}$	$\theta_{13,14}$	θ_{15}	$\theta_{16,17,18}$	θ_{19}	$\theta_{20,21}$	η		
full	-2.16	-2.24	-2.73	-2.74	-3.10	-3.12	-0.42	-	
pert.	-2.17	-2.26	-2.77	-2.76	-3.10	-3.14	-0.41	-	
$\eta = 0$	-3.08	-3.5	-3.41	-4	-3.94	-4.08	-	-	

Table 4.6: Fixed-point values of the cyclic melonic couplings and critical exponents in the truncation to sixth order for the cyclic-melonic multitrace fixed point. The couplings not displayed are all vanishing at the fixed point.

Candidate for 3D Quantum Gravity

From the analysis of the quartic beta functions, we expect three classes of fixed points that feature no dimensional reduction. These fixed point candidates are

- a *double cyclic-melonic single-trace* fixed point where only the multi-trace couplings $g_{4,2}^2$ and $g_{6,3}^3$ as well as two of the three cyclic-melonic single-trace couplings are non-zero (and color permutations thereof).
- an *isocolored melonic* fixed point, where all single-trace melonic interactions as well as the bubble interactions are interacting.
- an *isocolored* fixed point with *tetrahedral interaction*, where $g_{4,1}^{2,1}$, $g_{6,1}^{3,1}$, $g_{6,2}^{3,1}$, $g_{4,2}^2$ and $g_{6,3}^3$ are non-zero (and color permutations thereof).

We will mostly focus on the latter one of these three fixed points, the isocolored fixed point with tetrahedral interaction.

Isocolored fixed point with tetrahedral interaction

The name of the fixed point stems from the fact that the 'geometric' interaction $g_{4,1}^0$ is non-trivial, where 'geometric' refers to the fact that the corresponding cross-interaction admits a dual interpretation, as depicted in Fig. 4.6, where the cross-invariant corresponding to

$$C(T) = T_{a_1 a_2 a_3} T_{a_1 b_2 b_3} T_{b_1 a_2 b_3} T_{b_1 b_2 a_3} = \begin{array}{c} \bullet \text{---} \bullet \\ \diagup \quad \diagdown \\ \bullet \text{---} \bullet \\ \diagdown \quad \diagup \\ \bullet \text{---} \bullet \end{array} \quad (4.156)$$

is identified with a tetrahedron. The identification is based on the fact that each tensor can be represented by the face of a triangle, while each index of a tensor corresponds to an edge of that triangle. One would expect that such an interaction plays a crucial role, when trying to unravel a continuum limit with a three-dimensional geometric interpretation. As a reminder, within a quartic truncation it was possible to generate a non-trivial fixed point for $g_{4,1}^0$ by having $\eta = -3/4$. At sixth order, however, this requirement is no longer needed as the running of $g_{4,1}^0$ obtains an additional contribution from $g_{6,2}^1$. As a consequence the interpretation of Tab. 4.7 and Tab. 4.8 should be treated with the remark that the mechanism for the fixed point generation in the quartic truncation and the one in the hexic truncation are rather distinct and our criterion C.1 is in fact violated. The fact that the sixth order truncation is the first order in the truncation where the requirement $\eta = -3/4$ is no longer needed in order to generate a non-trivial fixed point for $g_{4,1}^0$ explains the significant shift in the critical exponents and in the anomalous dimension when enlarging the truncation from quartic to hexic order. To obtain a glance on whether the *isocolored fixed point with tetrahedral interaction* has any relation to three-dimensional quantum gravity a first step is to compare critical exponents on the discrete tensor model side with critical exponents derived on the continuum side. Ultimately, however, to draw stronger conclusions it is necessary to find more evidence for instance by comparing the scaling of geometric observables on both sides or by computing dimensional estimators such as the spectral dimension or the Hausdorff dimension. This is beyond the scope of this work and we will for now attempt to only compare critical exponents. On the continuum side, critical exponents associate to a scale-invariant UV regime haven been computed under the assumption of the Asymptotic Safety scenario. In three dimensions, using Euclidean signature, and assuming a Einstein-Hilbert truncation, a non-trivial fixed point with two relevant directions $\theta_1 \approx 2.5$ and $\theta \approx 0.8$ has been reported [258], while the discretized Wheeler-de-Witt equation yields a leading critical exponent of $\theta_1 = 11/6$ [259]. In order to make the comparison between the critical exponents sharper it is necessary to discuss the associated error resulting from truncating. The leading critical exponent in the scheme where the full anomalous dimension is considered at quartic order deviates from the one at hexic order by $\delta \approx 1.6$. It is therefore necessary to study larger truncations in order to make more precise statements about the numerical values of the critical exponents. The way to proceed by comparing critical exponents, however, is a sensible way to compare

the discrete and the continuum side. The idea of such an approach is identical to the one undertaken when studying the duality between matrix models, dynamical triangulations and continuum two-dimensional quantum gravity.

scheme	$g_{4,1}^{0*}$	$g_{4,1}^{2,1*}$	$g_{4,1}^{2,2*}$	$g_{4,1}^{2,3*}$	$g_{4,2}^{2*}$	
full	± 0.07	-0.04	-0.04	-0.04	-0.93	
pert.	± 0.09	-0.05	-0.05	-0.05	-1.12	
scheme	θ_1	θ_2	θ_3	θ_4	θ_5	η
full	2.98	-0.28 - i 0.22	-0.28 + i 0.22	-0.29	-0.29	-0.75
pert.	2.60	-0.27- i 0.21	-0.27 + i 0.21	-0.31	-0.31	-0.75

Table 4.7: The isocolored fixed point with tetrahedral interaction $g_{4,1}^0$ features an anomalous dimension of $\eta = -0.75$, as discussed in Sec. ???. It is clear then that for $\eta = 0$ no such fixed point exists. The sign of $g_{4,1}^{0*}$ is not determined by the fixed-point conditions, i.e., there are two fixed points.

scheme	$g_{4,1}^{0*}$	$g_{4,1}^{2,i*}$	$g_{4,2}^{2*}$	$g_{6,1}^{0,np*}$	$g_{6,1}^{0,p*}$		
full	± 0.42	-0.50	3.43	0	0		
pert.	± 0.46	-0.54	3.68	0	0		
$\eta = 0$	± 0.60	-0.71	5.09	0	0		
scheme	$\theta_{1,2}$	$\theta_{3,4}$	$\theta_{5,6}$	$\theta_{7,8}$	$\theta_{9,10}$		
full	$1.35 \pm 1.56 i$	0.13	$-0.02 \pm 5.10 i$	$-0.08 \pm 5.35 i$	$-0.08 \pm 5.35 i$		
pert.	$1.46 \pm 1.39 i$	0.15	$-0.11 \pm 4.83 i$	$-0.10 \pm 5.42 i$	$-0.10 \pm i 5.42$		
$\eta = 0$	$1.95 \pm 0.69 i$	0.38	$-0.03 \pm 5.96 i$	$-0.29 \pm 7.06 i$	$-0.29 \pm 7.06 i$		
scheme	$g_{6,1}^{2,i*}$	$g_{6,1}^{3,i*}$	$g_{6,2}^{1*}$	$g_{6,2}^{3,i*}$	$g_{6,3}^3$		
full	-5.33	4.19	± 2.65	-2.26	35.27		
pert.	-6.33	4.96	± 3.18	-2.56	39.82		
$\eta = 0$	-10.67	8.20	± 7.16	-4.35	67.32		
scheme	$\theta_{11,12}$	$\theta_{13,14}$	$\theta_{15,16,17}$	$\theta_{18,19}$	θ_{20}	θ_{21}	η
full	$-0.88 \pm 1.33i$	-1.40	-1.43	-2.00	-3.04	-4.80	-0.33
pert.	$-0.99 \pm 1.34i$	-1.41	-1.46	-2.04	-2.95	-5.36	-0.32
$\eta = 0$	-1.74	$-1.89 \pm 2.72i$	-2.07	-3	$-5.70 + 1.57i$	$-5.70 - 1.57i$	0

Table 4.8: Fixed-point values and critical exponents at sixth order in the truncation for the isocolored fixed point with tetrahedral interaction.

scheme	$g_{4,1}^{0*}$	$g_{4,1}^{2,i*}$	$g_{4,1}^{2,j*}$	$g_{4,1}^{2,k*}$	$g_{4,2}^{2*}$
full	0	$-0.24 \pm 0.06 i$	$-0.24 \pm 0.06 i$	0	$0.05 \mp 0.42 i$
pert.	0	$-0.28 \pm 0.07 i$	$-0.28 \pm 0.07 i$	0	$0.07 \mp 0.48 i$
$\eta=0$	0	$1.04 \pm 1.07 i$	$1.04 \pm 1.07 i$	0	-1
scheme	θ_1	θ_2	θ_3	θ_4	θ_5
full	2.57	0.11	-0.16	-0.66	-0.67
pert.	$1.82 \pm 0.11 i$	$0.56 \mp 0.13 i$	$0.53 \pm 1.80 i$	$-0.06 \pm 0.13 i$	$-0.56 \pm 0.13 i$
$\eta=0$	2	2	$0 \pm 5.12 i$	-1.5	-2

Table 4.9: There exists a pair of families of fixed points at which two representatives of $g_{4,1}^{2,i}$ are turned on. At quartic order the fixed point possesses two relevant directions, while in the scheme where $\eta = 0$ there is also one marginal direction. When taking into account the anomalous dimension in either the perturbative or the full scheme, all couplings taking non-trivial fixed point values are complex. Note that it is not clear, whether having complex couplings is actually problematic in a background-independent setting where there is no notion of space-time as there is no metric and hence also not a notion of signature. The action might therefore also be allowed to be complex. Moreover, the plus-minus sign indicates that there are two possible fixed points with complex-conjugate fixed point values for the couplings. The two fixed points are characterized by critical exponents whose real parts agree but with a different sign in front of the complex part of the critical exponents.

Double Cyclic-Melonic Single-Trace Fixed Point

The structure of the quartic beta functions also allows for a second family of fixed points⁹ at which interactions cannot be dimensionally reduced, which also persists once the truncation is extended by including hexic interactions. This fixed point has not been reported so far in the literature.

At quartic order the fixed point is characterized by two cyclic-melonic interactions, $g_{4,1}^{2,i}$ and $g_{4,1}^{2,j}$, and the multitrace interaction being turned on. For any given value of i and j , with $i \neq j$, there exists a pair of fixed points with complex conjugate fixed point values. When the truncation is extended by including hexic interactions the couplings take real fixed point values.

⁹By fixed point family, we mean that there exists a collection of fixed points for which $g_{4,1}^{2,i} = g_{4,1}^{2,j} \neq 0, \quad \forall i \neq j$.

sch.	$g_{4,1}^{2,i*}$	$g_{4,1}^{2,(j,k)*}$	$g_{4,2}^{2,*}$	$g_{6,1}^{3,1*}$	$g_{6,1}^{3,(2,3)*}$	$g_{6,i}^{3,1*}$	$g_{6,2}^{3,(j,k)*}$	$g_{6,3}^{3,*}$	
full	0	-0.13	-0.37	0	-0.01	0	-0.40	1.93	
pert	0	-0.15	-0.37	0	-0.02	0	-0.05	2.37	
$\eta = 0$	0	-0.45	-0.06	0	-0.43	0	-0.51	4.76	
sch.	θ_1	θ_2	θ_3	θ_4	θ_5	θ_6	θ_7	θ_8	θ_9
full	2.67	0.34	0.18	-0.31	-0.81	-1.27	-1.54	-1.66	-1.72
pert.	2.42	0.41	0.25	-0.32	-0.82	-1.23	-1.52	-1.64	-1.73(6)
$\eta = 0$	3.65	2.10	1.89	-0.87	-0.89	-1.5	-1.90	-2	-2.21
-	$\theta_{10,11}$	$\theta_{12,13}$	θ_{14}	$\theta_{15,16}$	θ_{17}	θ_{18}	$\theta_{19,20}$	θ_{21}	η
full	-1.22	-1.44	-1.73	-1.94	-2.01	-2.22	$-2.41 \pm 0.55 i$	-2.33	-0.59
pert.	-1.24	-1.44	-1.73(7)	-1.94	-1.97	-2.24	$-2.41 \pm 0.51 i$	-2.34	-0.58
$\eta = 0$	-2.61	-3	-3.10	-3.11	-3.16	-3.5	$-3.69 \pm 0.52 i$	-4	-

Table 4.10: Fixed-point values of the cyclic melonic couplings and critical exponents in the truncation to sixth order for the cyclic-melonic multitrace fixed point. The couplings not displayed are all vanishing at the fixed point.

4.4 Towards four-dimensional Quantum Gravity

Having explained the technicalities associated to the FRG and to the FRG for tensor models in particular, we have set the stage to study the case that is of upmost interest to us: A tensor model for four-dimensional quantum gravity. Naively, one would think that in analogy to the duality between matrix models and two-dimensional quantum gravity, a rank-4 tensor model would be an appropriate choice to investigate the possibility of uncovering a continuum limit that gives four-dimensional quantum gravity. We will therefore study a rank-4 $O(N')^4$ tensor model. Tensors then transform as

$$T_{a_1 a_2 a_3 a_4} = \sum_{b_i} O_{a_1 b_1} O_{a_2 b_2} O_{a_3 b_3} O_{a_4 b_4} T_{b_1 b_2 b_3 b_4}. \quad (4.157)$$

Just like in the rank-3 case invariants are built by contracting an index a_i of one tensor with the index a'_i of another tensor, where i denotes the position of the index in the tensor. The number of invariants at each interaction order is significantly larger in the rank-4 case. As a reminder at order T^4 , T^6 and T^8 there are respectively

$$14, 132, 4154$$

invariants. Using the same strategy as in the rank-3 case would therefore imply that studying a T^6 tensor model required us to derive 156 beta functions and consequently solve 156 coupled non-polynomial equations in order to identify fixed points. We will therefore study a truncation that assigns the same coupling to all members of a combinatorial family, that is invariants that are symmetric under color-exchange. In order to proceed that way, we will make use of the indicator, which was introduced

$$\begin{aligned}
\Gamma_N = Z_N & \left(\text{diagram} \right) + \bar{g}_{4,1}^2 \left(\text{diagram} + \text{diagram} + \text{diagram} + \text{diagram} \right) \\
& + \bar{g}_{4,1}^{0,(1,i)} \left(\text{diagram} + \text{diagram} + \text{diagram} \right) + \bar{g}_{4,2}^2 \left(\text{diagram} + \text{diagram} \right) \\
& + \bar{g}_{4,1}^{0,(i,j)} \left(\text{diagram} + \text{diagram} + \text{diagram} + \text{diagram} + \text{diagram} + \text{diagram} \right) \\
& + \quad T^6 \text{ interactions} \quad + \quad T^8 \text{ melonic interactions}
\end{aligned}$$

Figure 4.9: We are studying a real rank-4 tensor model. The full truncation is depicted above. We include all interactions up to order T^6 and additionally melonic T^8 interactions.

in Definition 4.1. Using the indicator, it turns out that there are

$$4, 20, 188$$

combinatorial families at order T^4 , T^6 and T^8 . These numbers are in agreement with the ones found by the authors of [250].

In the following we will consider a complete truncation up to order T^6 plus melonic T^8 invariants. In total we therefore take into account 170 invariants belonging to 31 combinatorial families implying the need to derive 31 beta functions. Given the size of the truncation, we will restrain from providing the diagrammatic or the Einstein summation representation of the full truncation. We will, however, provide a glance at the truncation by providing the kinetic term as well as the T^4 part as illustrated in Fig. 4.9.

Derivation of Beta Functions

The general algorithm for the derivation of the beta functions for the real rank-4 tensor model is the same as the one discussed previously for the rank-3 model. There is, however, a subtlety in the derivation of the combinatorial factors that contribute to the prefactor of the beta functions and a difference in the projection procedure onto the flow of the individual couplings. In the rank-3 model every invariant had a distinct coupling. Here, one same coupling is assigned to all members of the same color-symmetric family. This makes it slightly less obvious to track the degeneracies

of the pillow couplings due to the $\mathcal{P}^{-1}\mathcal{F}$ -expansion. As a little example in the rank-3 model the running of the multi-trace interaction had a contribution from a combination of pillow couplings $g_{4,1}^{2,i}g_{4,1}^{2,j}$ with $i \neq j$. The prefactor was given by $4 \times 4 \times 2! \times 1/2$, where the factors of four came from the two-point function, the factor of $1/2$ was the prefactor of the flow equation and importantly the factor of 2 followed from the fact the $\mathcal{P}^{-1}\mathcal{F}$ expansion generated $2!$ terms, one $g_{4,1}^{2,i}g_{4,1}^{2,j}$ and one $g_{4,1}^{2,j}g_{4,1}^{2,i}$. The fact that the couplings were different made it rather easy to track these degeneracies that resulted from the $\mathcal{P}^{-1}\mathcal{F}$ expansion. In the rank-4 case, where we assign the same coupling to each invariant of a combinatorial family these factors are still there, as can be understood from the following example, where we are interested in the second order of the $\mathcal{P}^{-1}\mathcal{F}$ expansion in order to determine the contribution of the quartic pillow couplings to the quartic multitrace coupling

$$\begin{aligned}
\partial_i g_{4,2}^2 \left(\begin{array}{c} \text{pillow diagram} \\ \text{pillow diagram} \end{array} \right) &\sim g_{4,1}^2 \frac{\delta^2}{\delta T \delta T} \left(\begin{array}{c} \text{pillow diagram} \\ \text{pillow diagram} \end{array} \right) + g_{4,1}^2 \frac{\delta^2}{\delta T \delta T} \left(\begin{array}{c} \text{pillow diagram} \\ \text{pillow diagram} \end{array} \right) \\
&\sim 2! (g_{4,1}^2)^2 \frac{\delta^2}{\delta T \delta T} \left(\begin{array}{c} \text{pillow diagram} \\ \text{pillow diagram} \end{array} \right) + \text{other terms.} \quad (4.158)
\end{aligned}$$

Note that in the second line we only kept the combination of invariants that actually contribute to the running of the multitrace coupling.

To summarize, it is important to be aware of this subtlety, which actually also has effects on the speed of the *Mathematica* algorithm. If distinct couplings are assumed for every invariant, the step 4.2.2 does not have to be performed for every combination of invariants.

Keeping in mind these additional subtleties due to the fact one couplings has been assigned for all invariants of a color-symmetric family, the derived quartic beta functions for the real rank-4 tensor model are the running of the pillow coupling $g_{4,1}^{2,i}$

$$\begin{aligned}
\partial_i g_{4,1}^{2,i} &= (3 + 2\eta) g_{4,1}^{2,i} + 48 \cdot \frac{4 - \eta}{12} \left(g_{4,1}^{0,(1,i)} \right)^2 + 96 \cdot \frac{4 - \eta}{12} \left(g_{4,1}^{0,(1,i)} \cdot g_{4,1}^{0,(i,j)} \right) \\
&\quad + 72 \cdot \frac{4 - \eta}{12} \left(g_{4,1}^{0,(i,j)} \right)^2 + 48 \cdot \frac{5 - \eta}{20} \left(g_{4,1}^{0,(i,j)} \cdot g_{4,1}^{2,i} \right) \\
&\quad + 48 \cdot \frac{5 - \eta}{20} \left(g_{4,1}^{0,(1,i)} \cdot g_{4,1}^{2,i} \right) + 8 \cdot \frac{6 - \eta}{60} \left(g_{4,1}^{2,i} \right)^2 \quad (4.159)
\end{aligned}$$

which has a contribution from every possible combination of pairs of couplings except $(g_{4,2}^2)^2$, the running of the multitrace invariant $g_{4,2}^2$

$$\begin{aligned} \partial_t g_{4,2}^2 &= (4 + 2\eta) g_{4,2}^2 + 8 \cdot \frac{7 - \eta}{252} (g_{4,2}^2)^2 + 64 \cdot \frac{6 - \eta}{60} (g_{4,2}^2 \cdot g_{4,1}^{2,i}) + 96 \cdot \frac{5 - \eta}{20} (g_{4,1}^{2,i})^2 \\ &\quad + 96 \cdot \frac{5 - \eta}{20} (g_{4,2}^2 \cdot g_{4,1}^{0,(i,j)}) + 96 \cdot \frac{5 - \eta}{20} (g_{4,2}^2 \cdot g_{4,1}^{0,(1,i)}) \\ &\quad + 192 \cdot \frac{4 - \eta}{12} (g_{4,1}^{0,(1,i)} \cdot g_{4,1}^{2,i}) + 192 \cdot \frac{4 - \eta}{12} (g_{4,1}^{0,(i,j)} \cdot g_{4,1}^{2,i}) \end{aligned} \quad (4.160)$$

the running of the so-called necklace coupling $g_{4,1}^{0,(1,i)}$

$$\partial_t g_{4,1}^{0,(1,i)} = (2 + 2\eta) g_{4,1}^{0,(1,i)} + 16 \cdot \frac{5 - \eta}{20} (g_{4,1}^{0,(1,i)})^2 + 16 \cdot \frac{5 - \eta}{20} (g_{4,1}^{0,(i,j)})^2 \quad (4.161)$$

and the running of the cross coupling $g_{4,1}^{0,(i,j)}$

$$\partial_t g_{4,1}^{0,(i,j)} = (2 + 2\eta) g_{4,1}^{0,(i,j)} + 16 \cdot \frac{5 - \eta}{20} (g_{4,1}^{0,(1,i)} \cdot g_{4,1}^{0,(i,j)}) \quad (4.162)$$

Of particular interest for us are those structurally allowed fixed points that feature no dimensional reduction. As a consequence, either the pillow coupling $g_{4,1}^{2,i}$, the necklace coupling $g_{4,1}^{1,(1,i)}$ or the cross coupling $g_{4,1}^{1,(i,j)}$ have to be turned on. Let us explore those possibilities. We will start by discussing the non-melonic sector, i.e. the one involving the necklace and the cross-interaction. The non-melonic sector is decoupled from the melonic one, in the sense that melonic couplings do not feed into the running of the non-melonic ones. The following discussion on fixed point mechanisms in the non-melonic sector will therefore be entirely independent of the melonic sector.

A priori, one can think of four possibilities for $\beta_{g_{4,1}^{0,(1,i)}}$ and $\beta_{g_{4,1}^{0,(i,j)}}$ to vanish. Either both $g_{4,1}^{0,(1,i)}$ and $g_{4,1}^{0,(i,j)}$ vanish, either they are both non-trivial or one vanishes while the other doesn't. Let us go through each of these scenarios. The case where both $\beta_{g_{4,1}^{0,(1,i)}}$ and $\beta_{g_{4,1}^{0,(i,j)}}$ are zero makes their running vanish identically. This is not surprising as we expect the Gaussian fixed point to be a trivial solution of the entire set of beta functions. Next, let us study the possibility of having a vanishing necklace coupling, while the cross coupling is non-trivial. The running of $g_{4,1}^{0,(1,i)}$ with $g_{4,1}^{0,(1,i)} = 0$ is given by

$$\beta_{g_{4,1}^{0,(i,j)}} \sim (g_{4,1}^{0,(i,j)})^2 \quad (4.163)$$

It is therefore not possible to have a fixed point where the necklace coupling vanishes while the cross coupling doesn't.

Similarly, it is also not possible to have both, the necklace and the cross coupling vanish. In order to understand why, let us have a closer look at the running of $g_{4,1}^{0,(i,j)}$. As can be seen from Eq. 4.162 the condition $g_{4,1}^{0,(1,i)} \neq 0$ puts a constraint on the fixed point solution of $g_{4,1}^{0,(1,i)}$, namely $g_{4,1}^{0,(1,i)}$ has to be given as

$$g_{4,1}^{0,(1,i)*} = -\frac{2+2\eta}{c_1}, \quad (4.164)$$

where c_1 is the prefactor associated to $(g_{4,1}^{0,(1,i)} \cdot g_{4,1}^{0,(i,j)})$ in Eq. 4.162 given by $c_1 = (16/20)(5-\eta)$. Under the above assumption, $g_{4,1}^{0,(i,j)}$ only stops running if

$$-\frac{(2+2\eta)^2}{c_1} + c_2 \frac{(2+2\eta)^2}{(c_1)^2} + c_3 (g_{4,1}^{0,(i,j)})^2 = 0 \quad (4.165)$$

is satisfied. Hereby, the constants c_2 and c_3 are the overall prefactors associated to $(g_{4,1}^{0,(1,i)})^2$ and $(g_{4,1}^{0,(i,j)})^2$ in Eq. 4.161. Crucially, $c_2 = c_1$, which is a non-trivial combinatorial coincidence which implies that the first two terms in the above equation cancel each other out, thus resulting in $g_{4,1}^{0,(i,j)} = 0$. This completes our analysis of the non-melonic sector. To summarize, there exist two possibilities for potential fixed points: One, where both, the necklace and the cross coupling vanish and one, where the cross coupling is zero while the necklace interaction is non-trivial.

Finding a continuum limit

The goal is to find a fixed point that cannot be dimensionally reduced by 'merging' specific groupings of indices. This would already provide a first hint that such a fixed point might be of potential interest for a phase of four-dimensional quantum gravity. A requirement that needs to be fulfilled in that case is that the fixed point necessarily has to feature a non-trivial fixed point value for the couplings other than the multi-trace interactions.

From studying the structure of the beta functions, we expect a fixed point where the entire melonic sector, in particular the cyclic-melonic sector, is fully interacting. This expectation is confirmed by the numerics: We identify a fixed point with a complex pair of two relevant directions, given by

$$\theta_{1,2} = 2.79 \pm 1.48i \quad (4.166)$$

in the perturbative scheme for the anomalous dimension. At this fixed point all melonic invariants are interacting. Let us point out that when taking into account the full non-perturbative anomalous dimension we did not find a real extension of the fixed point. This could be a consequence of the additional zeros of the beta functions due to their non-polynomial character, thus leading to fixed point collisions. To fully settle this question further extensions of the truncation are necessary. We leave this as open work for the future given that the derivation of beta functions and the

trunc.	$g_{4,2}^2$	$g_{4,1}^2$	$g_{6,3}^3$	$g_{6,1}^3$	$g_{6,2}^2$	$g_{8,4}^4$	$g_{8,3}^4$	$g_{8,1}^4$	$g_{8,2}^4$	$g_{8,2,s}^4$	$g_{8,2,m}^4$
T^4	11.3	-1.61	-	-	-	-	-	-	-	-	-
T^6	5.36	-0.98	230.1	-1.42	-12.43	-	-	-	-	-	-
T^8	3.50	-0.73	219.6	-1.68	-12.29	-300.2	272.8	-2.4	-19.0	-23.6	-6.1

Table 4.11: We find a fixed point characterized by two relevant directions. Shown above are all non-zero couplings.

posterior fixed point search become technically very involved.

We will discuss the implications our result in a brief moment. First, however, we will try to quantify the systematic error that is induced by the regulator and by truncating the full theory space allowed by symmetries. Hereby, it is assumed that the guiding principle introduced in C.3, whereby the inclusion of new operators with lower canonical scaling dimension should not induce new relevant directions, holds. This criterion is indeed satisfied within our truncation. While extending the truncation by including higher-order operators is therefore not expected to introduce new relevant directions, higher-order couplings directly feed into the running of lower order ones and thus also contribute to the stability matrix, thereby ultimately affecting the critical exponents. Indeed, one may attempt to quantify the systematic error associated to the largest irrelevant critical exponent θ_3 in term of its change as the truncation is increased. As the truncation is enlarged from fourth order to sixth order and from sixth order to eight order, the change of θ_3 is roughly $|\Delta\theta_3| \approx 0.5$. It is therefore not possible to entirely discard the possibility of a third relevant direction, given that within our truncation $\theta_3 = -0.28$.

Keeping in mind that a third relevant direction cannot be entirely discarded, let us discuss the implications of our results. As pointed out before, the fixed point action consists of only melonic diagrams. In [229] it has been discussed that taking the simple large- N' limit in a melonic model leads to a branched polymer phase, as also found in dynamical triangulations. Here, we argue that one needs to go beyond this simple limit and consider fixed points with additional relevant directions in order to escape the branched polymer phase. For the dynamical triangulations simulations, this could imply that more tuneable couplings have to be taken into account in order to reach a sensible continuum limit. Let us also remark that in matrix models the multitrace invariants actually correspond to higher-order curvature operators. Their inclusion might therefore be crucial in order to escape the branched polymer phase.

trunc.	η	$\theta_{1,2}$	θ_3	θ_4
T^4	0.86	$2.996 \pm i 1.227$	-0.288	-0.288
T^6	-0.62	$2.984 \pm i 1.369$	-0.752	-0.752
T^8	-0.49	$2.793 \pm i 1.478$	-0.21	-1.01

Table 4.12: We find a fixed point characterized by two relevant directions. Within the estimated systematic error it appears possible that the third critical exponent, θ_3 , could become positive under extensions of the truncation. Our notation for the couplings follows that used in [143, 1]: The first lower index denotes the number of tensors in the interaction, e.g., g_4 denotes all quartic interactions. The second lower index denotes the number of connected components of an interaction. The upper index indicates the number of “melonic” parts it includes. Additional lower indices denote distinct characteristics of an interaction structure. All other couplings that exist at quartic, hexic and octic order in tensors vanish exactly at the fixed point we explore here.

Solving multi-rectangular-matrix models

The fixed point found using functional RG methods in the real rank-4 matrix model only includes non-zero values for the single-trace melonic diagrams. This implies that the truncated fixed point action can be rewritten in terms of a multi-non-squared-matrix model. The kinetic term in the real rank-4 tensor model $T_{a_1 a_2 a_3 a_4} T_{a_1 a_2 a_3 a_4}$, for instance, can be decomposed as follows

$$T_{a_1 a_2 a_3 a_4} T_{a_1 a_2 a_3 a_4} = \sum_{i=1}^4 \frac{1}{4} M_{i a_i A} M_{i a_i A}, \quad (4.167)$$

where the M_i are matrices. Research in random matrix theory has established a powerful machinery to solve certain matrix models exactly. It is therefore an intriguing question whether it is possible to also solve the multi-matrix model that results from the fixed point action of the real rank-4 tensor model. A question that needs to be addressed in that regard is how square-matrix model techniques can be carried over to non-square-matrix models. The key difficulty is that one of the crucial steps in solving matrix model relies on the fact that square matrices can be decomposed in terms of their eigenvalues. This is no longer the case for non-square matrices. There exists however the method of singular value decomposition.

5 Gravitational Waves from an Electroweak Phase Transition

In the past chapters we have devoted our attention to the internal inconsistencies of general relativity and argued that these can be resolved by a theory of quantum gravity, which will allow us to zoom into the fundamental nature of space-time at shortest distances. At large scales, however, gravity is well-understood and highly successful with a rich variety of physical implications. One of these is the existence of gravitational waves. In the following, we are going to see how gravitational waves can allow us to learn new aspects about the matter content of our universe.

In the recent past, the Standard Model has been successfully confirmed as an effective theory for low-energy particle interactions at least up to the TeV scale, by the discovery of the Higgs at the LHC in 2012 [260]. Nonetheless, the Standard Model has some shortcomings, such as failing to provide a Dark Matter candidate, lacking a mechanism for the generation of neutrino masses or an explanation for the matter-antimatter asymmetry of the universe. Experimental confirmation of theoretical models attempting to address some of these shortcomings is still missing. This motivates the search for new experimental windows.

The field of Gravitational Wave astronomy has opened new promising ways to not only test the theory of General Relativity but also probe particle physics models. A cross-fertilization between gravitational-wave astronomy and particle detectors might therefore be just what is necessary in order to learn more about the open problems that the Standard Model fails to address.

The reason that gravitational waves might help to shine new light¹ on new physics is that many beyond the Standard Model scenarios predict a first order phase transition in the early universe, where the universe transitions from a metastable but initially stable phase to an energetically more favored one by means of a process of bubble nucleation, growth and merger [261, 262, 263, 264]. This transition leads to the release of latent heat, which acts as a source for gravitational waves [265, 266]. If the phase transition is strong enough, future space-based gravitational wave detectors such as LISA [267], expected to launch in 2030, or DECIGO might be able to detect these gravitational waves.

Phase transitions are quite common in the Standard Model. Examples are the electroweak phase transition or the QCD phase transition. However, assuming just the Standard Model, one finds that these phase transitions are cross-overs [268], where the universe smoothly transitions to its ground state at $T = 0$ without releasing latent heat, rather than first-order phase transitions. The detection of gravitational

¹Actually gravitational waves do not shine light. This is only meant in a metaphorical sense.

waves in the frequency range of LISA or DECIGO would therefore be an indication of additional physics not described by the Standard Model. Adding new matter content to provide an explanation for Dark Matter, for instance, can lead to first-order phase transitions. Gravitational Waves from phase transitions in a dark sector have been studied in [269, 270, 271]. Moreover, a departure from thermal equilibrium, which can be realized by a first-order phase transition, is one of the necessary requirements in order to generate a matter-antimatter asymmetry in our universe. Enlarging the Higgs-potential by a ϕ^6 operator, for example, which can be motivated from an effective field theory point of view as resulting from having integrated out some heavy particles, already leads to a first-order phase transition [272, 273, 274]. In the following we will set the stage to understand the concepts behind the generation of gravitational waves from first-order phase transitions by taking a closer look at phase transitions in the Standard Model and beyond. We will explain why the Standard Model only predicts cross-overs and how certain minimal extensions lead to first-order phase transitions, and consequently to the production of gravitational waves. Of particular interest to us will be the electroweak phase transition, which can be of relevance when addressing the matter-antimatter asymmetry in our universe [275]. We will explain how a first-order phase transition proceeds via the nucleation of bubbles of the symmetry-broken phase.

Having equipped the reader with the necessary background knowledge, we will consider three different extensions of the Standard Model Higgs potential, which are all motivated from an effective field theory point of view where heavy degrees of freedom of some unknown UV-theory have been integrated out. Those extensions will be the inclusion of a ϕ^6 operator, a Coleman-Weinberg inspired logarithmic contribution and a non-perturbative exponential term. An extension of the Higgs-potential is linked to a modification of the triple- and quartic Standard Model Higgs couplings, which could potentially be measured at the next LHC high-luminosity run [276]. The detection of gravitational waves provides an additional testing arm to probe the aforementioned extensions of the Standard Model Higgs potential. Thus, an interplay of collider experiments and gravitational wave astronomy will allow us to learn more about exciting new physics.

5.1 Phase Transitions in the Standard Model and Beyond

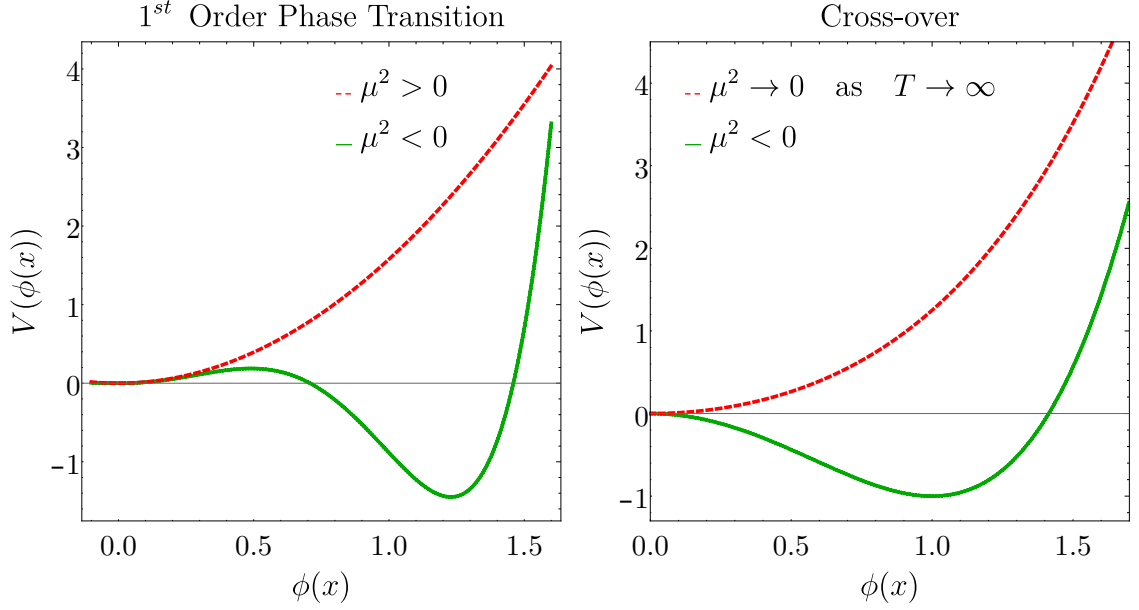
In the introduction we have learned that a first-order phase transition can lead to the generation of gravitational waves, whose detection provides an indication for new physics beyond the Standard Model. In the following, we are going to discuss one reason why the existence of a matter-antimatter asymmetry in our universe requires modifications of the Standard Model.

The Standard Model predicts a so-called cross-over, given the value of the Higgs self-

interaction λ where the universe smoothly transitions from a metastable symmetric ground state ($\langle h \rangle = 0$) to a global one at which the Higgs boson h acquires a vacuum expectation value ($\langle h \rangle = 246$ GeV), thus giving mass to the Standard Model particles. A schematic example comparing a first order phase transition to a cross-over is provided in Fig. 5.1. In order to determine the order of the electroweak phase transition in the Standard Model, numerical methods such as lattice simulations or resummation techniques have to be employed, as it turns out that the naive assumption of weak coupling which would allow to employ standard perturbation theory breaks down². Lattice simulations [268, 277, 278, 279, 280] have uncovered a two-dimensional phase diagram in terms of the temperature T and the ratio of the Higgs mass at zero temperature to a gauge boson mass. If the Higgs mass m_H is small with $m_H < 75$ GeV, the electroweak phase transition is of first order and a perturbative treatment of the Standard Model including thermal corrections is valid. For larger Higgs masses, the strength of the phase transition, quantified for instance in terms of the released latent heat, decreases and ultimately goes to zero as a critical point is reached where the electroweak phase transition in the Standard Model is of second order. Beyond this critical value, the phase transition is a cross-over and the system smoothly transitions from a metastable thermal ground state to its true ground state without releasing any latent heat³. Since the Higgs mass has been measured by the LHC to be $m_H \approx 125$ GeV, the renormalizable Standard Model exhibits a cross-over phase transition. Nonetheless, there exist a number of reasons to extend the renormalizable Standard Model. One reason is that a first-order phase transition leads to a departure from thermal equilibrium, which is one of the requirements that need to be satisfied to address the question of why there is

²This can be understood, e.g., by studying a scalar field with a ϕ^4 interaction term, whose Hamiltonian is given by $H_I = g^2 \int d^3x \hat{\phi}^4$. Applying thermal field theory, it turns out that the correct expansion parameter is not g^2 but rather $\epsilon = g^2 f(\vec{k})$, where $f(\vec{k})$ is the phase space density $f(\vec{k}) = 1/(e^{\beta\omega_{\vec{k}}} - 1)$, with $\omega_{\vec{k}} = \sqrt{\vec{k}^2 + m^2}$ and $\beta = 1/T$. The phase space density $f(\vec{k})$ approaches $T/\omega_{\vec{k}}$ in the limit where $\omega_{\vec{k}} \ll T$. In that case, for $k \lesssim g^2 T$, the expansion parameter ϵ becomes of order unity and in particular diverges in the case of massless particles in the infrared where $|\vec{k}| \rightarrow 0$. This picture is not yet complete, as massless particles also receive a mass via thermal corrections. One distinguishes between the electric mass, a thermal mass for the timelike components of the gauge boson and the magnetic mass, a thermal mass for the spacelike components. While the electric mass turns out to behave like a scalar mass with $m^2(T) = m_0^2 + cg^2 T^2$, where m_0 is the mass at vanishing temperature (in this case $m_0 = 0$) and c is a theory-dependent constant, the magnetic mass vanishes, causing the expansion parameter ϵ to diverge in the infrared limit. While this is not a problem for the Standard Model photon as it has no self-interaction terms, it is a problem for all other Standard Model gauge bosons and the application of perturbation theory consequently breaks down.

³To get a better understanding of second order phase transitions and cross-overs one can take the liquid-vapour phase transition of water as an illustrative example. At high pressure, the density of water smoothly decreases with temperature rather than exhibiting a sharp jump as the liquid-vapour phase transition takes place. At exactly the critical point, at $T = 374^\circ\text{C}$ and $p = 218$ atm, the correlation length of the density fluctuations diverges, leading to the phenomenon of critical opalescence where water acquires a milky appearance as the entire spectrum of visible light is scattered.



(a) Quartic Potential mimicking a first order PT. (b) Quartic Potential mimicking a cross-over.

Figure 5.1: Assuming a simple toy model, the above examples show why the inclusion of additional polynomial terms beyond a quartic potential modifies the character of the phase transition. If just a quartic potential is assumed the system will just continuously roll down into the new minimum. Indeed, the possibility where the quadratic coefficient is positive while the quartic one is also positive only allows for a saddle-point at $x = 0$, while if the quadratic term is negative a non-trivial minimum develops while the minimum at $x = 0$ becomes unstable, as can be easily checked. On the other hand including a hexic term, allows for the possibility of two minima, a metastable (local) one and a stable (global) one.

more matter than anti-matter in our universe.

Electroweak Baryogenesis

The mechanism behind producing an asymmetry between baryons and anti-baryons from an initially balanced state is called baryogenesis. The name originates from the fact that the asymmetry η can be described in terms of the net baryon number of the universe as $\eta = (n_B - n_{\bar{B}})/n_\gamma$, where n_B and $n_{\bar{B}}$ refer to the baryon and anti-baryon number density, respectively and n_γ denotes the number density of cosmic background radiation photons. The baryon asymmetry parameter today is $\eta \sim 10^{-10}$. For a review on the observational evidence of the matter-antimatter asymmetry in the early universe, we refer the reader to [281]. Several models introducing distinct new physics exist, but most of them satisfy the so-called Sakharov

criteria [282], which are

- Violation of baryon number conservation.
- C and CP violation.
- Departure from thermodynamic equilibrium.

The reasons behind these three requirements are the following: Baryon number needs to be violated because otherwise the universe cannot evolve from an initial state of baryon-antibaryon symmetry, where $\eta = 0$, to an asymmetric state with $\eta > 0$. In electroweak baryogenesis, baryon number is violated through sphaleron processes. C and CP symmetry need to be broken because otherwise any process leading to an excess of baryons has a counter-process compensating for that excess by leading to an increase of antibaryons. Finally, thermal equilibrium needs to be violated as otherwise any process $A \rightarrow B$ leading to an excess of baryons allows for a process $B \rightarrow A$ that compensates for this excess. The first two Sakharov conditions are model-specific and can be probed by precision measurements of the given model. The third condition, departure from thermal equilibrium, can be realized by means of a strong first-order phase transition, for instance at the electroweak scale [275, 283]. As discussed previously, a first-order phase transition is associated with a release of latent heat. For strong enough first-order phase transitions, the release of latent heat due to the transition from a metastable thermal ground state to a stable one leads to the production of gravitational waves that could be detectable by future space-based laser interferometers such as LISA or DECIGO. We will come to the production of gravitational waves after having introduced extensions of the Higgs potential that lead to a first-order phase transition.

Modifying the Higgs Potential

An interest in extending the Higgs-potential in the Standard Model can arise for at least two reasons. On the one hand, depending on the exact value of the top mass, the Higgs potential is metastable, even though the decay time of the metastable vacuum is much larger than the age of the universe. On the other hand several models for baryogenesis, as explained above, require a first-order electroweak phase transition, which can be triggered by small extension of the Higgs potential. We will follow [276] where new physics is parametrized by three different extensions of the Higgs potential defined at some cut-off scale Λ . These extensions are

$$V_{k=\Lambda} = \frac{\mu^2}{2} H^2 + \frac{\lambda_4}{4} H^4 + \Delta V, \quad (5.1)$$

with ΔV describing three different extensions of the Higgs potential where

$$\Delta V_{\lambda_6} = \frac{\lambda_6}{\Lambda^2} H^6, \quad (5.2)$$

can be motivated as being the leading contribution of new physics in an effective-field theory expansion,

$$\Delta V_{\lambda_{\text{ln},2}} = -\lambda_{\text{ln},2} \frac{\phi^2 \Lambda^2}{100} \ln \left(\frac{\phi^2}{2\Lambda^2} \right), \quad (5.3)$$

has the form of a Coleman-Weinberg effective potential, which follows from integrating out heavy fermions or scalars and

$$\Delta V_{\lambda_{\text{exp},4}} = \lambda_{\text{exp},4} \phi^4 \exp \left(\frac{-2\Lambda^2}{\phi^2} \right), \quad (5.4)$$

which is inspired from non-perturbative effects. As we introduce new physics by modifying the Standard Model Higgs potential we are still required to recover *IR* observables like the Higgs mass $m_H \approx 125$ GeV or the electroweak vacuum expectation value (vev) $v = 246$ GeV. If no new physics is assumed the quartic coupling λ_4 is fixed exactly by demanding that the correct Higgs mass m_H and the electroweak vev v are recovered in the IR. Indeed, an easy check, where we assume the broken phase of the renormalizable Standard Model Higgs potential and ignore Goldstone modes such that

$$V = \frac{\mu^2}{2}(v + H)^2 + \frac{\lambda_4}{4}(v + H)^4, \quad (5.5)$$

allows to derive the minimum v of the broken Higgs potential which is given by

$$v = \sqrt{\frac{-\mu^2}{\lambda_4}} = 246 \text{ GeV}. \quad (5.6)$$

as well as the Higgs mass

$$m_H = \sqrt{2\lambda_4}v \approx 125 \text{ GeV}. \quad (5.7)$$

The Higgs mass and the vev have been measured at the LHC with their experimental values shown above and thus fix the quartic coupling λ_4 and the mass parameter μ . Expanding Eq. (5.5) in powers of H and trading μ and λ_4 with the physical Higgs mass m_H and the vev v , it is also possible to obtain the Standard Model predictions for the physical triple and quartic Higgs couplings, which are given as

$$\lambda_{H^3,0} = \frac{3m_H^2}{v} \quad (5.8)$$

and

$$\lambda_{H^4,0} = \frac{3m_H^2}{v^2} \quad (5.9)$$

If, however, the Higgs potential has corrections as the ones introduced before, in order to modify the potential such that it accounts for a first order phase transition,

the quartic coupling is no longer fixed. Rather, the additionally introduced couplings that now also enter the Higgs mass and the electroweak vev and λ_4 have to be adjusted such that the correct IR physics is recovered at $T = 0$, i.e. such that observables still keep their corresponding experimental values. As an example, one may consider the effect of an H^6 operator. The Higgs mass, which has been already measured as well as the triple and the quartic Higgs couplings are now given as

$$m_H = \sqrt{2\lambda}v \left(1 + 12 \frac{\lambda_6 v^2}{\lambda_4 \Lambda^2} \right) \approx 125 \text{ GeV}, \quad (5.10)$$

$$\lambda_{H^3} = \frac{3m_H^2}{v} \left(1 + \frac{16\lambda_6 v^4}{m_H^2 \Lambda^2} \right), \quad (5.11)$$

$$\lambda_{H^4} = \frac{3m_H^2}{v} \left(1 + \frac{96\lambda_6 v^4}{m_H^2 \Lambda^2} \right), \quad (5.12)$$

where the λ_{H^3} and λ_{H^4} couplings will potentially be measured at the next high luminosity run at the LHC via Higgs pair production through gluon fusion. See [3] for a pedagogical review. Comparing the new form of the Higgs mass to the one derived from the renormalizable Standard Model in Eq. (5.7) it becomes apparent that the bare coupling λ_4 is no longer fixed by the experimental value of the Higgs mass. Rather, the Higgs mass is now a function of the bare quartic coupling λ_4 , the bare hexic coupling λ_6 and the cut-off scale Λ at which new physics is assumed. The exponential and logarithmic potentials will have similar effects in the sense that their couplings also enter the definition of the different physical observables.

The strength of the phase transition at the critical temperature T_c can be quantified by ϕ_c/T_c , where $\phi_c \equiv \langle \phi \rangle_c$ is the expectation value of the Higgs at the critical temperature T_c . At the critical temperature the effective potential $V(\phi)$ develops two degenerate minima at $\phi = 0$ and $\phi \neq 0$. Below the critical temperature, the non-trivial minimum becomes a global one and in the limit $T \rightarrow 0$, the field value at the minimum approaches the measured vev $v = 246 \text{ GeV}$. The field expectation value at the critical temperature, ϕ_c , is an order parameter: If $\phi_c \neq 0$, the phase transition is a first order one⁴. In order for to efficiently generate an asymmetry between baryons and anti-baryons, the phase transition has to be a *strong* first-order phase transition, characterized by $\phi_c/T_c \gtrsim 1$, since otherwise the baryon asymmetry is not explained [283].

In order to make the physical implications derived from a modification of the Higgs potential as precise as possible, a general set-up that has been discussed and introduced in [284] in order to discuss stability properties of the Higgs potential, is employed with the difference that the set-up includes the full modified Higgs potential with quantum and thermal corrections, the top-Yukawa-sector and its coupling

⁴As a reminder for the reader, a first-order phase transition is characterized by the fact that at some critical temperature T_c the potential features two degenerate minima in contrast to a cross-over or a higher-order phase transition, which only feature one minimum $\phi_c = 0$ that is continuously evolving with temperature. Hence, the fact that $\phi_c \neq 0$ is characteristic of a first-order phase transition.

y_t , a fiducial coupling g_F that mimics the $SU(2)$ and the $U(1)$ sectors as well as the $SU(3)$ gauge coupling g_3 . The IR values of the top-Yukawa-coupling y_t , μ^2 and λ will be fixed by the observational values of the top mass m_t , the Higgs mass m_H and the electroweak vev v

$$m_t = 173\text{GeV} \quad m_H = 125\text{GeV} \quad \text{and} \quad v = 246\text{GeV}, \quad (5.13)$$

for any given pair of either $\lambda_6, \lambda_{\text{ln},2}$ or $\lambda_{\text{exp},4}$ and Λ . Moreover, the $SU(3)$ gauge coupling is fixed by the requirement that

$$g(1\text{GeV}) = 1.06, \quad (5.14)$$

while its running will be the standard QCD running which allows for Asymptotic Freedom. The fiducial couplings $g_F = \{g, g'\}$ describing the electroweak sector can be assumed to be approximately constant with respect to the RG scale and hence also the temperature T .

The running of the full Higgs potential and the top-Yukawa coupling have been derived with the FRG at finite temperature. The FRG is well suited in order to study non-perturbative phenomena, while allowing to follow the separate dependence of the potentials on the three different relevant energy scales, the RG scale k , the temperature T and the value of the field ϕ . Here, the temperature T is an external energy scale of the system while ϕ can be regarded as an internal energy scale⁵.

The running of the couplings and the full Higgs potential represent a coupled set of partial differential equations that are solved numerically with a grid code, which transforms them into a large system of ordinary differential equations. The numerical background of the gridcode has been introduced in [285]. Besides specifying a truncation, that is described by the set-up that we have introduced above, the FRG requires a regulator. For technical reasons it is beneficial to introduce a regulator that only regularizes the spatial momenta leaving the temperature unaffected, which is compactified anyways. Such a regulator has also been discussed in the context of the quark-meson model [286]. A regulator allowing for a covariant treatment of the temperature and the spatial directions has been considered in [287]. The threshold functions derived from the FRG in that case are rather cumbersome.

5.2 Dynamics of Phase Transitions

The type of extensions introduced feature a first-order phase transition, which, if strong enough, can source Gravitational Waves that could be detectable by future

⁵The existence of an external energy scale T and an internal energy scale ϕ can be understood as follows: The temperature is related to the average translational kinetic energy of the system of interacting particles. As long as $T > T_c$, the particles are in the symmetric phase. When $T < T_c$, the entire system of interacting particles transitions to a new equilibrium state, which is characterized by the value of the field ϕ in the broken phase. At this point there will be two distinct energy scales ϕ and T .

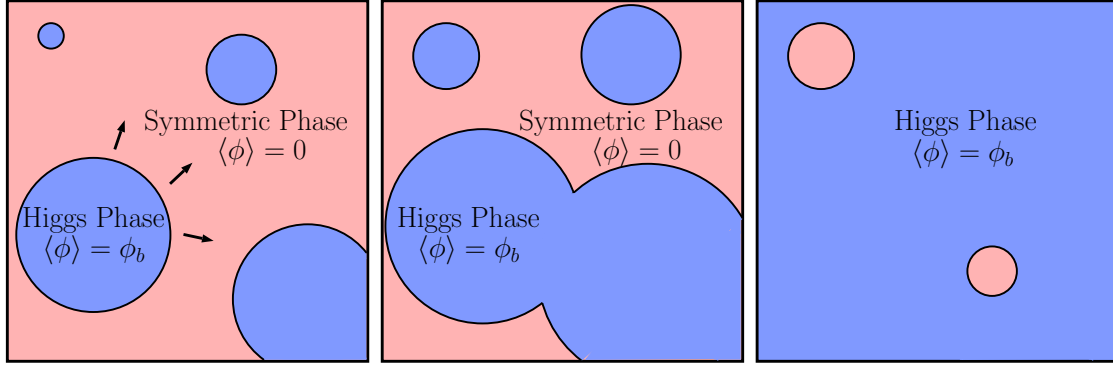


Figure 5.2: Thermal fluctuation lead to the nucleation of bubbles, where the Higgs is in a stable ground state. These bubbles expand into the regions where the Higgs persists in its metastable ground state. At early times, the bubbles do not overlap. Later, however, they merge until the entire fluid of Standard Model particles is in the stable ground state.

space-based GW interferometers such as LISA or DECIGO. In order to properly understand how gravitational waves are sourced one has to first understand the dynamics of a first-order phase transition. A first-order phase transition can be described via the nucleation of bubbles of the true ground state $\phi = \phi_b$ due to quantum or thermal fluctuations. If the temperature of the universe drops below a critical temperature, these bubbles begin to expand and interact with one another and a plasma of particles until the entire universe is covered by bubbles, the phase transition is completed and the universe has transitioned to its true equilibrium state. See Fig. 5.2 for a sketch of the process. Describing the exact dynamics of the phase transition and the resulting stochastic gravitational wave spectrum is very involved. It requires solving the equations of motion of the combined field-plasma system using lattice simulations. A review on the details of the nucleation of bubbles and their dynamics is provided in the appendix. While describing the entire process from the onset of the phase transition, when bubbles start to nucleate, to the final stages when a stochastic gravitational wave background is emitted is challenging, it is, however, possible to describe the stochastic background of gravitational waves resulting from the phase transition in terms of a few key quantities: These key quantities are

- the speed v_w at which the phase boundary is expanding,
- the available energy budget of the phase transition, which we will quantify by a parameter α ,
- the mean bubble separation R which can be linked to the inverse phase transition duration β ,

- a set of characteristic temperatures describing the evolution of the phase transition. Those temperatures are the critical temperature T_c at which the two minima of the potential become degenerate, the nucleation temperature T_n , which describes the onset of bubble nucleation and the percolation temperature T_p which characterizes the final stages of the phase transition. Close to the percolation temperature the nucleation rate grows as the exponential of an exponential.

We will introduce these key quantities as we proceed in describing the general picture, that is the following: Bubbles of the broken phase at time t nucleate with a certain probability density $\Gamma(t)$ that depends on the shape of the potential $V(t)$ at time t . This probability is commonly quantified as

$$\Gamma(t) = A(t)e^{-S(t)}, \quad (5.15)$$

where $A(t)$ is a time-dependent prefactor and $S(t)$ is the action. For later purposes it is beneficial to describe the history of the universe in terms of its thermal evolution. The temporal expansion history of the universe can be expressed in terms of its thermal history via

$$\frac{dT}{dt} = -H(T)T, \quad (5.16)$$

which depends on the field content of the universe through the Hubble parameter H , that is related to the energy density of the universe by the Friedmann equation

$$H(T) = \sqrt{\frac{\rho_{\text{rad}} + \rho_{\text{vac}}}{3M_{\text{Pl}}^2}}, \quad (5.17)$$

where M_{Pl} denotes the reduced Planck mass with $M_{\text{Pl}} = \sqrt{1/8\pi G} = 2.435 \times 10^{18}$ GeV. The energy density of radiation is given as

$$\rho_{\text{rad}} = g_{\text{eff}} \frac{\pi^2}{30} T^4, \quad (5.18)$$

where the relativistic degrees of freedom are quantified by g_{eff} , which follows from

$$g_{\text{eff}} = \sum_{i=\text{boson}} g_i \left(\frac{T_i}{T}\right)^4 + \frac{7}{8} \sum_{i=\text{fermion}} g_i \left(\frac{T_i}{T}\right)^4. \quad (5.19)$$

Here, g_i and T_i are the degrees of freedom and the temperature of the particle i , respectively. In the Standard Model, the number of effective relativistic degrees of freedom is $g_{\text{eff}} = 106.75$ before the electroweak phase transition has taken place. Hence, in the following we will be treating g_{eff} as constant. The vacuum energy density ρ_{vac} is defined as

$$\rho_{\text{vac}} = \Delta V_{\text{eff}} = - [V_{\text{eff}}(\phi = \langle \phi \rangle_T, T) - V_{\text{eff}}(\phi = 0, T)], \quad (5.20)$$

where $\langle\phi\rangle_T$ denotes the field value at the true equilibrium state. Eq. 5.16 allows to express quantities in terms of their temperature dependence. In particular, the probability to nucleate a bubble at temperature T can be shown to be given as [288, 289]

$$\Gamma(T) = T^4 \left(\frac{S_3(T)}{2\pi T} \right)^{3/2} \exp(-S_3(T)/T), \quad (5.21)$$

where $S_3(T)$ is the three-dimensional euclidean action. The three-dimensional euclidean action is minimized by spherically-symmetric field configurations of ϕ , which entails that $S_3(T)$ is given as

$$S_3(T) = 4\pi \int_0^\infty dr r^2 \left(\frac{1}{2} \left(\frac{d\phi}{dr} \right)^2 + V_{\text{eff}}(\phi, T) \right), \quad (5.22)$$

where $r = \sqrt{x^2 + y^2 + z^2}$ denotes the radial coordinate. The spherical symmetry of the field configurations of ϕ is at the origin modeling the phase transition by the nucleation of bubbles of the symmetry-broken phase, where $\phi \neq 0$. The process of bubble nucleation, growth and merger until the phase transition is completed, will not be instantaneous but rather the universe will cool down from the temperature T_c , where the potential develops two degenerate minima, to some temperature T , where the universe has fully transitioned to its true equilibrium state. The entire history of the phase transition can be described in terms of some key temperatures that we will introduce now. At the critical temperature T_c the potential develops two degenerate minima, that is

$$V_{\text{eff}}(\phi = 0, T_c) = V_{\text{eff}}(\phi = \langle\phi\rangle_{T_c}, T_c), \quad (5.23)$$

where $\langle\phi\rangle_{T_c}$ is the expectation value of the field in the broken phase at the critical temperature. First bubbles of the true equilibrium phase start to nucleate at a temperature T_n . In order to determine the *nucleation temperature* T_n , the decay rate $\Gamma(T)$ of the false vacuum is compared to the Hubble rate $H(T)$, which describes the expansion of the universe. Typically, the nucleation temperature is defined as the temperature at which one bubble N is nucleated per Hubble horizon on average. This implies the following relation

$$N(T_n) = \int_{T_n}^{T_c} \frac{dT}{T} \frac{\Gamma(T)}{H(T)^4} = 1. \quad (5.24)$$

For fast phase transitions, as discussed in the appendix in order to equip the reader with more detailed knowledge, the integrand dominates at $T \approx T_n$. In that case

$$N(T_n) = \frac{\Gamma(T_n)}{H(T_n)^4} \approx 1. \quad (5.25)$$

In the following we will be using the former definition of the nucleation temperature T_n . While the nucleation temperature denotes the onset of the phase transition, the

end is commonly marked by another key temperature, the percolation temperature T_p at which roughly 30% of the comoving volume have been converted to the true equilibrium state [290]. The decay rate $\Gamma(t)$ increases as the exponential of an exponential, as can be seen for instance by considering Eq. 5.22 and hence T_p can also be considered as marking the end of the phase transition. The average fractional volume in the metastable phase, where overlaps between bubbles are taken into account, is given by

$$P(t) = e^{-I(t)} \quad (5.26)$$

with

$$I(t) = \frac{4\pi}{3} \int_{t_c}^t dt' \Gamma(t') \frac{a(t')^3}{a(t)^3} r(t', t)^3, \quad (5.27)$$

where $P(t)$ and $I(t)$ are expressed as functions of time. $I(t)$ denotes the probability of finding a bubble of size

$$V(t, t') = \frac{4\pi}{3} \frac{a(t)^3}{a(t')^3} r(t', t), \quad (5.28)$$

nucleated at time t' (T') with a probability $\Gamma(t')$, at time t (T). Hereby, $r(t, t')$ denotes the comoving radius of the bubble given as

$$r(t, t') = \int_{t'}^t dt \frac{v_w(\tilde{t}) a(t)}{a(\tilde{t})}, \quad (5.29)$$

where v_w denotes the wall speed of the expanding bubble. In principle, v_w follows from the dynamics of the field-fluid system. Determining v_w is, however, rather cumbersome and typically the wall speed is provided as an input parameter of the model when discussing the production of gravitational waves. A larger value of v_w increases the chances of detecting a stochastic background of gravitational waves although the efficiency with which baryon asymmetry is generated decreases [291]. For a more detailed description on v_w we advise the reader to have a look at the appendix. In the limit $t - t_c \rightarrow 0$, $I(t)$ approaches zero as there will be no contribution from the decay rate $\Gamma(t)$, such that $P(t) = 1$, i.e. the probability to find the universe in the false vacuum is one. Conversely, in the limit $t \rightarrow \infty$, $P(t)$ goes to zero, which implies that the universe has fully transitioned to its true equilibrium state. Note that the exponential in Eq. 5.26 indicates that overlaps between bubbles are taken into account. In the case, where no overlaps are considered, the fractional volume in the metastable phase admits the intuitive form

$$P(t) = 1 - I(t), \quad (5.30)$$

where we remind the reader that $I(t)$ denotes the probability to find a bubble of size $V(t, t')$ at time t which has been nucleated at time t' with probability $\Gamma(t')$. To

deduce the percolation temperature indicating the onset of bubble percolation when 30% of the universe are covered by bubbles of the true equilibrium state [290] one needs to express $P(t)$ and therefore $I(t)$ in terms of its temperature dependence. The temperature dependence of $I(t)$ is given via

$$I(T) = \frac{4\pi}{3} \int_{T_c}^T dT' \frac{\Gamma(T')}{H(T')T'^4} \left(\int_T^{T'} dT'' \frac{v_w(T'')}{H(T'')} \right)^3. \quad (5.31)$$

The percolation of bubbles begins when $I(T_p) = 0.34$ such that the probability $P(T_p)$ of finding a point in the false vacuum is $P(T_p) \approx 0.7$. To summarize our discussion so far, we have introduced three characteristic temperature that describe the phase transition. Those are

- the critical temperature T_c , where two minima of the potential become degenerate,
- the nucleation temperature T_n at which one bubble is nucleated per Hubble horizon on average,
- and the percolation temperature T_p when approximately 30% of the universe has transitioned to the stable phase.

We will further introduce a fourth characteristic temperature later on, when discussing very slow phase transitions.

Mean bubble separation

Instead of directly considering the decay rate, an alternative way to keep track of the phase transition is to analyze the evolution of the number density of bubbles that can be quantified via [292, 293]

$$n_{\text{bubbles}}(t) = \int dt' \frac{a(t')^3}{a(t)^3} \Gamma(t') P(t'), \quad (5.32)$$

where we are multiplying the nucleation rate Γ with the fractional volume P because bubbles can only nucleate in the metastable phase. At late times, it can be shown that the number density can be expressed as

$$n_{\text{bubbles}}(t) \equiv \frac{1}{R_*^3}, \quad (5.33)$$

where we have introduced the mean bubble separation R_* that describes the distance between the centers of two nucleated bubbles. The mean bubble separation will be a relevant length scale when discussing the generation of gravitational waves.

Energy budget of the phase transition

Moreover, the distribution of the energy budget is also of particular interest in quantifying the gravitational wave spectra. The energy released during the phase transition is typically quantified in terms of a quantity that is denoted by α . Roughly, α denotes the strength of the phase transition. Providing an expression for α is still open research [294]. Most studies employ the so-called bag model where the entire field-fluid system is separated in two subsystems [295]: One subsystem is the interior of a bubble and the other one corresponds to the exterior. The fluid is assumed to be perfect and relativistic. The bag constant ϵ denotes the change in energy and pressure across the boundary of the two systems and enters the definition of α as follows

$$\alpha = \frac{\epsilon}{a_+ T^4}. \quad (5.34)$$

where a_+ is given as $a_+ = \pi^2 g_{\text{eff}}/30$. The challenge consists in establishing how a given particle-physics model can be mapped to the bag model. The currently most commonly applied map relates the bag constant ϵ to the change of the trace of the energy-momentum tensor $\theta = (e + 3p)/4$, where the energy density e is given by the $(0,0)$ -component of the stress-energy tensor, while the pressure p is captured by the spatial components of the stress-energy tensor $p = T_{ii}$, with $i = 1, 2, 3$ and no summation implied. Following this definition of the bag constant, α is specified as

$$\alpha = \frac{3}{4} \frac{\theta_+ - \theta_-}{a_+ T^4} \Big|_{T=T_p}, \quad (5.35)$$

where θ_+ and θ_- denote the trace of the energy-momentum tensor outside and inside the bubble, respectively. The energy density and the pressure can be derived from the effective potential as

$$e_{+/-} = V_{\text{eff}} - T \frac{\partial V_{\text{eff}}}{\partial T} \quad (5.36)$$

and

$$p_{+/-} = -V_{\text{eff}}. \quad (5.37)$$

This allows us to express α in terms of the effective potential

$$\alpha = \frac{1}{\rho_{\text{rad}}} \left(\rho_{\text{vac}} - \frac{T}{4} \frac{\partial \rho_{\text{vac}}}{\partial T} \right) \Big|_{T=T_p} = \frac{30}{\pi^2 g_{\text{eff}} T^4} \left(\Delta V_{\text{eff}} - \frac{T}{4} \frac{\partial \Delta V_{\text{eff}}}{\partial T} \right) \Big|_{T=T_p}, \quad (5.38)$$

where the radiation energy density ρ_{rad} and the vacuum energy density ρ_{vac} are given by Eq. 5.18 and Eq. 5.20, respectively. The physical interpretation of α is that it measures the latent heat released during the phase transition normalized by

the radiation energy and is therefore of direct importance for the gravitational wave spectrum. It is possible to identify two regimes: For fast phase transitions with weak supercooling, i.e., $T_p \lesssim T_c$, the vacuum energy density ρ_{vac} is negligible. For slow phase transitions which are associated to significant supercooling, i.e. the percolation temperature is significantly smaller than the critical temperature, $T_p \ll T_c$, the vacuum energy density becomes dominant⁶.

To recap, so far we have introduced a set of important temperatures that describe the thermal evolution of the phase transition. Hereby, the nucleation temperature T_n was defined as the temperature at which one bubble of the Higgs phase is nucleated per Hubble horizon. The nucleation temperature marks the onset of the phase transition. We also introduced the percolation temperature which sets the end of the phase transition. To discuss the spectrum of gravitational waves later on, we introduced a parameter α that quantifies the available energy budget of the phase transition while taking into account the interaction between the bubbles and the plasma of Standard Model particles by means of an approximation known as the bag model. So far, however, we have remained agnostic about other important physical quantities such as the mean number density of nucleated bubbles or the duration of the phase transition. We expect these quantities to be of direct relevance for the stochastic gravitational wave spectrum.

Let us therefore study the time scale of the phase transition a little bit closer. To do so, we will distinguish between phase transitions with mild supercooling, where the characteristic temperatures of the phase transition are very similar and phase transitions with strong supercooling, where there is a clear hierarchy between the critical temperature, the nucleation temperature and the percolation temperature. The exact distinction will become more apparent as we discuss the two possibilities in more detail. We will show that the (inverse) duration of the phase transition and the mean number density of bubbles at percolation time are actually related and can therefore be described by a single parameter β as long as the phase transition does not feature very strong supercooling.

First-order phase transition without strong supercooling

On an even more fundamental level the duration of the phase transition as well as the mean number density of bubbles follow from the nucleation rate $\Gamma(t)$. For fast enough phase transitions, the nucleation rate Γ can be approximated as

$$\Gamma \approx \Gamma_0(t_0)e^{\beta(t-t_0)}, \quad (5.40)$$

⁶An alternative way to express the energy budget of the phase transition is given by

$$\alpha = \frac{3}{4} \frac{e_+ - e_-}{a_+ T^4}, \quad (5.39)$$

where the bag model constant is related to the difference in energy between the broken and the symmetric phase.

where t_0 is a reference time typically equated with the percolation time t_p . The transition rate parameter β that has been introduced above is related to the inverse duration of the phase transition and defined as

$$\beta = - \left. \frac{d}{dt} \frac{S_3(T(t))}{T(t)} \right|_{t=t_0}. \quad (5.41)$$

and evaluated at the reference time t_0 . Eq. 5.16 permits to express the inverse duration of the phase transition in terms of its temperature dependence

$$\tilde{\beta} := \frac{\beta}{H(T)} = T \left. \frac{d(S_3/T)}{dT} \right|_{T=T_0}. \quad (5.42)$$

To understand how the duration of the phase transition and the mean number density are related let us recall that in Eq. 5.32 we expressed the mean number density n_{bubbles} in terms of the probability $P(\Gamma(t), t)$ of finding a point in the false vacuum, see Eq. 5.26, and the decay rate $\Gamma(t)$. In particular, the probability of finding a point in the false vacuum is related to the decay rate. Assuming that the decay rate takes the approximated form of Eq.5.40, it can be shown that the probability of finding a point in the false vacuum for a fast phase transition is

$$P(t) = \exp(-e^{\beta(t-t_0)}) \quad (5.43)$$

such that the number density n_{bubbles} in Eq. 5.32 is

$$n_B(t) = \frac{\beta^3}{8\pi v_w^3} (1 - P(t)), \quad (5.44)$$

where v_w denotes the wall-speed of the bubble. For $t \gtrsim t_p$, the phase transition completes very fast, see Eq. 5.43, such that $P(t \gtrsim t_p) \approx 0$. Thus, the mean bubble number density is simply

$$n_B(t) = \frac{\beta^3}{8\pi v_w^3}. \quad (5.45)$$

It is standard in the gravitational wave literature to interchange the mean number density by the mean bubble separation which are related by Eq. 5.33. Thus, the mean bubble separation is given by

$$R_* = (8\pi)^{1/3} v_w \beta^{-1} \Big|_{T=T_p} \quad (5.46)$$

and evaluated at the percolation temperature.

First-order phase transition with strong supercooling

In the case that the universe undergoes through a sufficiently long enough period of supercooling until the phase transition completes, the linear approximation of

the nucleation rate Γ given in Eq. 5.40 breaks down. In particular, the weight of the nucleation rate, $S_3(T)/T$, no longer decreases monotonically with decreasing temperature but actually features a minimum at a minimization temperature T_m . Since the parameter β is directly related to the change of $S_3(T)/T$ as a function of the temperature, see Eq. 5.42, β vanishes at the minimization temperature and can even become negative for temperatures below the minimization temperature. Thus, the linear approximation of the nucleation rate, Eq. 5.40, is no longer valid [296, 297, 298]. For a more appropriate approximation it is necessary to also consider the quadratic term in the expansion of the action $S(T) = S_3(T)/T$ such that the nucleation rate can be approximated as

$$\Gamma \propto \exp(-S_3/T) = \exp\left(\frac{1}{2}\beta_V^2(t - t_m)^2 + \dots\right), \quad (5.47)$$

where the reference time t_m is associated to the minimization temperature T_m . In the above expansion, we used that the fact close to the reference time t_m , $\beta \rightarrow 0$. Hence, the timescale of the phase transition is now determined by β_V

$$\beta_V \equiv \sqrt{-\frac{d^2}{dt^2}\left(\frac{S_3(T)}{T}\right)}\Bigg|_{t=t_m} = H(T)T \sqrt{\frac{d^2}{dT^2}\left(\frac{S_3(T)}{T}\right)}\Bigg|_{T=T_m} \quad (5.48)$$

In the following, we will introduce a common parameter $\tilde{\beta}$ that refers to β/H in the scenario with mild supercooling and to β_V/H in the case of strong supercooling. The initial number density when the probability to find a point in the false vacuum is one is given by [296]

$$n_B(t) = n_{\max} \frac{1 + \operatorname{erf}[\beta_V(t - t_m)/\sqrt{2}]}{2} \exp\left(-3H(t - t_m) + \left(\frac{3}{\sqrt{2}}\frac{H}{\beta_V}\right)^2\right) \quad (5.49)$$

in the case of strong supercooling. Hereby, n_{\max} is $n_{\max} = \sqrt{2\pi}\Gamma_{t_m}$ and $\operatorname{erf}(x)$ denotes the error function. Crucially, the derivation of the above equation assumes a constant Hubble parameter, which is valid assumption in the case of strong supercooling, where the vacuum energy ρ_{vac} is approximately temperature-independent and dominates over the radiation energy ρ_{rad} , which is negligible. Of particular interest for the estimation of the gravitational wave spectra is the number density at the end of the phase transition which is evaluated at $t - t_m \sim \sqrt{2}\beta_V^{-1}$ [299]. In that case

$$n_{\max} = \frac{\sqrt{2\pi}\Gamma(T_m)}{\beta_V}, \quad (5.50)$$

where $\Gamma(T_m)$ is the nucleation rate at the minimization temperature. The above number density entails the following mean bubble separation in the strong super-

cooling regime

$$R_* \equiv (n_{\max})^{-1/3} = \left[\frac{\sqrt{2\pi}\Gamma(T_m)}{\beta_V} \right]^{-1/3}. \quad (5.51)$$

5.2.1 Gravitational Waves from a Phase Transition

The field of gravitational waves from phase transitions is still evolving and there are many challenges and open questions to be tackled. In the following we will attempt to provide a short summary of the state-of-the art, highlighting open questions where they occur.

A first-order phase transition is characterized by the release of latent heat that contributes to the energy-momentum tensor of the field-fluid system. A strong enough phase transition can therefore act as a source for the production of detectable gravitational waves. A crucial aspect that is relevant in this discussion, is the redshift that the peak-frequency of the gravitational waves experiences due to the cosmic expansion of the universe. Hence, in order to relate the gravitational wave spectrum with a peak-frequency today f_{peak} to the one at the time of emission with a peak-frequency f_{peak}^* the expansion of the universe has to be taken into account. Assuming that the universe has entered the era of radiation-domination right after the phase transition and has henceforth expanded adiabatically, the two peak frequencies are related as

$$f_{\text{peak}} = \frac{h_*}{H_*} f_{\text{peak}}^* = 1.65 \times 10^{-5} \text{ Hz} \left(\frac{g_*}{100} \right)^{1/6} \left(\frac{T_{\text{reh}}}{100 \text{ GeV}} \right) \frac{f_{\text{peak}}^*}{H_*}, \quad (5.52)$$

where we have introduced the temperature at reheating T_{reh} , H_* denotes the Hubble rate at the time of production and $h_* = (a_*/a_0)H_*$ is the Hubble rate redshifted until the present time by the scale factors a_* at the time of emission and a_0 today. As a reminder g_* refers to the relativistic degrees of freedom. The reheating temperature follows from energy conservation $a_{\text{reh}}^3 \rho_{\text{rad}}(T_{\text{reh}}) = a_*^3 (\rho_{\text{rad}}(T_p) + \Delta V)$, such that [300]

$$T_{\text{reh}} \simeq T_p (1 + \alpha(T_p))^{1/4}. \quad (5.53)$$

Assessing the production of gravitational waves during a first-order phase transition is rather involved and requires a numerical approach. Simulations of thermal phase transitions have established the following picture: Gravitational waves are sourced in three different stages. At first the bubbles of the broken phase collide and merge with each other, giving a contribution $\hat{h}^2 \Omega_{\text{coll}}$ to the total power spectrum. This stage, however, is of short duration and the contribution of bubble collisions to the total gravitational wave spectrum turns out to be subdominant for most realistic scenarios ⁷. The collision of bubbles is followed by the generation of sound waves,

⁷A scenario characterized by the dominant contribution to the total power spectrum coming from bubble collisions is referred to as *runaway* scenario. In order to realize such a scenario the phase transition has to release a huge amount of energy which can be quantified in terms of α being of the order of 10^{12} [301]. Most values of α in the literature, however, tend to be typically of up to $\mathcal{O}(1)$.

which turns out to be the most powerful source of gravitational waves as the phase transition takes place. One can think of the expansion of bubbles as an explosion where the resulting compression wave expands in the relativistic Standard Model fluid as a sound wave once the bubbles have completely merged. The overlap of different sound waves then acts as a source of gravitational waves, characterized by a power spectrum $\hat{h}^2\Omega_{\text{sw}}$. Finally, the last source of gravitational waves comes from a turbulent regime, sourced by the non-linear behavior of the flow as it decays, creating vorticity and turbulence. The resulting power spectrum is given by $\hat{h}^2\Omega_{\text{turb}}$. Hence, the total power spectrum in a linearized approximation is just the sum of the power spectra generated during each of the stages⁸, i.e.,

$$\hat{h}^2\Omega_{\text{GW}}(f) = \hat{h}^2\Omega_{\text{coll}}(f) + \hat{h}^2\Omega_{\text{sw}}(f) + \hat{h}^2\Omega_{\text{turb}}(f). \quad (5.54)$$

The frequency dependence of the power spectra is determined from numerical simulations. Those simulations hint towards the fact that it is possible to quantify $\hat{h}^2\Omega_{\text{GW}}$ in terms of a few key parameters related to the released energy during the phase transition and the time-scale of the phase transition. From our previous discussions, we know that α provides a measure of the latent heat released during the phase transition, while the mean bubble separation R and the Hubble constant H set the timescale of the phase transition. It is therefore not unexpected that H_*R sets the peak frequency of the gravitational wave signal, as we will see in a moment, while the energy content of the phase transition, as measured by α and H_*R , will set the amplitude of the signal.

In line with [302, 303, 304], the gravitational wave power spectra, which have been derived in the so-called envelope approximation, where colliding bubble walls immediately lose their energy [305, 306], can be fitted to admit the following frequency dependence

$$\hat{h}^2\Omega_{\text{coll}}(f) = \hat{h}^2\Omega_{\text{coll}}^{\text{peak}} \frac{3.8(f/f_{\text{peak}}^{\text{coll}})^{2.8}}{1 + 2.8(f/f_{\text{peak}}^{\text{coll}})^{3.8}}, \quad (5.55a)$$

$$\hat{h}^2\Omega_{\text{sw}}(f) = \hat{h}^2\Omega_{\text{sw}}^{\text{peak}} \left(\frac{f}{f_{\text{peak}}^{\text{sw}}}\right)^3 \left[\frac{4}{7} + \frac{3}{7}\left(\frac{f}{f_{\text{peak}}^{\text{sw}}}\right)^2\right]^{-\frac{7}{2}}, \quad (5.55b)$$

$$\hat{h}^2\Omega_{\text{turb}}(f) = \frac{\hat{h}^2\Omega_{\text{turb}}^{\text{peak}}}{(1 + 8\pi f/h_*)} \left(\frac{f}{f_{\text{peak}}^{\text{turb}}}\right)^3 \left[1 + \left(\frac{f}{f_{\text{peak}}^{\text{turb}}}\right)\right]^{-\frac{11}{3}}, \quad (5.55c)$$

⁸It is still an open research question whether the sound wave regime and the turbulent regime can actually be considered separately.

where the peak frequencies read

$$f_{\text{peak}}^{\text{coll}} \simeq 1.65 \cdot 10^{-5} \text{ Hz} \left(\frac{g_*}{100} \right)^{\frac{1}{6}} \left(\frac{T_{\text{reh}}}{100 \text{ GeV}} \right) \left(\frac{(8\pi)^{\frac{1}{3}}}{H_* R} \right) \left(\frac{0.62v_w}{1.8 - 0.1v_w + v_w^2} \right), \quad (5.56a)$$

$$f_{\text{peak}}^{\text{sw}} \simeq 1.9 \cdot 10^{-5} \text{ Hz} \left(\frac{g_*}{100} \right)^{\frac{1}{6}} \left(\frac{T_{\text{reh}}}{100 \text{ GeV}} \right) \left(\frac{(8\pi)^{\frac{1}{3}}}{H_* R} \right), \quad (5.56b)$$

$$f_{\text{peak}}^{\text{turb}} \simeq 2.7 \cdot 10^{-5} \text{ Hz} \left(\frac{g_*}{100} \right)^{\frac{1}{6}} \left(\frac{T_{\text{reh}}}{100 \text{ GeV}} \right) \left(\frac{(8\pi)^{\frac{1}{3}}}{H_* R} \right). \quad (5.56c)$$

and are given in terms of the mean bubble separation R at percolation temperature, the bubble wall speed v_w , the reheating temperature T_{reh} and the Hubble rate at percolation temperature H_* . In the following computations of the gravitational wave spectra we will set the wall speed to one, i.e., $v_w = 1$ unless otherwise specified. Moreover, the peak amplitudes of the power spectra are given as

$$\hat{h}^2 \Omega_{\text{coll}}^{\text{peak}} \simeq 1.67 \cdot 10^{-5} \left(\frac{H_* R}{(8\pi)^{\frac{1}{3}}} \right)^2 \left(\frac{\kappa_{\text{coll}} \alpha}{1 + \alpha} \right)^2 \left(\frac{100}{g_*} \right)^{\frac{1}{3}} \frac{0.11v_w}{0.42 + v_w^2}, \quad (5.57a)$$

$$\hat{h}^2 \Omega_{\text{sw}}^{\text{peak}} \simeq 2.65 \cdot 10^{-6} \left(\frac{H_* R}{(8\pi)^{\frac{1}{3}}} \right) \left(\frac{\kappa_{\text{sw}} \alpha}{1 + \alpha} \right)^2 \left(\frac{100}{g_*} \right)^{\frac{1}{3}}, \quad (5.57b)$$

$$\hat{h}^2 \Omega_{\text{turb}}^{\text{peak}} \simeq 3.35 \cdot 10^{-4} \left(\frac{H_* R}{(8\pi)^{\frac{1}{3}}} \right) \left(\frac{\kappa_{\text{turb}} \alpha}{1 + \alpha} \right)^{\frac{3}{2}} \left(\frac{100}{g_*} \right)^{\frac{1}{3}}, \quad (5.57c)$$

where κ_{coll} , κ_{sw} and κ_{turb} are the efficiency factors that describe how much α , i.e. roughly speaking how much latent heat, is converted into the energy of the bubble wall and the bulk motion of bubbles. Since the efficiency factors indicate fractions of converted latent heat their values are smaller than one. These efficiency factors depend on the wall speed v_w and the strength of the phase transition α and are provided in the appendix. They are also determined from numerical simulations. For most common physical scenarios κ_{coll} is found to be negligibly small such that bubble collisions have a subdominant contribution to the total gravitational wave power spectrum. This is due to the fact that the plasma of Standard Model particles acts as a friction term reducing the transfer of kinetic energy stored in the bubble walls into the production of gravitational waves. A definition for κ_{coll} , given by Eq. (H.3), as well as a discussion on the relevant physics that enter are provided in the appendix. As a side remark it is also not yet settled whether the envelop approximation in fact also fully holds in the *non-runaway* case, where the bubble wall-speed reaches a constant terminal velocity. The field of gravitational waves from phase transitions is still evolving and there is no clear consensus on how to quantify the different efficiency factors. Two measures are, however, standard in the literature and it turns out that they agree with each to high precision except at very strong

supercooling, where $\alpha \gg 1$. One common way to quantify the efficiency factors κ_{sw} and κ_{turb} that quantify the distribution of the energy budget still available after bubbles have collided and merged to produce sound waves and a turbulent regime, respectively gives

$$\kappa_{\text{sw}} = \kappa_{\nu}, \quad (5.58)$$

while κ_{turb} can be given as

$$\kappa_{\text{turb}} = \epsilon \kappa_{\nu}, \quad (5.59)$$

where $\epsilon \approx 0.05 - 0.1$ and the efficiency factor κ_{ν} depends on the velocity of the bubble wall v_w . For the specific case where $v_w = 1$, one obtains

$$\kappa_{\nu} = \frac{\alpha_{\text{eff}}}{\alpha} \frac{\alpha_{\text{eff}}}{0.73 + 0.083\sqrt{\alpha_{\text{eff}} + \alpha_{\text{eff}}}}, \quad (5.60)$$

where we have introduced α_{eff} , which is a measure of the still available energy after bubbles have collided and merged, hence $\alpha_{\text{eff}} = (1 - \kappa_{\text{coll}})\alpha$. Recent studies, however, have shown that Eq. (5.58) and Eq. (5.59) underestimates the effects of turbulence when the production of sound waves falls down in less than a Hubble time. In that case the power spectrum of sound waves is reduced and the gravitational wave amplitude from turbulence becomes more significant instead. Overall, the total amplitude also decreases. A more careful analysis allows the efficiency factor κ_{sw} , describing the total available energy budget converted to sound waves, to be approximated as

$$\kappa_{\text{sw}} = (H_* \tau_{\text{sw}})^{1/2} \kappa_{\nu}, \quad (5.61)$$

while the fraction converted to turbulence can be quantified via

$$\kappa_{\text{turb}} = (1 - H_* \tau_{\text{sw}})^{2/3} \kappa_{\nu}. \quad (5.62)$$

Hereby, the factor $H_* \tau_{\text{sw}}$ gives an estimate of the relevance of the sound wave regime with τ_{sw} indicating the duration of the sound wave stage. In this thesis we will make use of this more recent definition of the efficiency factors κ_{sw} and κ_{turb} .

The duration of the sound wave period is limited by $\tau_{\text{sw}} = 1/H_*$ due to the fact that the universe expands, thus reducing the effective power of the source of gravitational waves from sound waves and washing out the non-linearities of the fluid that are at the root of the sound wave regime. The Hubble constant H_* is evaluated at the percolation temperature T_p . This is a reasonable identification since at the percolation temperature, which can be regarded as marking the onset of the phase transition, a significant amount of bubbles of the broken phase have nucleated and merged. Thus, the percolation temperature can be considered to be the relevant temperature in order to describe the lifetime of sound waves.

From a dimensional point of view the duration of the sound wave period should be

given as L_f/\bar{U}_f , where L_f is a characteristic length scale of the fluid flow, while \bar{U}_f is a characteristic velocity. As we have argued in preceding sections, the bubble dynamics is expected to be fully expressible in terms of a few key quantities such as the mean bubble separation R , the wall velocity v_w and α . It thus seems reasonable to identify the mean bubble separation R_* with the characteristic length scale of the fluid flow L_f . More precisely, as explained above, this quantity has to be evaluated at the percolation temperature T_p . The characteristic velocity of the fluid flow can be expressed in terms of the root-mean-square fluid velocity

$$\bar{U}_f^2 = \frac{3}{v_w(1+\alpha)} \int_{c_s}^{v_w} d\xi \xi^2 \frac{v(\xi)^2}{1-v(\xi)^2} \simeq \frac{3}{4} \frac{\alpha_{\text{eff}}}{1+\alpha_{\text{eff}}} \kappa_\nu, \quad (5.63)$$

which is a function of the speed of sound $c_s = 1/\sqrt{3}$, the characteristic speed for sound waves, the wall speed v_w , α and $v(\xi)$ is the velocity profile of the plasma. Moreover, we have assumed $v_w \simeq 1$ in the second equality and introduced an effective value of α , α_{eff} , which is a measure of the still available energy after bubbles have collided and merged, hence $\alpha_{\text{eff}} = (1 - \kappa_{\text{coll}})\alpha$. The efficiency factor κ_ν is the same efficiency factor that has also been introduced in Eq. (5.61) and Eq. (5.62) and for $v_w = 1$ is given by Eq. (5.60). So far, however, we have not factored in the expansion of the universe in the discussion of τ_{sw} . The age of the universe at the percolation time $1/H_*$ acts as a limiting time for the sound wave period as the effective power of the source of gravitational waves is effectively reduced as the universe expands. Phrased differently, the expansion of the universe washes out the energy budget of the phase transition. Hence, if the lifetime of the sound wave phase, $\tau_{\text{sw}} = R_*/\bar{U}_f$, is not shorter than the time that the universe takes to reduce the available effective power due to its expansion, the sound wave phase will effectively end at a time $1/H_*$. In turn, this also implies that there will be no more latent heat left to generate turbulence and the non-linearities of the flow, causing the turbulent regime, will fall off very quickly. This is indeed reflected in the definition of the efficiency factor κ_{urb} , which vanishes if $\tau_{\text{sw}} = 1/H_*$. Hence, in general, the duration of the sound wave period can be estimated as

$$\tau_{\text{sw}} = \min \left[\frac{1}{H_*}, \frac{R_*}{\bar{U}_f} \right], \quad (5.64)$$

where R_* is the mean bubble separation and \bar{U}_f is the root-mean-square fluid velocity. The above definition reflects the fact that the Hubble time $1/H_*$ sets a maximum time scale on the duration of the sound wave regime. At this point, we may also understand the definitions of κ_{sw} and κ_{urb} from a more physical point of view if we introduce the lifetime of the universe at percolation temperature, $\tau_{\text{univ}} = 1/H_*$. In that case, the efficiency factors of the sound wave and the turbulent phase admit the following form

$$\kappa_{\text{sw}} = \left(\frac{\tau_{\text{sw}}}{\tau_{\text{univ}}} \right)^{1/2} \kappa_\nu \quad (5.65)$$

and

$$\kappa_{\text{turb}} = \left(1 - \frac{\tau_{\text{sw}}}{\tau_{\text{univ}}}\right)^{2/3} \kappa_{\nu}, \quad (5.66)$$

respectively. The fraction $\tau_{\text{sw}}/\tau_{\text{univ}}$ simply reflects the fact that the duration of the sound wave regime competes with the expansion of the universe which distributes away the effective energy, that is in principle available to produce additional sound waves and turbulence, in a time τ_{univ} . We can see clearly that if the universe expands fast enough, effectively stopping the further production of sound waves, $\kappa_{\text{turb}} = 0$ and no turbulent fluid flow is generated.

5.3 Results

The gravitational wave spectra are computed in terms of the model-dependent parameters α and $\tilde{\beta} \equiv \beta/H$, which are related to the release of latent heat and the duration of the phase transition, respectively. Thus, a knowledge of α and $\tilde{\beta}$ allows to capture the effects of new physics on the gravitational wave spectrum resulting from a first-order phase transition. Varying the potentials freely leads to a scatter plot of $(\alpha, \tilde{\beta})$ -pairs [303]. Intriguingly, in our analysis of the modified Higgs potentials introduced previously, we find that this scatter reduces to a narrow band of allowed $(\alpha, \tilde{\beta})$ -pairs, see Fig. 5.3. This means that a wide range of BSM scenarios, described by our effective potentials, imply a relationship between the released energy during the phase transition and the inverse phase transition duration and, hence, predict a similar gravitational wave signal. The universal behavior displayed in Fig. 5.3 follows from equally universal curves for α and $\tilde{\beta}$ as functions of the vacuum expectation value ϕ_c/T_c , see Fig. 5.4. The strength of the phase transition is quantified by ϕ_c/T_c . With increasing ϕ_c/T_c , we observe that α increases while $\tilde{\beta}$ decreases. This is not surprising: α measures the release of latent heat during the phase transition and hence one would expect that it is also a measure of the strength of the phase transition. In particular, α takes into account the difference between the two phases of the potential, see Eq. 5.38. Hence, a larger value of α implies that the phase transition has undergone an extended period of supercooling where ΔV increases. Consequently, with an increasing period of supercooling, the duration of the phase transition will increase. This explains the fact that as the strength of the phase transition ϕ_c/T_c is increased, the inverse duration of the phase transition decreases. Conversely, this means that a stronger phase transition, as encoded in ϕ_c/T_c , takes more time to complete.

Overall, the ϕ_c/T_c dependence of α and $\tilde{\beta}$ shows an approximately universal behavior for the different types of potentials. In particular, for small $\phi_c/T_c \leq 1 - 2$, both $\log \alpha$ and $\log \tilde{\beta}$ display a linear dependence on $\log(\phi_c/T_c)$, pointing towards a universal power-law behavior. For larger values of $\phi_c/T_c \geq 1 - 2$, no simple power-law can be established. Universality, however, still holds true.

Thus, generic BSM physics, as introduced by the different modifications of the

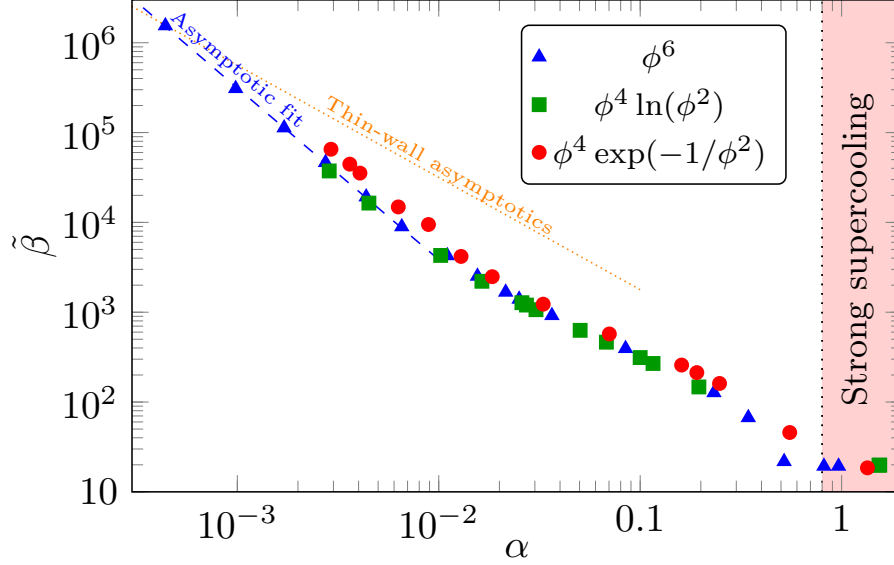


Figure 5.3: Displayed above are the pairs of $\tilde{\beta}$ and α values that can be accessed from the three modifications of the effective Higgs potential that we are considering. A nearly universal behavior between $\tilde{\beta}$ and α can be observed for all potentials. In particular, at small α we find an asymptotic power-law behavior with $\tilde{\beta} = 0.5 \cdot \alpha^{-1.9}$. The analysis of a simple ϕ^4 model allows us to obtain analytical results for $\tilde{\beta}$ and α as a function of ϕ_c/T_c , which can be combined to give a relation between $\tilde{\beta}$ and α as depicted above. Crucially, this derivation relies on the thin-wall approximation for which $T_c - T/T \ll 1$ and is, in particular, valid for weakly supercooled phase transitions, i.e., small α .

Higgs potential in Eq. 5.2, Eq. 5.3 and Eq. 5.4, lead to a universal relation between the energy released during the phase transition and the (inverse) duration of the phase transition. Currently, we do not have an exact explanation as to why this is the case. A possible argument to explain the universal behavior is that it arises as a standard consequence of the properties of RG flows, as also discussed in Ch. 2, when introducing the concept of universality: The specific details of the new physics introduced at some UV scale M_{NP} are washed out by thermal and quantum fluctuations below the UV scale. This intuition is, however, not confirmed, as the different finite-temperature potentials exhibit clear differences between the three classes of potentials. See for instance Fig.4 in [276]. Gaining a deeper understanding of the roots behind the universality observed in Fig. 5.3 and Fig. 5.4 is left for future work.

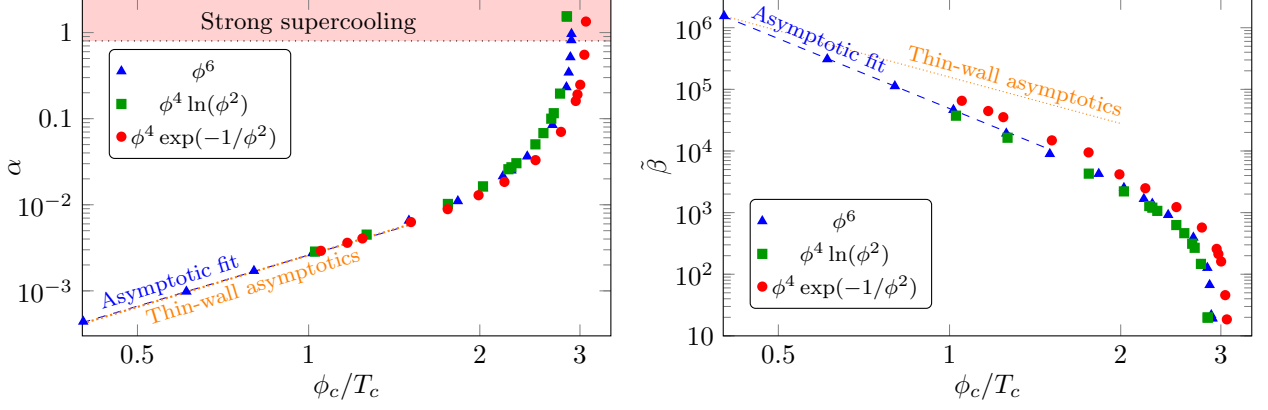


Figure 5.4: We show α (left panel) and $\tilde{\beta}$ (right panel) as a function of the order parameter ϕ_c/T_c for all classes of potentials. An almost universal relation between $\alpha, \tilde{\beta}$ and ϕ_c/T_c is found for all modifications. The red area marks the strong supercooling regime. At small ϕ_c/T_c , we find asymptotic power-law behaviours with $\alpha = 0.0026 \cdot (\phi_c/T_c)^{1.97}$ and $\tilde{\beta} = 48800 \cdot (\phi_c/T_c)^{-3.77}$.

Gravitational Wave Spectra

The gravitational wave spectra for the three classes of potentials can be compared to the LISA and DECIGO sensitivity curves. We find that for strong enough phase transitions, a gravitational wave signal could be detected by both LISA and DECIGO, see Fig. 5.5. Phase transition with $\phi_c/T_c \approx 2 - 2.7$ lie outside the sensitivity range of LISA. Detecting the gravitational wave signal emitted by phase transitions with smaller ϕ_c/T_c would require instruments that operate at higher frequencies and increased sensitivity, such as for example DECIGO. Alternative experiment set-ups such as AION or AEDGE, which rely on atom interferometry, might also be able to reach sensitivities of interest for electroweak phase transitions at lower ϕ_c/T_c [307]. In general, a stronger phase transition leads to a shift towards lower peak frequencies and a growth in the amplitude of the signal. The same pattern has also been reported for the class of ϕ^6 potentials [308]. From the universality of $\alpha(\tilde{\beta})$ discussed above, it is expected that this pattern is shared by all three classes of potentials, see Fig. 5.5. This explains why the peak-frequencies of the gravitational wave spectra lie in the exterior areas of the sensitivity curves of LISA and DECIGO.

The gravitational wave spectra are characterized by a number of key parameters, besides α and $\tilde{\beta}$, such as the efficiency factors that quantify how much energy is converted into the different sources of gravitational waves or the wall speed of the expanding bubbles. We have already touched upon ambiguities concerning the distribution of the energy budget of the phase transition. Nonetheless, it is established that the sound wave period acts as the dominant source of gravitational waves during a first-order phase transition. This is also confirmed by our results, see Fig. 5.6. Moreover, we have also tested the impact of the wall speed on the gravitational wave

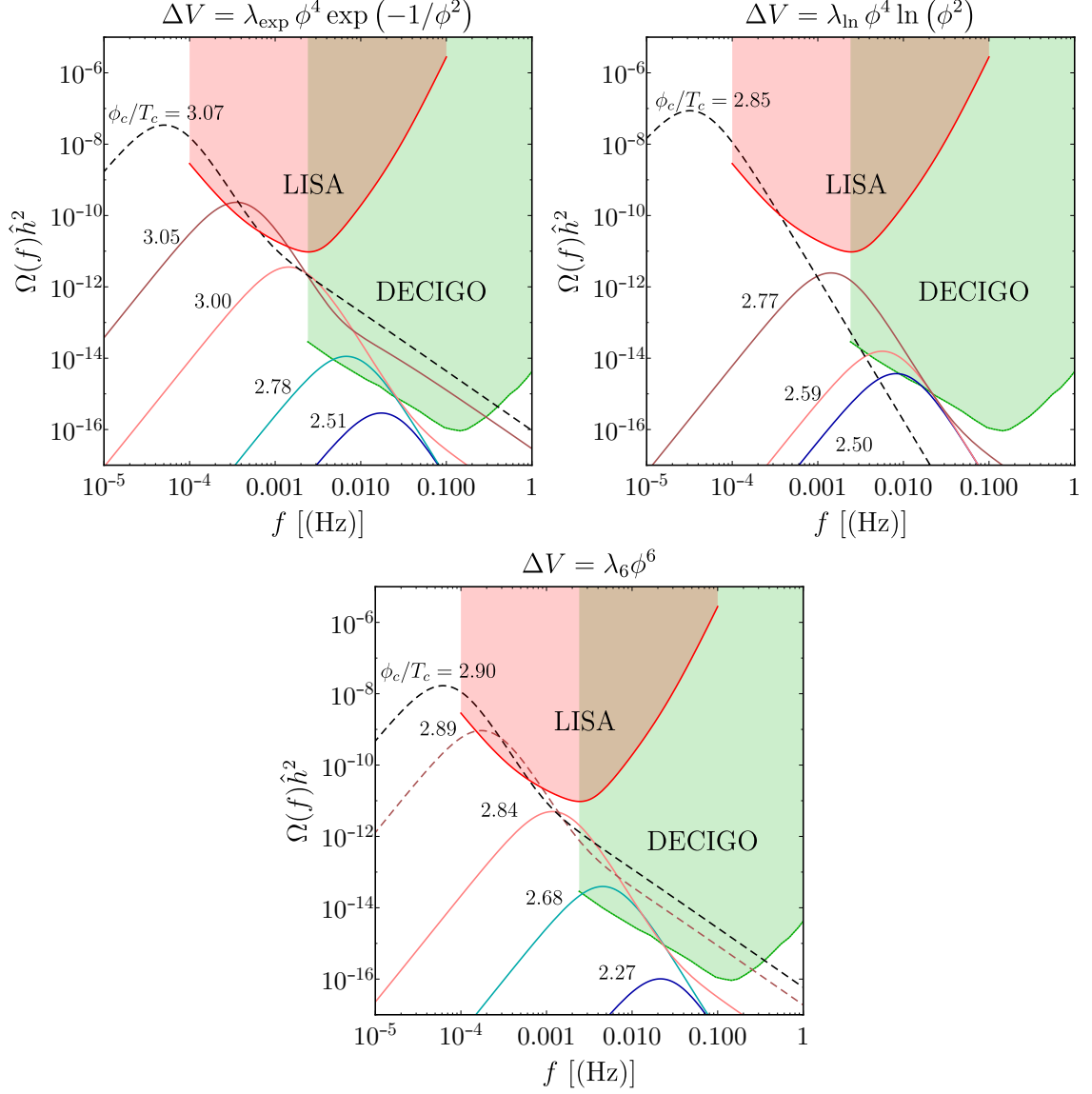


Figure 5.5: We depict the total GW power spectra of all three classes of modified Higgs potentials for different values of ϕ_c/T_c . The dashed lines in the figures indicate the strong supercooling regime at which the linearization of the action in order to determine β breaks down.

spectrum. The gravitational wave spectra depicted in Fig. 5.5 have been determined assuming bubbles expanding at the speed of light, i.e., $v_w = 1$. Slower expanding bubbles lead to a smaller amplitude at peak frequency. The difference between $v_w = 0.5$ and $v_w = 1$ can be nearly half an order of magnitude. As such, our choice of $v_w = 1$ that we use throughout this thesis to determine the gravitational wave spectra is a less conservative choice.

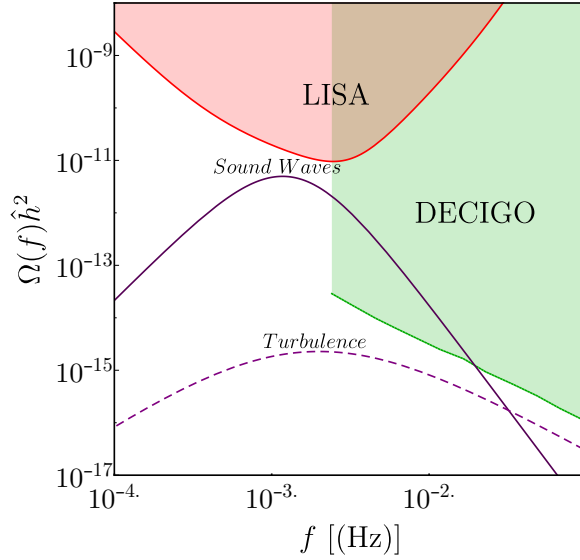


Figure 5.6: We show the contributions of sound waves and turbulence to the power spectrum using Eq. 5.61 and Eq. 5.62 for the polynomial modification of the Higgs potential for $\phi_c/T_c = 2.84$.

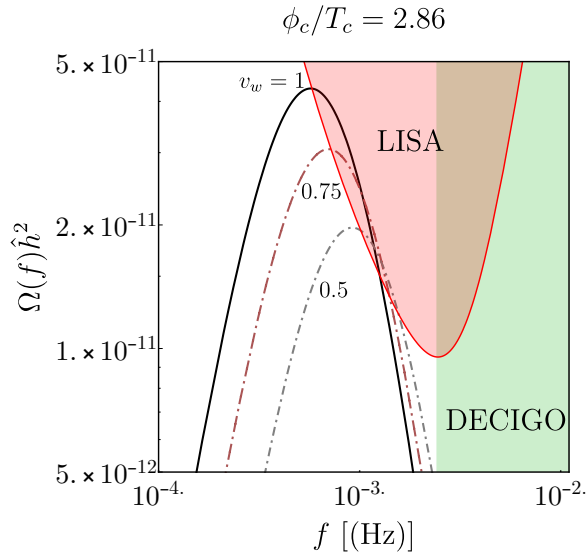


Figure 5.7: We compare the effect of different wall speeds on the gravitational wave spectrum for a representative value of ϕ_c/T_c of the polynomial ϕ^6 modification of the Standard Model Higgs potential. As the wall speed increases, the spectra are shifted towards larger amplitudes at smaller smaller peak frequencies.

Collider-signatures and GW-signatures

Let us now understand how a combined effort through collider physics and gravitational-waves astronomy can foster understanding about new physics. For that reason we will pay particular attention to universality and how it is possible to pinpoint different physics contributions.

The relevant quantity that informs about the detectability of a gravitational wave signal is the signal-to-noise ratio (SNR) [309, 310] which can be determined from the gravitational wave spectrum $\hat{h}^2\Omega_{\text{GW}}(f)$, the sensitivity curve of the detector $\hat{h}^2\Omega_{\text{sens}}(f)$ and the observation time \mathcal{T} that follows from the duration of the mission times the duty cycle, as in [311] where

$$\text{SNR} = \sqrt{\frac{\mathcal{T}}{s} \int_{f_{\text{min}}}^{f_{\text{max}}} df \frac{\hat{h}^2\Omega_{\text{GW}}}{\hat{h}^2\Omega_{\text{sens}}}}. \quad (5.67)$$

For LISA, an observation time of 4 years is assumed, with a duty cycle of 75% such that $\mathcal{T} = 12\pi \times 10^7 s$ [303]. Establishing a threshold SNR value is non-trivial as the detectability of a signal is subject to different aspects such as, for instance, the availability of matched filtering techniques which typically improve the signal. In our case as the spectrum is known these techniques can be applied. Furthermore, galactic binaries contribute to a stochastic background signal that needs to be taken into account [312, 313].

We find a SNR above 1 for cases where the peak amplitude at peak frequency of the gravitational wave signal lies in the LISA sensitivity range. The new physics leading to a first-order phase transition and consequently a GW signal also impacts observable properties of the Higgs-potential, namely the triple- and quartic-Higgs couplings. As we discussed in the introduction to the topic of gravitational waves from phase transition, both couplings are enhanced compared to the Standard Model prediction [276]. This allows us to compare the LHC observables to the SNR for the gravitational wave spectra of all three potentials. Strong enough phase transition can lead to a detectable signal by LISA as well as a measurable LHC signal. Thus, an interplay of collider physics and gravitational-wave astronomy could be used as a cross-check of the two signals. In particular, an enhancement of the triple- and quartic-Higgs couplings could also come from different new physics which preserves the cross-over at the electroweak scale and does not provide a mechanism for baryogenesis. Hence, an observation of gravitational waves by LISA or DECIGO would strengthen the case for a first-order phase transition at the electroweak scale. Moreover, even amongst those scenarios with electroweak baryogenesis, a symbiosis of the GW signal with the LHC signature could allow to learn more about the details of the new physics. Fig. 5.8 depicts how at a given SNR, the three different classes of potentials that we studied lead to different modifications of the triple- and quartic-Higgs couplings.

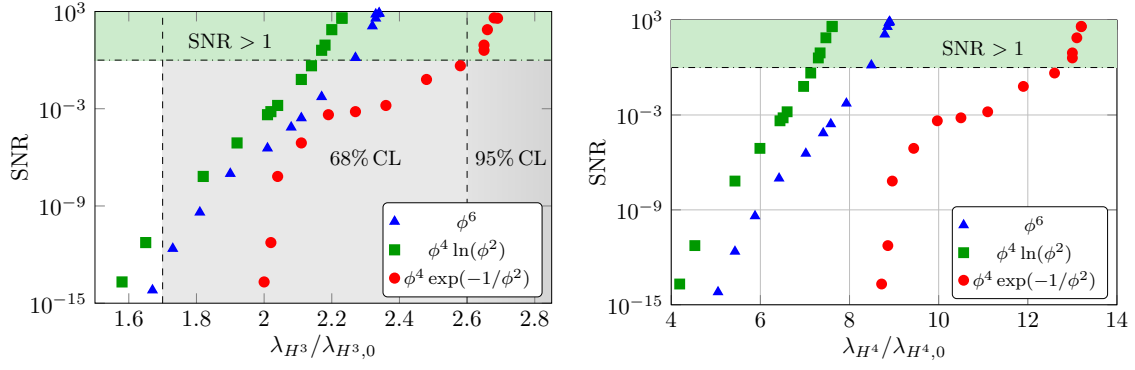


Figure 5.8: An interplay of collider physics and gravitational-wave astronomy could be used as a way to pinpoint new physics. On the left panel, we depict the pairs of SNR and triple-Higgs couplings that could be realized by each of the three classes of potentials. On the right panel, we show that for a given SNR, the different potentials predict different corrections to the quartic-Higgs coupling.

6 Conclusion & Outlook

There is still much to be learned about the wonders of our universe. What is the fundamental nature of space-time? What are the fundamental particles in our universe? What is the origin of mass? These are very deep and fundamental questions that will fascinate many generations of scientists to come. We have attempted to provide new perspectives to some of these questions.

At shortest scales, gravity breaks down and it is argued that a theory of quantum gravity is required to describe space-time in the quantum regime. A crucial aspect is whether space-time is fundamentally discrete or not. In that regard, we have discussed the subtleties associated to the notion of discreteness in quantum gravity. We have argued that in theories which motivate a physically discrete picture of space-time at shortest distances, one can also take a different standpoint, where discreteness is actually viewed as a way to regularize the theory and the actual physics follows from taking the continuum limit. Crucially, the continuum limit does not necessarily have to imply that the resulting physics turns out to be continuous. Asymptotic safety, for instance, is a continuum theory of quantum gravity that features elements of discreteness, such as, e.g., a minimal length.

One of the properties of a continuum limit is that it entails universality, whereas different microscopic formulations can provide access to the same physics. This opens the door to explore possible relationships between different approaches to quantum gravity and exploit their different strengths. Progress in learning about the fundamental nature of space-time will greatly benefit from a diversity of ideas and approaches.

This conviction has served as our inspiration to pursue a discrete strategy to make sense of the path-integral for quantum gravity, where the idea is to discretize the path-integral in terms of small building blocks of space-time, which allow to construct a discrete approximation to random geometries. Discreteness is introduced as a regulator taming the divergences that are associated to a naive quantization of GR. These building blocks of space-time are not considered to be physical or “fundamental” but can be viewed as auxiliary, unphysical objects, allowing to define a regularized path integral. Ultimately, the effects associated to this discretization are removed in the continuum limit which is characterized by a second-order phase transition. Universality then implies that the microscopic details, in particular the exact shape of the building blocks, do not matter. This strategy is the underlying pillar of dynamical triangulations and tensor models. In two dimensions, there exists a direct correspondence between the two approaches and continuous Liouville quantum gravity. Revealing whether this correspondence also holds in higher dimensions and understand if the continuum limits of dynamical triangulations and tensor models

potentially belong to the universality class of asymptotically safe quantum gravity will require progress on all sides.

In that spirit, we have undertaken first steps to systematically explore the continuum limit of tensor models in three and four dimensions using a background-independent formulation of the functional renormalization group. In four dimensions we have found intriguing evidence that there exists a universality class for tensor models that is not incompatible with the Reuter universality class of asymptotic safety.

This begs the question whether dynamical triangulations, tensor models and asymptotic safety might actually be three sides of the same triangle. Exploring this question will be the engine of future work and will require more knowledge about the geometry that underpins the fixed point that we have identified in four dimensional tensor models. Steps in that direction are the comparison of the scaling of geometric operators between the different approaches. This will require systematic studies of composite operators on the tensor model side following the same spirit as the works [314, 315, 316, 317] performed to study the scaling of geometric operators in asymptotic safety. In the same vein, dimensional estimators such as the spectral dimension or the Hausdorff dimension are also of interest in order to learn more about the physical properties of the continuum limit. Understanding these dimensional estimators in the context of tensor models is therefore one important direction of future work. A route to access the spectral dimension could go through the Feynman graph structure at the fixed point. A diffusion process set up on that graph could give access to the spectral dimension [318]. Such steps will be crucial in order to learn more about the geometry that underlies the continuum limit of tensor models. The fixed point action associated to the fixed point that we have identified as a potential candidate for four-dimensional quantum gravity can be rewritten as a rectangular multi-matrix model. The standard matrix-model techniques that we reviewed in this thesis are only applicable to square-matrices as they crucially rely on the ability to diagonalize a matrix in terms of its eigenvalues. It is, however, possible to study rectangular matrices in the large- N limit by decomposing the matrices through a singular value decomposition [319]. Being able to solve these models exactly could potentially provide access to precise and regulator-independent values of the critical exponents associated to the candidate-fixed point for four-dimensional quantum gravity allowing to make powerful statements about its universality class. On the technical side, we have made substantial progress in understanding the nuances associated to renormalization group flows in background-independent settings. We have developed and put in practice a generic strategy that allows to systematically study the renormalization group flow of tensor models invariant under any symmetry of choice using the functional renormalization group.

The first step of the strategy consists in specifying the truncation of the scale-dependent effective action, which is constructed from bottom up using a straightforward algorithm; the only input being invariants of interaction-order four. One crucial question in setting up the truncation concerns the assignment of couplings to the invariants. This can be done in two distinct ways: Either one coupling is associated to each tensor invariant or the same coupling is assigned to all invariants

belonging to the same color-symmetric family. In order to realize the latter way of assigning couplings, we have introduced a novel combinatorial object, the indicator, which allows to collect graphs that are invariant under permutations of their color. While so far all evidence hints towards the fact that this is indeed the case, an open question concerning the indicator is whether it uniquely specifies a family of color-symmetric graphs. Closely related to this point, the indicator could also be of interest from a purely mathematical standpoint due to its potential relation to the reconstruction conjecture [320, 321], which states that every graph with more than two vertices is uniquely reconstructable from its deck, which is obtained by removing one vertex from the graph. Studying the properties of the indicator in more detail would, thus, be certainly interesting.

The studies performed in this work have focussed on analyzing truncations that include all invariants up to a certain interaction order. The combinatorial properties of single- and multi-trace melonic interactions, however, allow in principle to resum the melonic sectors of the theory space. An interesting possible direction of future work could consist in considering complete truncations up to a certain interaction-order, while simultaneously taking into account extensions of the truncation in certain sectors.

On a more general note, progress in understanding tensor models and their wide range of applications could also be fostered by understanding the links between results derived from the functional renormalization group and studies performed using the Dyson-Schwinger equations.

Tackling the open questions pointed out above will lead to a deeper understanding of the continuum limit of tensor models and its connection to other approaches of quantum gravity, such as dynamical triangulations or asymptotic safety, with the final objective of learning more about the fundamental nature of space-time. Each of the different approaches comes with a set of advantages. The asymptotic safety approach to quantum gravity, e.g., quantizes degrees of freedom that are already well-known and thus, allows to connect microscopic UV physics to the IR-world that we live in. Crucially, however, computations in Asymptotic Safety introduce an auxiliary background. The strength of the tensor model approach is that it makes no reference to a background. If it turns out that these approaches belong to the same universality class, exploring the strengths of the two approaches would allow to make even stronger statements about the existence of a gravitational UV fixed point implying that space-time at shortest distances might have a fractal-like structure.

We motivated the need for a theory of quantum gravity from the existence of singularities, for example, in the center of black holes. The macroscopic physics of black holes is much better understood. The merger of two black holes, for examples, has led to the production of gravitational waves whose waveform was found to be in agreement with the predictions of GR.

While the gravitational waves detected so far were sourced by the merger of astrophysical objects such as black holes [4] or neutron stars [322], they can also be produced in different ways, allowing to learn new things about the matter content of our universe and its fundamental properties and the mechanism of mass gener-

ation. In the Standard Model of particle physics, particles acquire their mass by electroweak and chiral symmetry breaking. In the Standard Model these phase-transitions are cross-overs. New physics, e.g., in order to explain the origin of the matter-antimatter asymmetry in our universe, can lead to first-order phase transitions that source a stochastic background of gravitational waves. For strong enough first-order phase transitions, this stochastic background could lie in the sensitivity range of future space-based laser interferometers LISA and DECIGO.

In this thesis, we have explored new physics at the TeV-scale parametrized by three different higher-order operators in the Higgs potential which all lead to first-order electroweak phase transitions. These extensions predict modifications of the triple- and quartic-Higgs couplings. The next high-luminosity run at the LHC will allow for a detection of modifications of the Standard Model prediction for the triple-Higgs coupling $\lambda_{H^3, \text{SM}}$ of $\lambda_{H^3}/\lambda_{H^3, \text{SM}} > 1.7$ at a confidence level of 68%. Measuring a modification of the triple-Higgs coupling is therefore an indirect hint pointing towards the existence of a first-order phase transition in the early universe. However, in order to uniquely fix the shape of the Higgs potential more experimental information is needed. A synergy between collider physics and gravitational wave astronomy could allow to bridge this gap. This served as our motivation to study the gravitational wave spectrum of different modifications of the Higgs potential.

From the finite-temperature effective Higgs potential, derived in [276], we extracted key parameters that describe the gravitational wave signal sourced by a first-order phase transition. In particular, the energy released by the phase-transition, measured by α , and the duration of the phase transition parametrized by $\tilde{\beta}$, show a universal dependence on the strength of the phase-transition, ϕ_c/T_c . As a result, we found that $\tilde{\beta}(\alpha)$ displays a clustering behavior around a common curve. This is a non-trivial result that is not a priori expected, given that the effective potentials resulting from the classes of new-physics contributions differ. Future work will be devoted towards understanding the roots of this qualitative universality in more detail. In particular, it will be highly interesting to understand in how far this universal behavior also persists for potentials that predict a lower scale of new physics. Our current intuition is that in that case a larger parameter space in the $(\alpha, \tilde{\beta})$ -plane is available when the parameters of the model are varied. If indeed, universality also turns out to apply to an even broader range of classes of new-physics contributions, this could put ad-hoc modifications of the effective potential under scrutiny since such potentials might not be available for a new-physics scale high enough to have avoided direct detection to date. Tackling this question will require the analysis of new physics contributions at lower cut-off scales.

Another interesting route that one could take in the future, is to use gravitational waves as a way to constrain Dark Matter models. In particular, within the framework of asymptotic safety, one could study models of Dark Matter that are UV-complete, e.g., as done in [323]. This could provide an interesting window to reveal possible imprints of Dark Matter and asymptotic safety.

To conclude, in this thesis we have explored the fascinating implications of gravity. One of the alluring consequences of a dynamical space-time, the existence of

gravitational waves, was initially even doubted by Einstein himself. Today we know that these ripples of space-time are very much real. They not only allow to test the theory of general relativity but also open new exciting ways to learn more about the fundamental particles of our universe and their interactions. As successful as GR is, at shortest distances the theory breaks down, which points towards the need of new gravitational effects at these distances. Including quantum gravitational effects could be a way to resolve the singularities of GR. In that spirit, we have studied the continuum limit of a particular approach to quantum gravity, tensor models, and discussed its connection to other approaches of quantum gravity in the hope that establishing links between different theories of quantum gravity will foster a deeper understanding of the fundamental nature of space-time.

Part II

Appendix

A Liouville

Liouville Gravity

The reader might think that two-dimensional quantum gravity might seem trivial: We have just argued that the classical equations of motion are always satisfied independently of the underlying space-time as a consequence of two-dimensional gravity being purely topological, i.e.,

$$\int d^2x \sqrt{g} R = \chi \tag{A.1}$$

is a mere constant given by the Euler character χ , which is a topological quantity. However, in two dimensions, classical gravity can be shown to not only be diffeomorphism invariant but also to be classically conformal. This observation is crucial for the quantum picture given that conformal invariance is broken at the quantum level due to the measure term not being invariant under conformal transformations. In order to restore conformal invariance one is led to introduce the so-called Liouville action which renders two-dimensional quantum gravity non-trivial by introducing an additional gravitational interaction on top of the ones due to the Einstein-Hilbert action. In order to discuss these points in detail, consider the path-integral for two-dimensional quantum gravity coupled to conformal matter

$$Z = \int \frac{\mathcal{D}g}{Vol(\text{diff})} \mathcal{D}\chi \exp \left(-\beta_0 \int R - \gamma_0 A - S_M[\chi] \right), \tag{A.2}$$

where $S[\chi]$ is an action describing conformal matter χ , i.e.

$$S_M[\chi] = \int d^2\zeta \sqrt{g} g^{\mu\nu} \partial_\mu \chi \partial_\nu \chi, \tag{A.3}$$

β_0 is related to the inverse bare Newton coupling, γ_0 is the bare cosmological constant and A is the space-time area given by $A = \int d^2x \sqrt{g}$. As discussed previously, classical two-dimensional gravity is trivial as there are no local degrees of freedom but only global ones related to the topology of space-time. The quantum theory, however, is non-trivial. This is due to the conformal anomaly. At the classical level, Weyl invariance is a symmetry of the action. At the quantum level, however, it turns out that the measures $\mathcal{D}\chi$ and $\mathcal{D}g$ transform non-trivially under Weyl transformations $g_{\mu\nu} \rightarrow e^\sigma g_{\mu\nu}$, with σ denoting the conformal mode. Indeed, $\mathcal{D}\chi$ transforms, for instance, as

$$\mathcal{D}_{e^\sigma g} \chi = \exp \left(\frac{D}{48\pi} S_L(\sigma) \right) \mathcal{D}_g \chi, \tag{A.4}$$

where $S_L(\sigma)$ is the Liouville action

$$S_L(\sigma) = \int d^2\xi \sqrt{g} \left(\frac{1}{2} g^{\mu\nu} \partial_\mu \sigma \partial_\nu \sigma + R\sigma + \gamma e^\sigma \right). \quad (\text{A.5})$$

The above action introduces an interaction term $R\sigma$, rendering the quantum theory of two-dimensional gravity non-trivial.

In Eq. (A.2), we have introduced the volume of the diffeomorphism group, $Vol(\text{diff})$, in order to emphasize that the path-integral consists of a sum over families of an infinite number of equivalent metric configurations that need to be removed. In order to get rid of this spurious redundancy it is necessary to fix a gauge. In the path-integral approach to QFT this requires the introduction of Faddeev-Popov ghosts. We will defer from going through the detailed steps and instead just provide the resulting partition function that follows from Eq. (A.2),

$$Z = \int [d\tau] \mathcal{D}_g \sigma \mathcal{D}_g(\text{gh}) \mathcal{D}_g \chi \exp \left(-S_M[\chi] - S_{\text{gh}} - \frac{\gamma_0}{2\pi} \int d^2\xi \sqrt{g} \right), \quad (\text{A.6})$$

where $[d\tau]$ corresponds to the integration over moduli¹, $\mathcal{D}\sigma$ corresponds to the measure of the conformal mode, the ghost fields are collected by the measure term $\mathcal{D}(\text{gh}) = \mathcal{D}a \mathcal{D}\bar{a} \mathcal{D}b \mathcal{D}\bar{b}$ and $\mathcal{D}\chi$ is the measure of the conformal matter field. The measure terms are invariant under diffeomorphisms but not under conformal transformations $g_{\mu\nu} \rightarrow e^\sigma g_{\mu\nu}$. Indeed, the overall measure will transform as

$$\mathcal{D}_{e^\phi \hat{g}} \mathcal{D}_{e^\phi \hat{g}}(\text{gh}) \mathcal{D}_{e^\phi \hat{g}} \chi = J(\phi, \hat{g}) \mathcal{D}_{\hat{g}} \phi \mathcal{D}_{\hat{g}}(\text{gh}) \mathcal{D}_{\hat{g}} \chi, \quad (\text{A.7})$$

where the Jacobian $J(\phi, \hat{g})$ is assumed to be given as

$$J(\phi, \hat{g}) = \exp \left(\int d^2\xi \sqrt{\hat{g}} \left(\tilde{a} \hat{g}^{\mu\nu} \partial_\mu \phi \partial_\nu \phi + \tilde{b} \hat{R} \phi + \gamma e^{\tilde{c}\phi} \right) \right). \quad (\text{A.8})$$

which is the exponential of a Liouville-like action. To obtain a normalized kinetic term for ϕ , we perform the additional rescaling $\phi \rightarrow \sqrt{\frac{12}{25-D}} \phi$.

In that case, two-dimensional Liouville gravity takes the following form

$$Z = \int [d\tau] \mathcal{D}_{\hat{g}} \phi \mathcal{D}_{\hat{g}}(\text{gh}) \mathcal{D}_{\hat{g}} \chi e^{-S_M(\chi, \hat{g}) - S_{\text{gh}}(b, c, \bar{b}, \bar{c}; \hat{g})} \exp \left(\int d^2\xi \sqrt{\hat{g}} \left(\frac{1}{8\pi} \hat{g}^{\mu\nu} \partial_\mu \phi \partial_\nu \phi + \frac{Q}{8\pi} \hat{R} \phi + \gamma e^{\alpha\phi} \right) \right). \quad (\text{A.9})$$

¹The moduli space \mathcal{M}_h is the finite dimensional compact space of metrics obtained after gauge fixing, that is the space of metrics modulo diffeomorphisms and Weyl transformations. For each element $\tau \in \mathcal{M}_h$ it is possible to choose a representative metric \hat{g} . The orbits that follow from acting with the diffeomorphism and the Weyl group on \hat{g} then span the full space of metrics: Given a slice $\hat{g}(\tau)$, the full space of metrics g is generated by $f^*g = e^\sigma \hat{g}$, where f represents the action of diffeomorphism and Weyl transformations are accounted by the term e^σ , where σ is the conformal mode.

where the coefficients Q and α are given as

$$Q = \frac{25 - D}{3} \quad \text{and} \quad \alpha = \frac{1}{\sqrt{12}} \left(\sqrt{25 - D} - \sqrt{1 - D} \right). \quad (\text{A.10})$$

such that the expression in Eq. (A.9) can be shown to remain invariant under infinitesimal diffeomorphisms. To make contact with the dynamical triangulations and matrix models discussion, we are interested in the so-called string susceptibility, which describes how the partition function scales for fixed large areas. The area can be fixed by including a delta constraint in the path-integral such that

$$Z(A) = \int \mathcal{D}\chi \mathcal{D}g e^S \delta \left(\int d^2\xi \sqrt{\hat{g}} e^{\alpha\phi} - A \right), \quad (\text{A.11})$$

where the integration over ghost fields and moduli has been collected into the measure $\mathcal{D}\chi$. For large areas, the scaling of the partition function can be expressed as

$$\lim_{A \rightarrow \infty} \sim A^{(\gamma-2)\frac{\chi}{2}-1} \quad (\text{A.12})$$

and also serves as a definition for the string susceptibility γ . In order to determine γ , we can use a scaling argument. The starting point is to consider the rescaling $\phi \rightarrow \phi + \rho/\alpha$, for some constant ρ . The measure is left invariant under this rescaling, while the action only receives a non-trivial modification from²

$$\int d^2\xi \frac{Q}{8\pi} \hat{R}\phi \rightarrow \int d^2\xi \frac{Q}{8\pi} \hat{R}\phi + \int d^2\xi \frac{\rho}{\alpha} \frac{Q}{8\pi} \hat{R}. \quad (\text{A.13})$$

The second term, however, can be expressed in terms of the Euler character χ using the fact that $\int \sqrt{g} R = 4\pi\chi$. Moreover, the delta function can be rewritten as

$$\delta \left(\int d^2\xi \sqrt{\hat{g}} e^{\alpha\phi} - A \right) \Big|_{\phi \rightarrow \phi + \rho/\alpha} = e^{-\rho} \delta \left(\int d^2\xi \sqrt{\hat{g}} e^{\alpha\phi} - e^{-\rho} A \right) \quad (\text{A.14})$$

using the identity $\delta(\lambda x) = 1/|\lambda|\delta(x)$. We may thus write

$$Z(A) = \exp \left(-\frac{Q\rho\chi}{2\alpha} - \rho \right) Z(e^{-\rho} A). \quad (\text{A.15})$$

We may now choose $A = e^\rho$, in which case

$$Z(A) = A^{-\frac{Q\chi}{2\alpha}-1} Z(1). \quad (\text{A.16})$$

To determine the string susceptibility, we may compare the above scaling of $Z(A)$ with A with the scaling given by Eq. (A.12) in order to read off

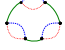
$$\gamma = 2 - \frac{Q}{\alpha} = \frac{1}{12} \left((D-1) - \sqrt{(D-25)(D-1)} \right). \quad (\text{A.17})$$

²The $e^{-\alpha\phi}$ term receives an additional constant modification $e^{-\rho}$.

To make contact with matrix models, we introduce the notation $D = 1 - \frac{6}{m(m+1)}$ such that the string susceptibility is given as

$$\gamma = -\frac{1}{m}. \tag{A.18}$$

B Computations with the FRG

This appendix tries to give a detailed account of how to perform technical computations using the FRG for tensor models. In particular, we will show how to derive a particular contribution to the running of the coupling $g_{6,1}^{3,1}$ associated to . The example-model to be used is the real rank-3 tensor model.

The starting point is the FRGE

$$\partial_t \Gamma_N = \frac{1}{2} \text{Tr} \left(\left(\Gamma_N^{(2)} + R_N \right)^{-1} \partial_t R_N \right) \quad (\text{B.1})$$

which can be re-expressed through the $\mathcal{P}^{-1}\mathcal{F}$ expansion as

$$\partial_t \Gamma_N = \frac{1}{2} \text{Tr} (\partial_t R_N) \mathcal{P}^{-1} + \frac{1}{2} \sum_{n=1}^{\infty} (-1)^n \text{Tr} [(\partial_t R_N) \mathcal{P}^{-1} (\mathcal{P}^{-1} \mathcal{F})^n] \quad (\text{B.2})$$

with

$$\mathcal{P} = \Gamma_N^{(2)} \Big|_{T=0} + R_N \quad (\text{B.3})$$

and

$$\mathcal{F} = \Gamma_N^{(2)} - \Gamma_N^{(2)} \Big|_{T=0}. \quad (\text{B.4})$$

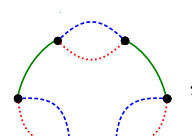
A concrete piece that appears in the computation of the running $g_{6,1}^{3,1}$ is

$$\begin{aligned} & \text{Tr} \left(\partial_t R_N \mathcal{P}^{-1} (\mathcal{P}^{-1} \mathcal{F})^3 \right) \\ & \sim \sum_{\{I_i\}} \frac{1}{2} \times \frac{3!}{2!} \times g_{4,1}^0 (g_{4,1}^{2,1})^2 Z_N \left((1-\eta) \frac{N}{a_1 + a_2 + a_3} + \eta \right) \prod_{i=1}^3 \delta_{a_i b_i} \\ & \times \frac{1}{Z_N} \frac{\prod_{i=1}^3 \delta_{b_i c_i}}{\left(1 - \frac{N}{b_1 + b_2 + b_3}\right) \Theta(b_1, b_2, b_3)} \times \frac{1}{Z_N} \frac{\prod_{i=1}^3 \delta_{c_i d_i}}{\left(1 - \frac{N}{c_1 + c_2 + c_3}\right) \Theta(c_1, c_2, c_3)} \\ & \times (4g_{4,1}^0 T_{d_1 d_2 \alpha_3} T_{e_1 e_2 \alpha_3} \delta_{d_3 e_3}) \\ & \times \frac{1}{Z_N} \frac{\prod_{i=1}^3 \delta_{e_i f_i}}{\left(1 - \frac{N}{e_1 + e_2 + e_3}\right) \Theta(e_1, e_2, e_3)} (4g_{4,1}^{2,1} T_{f_1 \beta_2 \beta_3} T_{g_1 \beta_2 \beta_3} \delta_{f_2 g_2} \delta_{f_3 g_3}) \\ & \times \frac{1}{Z_N} \frac{\prod_{i=1}^3 \delta_{g_i h_i}}{\left(1 - \frac{N}{g_1 + g_2 + g_3}\right) \Theta(g_1, g_2, g_3)} (4g_{4,1}^{2,1} T_{h_1 \gamma_2 \gamma_3} T_{a_1 \gamma_2 \gamma_3} \delta_{h_2 a_2} \delta_{h_3 a_3}), \quad (\text{B.5}) \end{aligned}$$

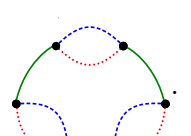
where I_i denotes the set of indices $I_i = \{a_i, b_i, c_i, d_i, e_i, f_i, g_i\}$ and greek indices indicate internal contractions between two tensors while latin indices point to contractions between different pieces of the $\mathcal{P}^{-1}\mathcal{F}$ expansion. Performing the contractions with the delta functions the above expression can be simplified to give

$$\begin{aligned}
& \text{Tr} \left(\partial_t R_N \mathcal{P}^{-1} (\mathcal{P}^{-1} \mathcal{F})^3 \right) \\
& \sim 96 g_{4,1}^0 (g_{4,1}^{2,1})^2 N \frac{1}{Z_N^3} \left(\frac{a_1 + a_2 + a_3}{N} \right)^2 \left((1 - \eta) \frac{N}{a_1 + a_2 + a_3} + \eta \right) \Theta(a_1, a_2, a_3) \\
& \times \frac{1}{1 - \left(\frac{N}{e_1 + a_2 + a_3} - 1 \right) \Theta(e_1, a_2, a_3)} \frac{1}{1 - \left(\frac{N}{g_1 + a_2 + a_3} - 1 \right) \Theta(g_1, a_2, a_3)} \\
& \times T_{a_1 a_2 \alpha_3} T_{e_1 a_2 \alpha_3} T_{e_1 \beta_2 \beta_3} T_{g_1 \beta_2 \beta_3} T_{g_1 \gamma_2 \gamma_3} T_{a_1 \gamma_2 \gamma_3}, \tag{B.6}
\end{aligned}$$

where only the third index i_3 can be contracted freely through the delta functions. The projection prescription requires to set indices that appear simultaneously in the threshold function F and in the tensors to zero. This leaves us with the following expression

$$\begin{aligned}
& \text{Tr} \left(\partial_t R_N \mathcal{P}^{-1} (\mathcal{P}^{-1} \mathcal{F})^3 \right) \\
& \sim \sum_{a_3} 96 g_{4,1}^0 (g_{4,1}^{2,1})^2 N \frac{1}{Z_N^3} \left(\frac{a_3}{N} \right)^2 \Theta(a_3) \left((1 - \eta) \frac{N}{a_3} + \eta \right) \\
& \times \frac{1}{1 - \left(\frac{N}{a_3} - 1 \right) \Theta(a_3)} \frac{1}{1 - \left(\frac{N}{a_3} - 1 \right) \Theta(a_3)} \text{Diagram}, \tag{B.7}
\end{aligned}$$


where we make the sum over the threshold index a_3 explicit. The step functions in the denominator are always fulfilled due to the step function also appearing in the nominator. We can therefore further simplify the above expression in order to obtain

$$\begin{aligned}
& \text{Tr} \left(\partial_t R_N \mathcal{P}^{-1} (\mathcal{P}^{-1} \mathcal{F})^3 \right) \\
& \sim \sum_{a_3} 96 g_{4,1}^0 (g_{4,1}^{2,1})^2 N \frac{1}{Z_N^3} \left(\frac{a_3}{N} \right)^4 \Theta(a_3) \left((1 - \eta) \frac{N}{a_3} + \eta \right) \text{Diagram}. \tag{B.8}
\end{aligned}$$


We are ultimately interested in the large- N limit, where the threshold sums transform into threshold integrals according to

$$\sum_{i=1}^R \sum_{a_i=1}^N \frac{a_i}{N} = \sum_{i=1}^R \sum_{\Delta x_i=0}^1 \Delta x_i \longrightarrow \prod_{i=1}^R \int_0^1 dx_i = \prod_{i=1}^R \int_0^N \frac{da_i}{N}, \tag{B.9}$$

where we performed the change of variable $a_i/N = \Delta x_i$ and R denotes the number of indices that are not set to zero can range between 1 and the rank of the tensor model depending on the combinatorics. In the large- N limit one is therefore led to perform the following sum

$$\begin{aligned}
& \text{Tr} \left(\partial_t R_N \mathcal{P}^{-1} (\mathcal{P}^{-1} \mathcal{F})^3 \right) \\
& \sim \int_0^N da_3 96 \frac{g_{4,1}^0}{Z_N} \left(\frac{g_{4,1}^{2,1}}{Z_N} \right)^2 \Theta(a_3) \left((1-\eta) \left(\frac{a_3}{N} \right)^3 + \eta \left(\frac{a_3}{N} \right)^4 \right) \text{Diagram} \\
& = 96 I_3^1 \frac{g_{4,1}^0}{Z_N} \left(\frac{g_{4,1}^{2,1}}{Z_N} \right)^2 \text{Diagram} \tag{B.10}
\end{aligned}$$

The above computation can be straightforwardly carried out for summations over more indices. The resulting threshold integrals are given by

$$\mathcal{I}_1^1 = \frac{1}{3} \eta N^r + \frac{1}{2} N^r (r - \eta), \tag{B.11}$$

$$\mathcal{I}_1^2 = \frac{1}{4} \eta N^{2r} + \frac{1}{3} N^{2r} (r - \eta), \tag{B.12}$$

$$\mathcal{I}_1^3 = \frac{1}{10} \eta N^{3r} + \frac{1}{8} N^{3r} (r - \eta), \tag{B.13}$$

$$\mathcal{I}_2^1 = \frac{1}{4} \eta N^r + \frac{1}{3} N^r (r - \eta), \tag{B.14}$$

$$\mathcal{I}_2^2 = \frac{1}{5} \eta N^{2r} + \frac{1}{4} N^{2r} (r - \eta), \tag{B.15}$$

$$\mathcal{I}_2^3 = \frac{1}{12} \eta N^{3r} + \frac{1}{10} N^{3r} (r - \eta), \tag{B.16}$$

$$\mathcal{I}_3^1 = \frac{1}{5} \eta N^r + \frac{1}{4} N^r (r - \eta), \tag{B.17}$$

$$\mathcal{I}_3^2 = \frac{1}{6} \eta N^{2r} + \frac{1}{5} N^{2r} (r - \eta), \tag{B.18}$$

$$\mathcal{I}_3^3 = \frac{1}{14} \eta N^{3r} + \frac{1}{12} N^{3r} (r - \eta), \tag{B.19}$$

for the real rank-3 tensor model assuming the modified Litim-regulator of Eq. (4.111). Hereby, the lower index counts the order of the $\mathcal{P}^{-1} \mathcal{F}$ expression, while the upper index counts the number of indices over the integration is performed.

C Mathematica for Models

To make progress in the tensor model program for quantum gravity with the FRG, it is necessary to study large truncations in order to make more definite statements about convergence of critical exponents that allow for comparisons with continuum approaches, e.g., with the Asymptotic Safety program. Calculations can be greatly simplified if they are performed numerically. A general algorithm that allows to derive beta functions to all interaction orders has been introduced in Sec. 4. Here, we provide the *Mathematica* code in order to implement the algorithm.

To this end the *xAct*¹ packages *xTensor*, *xPert* and *xTras* are required. To set the stage, it is necessary to make some preliminary definitions on the symmetry of the tensors and the contraction pattern of indices. The command *DefManifold* defines the manifold by taking the dimension of the manifold and the set of indices that will be used canonically as arguments. Moreover, *DefMetric* defines the metric. In tensor models there is of course no physical metric but nonetheless one needs an object that implements the contractions of indices, e.g., by means of delta functions. Of great important is also the specification of the symmetry of the tensor, which is provided by *DefTensor*.

A concrete example of how the initialization of the code could look like would be

$$\begin{aligned} &\mathbf{DefManifold}[\Sigma, d, \{a_i\}]; \\ &\mathbf{DefMetric}[1, g[-a, -b], \text{CD}, \{";", "\nabla"\}, \text{FlatMetric} \rightarrow \text{True}]; \\ &\mathbf{DefTensor}[\phi[-a, -b, -c], \Sigma]; \end{aligned} \tag{C.1}$$

The above example initializes a real rank-3 tensor model and can be straightforwardly rewritten for different tensor models: A symmetric rank-3 tensor model is initialized by having $\mathbf{DefTensor}[\phi[-a, -b, -c], \Sigma, \text{Symmetric}[\{-a, -b, -c\}];$, while a complex rank-3 tensor model can be set-up by introducing, for instance, two rank-3 tensors ϕ_1 and ϕ_2 .

Once the code is initialized, we can introduce the invariants of interaction order four, which as discussed in the section on the general set-up of the algorithm, are the only input needed once the symmetry of the tensor model has been given. For the real rank-3 tensor model with no color symmetry between the couplings, for instance,

¹*xAct* is a family of packages that allows for index manipulations in the *Wolfram Language*.

one will have

$$\begin{aligned}
\text{QI}[1] &= g_{4,2}^2 \phi[-a_1, -b_1, -c_1] \phi[a_1, b_1, c_1] \phi[-a_2, -b_2, -c_2] \phi[a_2, b_2, c_2] // \text{ContractMetric}; \\
\text{QI}[2] &= g_{4,1}^{2,1} \phi[-a_1, -b_1, -c_1] \phi[a_2, b_1, c_1] \phi[-a_2, -b_2, -c_2] \phi[a_1, b_2, c_2] // \text{ContractMetric}; \\
\text{QI}[2] &= g_{4,1}^{2,2} \phi[-a_1, -b_1, -c_1] \phi[a_1, b_2, c_1] \phi[-a_2, -b_2, -c_2] \phi[a_2, b_1, c_2] // \text{ContractMetric}; \\
\text{QI}[3] &= g_{4,1}^{2,2} \phi[-a_1, -b_1, -c_1] \phi[a_1, b_1, c_2] \phi[-a_2, -b_2, -c_2] \phi[a_2, b_2, c_1] // \text{ContractMetric}; \\
\text{QI}[4] &= g_{4,1}^0 \phi[-a_1, -b_1, -c_1] \phi[a_1, b_2, c_2] \phi[-a_2, b_1, -c_2] \phi[a_2, -b_2, c_1] // \text{ContractMetric};
\end{aligned}$$

The next steps consists in implementing a way to compute the two-point function of any invariant. To that end, we introduce a function $\mathbf{TP}[a_1, a_2, a_3, b_1, b_2, b_3]$ which is defined as

$$\mathbf{TP}[a_{1_}, a_{2_}, a_{3_}, b_{1_}, b_{2_}, b_{3_}] := \text{VarD}[\phi[b_1, b_2, b_3]][\#] \& @ \text{VarD}[\phi[a_1, a_2, a_3]][\#] \&.$$

Given that the symmetries of the tensor ϕ have already been specified it is not necessary to additionally take care of this in the definition of the two-point function. The two-point function allows to construct higher-order invariants via the $\mathcal{P}^{-1}\mathcal{F}$ -expansion explained in the main text. The construction of ϕ^6 invariants can be implemented in the following way in *Mathematica*

$$\begin{aligned}
&\text{HexicInvariants} = \\
&(\text{Table}[(\mathbf{TP}[-a_1, -a_2, a_3, -b_1, b_2, b_3] @ \text{QI}[i] // \text{CollectTensors}) * \\
&(\mathbf{TP}[b_1, b_2, b_3, -c_1, -c_2, -c_3] @ \text{QI}[j] // \text{CollectTensors}) * \\
&(\mathbf{TP}[c_1, c_2, c_3, a_1, a_2, a_3] @ \text{QI}[k] // \text{CollectTensors}) // \text{ContractMetric} // \text{ToCanonical} \\
&, \{i, 1, \text{Length}[\text{QI}]\}, \{j, 1, \text{Length}[\text{QI}]\}, \{k, 1, \text{Length}[\text{QI}]\}]; \quad (\text{C.2})
\end{aligned}$$

For practical purposes, it is beneficial to split the computation for all i, j and k into small steps.

D β -functions of the real rank-3 tensor model

We list the explicit forms of the beta functions for the $\mathcal{O}(N)^3$ model. To show the explicit forms, we define the threshold functions, which rely on a parameter r defined in the regulator:

$$\mathcal{I}_1^1 = \frac{1}{3}\eta N^r + \frac{1}{2}N^r(r - \eta), \quad (\text{D.1})$$

$$\mathcal{I}_1^2 = \frac{1}{4}\eta N^{2r} + \frac{1}{3}N^{2r}(r - \eta), \quad (\text{D.2})$$

$$\mathcal{I}_1^3 = \frac{1}{10}\eta N^{3r} + \frac{1}{8}N^{3r}(r - \eta), \quad (\text{D.3})$$

$$\mathcal{I}_2^1 = \frac{1}{4}\eta N^r + \frac{1}{3}N^r(r - \eta), \quad (\text{D.4})$$

$$\mathcal{I}_2^2 = \frac{1}{5}\eta N^{2r} + \frac{1}{4}N^{2r}(r - \eta), \quad (\text{D.5})$$

$$\mathcal{I}_2^3 = \frac{1}{12}\eta N^{3r} + \frac{1}{10}N^{3r}(r - \eta), \quad (\text{D.6})$$

$$\mathcal{I}_3^1 = \frac{1}{5}\eta N^r + \frac{1}{4}N^r(r - \eta), \quad (\text{D.7})$$

$$\mathcal{I}_3^2 = \frac{1}{6}\eta N^{2r} + \frac{1}{5}N^{2r}(r - \eta), \quad (\text{D.8})$$

$$\mathcal{I}_3^3 = \frac{1}{14}\eta N^{3r} + \frac{1}{12}N^{3r}(r - \eta), \quad (\text{D.9})$$

where the lower index denotes the order in the $\mathcal{P}^{-1}\mathcal{F}$ expansion and the upper index refers to the number of indices that are integrated over. The anomalous dimension η is given by

$$\eta = 4\mathcal{I}_1^3 \tilde{g}_{4,2}^2 N^{[g_{4,2}^2]} + 4\mathcal{I}_1^2 (\tilde{g}_{4,1}^{2,1} + \tilde{g}_{4,1}^{2,2} + \tilde{g}_{4,1}^{2,3}) N^{[g_{4,1}^{2,i}]} + 12\mathcal{I}_1^1 \tilde{g}_{4,1}^0 N^{[g_{4,1}^0]} \quad (\text{D.10})$$

The beta function of the quartic cross interaction $\tilde{g}_{4,1}^0$ is

$$\begin{aligned} \tilde{\beta}_{\tilde{g}_{4,1}^0} = & (-[g_{4,1}^0] + 2\eta) \tilde{g}_{4,1}^0 + 16\mathcal{I}_2^1 (\tilde{g}_{4,1}^{2,1} + \tilde{g}_{4,1}^{2,2} + \tilde{g}_{4,1}^{2,3}) \tilde{g}_{4,1}^0 N^{[g_{4,1}^{2,i}]} \\ & - \mathcal{I}_1^2 (\tilde{g}_{6,1}^{1,1} + \tilde{g}_{6,1}^{1,2} + \tilde{g}_{6,1}^{1,3}) N^{[g_{6,1}^{1,i}] - [g_{4,1}^0]} - \mathcal{I}_1^3 \tilde{g}_{6,2}^1 N^{[g_{6,2}^1] - [g_{4,1}^0]} \\ & - 6\mathcal{I}_1^1 \tilde{g}_{6,1}^{0,p} N^{[g_{6,1}^{0,p}] - [g_{4,1}^0]}. \end{aligned} \quad (\text{D.11})$$

The beta function for the coupling $\tilde{g}_{4,1}^{2,i}$ associated to the cyclic melon with preferred color i is

$$\begin{aligned}
\tilde{\beta}_{\tilde{g}_{4,1}^{2,i}} = & (-[g_{4,1}^{2,i}] + 2\eta) \tilde{g}_{4,1}^{2,i} + 8\mathcal{I}_2^1 (\tilde{g}_{4,1}^0)^2 N^{2[g_{4,1}^0] - [g_{4,1}^{2,i}]} + 16\mathcal{I}_2^1 (\tilde{g}_{4,1}^{2,i} \tilde{g}_{4,1}^0) N^{[g_{4,1}^0]} \\
& + 8\mathcal{I}_2^2 (\tilde{g}_{4,1}^{2,i})^2 N^{[g_{4,1}^{2,i}]} - 5\mathcal{I}_1^1 \tilde{g}_{6,1}^{1,i} N^{[g_{6,1}^{1,i}] - [g_{4,1}^{2,i}]} - \mathcal{I}_1^3 \tilde{g}_{6,2}^{3,i} N^{[g_{6,2}^{3,i}] - [g_{4,1}^{2,i}]} \\
& - 3\mathcal{I}_1^2 \tilde{g}_{6,1}^{3,i} N^{[g_{6,1}^{3,i}] - [g_{4,1}^{2,i}]} - 3\mathcal{I}_1^1 \tilde{g}_{6,1}^{0,np} N^{[g_{6,1}^{0,np}] - [g_{4,1}^{2,i}]} \\
& - 2\mathcal{I}_1^2 \tilde{g}_{6,1}^{2,i} N^{[g_{6,1}^{2,i}] - [g_{4,1}^{2,i}]} - \mathcal{I}_1^1 \tilde{g}_{6,1}^{0,p} N^{[g_{6,1}^{0,p}] - [g_{4,1}^{2,i}]} .
\end{aligned} \tag{D.12}$$

The beta function of the coupling $\tilde{g}_{4,2}^2$ related to the disconnected melonic interaction reads

$$\begin{aligned}
\tilde{\beta}_{\tilde{g}_{4,2}^2} = & (-[g_{4,2}^2] + 2\eta) \tilde{g}_{4,2}^2 + 16\mathcal{I}_2^1 (\tilde{g}_{4,1}^{2,1} \tilde{g}_{4,1}^{2,2} + \tilde{g}_{4,1}^{2,1} \tilde{g}_{4,1}^{2,3} + \tilde{g}_{4,1}^{2,2} \tilde{g}_{4,1}^{2,3}) N^{2[g_{4,1}^{2,i}] - [g_{4,2}^2]} \\
& + 48\mathcal{I}_2^1 \tilde{g}_{4,2}^2 \tilde{g}_{4,1}^0 N^{[g_{4,1}^0]} + 16\mathcal{I}_2^2 \tilde{g}_{4,2}^2 (\tilde{g}_{4,1}^{2,1} + \tilde{g}_{4,1}^{2,2} + \tilde{g}_{4,1}^{2,3}) N^{[g_{4,1}^{2,i}]} \\
& + 8\mathcal{I}_2^3 (\tilde{g}_{4,2}^2)^2 N^{[g_{4,2}^2]} - 3\mathcal{I}_1^3 \tilde{g}_{6,3}^3 N^{[g_{6,3}^3] - [g_{4,2}^2]} \\
& - 2\mathcal{I}_1^2 (\tilde{g}_{6,2}^{3,1} + \tilde{g}_{6,2}^{3,2} + \tilde{g}_{6,2}^{3,3}) N^{[g_{6,2}^{3,i}] - [g_{4,2}^2]} - \mathcal{I}_1^1 (\tilde{g}_{6,1}^{2,1} + \tilde{g}_{6,1}^{2,2} + \tilde{g}_{6,1}^{2,3}) N^{[g_{6,1}^{2,i}] - [g_{4,2}^2]} \\
& - 6\mathcal{I}_1^1 \tilde{g}_{6,2}^1 N^{[g_{6,2}^1] - [g_{4,2}^2]} .
\end{aligned} \tag{D.13}$$

The running of the cyclic melons is encapsulated in the following expression

$$\begin{aligned}
\tilde{\beta}_{\tilde{g}_{6,1}^{3,i}} = & (-[g_{6,1}^{3,i}] + 3\eta) \tilde{g}_{6,1}^{3,i} + 8\mathcal{I}_2^1 \tilde{g}_{6,1}^{1,i} \tilde{g}_{4,1}^0 N^{[g_{6,1}^{1,i}] + [g_{4,1}^0] - [g_{6,1}^{3,i}]} \\
& + 32\mathcal{I}_2^1 \tilde{g}_{6,1}^{1,i} \tilde{g}_{4,1}^{2,i} N^{[g_{6,1}^{1,i}] + [g_{4,1}^{2,i}] - [g_{6,1}^{3,i}]} + 24\mathcal{I}_2^2 \tilde{g}_{6,1}^{3,i} \tilde{g}_{4,1}^{2,i} N^{[g_{4,1}^{2,i}]} + 48\mathcal{I}_2^1 \tilde{g}_{6,1}^{3,i} \tilde{g}_{4,1}^0 N^{[g_{4,1}^0]} \\
& - 8\mathcal{I}_2^1 \sum_{j,k}^3 \tilde{g}_{4,1}^{2,i} (\tilde{g}_{6,1}^{2,j} + \tilde{g}_{6,1}^{2,k}) (\delta_{ij} - 1)(\delta_{jk} - 1)(\delta_{ik} - 1) N^{[g_{4,1}^{2,i}] + [g_{6,1}^{2,i}] - [g_{6,1}^{3,i}]} \\
& - 192\mathcal{I}_3^1 (\tilde{g}_{4,1}^{2,i})^2 \tilde{g}_{4,1}^0 N^{2[g_{4,1}^{2,i}] + [g_{4,1}^0] - [g_{6,1}^{3,i}]} - 32\mathcal{I}_3^2 (\tilde{g}_{4,1}^{2,i})^3 N^{3[g_{4,1}^{2,i}] - [g_{6,1}^{3,i}]} .
\end{aligned} \tag{D.14}$$

The ‘‘Cat Diagram’’, i.e. $g_{6,1}^{1,i}$, runs as follows

$$\begin{aligned}
\tilde{\beta}_{\tilde{g}_{6,1}^{1,i}} = & (-[g_{6,1}^{1,i}] + 3\eta) \tilde{g}_{6,1}^{1,i} + 16\mathcal{I}_2^1 \tilde{g}_{6,1}^{1,i} \tilde{g}_{4,1}^0 N^{[g_{4,1}^0]} + 8\mathcal{I}_2^2 \tilde{g}_{6,1}^{1,i} \tilde{g}_{4,1}^{2,i} N^{[g_{4,1}^{2,i}]} \\
& + 24\mathcal{I}_2^1 \tilde{g}_{6,1}^{3,i} \tilde{g}_{4,1}^0 N^{[g_{6,1}^{3,i}] + [g_{4,1}^0] - [g_{6,1}^{1,i}]} \\
& - 8\mathcal{I}_2^1 \sum_{j,k}^3 (\tilde{g}_{6,1}^{2,j} + \tilde{g}_{6,1}^{2,k}) \tilde{g}_{4,1}^0 (\delta_{ij} - 1)(\delta_{jk} - 1)(\delta_{ik} - 1) N^{[g_{6,1}^{2,i}] + [g_{4,1}^0] - [g_{6,1}^{1,i}]} \\
& + 16\mathcal{I}_2^1 \tilde{g}_{6,1}^{0,p} \tilde{g}_{4,1}^0 N^{[g_{6,1}^{0,p}] + [g_{4,1}^0] - [g_{6,1}^{1,i}]} \\
& + 32\mathcal{I}_2^1 \tilde{g}_{6,1}^{0,p} \tilde{g}_{4,1}^{2,i} N^{[g_{6,1}^{0,p}] + [g_{4,1}^{2,i}] - [g_{6,1}^{1,i}]} \\
& + 96\mathcal{I}_3^1 \sum_{j,k}^3 \tilde{g}_{4,1}^{2,i} (\tilde{g}_{4,1}^{2,j} + \tilde{g}_{4,1}^{2,k}) \tilde{g}_{4,1}^0 (\delta_{ij} - 1)(\delta_{jk} - 1)(\delta_{ik} - 1) N^{2[g_{4,1}^{2,i}] + [g_{4,1}^0] - [g_{6,1}^{1,i}]} \\
& - 96\mathcal{I}_3^1 (\tilde{g}_{4,1}^{2,i})^2 \tilde{g}_{4,1}^0 N^{2[g_{4,1}^{2,i}] + [g_{4,1}^0] - [g_{6,1}^{1,i}]} .
\end{aligned} \tag{D.15}$$

The coupling $\tilde{g}_{6,2}^1$ exhibits the following scale-dependence

$$\begin{aligned}
\tilde{\beta}_{\tilde{g}_{6,2}^1} &= (-[g_{6,2}^1] + 3\eta) \tilde{g}_{6,2}^1 + 16 \mathcal{I}_2^1 \tilde{g}_{4,1}^0 (\tilde{g}_{6,2}^{3,1} + \tilde{g}_{6,2}^{3,2} + \tilde{g}_{6,2}^{3,3}) N^{[g_{4,1}^0] + [g_{6,2}^{3,i}] - [g_{6,2}^1]} \\
&\quad + 48 \mathcal{I}_2^1 \tilde{g}_{6,1}^{0,p} \tilde{g}_{4,2}^2 N^{[g_{6,1}^{0,p}] + [g_{4,2}^2] - [g_{6,2}^1]} \\
&\quad - 4 \mathcal{I}_2^1 \sum_{i,j,k}^3 \tilde{g}_{6,1}^{1,i} \left(\tilde{g}_{4,1}^{2,j} + \tilde{g}_{4,1}^{2,k} \right) (\delta_{ij} - 1)(\delta_{jk} - 1)(\delta_{ik} - 1) N^{[g_{6,1}^{1,i}] + [g_{4,1}^{2,i}] - [g_{6,2}^1]} \\
&\quad + 8 \mathcal{I}_2^3 \tilde{g}_{6,2}^1 \tilde{g}_{4,2}^2 N^{[g_{4,2}^2]} + 24 \mathcal{I}_2^1 \tilde{g}_{6,2}^1 \tilde{g}_{4,1}^0 N^{[g_{4,1}^0]} \\
&\quad + 8 \mathcal{I}_2^2 (\tilde{g}_{6,1}^{1,1} + \tilde{g}_{6,1}^{1,2} + \tilde{g}_{6,1}^{1,3}) \tilde{g}_{4,2}^2 N^{[g_{6,1}^{1,i}] + [g_{4,2}^2] - [g_{6,2}^1]} \\
&\quad + 16 \mathcal{I}_2^2 \tilde{g}_{6,2}^1 (\tilde{g}_{4,1}^{2,1} + \tilde{g}_{4,1}^{2,2} + \tilde{g}_{4,1}^{2,3}) N^{[g_{4,1}^{2,i}]} \tag{D.16}
\end{aligned}$$

The running of the hexic cross diagram, $\tilde{g}_{6,1}^{0,np}$ is given by

$$\begin{aligned}
\tilde{\beta}_{\tilde{g}_{6,1}^{0,np}} &= (-[\tilde{g}_{6,1}^{0,np}] + 3\eta) \tilde{g}_{6,1}^{0,np} \\
&\quad + 8 \mathcal{I}_2^1 [\tilde{g}_{6,1}^{1,1} (\tilde{g}_{4,1}^{2,2} + \tilde{g}_{4,1}^{2,3}) + \tilde{g}_{6,1}^{1,2} (\tilde{g}_{4,1}^{2,1} + \tilde{g}_{4,1}^{2,3}) + \tilde{g}_{6,1}^{1,3} (\tilde{g}_{4,1}^{2,1} + \tilde{g}_{4,1}^{2,2})] N^{[g_{6,1}^{1,i}] + [g_{4,1}^{2,i}] - [g_{6,1}^{0,np}]} \\
&\quad + 24 \mathcal{I}_2^1 \tilde{g}_{6,1}^{0,np} (\tilde{g}_{4,1}^{2,1} + \tilde{g}_{4,1}^{2,2} + \tilde{g}_{4,1}^{2,3}) N^{[g_{4,1}^{2,i}]} \\
&\quad - 96 \mathcal{I}_3^1 (\tilde{g}_{4,1}^0)^2 (\tilde{g}_{4,1}^{2,1} + \tilde{g}_{4,1}^{2,2} + \tilde{g}_{4,1}^{2,3}) N^{2[g_{4,1}^0] + [g_{4,1}^{2,i}] - [g_{6,1}^{0,np}]} \\
&\quad - 96 \mathcal{I}_3^1 (\tilde{g}_{4,1}^0)^3 N^{3[g_{4,1}^0] - [g_{6,1}^{0,np}]} \tag{D.17}
\end{aligned}$$

The beta function associated to the triple disconnected melon is given by

$$\begin{aligned}
\tilde{\beta}_{\tilde{g}_{6,3}^3} &= (-[g_{6,3}^3] + 3\eta) \tilde{g}_{6,3}^3 + 24 \mathcal{I}_2^2 \tilde{g}_{6,3}^3 (\tilde{g}_{4,1}^{2,1} + \tilde{g}_{4,1}^{2,2} + \tilde{g}_{4,1}^{2,3}) N^{[g_{4,1}^{2,i}]} \\
&\quad + 72 \mathcal{I}_2^1 \tilde{g}_{6,3}^3 \tilde{g}_{4,1}^0 N^{[g_{4,1}^0]} + 24 \mathcal{I}_2^3 \tilde{g}_{6,3}^3 \tilde{g}_{4,2}^2 N^{[g_{4,2}^2]} \\
&\quad + 16 \mathcal{I}_2^2 (\tilde{g}_{6,2}^{3,1} + \tilde{g}_{6,2}^{3,2} + \tilde{g}_{6,2}^{3,3}) \tilde{g}_{4,2}^2 N^{[g_{6,2}^{3,i}] + [g_{4,2}^2] - [g_{6,3}^3]} \\
&\quad + 48 \mathcal{I}_2^1 \tilde{g}_{6,2}^1 \tilde{g}_{4,2}^2 N^{[g_{6,2}^1] + [g_{4,2}^2] - [g_{6,3}^3]} \\
&\quad + 8 \mathcal{I}_2^1 (\tilde{g}_{6,1}^{2,1} + \tilde{g}_{6,1}^{2,2} + \tilde{g}_{6,1}^{2,3}) \tilde{g}_{4,2}^2 N^{[g_{6,1}^{2,i}] + [g_{4,2}^2] - [g_{6,3}^3]} \\
&\quad - 192 \mathcal{I}_3^1 \tilde{g}_{4,2}^2 (\tilde{g}_{4,1}^{2,1} \tilde{g}_{4,1}^{2,2} + \tilde{g}_{4,1}^{2,1} \tilde{g}_{4,1}^{2,3} + \tilde{g}_{4,1}^{2,2} \tilde{g}_{4,1}^{2,3}) N^{2[g_{4,1}^{2,i}] + [g_{4,2}^2] - [g_{6,3}^3]} \\
&\quad - 96 \mathcal{I}_3^2 (\tilde{g}_{4,1}^{2,1} + \tilde{g}_{4,1}^{2,2} + \tilde{g}_{4,1}^{2,3}) (\tilde{g}_{4,2}^2)^2 N^{2[g_{4,2}^2] + [g_{4,1}^{2,i}] - [g_{6,3}^3]} \\
&\quad - 288 \mathcal{I}_3^1 \tilde{g}_{4,1}^0 (\tilde{g}_{4,2}^2)^2 N^{[g_{4,1}^0] + 2[g_{4,2}^2] - [g_{6,3}^3]} - 32 \mathcal{I}_3^3 (\tilde{g}_{4,2}^2)^3 N^{3[g_{4,2}^2] - [g_{6,3}^3]}. \tag{D.18}
\end{aligned}$$

The anti-cyclic melons run as follows

$$\begin{aligned}
\tilde{\beta}_{\tilde{g}_{6,1}^{2,i}} &= (-[g_{6,1}^{2,i}] + 3\eta) \tilde{g}_{6,1}^{2,i} \\
&+ 96 \mathcal{I}_3^1 \sum_{j,k}^3 \tilde{g}_{4,1}^{2,j} \tilde{g}_{4,1}^{2,k} \tilde{g}_{4,1}^0 (\delta_{ij} - 1)(\delta_{jk} - 1)(\delta_{ik} - 1) N^{2[g_{4,1}^{2,i}] + [g_{4,1}^0] - [g_{6,1}^{2,i}]} \\
&+ 48 \mathcal{I}_3^1 \sum_{j,k}^3 \left(\tilde{g}_{4,1}^{2,j} + \tilde{g}_{4,1}^{2,k} \right) (\tilde{g}_{4,1}^0)^2 (\delta_{ij} - 1)(\delta_{jk} - 1)(\delta_{ik} - 1) N^{2[g_{4,1}^0] + [g_{4,1}^{2,i}] - [g_{6,1}^{2,i}]} \\
&+ 96 \mathcal{I}_3^1 \sum_{j,k}^3 (\tilde{g}_{4,1}^{2,j})^2 \tilde{g}_{4,1}^{2,k} (\delta_{ij} - 1)(\delta_{jk} - 1)(\delta_{ik} - 1) N^{3[g_{4,1}^{2,i}] - [g_{6,1}^{2,i}]} \\
&- 16 \mathcal{I}_2^1 \sum_{j,k}^3 \tilde{g}_{6,1}^{1,j} \tilde{g}_{4,1}^{2,k} (\delta_{ij} - 1)(\delta_{jk} - 1)(\delta_{ik} - 1) N^{[g_{6,1}^{1,i}] + [g_{4,1}^{2,i}] - [g_{6,1}^{2,i}]} \\
&- 8 \mathcal{I}_2^1 \sum_{j,k}^3 \left(\tilde{g}_{6,1}^{1,j} + \tilde{g}_{6,1}^{1,k} \right) \tilde{g}_{4,1}^0 (\delta_{ij} - 1)(\delta_{jk} - 1)(\delta_{ik} - 1) N^{[g_{6,1}^{1,i}] + [g_{4,1}^0] - [g_{6,1}^{2,i}]} \\
&- 24 \mathcal{I}_2^1 \sum_{j,k}^3 \tilde{g}_{6,1}^{3,j} \tilde{g}_{4,1}^{2,k} (\delta_{ij} - 1)(\delta_{jk} - 1)(\delta_{ik} - 1) N^{[g_{6,1}^{3,i}] + [g_{4,1}^{2,i}] - [g_{6,1}^{2,i}]} \\
&- 12 \mathcal{I}_2^1 \sum_{j,k}^3 \left(\tilde{g}_{4,1}^{2,j} + \tilde{g}_{4,1}^{2,k} \right) \tilde{g}_{6,1}^{0,np} (\delta_{ij} - 1)(\delta_{jk} - 1)(\delta_{ik} - 1) N^{[g_{4,1}^{2,i}] + [g_{6,1}^{0,np}] - [g_{6,1}^{2,i}]} \\
&- 4 \mathcal{I}_2^1 \sum_{j,k}^3 \left(\tilde{g}_{4,1}^{2,j} + \tilde{g}_{4,1}^{2,k} \right) \tilde{g}_{6,1}^{0,p} (\delta_{ij} - 1)(\delta_{jk} - 1)(\delta_{ik} - 1) N^{[g_{6,1}^{0,p}] + [g_{4,1}^{2,i}] - [g_{6,1}^{2,i}]} \\
&- 4 \mathcal{I}_2^2 \sum_{j,k}^3 \left(\tilde{g}_{4,1}^{2,j} + \tilde{g}_{4,1}^{2,k} \right) \tilde{g}_{6,1}^{2,i} (\delta_{ij} - 1)(\delta_{jk} - 1)(\delta_{ik} - 1) N^{[g_{4,1}^{2,i}]} \\
&+ 40 \mathcal{I}_2^1 \tilde{g}_{6,1}^{2,i} \tilde{g}_{4,1}^0 N^{[g_{4,1}^0]} - 192 \mathcal{I}_3^1 \tilde{g}_{4,1}^{2,1} \tilde{g}_{4,1}^{2,2} \tilde{g}_{4,1}^{2,3} N^{3[g_{4,1}^{2,i}] - [g_{6,1}^{2,i}]} \tag{D.19}
\end{aligned}$$

Finally, $\tilde{g}_{6,2}^{3,i}$ exhibits the following running

$$\begin{aligned}
\tilde{\beta}_{\tilde{g}_{6,2}^{3,i}} &= (-[g_{6,2}^{3,i}] + 3\eta) \tilde{g}_{6,2}^{3,i} + 24 \mathcal{I}_2^2 \tilde{g}_{4,1}^{2,i} \tilde{g}_{6,2}^{3,i} N^{[g_{4,1}^{2,i}]} + 56 \mathcal{I}_2^1 \tilde{g}_{6,2}^{3,i} \tilde{g}_{4,1}^0 N^{[g_{4,1}^0]} \\
&\quad - 4 \mathcal{I}_2^2 \sum_{j,k}^3 \tilde{g}_{6,2}^{3,i} \left(\tilde{g}_{4,1}^{2,j} + \tilde{g}_{4,1}^{2,k} \right) (\delta_{ij} - 1)(\delta_{jk} - 1)(\delta_{ik} - 1) N^{[g_{4,1}^{2,i}]} \\
&\quad + 8 \mathcal{I}_2^3 \tilde{g}_{6,2}^{3,i} \tilde{g}_{4,2}^2 N^{[g_{4,2}^2]} + 40 \mathcal{I}_2^1 \tilde{g}_{6,1}^{1,i} \tilde{g}_{4,2}^2 N^{[g_{6,1}^{1,i}] + [g_{4,2}^2] - [g_{6,2}^{3,i}]} \\
&\quad - 12 \mathcal{I}_2^1 \sum_{j,k}^3 \tilde{g}_{6,1}^{3,i} \left(\tilde{g}_{4,1}^{2,j} + \tilde{g}_{4,1}^{2,k} \right) (\delta_{ij} - 1)(\delta_{jk} - 1)(\delta_{ik} - 1) N^{[g_{6,1}^{3,i}] + [g_{4,1}^{2,i}] - [g_{6,2}^{3,i}]} \\
&\quad + 24 \mathcal{I}_2^2 \tilde{g}_{6,1}^{3,i} \tilde{g}_{4,2}^2 N^{[g_{6,1}^{3,i}] + [g_{4,2}^2] - [g_{6,2}^{3,i}]} \\
&\quad - 4 \mathcal{I}_2^2 \sum_{j,k}^3 \tilde{g}_{4,2}^2 \left(\tilde{g}_{6,1}^{2,j} + \tilde{g}_{6,1}^{2,k} \right) (\delta_{ij} - 1)(\delta_{jk} - 1)(\delta_{ik} - 1) N^{[g_{4,2}^2] + [g_{6,1}^{2,i}] - [g_{6,2}^{3,i}]} \\
&\quad + 16 \mathcal{I}_2^1 \tilde{g}_{6,2}^1 \tilde{g}_{4,1}^0 N^{[g_{6,2}^1] + [g_{4,1}^0] - [g_{6,2}^{3,i}]} \\
&\quad - 8 \mathcal{I}_2^1 \sum_j^3 \tilde{g}_{6,1}^{2,j} \tilde{g}_{4,1}^{2,j} (\delta_{ij} - 1) N^{[g_{6,1}^{2,i}] + [g_{4,1}^{2,i}] - [g_{6,2}^{3,i}]} \\
&\quad - 8 \mathcal{I}_2^1 \sum_{j,k}^3 \tilde{g}_{4,1}^{2,i} \left(\tilde{g}_{6,1}^{2,j} + \tilde{g}_{6,1}^{2,k} \right) (\delta_{ij} - 1)(\delta_{jk} - 1)(\delta_{ik} - 1) N^{[g_{4,1}^{2,i}] + [g_{6,1}^{2,i}] - [g_{6,2}^{3,i}]} \\
&\quad + 48 \mathcal{I}_3^1 \sum_{j,k}^3 \left(\tilde{g}_{4,1}^{2,i} \right)^2 \left(\tilde{g}_{4,1}^{2,j} + \tilde{g}_{4,1}^{2,k} \right) (\delta_{ij} - 1)(\delta_{jk} - 1)(\delta_{ik} - 1) N^{3[g_{4,1}^{2,i}] - [g_{6,2}^{3,i}]} \\
&\quad + 32 \mathcal{I}_2^1 \tilde{g}_{6,2}^1 \tilde{g}_{4,1}^{2,i} N^{[g_{6,2}^1] + [g_{4,1}^{2,i}] - [g_{6,2}^{3,i}]} + 24 \mathcal{I}_2^1 \tilde{g}_{6,1}^{0,np} \tilde{g}_{4,2}^2 N^{[g_{6,1}^{0,np}] + [g_{4,2}^2] - [g_{6,2}^{3,i}]} \\
&\quad - 96 \mathcal{I}_3^2 \left(\tilde{g}_{4,1}^{2,i} \right)^2 \tilde{g}_{4,2}^2 N^{2[g_{4,1}^{2,i}] + [g_{4,2}^2] - [g_{6,2}^{3,i}]} - 96 \mathcal{I}_3^1 \left(\tilde{g}_{4,1}^0 \right)^2 \tilde{g}_{4,2}^2 N^{2[g_{4,1}^0] + [g_{4,2}^2] - [g_{6,2}^{3,i}]} \\
&\quad + 8 \mathcal{I}_2^1 \tilde{g}_{6,1}^{0,p} \tilde{g}_{4,2}^2 N^{[g_{6,1}^{0,p}] + [g_{4,2}^2] - [g_{6,2}^{3,i}]} \tag{D.20}
\end{aligned}$$

The planar diagram with no sub-melons beta function

$$\begin{aligned}
\tilde{\beta}_{\tilde{g}_{6,1}^{0,p}} &= (-[g_{6,1}^{0,p}] + 3\eta) \tilde{g}_{6,1}^{0,p} + 72 \mathcal{I}_2^1 \tilde{g}_{6,1}^{0,np} \tilde{g}_{4,1}^0 N^{[g_{4,1}^0] + [g_{6,1}^{0,np}] - [g_{6,1}^{0,p}]} + 24 \mathcal{I}_2^1 \tilde{g}_{6,1}^{0,p} \tilde{g}_{4,1}^0 N^{[g_{4,1}^0]} \\
&\quad + 16 \mathcal{I}_2^1 \tilde{g}_{4,1}^0 \left(\tilde{g}_{6,1}^{1,1} + \tilde{g}_{6,1}^{1,2} + \tilde{g}_{6,1}^{1,3} \right) N^{[g_{4,1}^0] + [g_{6,1}^{1,i}] - [g_{6,1}^{0,p}]} \\
&\quad + 24 \mathcal{I}_2^1 \tilde{g}_{6,1}^{0,p} \left(\tilde{g}_{4,1}^{2,1} + \tilde{g}_{4,1}^{2,2} + \tilde{g}_{4,1}^{2,3} \right) N^{[g_{4,1}^{2,i}]} \tag{D.21}
\end{aligned}$$

E Bubble Nucleation

In the following we will discuss the process of bubble nucleation in more detail. Already from an intuitive point of view it is clear that there are two competing factors determining the nucleation and growth of bubbles: On the one hand the nucleation rate of these bubbles driving the phase transition and on the other hand the expansion of the universe.

In the following we assume a potential with two minima, one local one and one global one. We will discuss the process of bubble nucleation in an analytical way. This requires a set of simplifications but will be useful in order to set up the formalism to discuss more realistic scenarios. In particular we will assume that the phase transition happens very fast.

In the path integral formalism one writes

$$Z = \int d\pi d\phi e^{-\beta H} \quad (\text{E.1})$$

where the Hamiltonian H reads

$$H = \int d^3x \left(\frac{1}{2}\pi^2 + \frac{1}{2}(\vec{\nabla}\phi)^2 + V_T(\phi) \right), \quad (\text{E.2})$$

with π denoting the conjugate momentum of the field ϕ . From the path-integral one can infer the transition rate to tunnel from the false to the true vacuum. At finite temperature T it is possible to define the transition rate by considering a Boltzmann distribution of particles on the left side of the barrier where the false vacuum is located. One can then relate Γ/V with the probability current per unit volume through the barrier as follows

$$\frac{\Gamma}{V} = \frac{1}{Z} \int d\pi d\phi (2\pi\hbar)^{-1} \left(\exp(-\beta(\frac{1}{2}\pi^2 + V(\phi))) \right) \delta(\phi - \phi_m) p \theta(p), \quad (\text{E.3})$$

where the step function forbids particles coming from the right, that is there is only flux towards increasing field values, while the delta function selects the saddle point at the barrier as we are ultimately interested in computing the probability of finding a particle on top of the barrier¹. A saddle point approximation yields the nucleation rate per unit volume (See some review for the details)

$$\frac{\Gamma}{V} \sim T^4 \left(\frac{S_3}{2\pi T} \right)^{3/2} \exp(-S_3/T), \quad (\text{E.4})$$

¹The non-trivial saddle point is also referred to as instanton.

where S_3 denotes the three dimensional Euclidean action, also known as the instanton action due to the fact that the dominant contribution to Γ/V comes from a non-trivial saddle point solution. The dimensional reduction results as a consequence of the fact that at finite temperature the Euclidean time, given by $\beta = 1/T$, is no longer a relevant scale and the system is dimensionally reduced: At low temperatures $T \rightarrow 0$ such that $\beta = 1/T \rightarrow \infty$ and β can essentially be treated like an additional spatial direction. At higher temperatures, β decreases and the four-volume is compressed until a point is reached where the solutions to the equation of motion of ϕ no longer respect the four-dimensional rotational symmetry featured at low temperatures but a three-dimensional rotational symmetry. In that case the dynamics of ϕ becomes independent of T and one may rewrite the Euclidean action

$$S_E[\phi] = \beta \int_x \mathcal{L}_E \equiv \beta S_{3d}[\phi], \quad (\text{E.5})$$

where the integration over the euclidean time could be easily performed yielding the factor β .

The 3d Euclidean action is defined as

$$S_{3d} = 4\pi \int_0^\infty dr r^2 \left(\frac{1}{2} \left(\frac{d\phi}{dr} \right)^2 + V(\phi(r)) \right), \quad (\text{E.6})$$

where r denotes the radial coordinate given that we assumed spherical field configurations as they minimize S_3 . The spherical symmetry suggests to refer to such field configurations as bubbles. At the stationary point, they satisfy the following equation of motion

$$\frac{d^2\phi}{dr^2} + \frac{2}{r} \frac{d\phi}{dr} = \frac{dV}{d\phi}, \quad (\text{E.7})$$

with the boundary conditions

$$\left. \frac{d\phi}{dr} \right|_{r=0} = 0 \quad \text{and} \quad \lim_{r \rightarrow \infty} \phi(r) = 0, \quad (\text{E.8})$$

where the last condition implies that the metastable minimum sits at $\phi = 0$. The above equation admits an intuitive interpretation if we assume for a moment that $r \rightarrow t$, $\phi \rightarrow x$ and $V \rightarrow -U$. In that case one is led to study a well known classical problem of a particle in a valley with a friction term. The idea is that the particle starts at $t = 0$ near the top of the upper hill and rolls towards the top of the other, lower hill. Due to the friction term the particle has to be placed at $t = 0$ somewhere above the hill that it is rolling towards. Back to the problem of the decay of a metastable vacuum due to thermal fluctuations, this means conversely that the true vacuum has to be lower than the metastable one, which in turn implies that the universe will not transition at the critical temperature T_c , where both minima are

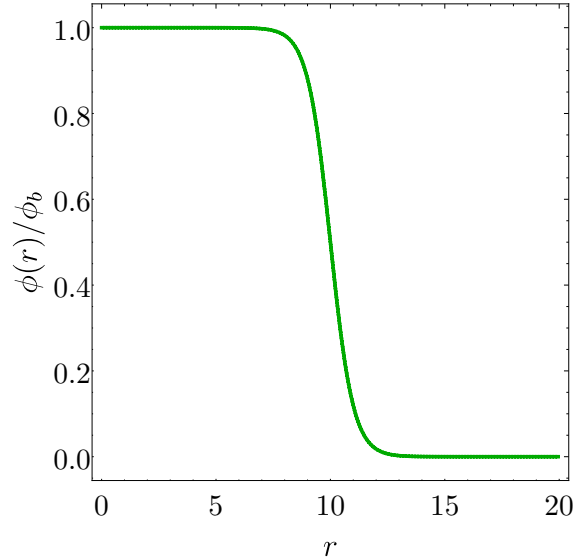


Figure E.1: Profile of the critical bubble, characterized by Eq. (E.10) using $R_c = 10$ and $\ell_w = 1$. For values $r < R_c$, the bubble $\phi(r) = \phi_b$, while for larger values, $\phi(r)$, motivating to refer to these configurations as bubbles.

degenerate but will first supercool to some lower temperature T_n before transitioning to the true vacuum. The equation of motion Eq. (E.7) admits the trivial solution $\phi = 0$. In order to determine the non-trivial instanton solution one usually employs the so-called shooting method ² is sometimes also referred to as the critical bubble. Let us assume in the following a quartic potential such as the one given by the high-temperature expansion of the Higgs-potential in Eq. ???. Such a potential admits a non-trivial analytical solution for the equation of motion of the field ϕ . To see this it is convenient to rescale the potential in the following form

$$V(\phi) = \frac{\lambda}{4} \phi^2 (\phi - \phi_b)^2. \quad (\text{E.9})$$

for which the Eq. E.7 admits the following analytical solution

$$\phi = \frac{\phi_b}{2} \left(1 - \tanh \left(\frac{r - R_c(T)}{\ell_w} \right) \right), \quad (\text{E.10})$$

where the radius of the critical bubble, R_c , carries the temperature dependence of ϕ and is defined as the radius of the bubble that extremizes S_3 , and $\ell_w = 1/M(T_c)$. Indeed, assuming the so-called thin-wall approximation, where $R_c \gg \ell_w$, it is possible to check that for $r < R_c$, $\phi \approx \phi_b$, while for $r > R_c$, $\phi \rightarrow 0$. Fig. E.1 shows a typical behaviour of $\phi(r)$. Let us stress that the above scenario is over-simplified. In particular, we have neglected the expansion of the universe in order to determine the

²Alternatively, the non-trivial solution of Eq. (E.7).

dynamics of ϕ . This corresponds to the assumption that the duration of the phase transition is much shorter than a Hubble time H_n^{-1} , where the Hubble parameter captures the expansion of the universe. In simple words, the phase transition is over before the universe has had significant time to expand.³ For more realistic scenarios one has to employ the so-called shooting method in order to solve the instanton equation of motion Eq. (E.7).

³For slow phase transitions where the expansion of the universe is relevant, we can already expect that the expansion of the universe will further slow down the phase transition.

F Hydrodynamics of expanding bubbles for fast PTs

A first-order phase transition proceeds through the process of bubble nucleation. Here, we explain how bubbles nucleate and expand in a plasma of particles.

We expect bubbles of the broken phase to grow as this phase is energetically favored and we therefore naively expect that at some temperature T_n the universe should be covered by bubbles of the true phase for the phase transition to finalize. Ultimately, we will therefore be interested in determining the fraction of the universe covered by bubbles of the true phase at a given point in time. Crucially, this will rely not only on the rate of bubble nucleation but also on their growth. This section will therefore be devoted to the growth of bubbles taking into account interactions with Standard Model particles. Before jumping into the details let us first think about the concepts that might be relevant to discuss such dynamics. As a reminder, to simplify things, we are for now focussing on fast phase transition, where the expansion of the universe can be neglected. In order for a bubble to expand, the pressure exerted on the interior of the bubble has to exceed the pressure exerted on the exterior of that bubble. The difference in pressure is caused by the fact that the stable phase "carried" by the bubbles is energetically favored and one can therefore expect that this will cause the bubble to grow in order to complete the phase transition. Indeed, we can approximate the total pressure by

$$p = \frac{\pi^2}{90} g_{\text{eff}} T^4 - V_T(\phi^4). \quad (\text{F.1})$$

As expected, we have two contributions, one due to the relativistic plasma of particles which is modeled as radiation and the other one due to the potential. We also see that in order for the bubble to expand, the potential value at the broken phase $V(\phi_b)$ has to be smaller than the one at the metastable phase $V(\phi = 0)$, as expected. The effective number of relativistic degrees of freedom is determined as

$$g_{\text{eff}} = \sum_{i=\text{boson}} g_i \left(\frac{T_i}{T} \right)^4 + \frac{7}{8} \sum_{i=\text{fermion}} g_i \left(\frac{T_i}{T} \right)^4, \quad (\text{F.2})$$

where g_i and T_i are the degrees of freedom and the temperature of the particle i , respectively. Assuming that the full energy-momentum tensor of the scalar field ϕ driving the phase transition and the plasma is conserved one can derive

$$\square\phi + V'_T(\phi) = -\eta_T(\phi) u^\mu \partial_\mu \phi, \quad (\text{F.3})$$

which describes the interaction of ϕ with a plasma of Standard Model particles, which is assumed to be initially in equilibrium and Boltzmann distributed, before bubbles start nucleating and growing. The above equation of motion resembles the standard Klein-Gordon equation with a friction term $\eta_T(\phi)u^\mu\partial_\mu\phi$ caused by the plasma of particles that increases with the velocity of the bubble wall. Initially the bubble expands in an accelerated manner until an equilibrium is reached between the expanding bubble wall and the plasma such that the wall keeps growing in a steady-state at a constant terminal velocity in the so-called *non-runaway case*. Alternatively, it is also possible that the bubble runs away and not reach a constant terminal velocity. This possibility is known as *run-away* scenario. Hereby, $\eta_T = \eta dm(\phi)^2/d\phi$, where η is some proportionality factor which might depend on the field value ϕ , the temperature T and the fluid γ factor, measures the departure from equilibrium of the Standard Model plasma due to its interaction with the bubbles. There are two common choices for η_T employed in numerical simulations, $\eta_T \approx \text{const.}$ [324] and $\eta_T \approx \hat{\eta}\phi^2/T$, where $\hat{\eta}$ is a dimensionless constant. Moreover, u^μ denotes the four-velocity which in the rest frame of the universe and assuming the bubbles to be macroscopic objects such that their walls can be approximated to be planar is given by

$$u^\mu = \gamma_w(1, 0, 0, -v_w), \quad (\text{F.4})$$

where additionally we assumed the wall to be moving in the z -direction at constant speed. The equation of motion Eq. (F.3) then takes the following form

$$-\partial_z^2\phi(t, z) - V_T'(\phi) = -\eta_T(\phi)\gamma_w v_w \partial_z\phi. \quad (\text{F.5})$$

In order to determine the fraction of the universe that is covered by bubbles, we are, as already mentioned, not only interested in the nucleation rate of an individual bubble but also in their size. The size will necessarily depend on the wall speed, i.e. the speed at which the radius of the bubble is growing. Concretely, assuming perfect spherical symmetry the volume of an individual bubble at time t nucleated at time t' is given by

$$\mathcal{V}(t - t') = \frac{4\pi}{3}v_w^3(t - t')^3, \quad (\text{F.6})$$

where the wall speed v_w is set by Eq. (F.5). Let us stress again that we are assuming a fast phase transition, such that the scale factor of the universe remains roughly constant. Our objective is to solve Eq. (F.5) in order to determine the wall speed v_w . The above differential equation can be rewritten by multiplying both sides with $\partial_z\phi$ and integrating over z such that

$$\int dz \left(\frac{1}{2}\partial_z(\partial_z\phi)^2 - \frac{dV_T}{d\phi}\partial_z\phi \right) = \int dz \eta_T(\phi)\gamma_w v_w (\partial_z\phi)^2. \quad (\text{F.7})$$

Performing the integral over z yields

$$V_T(z = +\infty) - V_T(z = -\infty) \equiv \Delta V_T \approx \gamma_w v_w \int dz \eta_T(\phi)(\partial_z\phi)^2, \quad (\text{F.8})$$

where we have crucially assumed that the temperature across the wall is constant, i.e. there is no z -dependence on the temperature. This assumption, which is valid for weak phase transitions, allows us to recast $dV_T(\phi)/d\phi\partial_z\phi$ as $dV_T(\phi)/dz$. An implicit dependence of the potential on z via the temperature T would have led to an additional term $(dV_T(\phi)/dT)\partial_z T$ that one has to consider. Note that the condition that the temperature remains approximately constant across the wall is a necessary condition for the wall speed to be constant. The boundaries at $z = \infty$ and $z = -\infty$ correspond to the thin-wall approximation. In order to determine v_w to compute the size of a bubble to finally access the fraction of the universe in the stable phase one has to solve Eq. (F.8), where one assumes that the profile of ϕ is given by solving the critical bubble equation Eq. (E.7). Strictly, speaking one would have to solve the complete set of coupled differential equations that one can derive from the energy-momentum tensor for the fluid-field system. This is, however, very challenging in practice [325, 326]. The fractional volume of the universe in the stable phase at time $t' + dt'$ is given by the number of bubbles nucleated in a time-interval $[t', t' + dt']$ times the volume of a bubble nucleated at time t' . One can also think of the fractional volume as the probability $P(t)$ for a point in space to remain in the false vacuum. As the universe is large the probability is an accurate description for the actual volume of the universe in the metastable phase. We therefore have for the fractional volume of the universe in the metastable phase

$$h(t) = 1 - \int_{t_c}^t dt' \frac{4\pi}{3} v_w^3 (t - t')^3 \frac{\Gamma(t')}{\mathcal{V}}, \quad (\text{F.9})$$

when no overlaps between bubbles are taken into account. For the more complicated case where overlaps are taken into account one finds

$$h(t) = \exp\left(-\int_{t_c}^t dt' \frac{4\pi}{3} v_w^3 (t - t')^3 \frac{\Gamma(t')}{\mathcal{V}}\right). \quad (\text{F.10})$$

At early times one can Taylor expand the exponential in order to arrive at Eq. (F.9), which is what one would expect as bubbles have not yet had sufficient time to grow and collide with each other. Furthermore, in the late-time limit $t \rightarrow \infty$, $h(t) \rightarrow 0$, which indicates that the universe has fully transitioned to its true vacuum. To compute $h(t)$ one would need to solve v_w from the field-fluid dynamics and insert Eq. (E.4). In practice, however, v_w is assumed to be an additional input parameter that needs to be fixed by hand. The above integral can be solved using a steepest descent method. Physically, this means that $h(t)$ changes so rapidly that only values of $S(t') = S_3(t')/T(t')$ near $t' = t$ contribute such that we may expand $S(t')$ in powers of $t - t'$. Assuming further that the time evolution of the nucleation rate is dominated by the exponential we may then write

$$\Gamma(t) = \Gamma_N \exp(-S(t_N) - S'(t_H)(t - t_N)), \quad (\text{F.11})$$

where t_N is the nucleation time and is defined as the instant in time where one bubble is nucleated per Hubble horizon, i.e.

$$\Gamma_N = H^4 \quad (\text{F.12})$$

and

$$e^{-S(t_N)} = 1. \quad (\text{F.13})$$

One can think of the nucleation time as the onset of the phase transition ¹. Another relevant time, which sets the end of the phase transition, is the time at which

$$h(t_f) = \frac{1}{e}. \quad (\text{F.14})$$

This means that at this reference time roughly 34% of the universe is still in the metastable phase. Using t_f as a reference time we can write the fractional volume in the metastable phase as

$$h(t) = \exp(e^{\beta(t-t_f)}), \quad (\text{F.15})$$

where we introduced the phase transition rate parameter β defined as

$$\beta = -\left. \frac{dS(t)}{dt} \right|_{t=t_f}. \quad (\text{F.16})$$

The fractional volume of the universe in the metastable phase decreases as the exponential of an exponential and therefore the reference time t_f is a valid time to mark the end of the phase transition. The reference time t_f also admits a different interpretation besides being the time at which 66% of the universe is covered by bubbles: It also marks the time when the rate of the change of $h(t)$ has a maximum that is

$$\left. \frac{d}{dt} \left(\frac{dh(t)}{dt} \right) \right|_{t=t_f} = 0, \quad (\text{F.17})$$

which can be easily checked by using Eq. (F.15). The relevant length scale in quantifying the gravitational wave spectrum produced during a phase transition is set by the mean bubble separation, which can be derived from the bubble number density. The total number of bubbles can be quantified via

$$N_{\text{bubbles}}(t) = \mathcal{V} \int dt' \frac{\Gamma(t')}{\mathcal{V}} h(t'), \quad (\text{F.18})$$

¹A more accurate definition of the nucleation time with its associated nucleation temperature is given by the integral condition

$$\int_{t_c}^{t_n} \frac{\Gamma/V}{H^3} = 1.$$

For fast phase transitions Eq. F.12 is an accurate approximation, however for slow phase transitions, that typically tend to be stronger and therefore have a higher chance to source detectable gravitational waves, the above condition has to be taken into account

where we are multiplying the nucleation rate Γ with the fractional volume h because bubbles can only nucleate in the metastable phase. Close to the end of the phase transition, we have argued that Eq. (F.15) is a reliable estimate of the fractional volume. Moreover, we may assume that the time evolution of the nucleation is dominated by the exponential decay term similarly to Eq. (F.11). In that case the total number of bubbles simplifies to

$$N_{\text{bubbles}}(t) = \int^t dt' \Gamma(t_f) e^{-S(t_f) + \beta(t-t_f)} h(t') = \Gamma(t_f) \frac{e^{-S(t_f)}}{\beta} \int^t dt' \frac{dh(t')}{dt'} \quad (\text{F.19})$$

$$= \Gamma(t_f) e^{-S(t_f)} \frac{1}{\beta} (1 - h(t)). \quad (\text{F.20})$$

At late times, at the end of the phase transition $h(t)$ tends to zero, such that the final number density is given by

$$n_{\text{bubbles}} = \frac{N_{\text{bubbles}}}{\mathcal{V}} = \frac{\Gamma(t_f) e^{-S(t_f)}}{\mathcal{V}} \frac{1}{\beta} \quad (\text{F.21})$$

The above relation can be further simplified by making use of the definition of the reference time t_f which implies the following relationship

$$\frac{\Gamma(t_f)}{\mathcal{V}} e^{-S(t_f)} = \frac{\beta^4}{3!} \frac{3}{4\pi} \frac{1}{v_w^3}. \quad (\text{F.22})$$

The number density of bubbles towards the end of the phase transition then takes the following form

$$n_{\text{bubbles}} = \frac{\beta^3}{8\pi v_w^3} \equiv \frac{1}{R_*^3}, \quad (\text{F.23})$$

where we introduced the mean bubble separation R_* , which we will show later is relevant in setting the peak frequency of the gravitational wave spectrum.

So far we have introduced two reference times, the nucleation time t_N and the time t_f at which roughly 34% of the vacuum is still in the metastable phase. It is, however, common to introduce a third time, the so-called percolation time, which lies very close to the reference time t_f and can therefore also be used as an estimate for the end of the phase transition. The percolation time is also commonly used in the literature to quantify the spectrum of gravitational waves that follow from a first-order phase transition.

G Gravitational Waves - A primer

Gravitational Waves are perturbations of space-time around some background which justifies the common statement that they can be interpreted as ripples of space-time. These perturbations can be shown to satisfy a wave equation, hence the name gravitational wave. For this purpose consider a flat background metric η and some small perturbation on top of it such that the actual space-time metric g is given by

$$g_{\mu\nu} = \eta_{\mu\nu} + h_{\mu\nu}, \quad (\text{G.1})$$

with $h_{\mu\nu} \ll 1$. Assuming such a background it is possible to derive a wave equation for the components of h that satisfies

$$\square h^{\mu\nu} = -16\pi T^{\mu\nu}, \quad (\text{G.2})$$

where the perturbations are transverse, $\partial_\mu h^{\mu\nu} = 0$, and traceless $h^\mu{}_\mu = 0$ as a result of the freedom one has in choosing a coordinate system¹. The gauge constraints following from the transverse and the tracelessness condition reduce the number of degree of freedom of the metric to two physical propagating ones, typically referred to as 'plus' (+) and 'cross' polarizations (\times), corresponding to a contraction of space in one direction and an expansion in the other one. The global space-time of our universe is well approximated by the FLRW metric. Let us therefore focus on small perturbations of such a space-time. Of particular interest is the observation that gravitational waves carry away radiation and therefore are a source of energy-momentum described by

$$T_{\mu\nu}^{\text{GW}} = \frac{1}{32\pi G} \langle \partial_\mu h_{ij} \partial_\nu h_{ij} \rangle \quad (\text{G.3})$$

As observers on earth we are interested in the frequency-dependent power spectrum of the energy density of gravitational waves. The power spectrum quantifies the distribution of the energy density carried by gravitational waves per unit time in terms of the frequency components contributing to the total gravitational wave signal. The total energy density is then found by integrating over all spectral components.

As a first step in determining the power spectrum of a gravitational wave signal we determine the energy density of a gravitational wave given by

$$\rho_{\text{GW}} = \frac{1}{32\pi G} \langle \dot{h}_{ij}^2 \rangle, \quad (\text{G.4})$$

¹In more technical words the traceless-transverse condition follows from choosing the Lorentz Gauge, which is actually a class of gauges (i.e. one still has some "additional" class of freedom when choosing the Lorentz gauge). See [327] for details.

which follows from the $\mu = \nu = 0$ component of the energy-momentum tensor. A spatial Fourier transform of the metric allows to quantify the contribution of a given frequency interval df to the total energy density ρ_{GW} . It is, however, more standard in the gravitational waves literature, to give the spectrum of the energy density per logarithm of the frequency f , i.e.,

$$\frac{d\rho_{GW}}{d\ln f} = \frac{\pi}{4G} f^3 S_h(f), \quad (\text{G.5})$$

where $S_h(f)$ is the one-sided strain power spectral density defined for positive frequencies $f > 0$. Knowledge of $S_h(f)$ allows to derive another key quantity of interest, the amplitude $h(f)$ of a gravitational wave spectrum at a given frequency f , by simply considering the square root of the strain power spectral density, $h(f) = \sqrt{S_h(f)}$. Rather than working with the gravitational wave energy density, it is more convenient to introduce the fractional energy density

$$\Omega = \frac{\rho_{GW}}{\rho_{tot}} \quad (\text{G.6})$$

of the gravitational wave signal with respect to the total energy density of the universe. The spectral density related to the fractional energy density is given by

$$\frac{d\Omega_{GW}}{d\ln f} = \frac{1}{\rho_{tot}} \frac{d\rho_{GW}}{d\ln f} = \frac{2\pi^2}{3H^2} f^3 S_h(f), \quad (\text{G.7})$$

where H is the Hubble constant of the universe which parametrizes its total energy content as follows

$$H^2 = \frac{8\pi G \rho_{tot}}{3}. \quad (\text{G.8})$$

The spectral fractional energy density introduced in Eq. (G.7) is also referred to as the gravitational wave power spectrum. In the following we are going to use the following notation to refer to the power spectrum

$$\frac{d\Omega_{GW}}{d\ln f} \equiv \hat{h}^2 \Omega_{GW}, \quad (\text{G.9})$$

where Ω_{GW} should not be confused with the fractional energy density Ω and \hat{h} denotes the dimensionless Hubble constant defined as $\hat{h} = H/100\text{km}/(s \cdot \text{Mpc})$. Finally, when studying the gravitational wave power spectrum in an expanding Friedmann-Lemaître-Robertson-Walker (FLRW) universe the frequencies of the gravitational wave spectrum are redshifted due to the expansion of the universe. In particular, the peak frequencies today are related to the peak frequencies at emission via

$$f_{\text{peak}} = \frac{a_*}{a} f_{\text{peak}}^*, \quad (\text{G.10})$$

where a_* and a are the scale factor of the universe at the time of emission and today, respectively. Hence, given a specific expansion history of the universe f_{peak} and f_{peak}^*

can be calculated.

Of interest to us in this thesis is the electroweak epoch. If one assumes that the universe transitioned into radiation-domination right after the phase transition and has continuously expanded, one obtains

$$f_{\text{peak}} = \frac{h_*}{H_*} f_{\text{peak}}^* = 1.65 \times 10^{-5} \text{ Hz} \left(\frac{g_*}{100} \right)^{1/6} \left(\frac{T_{\text{reh}}}{100 \text{ GeV}} \right) \frac{f_{\text{peak}}^*}{H_*}, \quad (\text{G.11})$$

where g_* denotes the relativistic degrees of freedom at the time of production and T_{reh} is the reheating temperature, which can be determined from energy conservation $a_{\text{reh}}^3 \rho_{\text{rad}}(T_{\text{reh}}) = a_*^3 (\rho_{\text{rad}}(T_p) + \Delta V)$, such that

$$T_{\text{reh}} = \left(\frac{a_*}{a_{\text{reh}}} \right)^{3/4} \left(\frac{30 \rho_{\text{rad}}(T_p)}{g_* \pi^2} \left(1 + \frac{\Delta V}{\rho_{\text{rad}}(T_p)} \right) \right)^{1/4} \simeq T_p (1 + \alpha(T_p))^{1/4}, \quad (\text{G.12})$$

where T_p is the percolation temperature that marks the end of the cosmological phase transition, $\rho_{\text{rad}}(T_p)$ is the radiation energy density evaluated at percolation temperature, ΔV denotes the vacuum energy at percolation temperature.

H Efficiencies of gravitational wave production processes

The gravitational wave spectra depend on efficiency factors that describe the fractions of vacuum energy transferred into the dynamics of bubbles. κ_{coll} denotes the fraction stored in the bubble wall, while the energy converted into bulk motion of the fluid are characterized by κ_{sw} and κ_{turb} . In this appendix, we specify these factors. To do so, we introduce the quantities, denoted by α_∞ and α_{eq} , analogous to α ,

$$\alpha_\infty = \frac{\Delta P_{\text{LO}}}{\rho_{\text{rad}}} = \frac{\Delta m^2 T^2}{24\rho_{\text{rad}}}, \quad \alpha_{\text{eq}} = \frac{\Delta P_{\text{NLO}}}{\rho_{\text{rad}}} = \frac{g^2 \Delta m_V T^3}{24\rho_{\text{rad}}}. \quad (\text{H.1})$$

Here $\Delta m^2 = \sum_i c_i N_i \Delta m_i^2$ is the squared mass difference between the symmetric and broken phases, weighted by N_i the number of degrees of freedom for particle species i and factors $c_i = 1$ for a boson and $c_i = 1/2$ for a fermion, while $g^2 \Delta m_V = \sum_i g_i^2 N_i \Delta m_i$ is the mass difference weighted by the gauge coupling constant g_i . ΔP_{LO} and ΔP_{NLO} correspond to the leading and the next-to-leading order friction forces from the plasma around the bubbles [328]. For the SM particle content, these quantities yield

$$\alpha_\infty \simeq 4.8 \cdot 10^{-3} \left(\frac{\phi_*}{T_*} \right)^2, \quad \alpha_{\text{eq}} \simeq 7.3 \cdot 10^{-4} \left(\frac{\phi_*}{T_*} \right). \quad (\text{H.2})$$

The efficiency factor κ_{coll} is the fraction of the energy stored in the bubble wall, namely it is defined by $\kappa_{\text{coll}} = E_{\text{wall}}/E_V$, where E_{wall} is the energy of the bubble wall and E_V is that of the vacuum energy. More specifically, κ_{coll} can be expressed as

$$\kappa_{\text{coll}} = \begin{cases} \frac{\gamma_{\text{eq}}}{\gamma_*} \left[1 - \frac{\alpha_\infty}{\alpha} \left(\frac{\gamma_{\text{eq}}}{\gamma_*} \right)^2 \right] & \gamma_* > \gamma_{\text{eq}} \\ 1 - \frac{\alpha_\infty}{\alpha} & \gamma_* \leq \gamma_{\text{eq}} \end{cases}, \quad (\text{H.3})$$

where γ_{eq} and γ_* stand for the Lorentz factors for the terminal velocity of the wall and

$$\gamma_{\text{eq}} = \frac{\alpha - \alpha_\infty}{\alpha_{\text{eq}}}, \quad \gamma_* = \frac{2 R_*}{3 R_0}. \quad (\text{H.4})$$

Here, r_0 is the initial bubble radius which is given by

$$r_0 = \left[\frac{3S_3}{4\pi\rho_{\text{vac}}} \right]^{\frac{1}{3}}. \quad (\text{H.5})$$

The remnant $\alpha_{\text{eff}} = \alpha(1 - \kappa_{\text{coll}})$ is transferred into the bulk motion of bubbles which produces gravitational waves from sound wave and turbulence. Note that for a large α , κ_{coll} tends to be unity and then $\alpha_{\text{eff}} \simeq 0$, so that gravitational waves from the bulk motion of bubbles are suppressed.

The efficiency factor κ_v is defined by [295]

$$\kappa_v(\alpha, v_w) = \frac{3}{\rho_{\text{vac}} v_w^3} \int_{c_s}^{v_w} w(\xi) \xi^2 \frac{v(\xi)^2}{1 - v(\xi)^2} d\xi, \quad (\text{H.6})$$

where $c_s = 1/\sqrt{3}$ is the speed of sound and $w(\xi)$ is the plasma enthalpy profile,

$$w(\xi) = w_0 \exp \left[(1 - c_s^{-2}) \int_{v_0}^{v(\xi)} dv' \frac{\mu(\xi, v')}{1 - v'^2} \right]. \quad (\text{H.7})$$

Here, we defined the Lorentz boost factor

$$\mu(\xi, v) = \frac{\xi - v}{1 - \xi v}, \quad (\text{H.8})$$

and the plasma velocity profile $v(\xi)$ which is obtained from the differential equation

$$\frac{2v}{\xi} = \frac{1 - \xi v}{1 - v^2} [c_s^{-2} \mu(\xi, v) - 1] \frac{\partial v}{\partial \xi}. \quad (\text{H.9})$$

Depending on the initial conditions, the solutions to (H.9) are classified into three different types [295]: (i) deflagrations, (ii) detonations and (iii) hybrids. (i): The bubble-wall velocity is subsonic, i.e., $v_w < c_s$. There is the fluid with non-zero velocity outside the bubble wall. The static fluid does not collide with the wall. In such a case, the gravitational wave signal from sound waves tends to be suppressed [?]. (ii): The bubble wall velocity is supersonic ($v_w > c_s$). The active fluid is inside the wall, while the wall hits the fluid at rest. Hence, the strong gravitational waves from sound waves and turbulence could be produced. (iii): The bubble wall moves at a supersonic speed, but smaller than the Chapman-Jouguet detonation velocity v_J which is defined by

$$v_J = \frac{\sqrt{2\alpha_{\text{eff}}/3 + \alpha_{\text{eff}}^2} + \sqrt{1/3}}{1 + \alpha_{\text{eff}}}. \quad (\text{H.10})$$

This case is a combination of the two cases (i) and (ii), namely the wall is inside the active fluid.

The fitting analysis to the numerically evaluated efficiency factor tells us that for

the three different cases, (H.6) can be well described by the following formula [295]:

$$\kappa_v(\alpha_{\text{eff}}, v_w) = \frac{\alpha_{\text{eff}}}{\alpha} \times \begin{cases} \frac{c_s^{11/5} \kappa_A \kappa_B}{(c_s^{11/5} - v_w^{11/5}) \kappa_B + v_w c_s^{6/5} \kappa_A} & \text{for } v_w \lesssim c_s \\ \kappa_B + (v_w - c_s) \delta\kappa + \frac{(v_w - c_s)^3}{(v_J - c_s)^3} [\kappa_C - \kappa_B - (v_J - c_s) \delta\kappa] & \text{for } c_s < v_w < v_J, \\ \frac{(v_J - 1)^3 v_J^{5/2} v_w^{-5/2} \kappa_C \kappa_D}{[(v_J - 1)^3 - (v_w - 1)^3] v_J^{5/2} \kappa_C + (v_w - 1)^3 \kappa_D} & \text{for } v_J \lesssim v_w \end{cases} \quad (\text{H.11})$$

where the efficiency factors for different wall-velocity regions read

$$\kappa_A \simeq \frac{6.9 \alpha_{\text{eff}}}{1.36 - 0.037 \sqrt{\alpha_{\text{eff}}} + \alpha_{\text{eff}}} v_w^{6/5} \quad (v_w \ll c_s), \quad (\text{H.12})$$

$$\kappa_B \simeq \frac{\alpha_{\text{eff}}^{2/5}}{0.017 + (0.997 + \alpha_{\text{eff}})^{2/5}} \quad (v_w = c_s), \quad (\text{H.13})$$

$$\kappa_C \simeq \frac{\sqrt{\alpha_{\text{eff}}}}{0.135 + \sqrt{0.98 + \alpha_{\text{eff}}}} \quad (v_w = v_J), \quad (\text{H.14})$$

$$\kappa_D \simeq \frac{\alpha_{\text{eff}}}{0.73 + 0.083 \sqrt{\alpha_{\text{eff}}} + \alpha_{\text{eff}}} \quad (v_w = 1). \quad (\text{H.15})$$

In (H.11) for $c_s \lesssim v_w < v_J$, the efficiency factor κ_v depends on $\delta\kappa$ which is the derivative of κ_v with respect to v_w at $v_w = c_s$, approximately given by

$$\delta\kappa \simeq -0.9 \log \left(\frac{\sqrt{\alpha_{\text{eff}}}}{1 + \sqrt{\alpha_{\text{eff}}}} \right). \quad (\text{H.16})$$

I Result tables for the gravitational wave spectra

λ_6	ϕ_c/T_c	α	$\tilde{\beta}$	$R \cdot \text{GeV}$	$H(T_p)/\text{GeV}$	T_c/GeV	T_n/GeV	T_p/GeV	$T_{\text{reh}}/\text{GeV}$	SNR	$\lambda_{H^3}/\lambda_{H^3,0}$	$\lambda_{H^4}/\lambda_{H^4,0}$
58	1.02	0.00274	46400	$3.40 \cdot 10^9$	$1.86 \cdot 10^{-14}$	116	115	115	115	$1.97 \cdot 10^{-20}$	1.67	5.05
64	1.26	0.00436	19200	$8.91 \cdot 10^9$	$1.71 \cdot 10^{-14}$	112	111	110	111	$6.37 \cdot 10^{-15}$	1.73	5.43
72	1.50	0.00655	8950	$2.12 \cdot 10^{10}$	$1.54 \cdot 10^{-14}$	107	105	105	105	$2.33 \cdot 10^{-12}$	1.81	5.88
82	1.83	0.0110	4260	$5.63 \cdot 10^{10}$	$1.22 \cdot 10^{-14}$	97.8	93.6	93.2	93.5	$4.06 \cdot 10^{-10}$	1.90	6.42
93	2.03	0.0156	2520	$1.05 \cdot 10^{11}$	$1.11 \cdot 10^{-14}$	96.1	89.5	88.9	89.3	$9.84 \cdot 10^{-8}$	2.01	7.02
101	2.20	0.0215	1670	$1.82 \cdot 10^{11}$	$9.61 \cdot 10^{-15}$	92.4	83.4	82.6	83.0	$3.66 \cdot 10^{-6}$	2.08	7.41
104	2.27	0.0251	1400	$2.35 \cdot 10^{11}$	$8.92 \cdot 10^{-15}$	90.7	80.4	79.5	80.0	0.0000714	2.11	7.58
112	2.42	0.0365	917	$4.27 \cdot 10^{11}$	$7.48 \cdot 10^{-15}$	87.5	73.8	72.6	73.3	0.000267	2.17	7.93
124	2.68	0.0846	394	$1.49 \cdot 10^{12}$	$4.98 \cdot 10^{-15}$	82.1	60.6	58.7	59.9	0.00541	2.27	8.49
130	2.84	0.232	127	$7.24 \cdot 10^{12}$	$3.18 \cdot 10^{-15}$	78.9	48.6	45.6	48.0	1.40	2.32	8.79
132	2.87	0.344	67.0	$1.61 \cdot 10^{13}$	$2.72 \cdot 10^{-15}$	78.4	44.5	41.2	44.3	126	2.33	8.85
132.2	2.89	0.518	21.7	$5.69 \cdot 10^{13}$	$2.37 \cdot 10^{-15}$	78.0	41.8	37.3	41.4	379	2.33	8.88
132.6	2.90	0.817	19.3	$1.22 \cdot 10^{14}$	$2.07 \cdot 10^{-15}$	77.8	39.1	33.3	38.6	675	2.34	8.90
132.9	2.90	0.966	19.3	$1.74 \cdot 10^{14}$	$1.99 \cdot 10^{-15}$	77.8	38.2	32.0	37.9	811	2.34	8.90

Table I.1: Summary of results for the ϕ^6 modification of the potential.

λ_{in}	ϕ_c/T_c	α	$\tilde{\beta}$	$R \cdot \text{GeV}$	$H(T_p)/\text{GeV}$	T_c/GeV	T_n/GeV	T_p/GeV	$T_{\text{reh}}/\text{GeV}$	SNR	$\lambda_{H^3}/\lambda_{H^3,0}$	$\lambda_{H^4}/\lambda_{H^4,0}$
0.36	1.03	0.00286	37400	$4.13 \cdot 10^9$	$1.90 \cdot 10^{-14}$	117	116	116	116	$2.05 \cdot 10^{-14}$	1.58	4.19
0.4	1.27	0.00450	16400	$1.03 \cdot 10^{10}$	$1.74 \cdot 10^{-14}$	113	111	111	111	$5.51 \cdot 10^{-12}$	1.65	4.53
0.51	1.76	0.0102	4290	$5.08 \cdot 10^{10}$	$1.35 \cdot 10^{-14}$	103	98.3	97.8	98.1	$6.63 \cdot 10^{-8}$	1.82	5.43
0.58	2.03	0.0164	2210	$1.20 \cdot 10^{11}$	$1.10 \cdot 10^{-14}$	96.5	89.2	88.5	88.8	$7.75 \cdot 10^{-6}$	1.92	5.99
0.64	2.25	0.0259	1280	$2.58 \cdot 10^{11}$	$8.90 \cdot 10^{-15}$	91.6	80.3	79.4	79.9	0.000429	2.01	6.44
0.65	2.27	0.0273	1200	$2.80 \cdot 10^{11}$	$8.70 \cdot 10^{-15}$	91.0	79.5	78.5	79.0	0.0640	2.02	6.51
0.66	2.32	0.0304	1070	$3.33 \cdot 10^{11}$	$8.26 \cdot 10^{-15}$	89.9	77.5	76.4	76.4	0.00159	2.04	6.60
0.71	2.51	0.0503	628	$7.20 \cdot 10^{11}$	$6.47 \cdot 10^{-15}$	85.9	68.9	67.4	68.2	0.064	2.11	6.97
0.735	2.59	0.0680	464	$1.13 \cdot 10^{12}$	$5.61 \cdot 10^{-15}$	84.2	64.3	62.5	63.6	0.448	2.14	7.13
0.76	2.67	0.100	313	$2.00 \cdot 10^{12}$	$4.69 \cdot 10^{-15}$	82.5	58.9	56.8	58.2	4.04	2.17	7.30
0.765	2.70	0.116	269	$2.49 \cdot 10^{12}$	$4.38 \cdot 10^{-15}$	81.9	57.0	54.7	56.2	8.42	2.18	7.34
0.7825	2.77	0.196	147	$5.72 \cdot 10^{12}$	$3.48 \cdot 10^{-15}$	80.4	50.8	48.0	50.2	75.8	2.20	7.47
0.8	2.85	1.53	19.8	$3.48 \cdot 10^{14}$	$1.83 \cdot 10^{-15}$	78.8	36.3	28.8	36.4	383	2.23	7.61

Table I.2: Summary of results for the logarithmic modification of the potential.

$\lambda_{\text{exp}}/10^{10}$	ϕ_c/T_c	α	$\tilde{\beta}$	$R \cdot \text{GeV}$	$H(T_p)/\text{GeV}$	T_c/GeV	T_n/GeV	T_p/GeV	$T_{\text{reh}}/\text{GeV}$	SNR	$\lambda_{H^3}/\lambda_{H^3,0}$	$\lambda_{H^4}/\lambda_{H^4,0}$
1.3	1.05	0.00292	65200	$2.67 \cdot 10^9$	$1.68 \cdot 10^{-14}$	110	110	109	110	$1.62 \cdot 10^{-15}$	2.00	8.72
1.5	1.17	0.00362	44500	$4.00 \cdot 10^9$	$1.65 \cdot 10^{-14}$	109	108	108	108	$2.14 \cdot 10^{-14}$	2.02	8.86
1.6	1.24	0.00406	35400	$5.12 \cdot 10^9$	$1.62 \cdot 10^{-14}$	108	107	107	107	$9.80 \cdot 10^{-14}$	2.04	8.96
2.3	1.51	0.00630	14900	$1.33 \cdot 10^{10}$	$1.48 \cdot 10^{-14}$	104	103	103	103	$3.11 \cdot 10^{-11}$	2.11	9.44
3.5	1.76	0.00889	9470	$2.34 \cdot 10^{10}$	$1.32 \cdot 10^{-14}$	99.9	97.3	97.0	97.3	$9.46 \cdot 10^{-10}$	2.19	9.97
5.4	1.99	0.0129	4180	$6.03 \cdot 10^{10}$	$1.16 \cdot 10^{-14}$	95.7	91.3	90.9	91.2	$1.83 \cdot 10^{-7}$	2.27	10.5
8.2	2.21	0.0184	2490	$1.18 \cdot 10^{11}$	$9.97 \cdot 10^{-15}$	91.4	84.7	84.1	84.5	$7.28 \cdot 10^{-6}$	2.36	11.1
14.5	2.51	0.0330	1230	$3.15 \cdot 10^{11}$	$7.58 \cdot 10^{-15}$	85.6	74.1	73.2	73.8	0.00121	2.48	11.9
23.8	2.78	0.0703	573	$9.74 \cdot 10^{11}$	$5.25 \cdot 10^{-15}$	80.3	61.9	60.5	61.5	0.259	2.58	12.6
33	2.95	0.161	258	$3.16 \cdot 10^{12}$	$3.59 \cdot 10^{-15}$	77.1	51.3	49.1	51.0	21.0	2.65	13.0
33.8	2.97	0.191	213	$4.14 \cdot 10^{12}$	$3.33 \cdot 10^{-15}$	76.1	49.3	47.0	49.1	44.2	2.65	13.0
35.4	3.00	0.248	161	$6.09 \cdot 10^{12}$	$2.99 \cdot 10^{-15}$	75.2	46.6	44.0	46.5	112	2.66	13.1
39	3.05	0.553	45.8	$2.86 \cdot 10^{13}$	$2.24 \cdot 10^{-15}$	74.8	39.8	36.1	40.3	846	2.68	13.2
40.2	3.07	1.34	18.5	$2.25 \cdot 10^{14}$	$1.77 \cdot 10^{-15}$	76.6	34.6	28.9	35.8	787	2.69	13.2

Table I.3: Summary of results for the exponential modification of the potential.

J Lists

J.1 List of Figures

2.1	Depiction of the concept of universality.	20
2.2	Illustration of a relevant and an irrelevant direction and the critical hypersurface.	21
2.3	Phase diagram of a predator-prey model to illustrate the concept of relevant and irrelevant directions.	23
2.4	Graphical depiction of the philosophy behind the FRG. The scale-dependent effective action Γ_k interpolates between the microscopic action S in the UV and the full quantum-effective action Γ in the IR as the RG scale goes to zero.	25
3.1	Illustration of the principle behind the continuum limit.	36
3.2	Phase diagram of DT uncovered from Monte Carlo simulations. The parameter κ_4 needs to be tuned to a critical value in order find the continuum limit.	37
3.3	Phase diagram of CDT	40
3.4	Depiction of the duality between the Feynman graph expansion of the free energy of a matrix model and a random triangulation. The vertices in the matrix model correspond to triangles and the propagators to edges of the triangles. The thickened structure of the lines is due to the fact that matrices carry two indices.	42
4.1	General idea of how matrix models relate to Dynamical Triangulations and 2d Quantum Gravity.	48
4.2	The gravitational path-integral including gravitational, matter and topological fluctuations.	52
4.3	Graphical depiction of the deficit angle	54
4.4	Continuum Limit in the dynamical triangulations approach. The average number of triangles is increased while the volume of the triangulation is kept finite. The continuum limit corresponds to the limit where the average number of triangles diverges.	59
4.5	Part of a random triangulation. At A and C the triangulation is locally flat as six equilateral triangles are meeting at one vertex. At B the triangulation is curved, as there are less than six triangles meeting at one vertex.	61

4.6	Geometrical interpretation of the cross-interaction: The tensor is replaced by the face of a triangle, while its indices are represented by the edges of that triangle. With this identification in mind, the cross interaction $T_{a_1 a_2 a_3} T_{a_1 b_2 b_3} T_{b_1 b_2 a_3} T_{b_1 a_2 b_3}$, which can be diagrammatically represented as shown in Eq. 4.78, is dual to a tetrahedron. One therefore expects that such an invariant might be of relevance for a possible three-dimensional quantum gravity phase.	84
4.7	Depicted above is the truncation of Γ_N for the real rank-3 model studied in this work using the graphical representation introduced in Eq. (4.78) for the invariants.	87
4.8	Dimensional reduction of the pillow invariant.	96
4.9	We are studying a real rank-4 tensor model. The full truncation is depicted above. We include all interactions up to order T^6 and additionally melonic T^8 interactions.	111
5.1	Depiction of a first-order phase transition and a cross-over	120
5.2	Thermal fluctuation lead to the nucleation of bubbles, where the Higgs is in a stable ground state. These bubbles expand into the regions where the Higgs persists in its metastable ground state. At early times, the bubbles do not overlap. Later, however, they merge until the entire fluid of Standard Model particles is in the stable ground state.	125
5.3	Displayed above are the pairs of $\tilde{\beta}$ and α values that can be accessed from the three modifications of the effective Higgs potential that we are considering. A nearly universal behavior between $\tilde{\beta}$ and α can be observed for all potentials. In particular, at small α we find an asymptotic power-law behavior with $\tilde{\beta} = 0.5 \cdot \alpha^{-1.9}$. The analysis of a simple ϕ^4 model allows us to obtain analytical results for $\tilde{\beta}$ and α as a function of ϕ_c/T_c , which can be combined to give a relation between $\tilde{\beta}$ and α as depicted above. Crucially, this derivation relies on the thin-wall approximation for which $T_c - T/T \ll 1$ and is, in particular, valid for weakly supercooled phase transitions, i.e., small α	140
5.4	We show α (left panel) and $\tilde{\beta}$ (right panel) as a function of the order parameter ϕ_c/T_c for all classes of potentials. An almost universal relation between $\alpha, \tilde{\beta}$ and ϕ_c/T_c is found for all modifications. The red area marks the strong supercooling regime. At small ϕ_c/T_c , we find asymptotic power-law behaviours with $\alpha = 0.0026 \cdot (\phi_c/T_c)^{1.97}$ and $\tilde{\beta} = 48800 \cdot (\phi_c/T_c)^{-3.77}$	141
5.5	We depict the total GW power spectra of all three classes of modified Higgs potentials for different values of ϕ_c/T_c . The dashed lines in the figures indicate the strong supercooling regime at which the linearization of the action in order to determine β breaks down.	142

5.6	We show the contributions of sound waves and turbulence to the power spectrum using Eq. 5.61 and Eq. 5.62 for the polynomial modification of the Higgs potential for $\phi_c/T_c = 2.84$	143
5.7	We compare the effect of different wall speeds on the gravitational wave spectrum for a representative value of ϕ_c/T_c of the polynomial ϕ^6 modification of the Standard Model Higgs potential. As the wall speed increases, the spectra are shifted towards larger amplitudes at smaller smaller peak frequencies.	143
5.8	An interplay of collider physics and gravitational-wave astronomy could be used as a way to pinpoint new physics. On the left panel, we depict the pairs of SNR and triple-Higgs couplings that could be realized by each of the three classes of potentials. On the right panel, we show that for a given SNR, the different potentials predict different corrections to the quartic-Higgs coupling.	145
E.1	Profile of the critical bubble	173

J.2 List of Tables

4.1	The cyclic-melonic single-trace fixed point features one relevant direction in the quartic truncation.	100
4.2	The cyclic-melonic single-trace fixed point only features cyclic melonic couplings and one associated relevant direction in the truncation to sixth order. Given the systematic error of the truncation and the small value $\theta_2 = -0.03$, a second positive critical exponent might exist at higher orders in the truncation.	101
4.3	The multitrace-bubble fixed point features two relevant directions in the truncation to quartic order, with one of the positive critical exponents rather close to zero, calling for an extension of the truncation to confirm its relevance.	103
4.4	Results for the multitrace-bubble fixed point at order T^6 in the truncation. The leading critical exponent is close to our bound $\theta < 3.5$, yet the explicit extension to T^8 shows the fixed point persists.	103
4.5	At quartic order the fixed point possesses two relevant directions. Compared to the complex model, one finds a new irrelevant direction (θ_3) which is associated to the "tetrahedral" interaction. There is good agreement between the complex and the real model at quartic level.	105
4.6	Fixed-point values of the cyclic melonic couplings and critical exponents in the truncation to sixth order for the cyclic-melonic multitrace fixed point. The couplings not displayed are all vanishing at the fixed point.	105

4.7	The isocolored fixed point with tetrahedral interaction $g_{4,1}^0$ features an anomalous dimension of $\eta = -0.75$, as discussed in Sec. ???. It is clear then that for $\eta = 0$ no such fixed point exists. The sign of $g_{4,1}^{0*}$ is not determined by the fixed-point conditions, i.e., there are two fixed points.	108
4.8	Fixed-point values and critical exponents at sixth order in the truncation for the isocolored fixed point with tetrahedral interaction.	108
4.9	Fixed point values and critical exponents of the double cyclic-melonic single-trace fixed point in the rank-3 real tensor model.	109
4.10	Fixed-point values of the cyclic melonic couplings and critical exponents in the truncation to sixth order for the cyclic-melonic multitrace fixed point. The couplings not displayed are all vanishing at the fixed point.	110
4.11	We find a fixed point characterized by two relevant directions. Shown above are all non-zero couplings.	115
4.12	Critical exponents associated to a potential fixed point for four-dimensional quantum gravity from tensor models.	116
I.1	Summary of results for the ϕ^6 modification of the potential.	189
I.2	Summary of results for the logarithmic modification of the potential.	190
I.3	Summary of results for the exponential modification of the potential.	191

K Own publications

I have collaborated on the following work which has been included in this thesis:

- **Phase transitions in the early universe**

Mark Hindmarsh, Marvin Lüben, Johannes Lumma, Martin Pauly

submitted to: SciPost Lecture Notes

e-Print: arXiv:2008.09136

- **Towards background independent quantum gravity with tensor models**

Astrid Eichhorn, Tim Koslowski, Johannes Lumma, Antônio D. Pereira

published in: Class. Quantum Grav. 36 155007

e-Print: arXiv:1811.00814

- **Universal critical behavior in tensor models for four-dimensional quantum gravity**

Astrid Eichhorn, Tim Koslowski, Johannes Lumma, Antônio D. Pereira, Arslan Sikandar

published in: JHEP 02 (2020) 110

e-Print: arXiv:1912.05314

- **Universal gravitational-wave signatures from heavy new physics in the electroweak sector**

Astrid Eichhorn, Johannes Lumma, Jan M. Pawłowski, Manuel Reichert, Masatoshi Yamada

e-Print: arXiv:2010.00017

The following publication was not used in this thesis:

- **Quantum gravity fluctuations flatten the Planck-scale Higgs potential**

Astrid Eichhorn, Yuta Hamada, Johannes Lumma, Masatoshi Yamada

published in: Phys.Rev.D 97 (2018) 8, 086004

e-Print: arXiv:1712.00319

The results presented in Ch. 4.3 are based on the work [1] in collaboration with Astrid Eichhorn, Tim Koslowski and Antônio D. Pereira. Ch. 4.4 is a product of a joint collaboration with Astrid Eichhorn, Antônio D. Pereira and Arslan Sikandar [2].

Ch. 5 includes an introductory part which has benefited from a project with Mark Hindmarsh, Marvin Lüben and Martin Pauly [3]. The results presented in Ch. 5 are a result of work together with Astrid Eichhorn, Jan M. Pawlowski, Manuel Reichert and Masatoshi Yamada and will be reported in a forthcoming publication.

L Bibliography

- [1] Astrid Eichhorn, Johannes Lumma, Tim Koslowski, and Antonio D. Pereira. Towards background independent quantum gravity with tensor models. *Classical and Quantum Gravity*, 36(15):155007, jul 2019.
- [2] Astrid Eichhorn, Johannes Lumma, Antonio D. Pereira, and Arslan Sikan-dar. Universal critical behavior in tensor models for four-dimensional quantum gravity. *Journal of High Energy Physics*, 2020(2):110, feb 2020.
- [3] Mark B Hindmarsh, Marvin Lüben, Johannes Lumma, and Martin Pauly. Phase transitions in the early universe. Technical report, 2020.
- [4] B. P. Abbott and Et Al. Observation of gravitational waves from a binary black hole merger. *Physical Review Letters*, 116(6):061102, feb 2016.
- [5] EHT Collaboration. First M87 Event Horizon Telescope Results. II. Array and Instrumentation. *The Astrophysical Journal*, 875(1):L2, jun 2019.
- [6] EHT Collaboration. First M87 Event Horizon Telescope Results. III. Data Processing and Calibration. *The Astrophysical Journal*, 875(1):L3, jun 2019.
- [7] EHT Collaboration. First M87 Event Horizon Telescope Results. V. Physical Origin of the Asymmetric Ring. *The Astrophysical Journal*, 875(1):L5, jun 2019.
- [8] Leo P. Kadanoff. Scaling laws for ising models near Tc. *Physica Physique Fizika*, 2(6):263–272, jun 1966.
- [9] K. Beach, R. Gooding, and F Marsiglio. Reliable Padé analytical continuation method based on a high-accuracy symbolic computation algorithm. *Physical Review B - Condensed Matter and Materials Physics*, 61(8):5147–5157, 2000.
- [10] Kenneth G. Wilson. Renormalization group and critical phenomena. I. Renormalization group and the Kadanoff scaling picture. *Physical Review B*, 4(9):3174–3183, nov 1971.
- [11] Kenneth G. Wilson. Renormalization group and critical phenomena. II. Phase-space cell analysis of critical behavior. *Physical Review B*, 4(9):3184–3205, nov 1971.
- [12] Harald Grosse and Raimar Wulkenhaar. Renormalisation of ϕ 4-theory on noncommutative R4 in the matrix base. *Communications in Mathematical Physics*, 256(2):305–374, jun 2005.

- [13] Alessandro Sfondrini and Tim A. Koslowski. Functional renormalization of noncommutative scalar field theory. *International Journal of Modern Physics A*, 26(23):4009–4051, jun 2011.
- [14] H.I. Freedman. *Deterministic mathematical models in population ecology*, volume 57. Marcel Dekker, Inc., New York, jan 1980.
- [15] A M Lyapunov. The general problem of the stability of motion. 1892.
- [16] Christof Wetterich. Exact evolution equation for the effective potential. *Physics Letters B*, 301(1):90–94, feb 1993.
- [17] Tim R. Morris. The Exact Renormalization Group and approximate solutions. *International Journal of Modern Physics A*, 09(14):2411–2449, jun 1994.
- [18] Ulrich Ellwanger. Flow equations for N point functions and bound states. *Zeitschrift für Physik C Particles and Fields*, 62(3):503–510, aug 1994.
- [19] Elisa Manrique and Martin Reuter. Bare vs. Effective fixed point action in asymptotic safety: The reconstruction problem. In *Proceedings of Science*, may 2008.
- [20] Tim R. Morris and Zoë H. Slade. Solutions to the reconstruction problem in asymptotic safety. *Journal of High Energy Physics*, 2015(11):1–27, nov 2015.
- [21] Daniel F. Litim. Derivative expansion and renormalisation group flows. *Journal of High Energy Physics*, 5(11):1–17, nov 2001.
- [22] Daniel F. Litim. Optimized renormalization group flows. *Physical Review D - Particles, Fields, Gravitation and Cosmology*, 64(10):17, mar 2001.
- [23] Jan M. Pawłowski. Aspects of the functional renormalisation group. *Annals of Physics*, 322(12):2831–2915, dec 2007.
- [24] C. Bagnuls and C. Bervillier. Exact renormalization group equations: An introductory review, feb 2001.
- [25] Jürgen Berges, Nikolaos Tetradis, and Christof Wetterich. Non-perturbative renormalization flow in quantum field theory and statistical physics, may 2002.
- [26] Janos Polonyi. Lectures on the functional renormalization group method. *Open Physics*, 1(1):1–71, oct 2006.
- [27] Oliver J. Rosten. Fundamentals of the exact renormalization group, mar 2012.
- [28] Holger Gies. Introduction to the functional RG and applications to gauge theories. *Lecture Notes in Physics*, 852:287–348, nov 2012.

- [29] Bertrand Delamotte. An introduction to the nonperturbative renormalization group. *Lecture Notes in Physics*, 852:49–132, feb 2012.
- [30] G. 't Hooft and M. Veltman. One-loop divergencies in the theory of gravitation. *Ann. Inst. H. Poincare Phys. Theor.*, 20(1):69–94, 1974.
- [31] Marc H. Goroff and Augusto Sagnotti. Quantum gravity at two loops. *Physics Letters B*, 160(1-3):81–86, oct 1985.
- [32] S. W. Hawking. Gravitational radiation from colliding black holes. *Physical Review Letters*, 26(21):1344–1346, may 1971.
- [33] J. D. Bekenstein. Black holes and the second law. *Lettere Al Nuovo Cimento Series 2*, 4(15):737–740, aug 1972.
- [34] Jacob D Bekenstein. Generalized second law of thermodynamics in black-hole physics. *Physical Review D*, 9(12):3292–3300, 1974.
- [35] Jacob D Bekensteing. Black Holes and Entropy*. Technical Report 8.
- [36] S. W. Hawking. Particle creation by black holes. *Communications in Mathematical Physics*, 43(3):199–220, 1975.
- [37] S. W. Hawking. Black holes and thermodynamics. *Physical Review D*, 13(2):191–197, jan 1976.
- [38] Sergey N. Solodukhin. Entanglement entropy of black holes. *Living Reviews in Relativity*, 14, apr 2011.
- [39] Carlo Pagani and Martin Reuter. Finite entanglement entropy in asymptotically safe quantum gravity. *Journal of High Energy Physics*, 2018(7), apr 2018.
- [40] Hermann Nicolai and Kasper Peeters. Loop and spin foam quantum gravity: A brief guide for beginners. *Lecture Notes in Physics*, 721:151–184, 2007.
- [41] Cliff P. Burgess. Quantum gravity in everyday life: General relativity as an effective field theory, nov 2004.
- [42] John F. Donoghue, Mikhail M. Ivanov, and Andrey Shkerin. EPFL Lectures on General Relativity as a Quantum Field Theory. feb 2017.
- [43] John F. Donoghue. Leading quantum correction to the Newtonian potential. *Physical Review Letters*, 72(19):2996–2999, oct 1994.
- [44] Kenneth G. Wilson and Michael E. Fisher. Critical exponents in 3.99 dimensions. *Physical Review Letters*, 28(4):240–243, jan 1972.
- [45] C. Wetterich. Quantum scale symmetry. jan 2019.

- [46] C Wetterich. Fundamental Scale Invariance. 2020.
- [47] Xavier Calmet, Sabine Hossenfelder, and Roberto Percacci. Deformed special relativity from asymptotically safe gravity. *Physical Review D - Particles, Fields, Gravitation and Cosmology*, 82(12), aug 2010.
- [48] Roberto Percacci and Gian Paolo Vacca. Asymptotic safety, emergence and minimal length. *Classical and Quantum Gravity*, 27(24), aug 2010.
- [49] M. Reuter. Nonperturbative evolution equation for quantum gravity. *Physical Review D - Particles, Fields, Gravitation and Cosmology*, 57(2):971–985, jan 1998.
- [50] M. Reuter. Nonperturbative evolution equation for quantum gravity. *Physical Review D - Particles, Fields, Gravitation and Cosmology*, 57(2):971–985, may 1998.
- [51] O. Lauscher and M. Reuter. Ultraviolet fixed point and generalized flow equation of quantum gravity. *Physical Review D - Particles, Fields, Gravitation and Cosmology*, 65(2), dec 2002.
- [52] M. Reuter and F. Saueressig. Renormalization group flow of quantum gravity in the Einstein-Hilbert truncation. *Physical Review D - Particles, Fields, Gravitation and Cosmology*, 65(6):26, oct 2002.
- [53] O. Lauscher and M. Reuter. Flow equation of quantum Einstein gravity in a higher-derivative truncation. *Physical Review D - Particles, Fields, Gravitation and Cosmology*, 66(2):50, may 2002.
- [54] Daniel F. Litim. Fixed points of quantum gravity. *Physical Review Letters*, 92(20), may 2004.
- [55] Dario Benedetti, Pedro F. Machado, and Frank Saueressig. Asymptotic safety in higher-derivative gravity. *Modern Physics Letters A*, 24(28):2233–2241, jan 2009.
- [56] Dario Benedetti, Pedro F. Machado, and Frank Saueressig. Taming perturbative divergences in asymptotically safe gravity. *Nuclear Physics B*, 824(1-2):168–191, feb 2010.
- [57] Tobias Denz, Jan M. Pawłowski, and Manuel Reichert. Towards apparent convergence in asymptotically safe quantum gravity. *European Physical Journal C*, 78(4), dec 2018.
- [58] Yuta Hamada and Masatoshi Yamada. Asymptotic safety of higher derivative quantum gravity non-minimally coupled with a matter system. *Journal of High Energy Physics*, 2017(8), mar 2017.

- [59] Kevin Falls, Callum R. King, Daniel F. Litim, Kostas Nikolakopoulos, and Christoph Rahmede. Asymptotic safety of quantum gravity beyond Ricci scalars. *Physical Review D*, 97(8), dec 2018.
- [60] Kevin Falls, Nobuyoshi Ohta, and Roberto Percacci. Towards the determination of the dimension of the critical surface in asymptotically safe gravity. apr 2020.
- [61] Yannick Kluth and Daniel Litim. Fixed Points of Quantum Gravity and the Dimensionality of the UV Critical Surface. 2020.
- [62] Lando Bosma, Benjamin Knorr, and Frank Saueressig. Resolving Spacetime Singularities within Asymptotic Safety. *Physical Review Letters*, 123(10), apr 2019.
- [63] Pietro Donà, Astrid Eichhorn, and Roberto Percacci. Matter matters in asymptotically safe quantum gravity. *Physical Review D - Particles, Fields, Gravitation and Cosmology*, 89(8), nov 2014.
- [64] Nicolai Christiansen, Daniel F Litim, Jan M Pawłowski, and Manuel Reichert. One force to rule them all: asymptotic safety of gravity with matter. 2017.
- [65] J Meibohm, J M Pawłowski, and M Reichert. Asymptotic safety of gravity-matter systems. *Physical Review D*, 93(8), 2016.
- [66] Astrid Eichhorn. Status of the Asymptotic Safety Paradigm for Quantum Gravity and Matter. *Foundations of Physics*, 48(10):1407–1429, sep 2018.
- [67] Astrid Eichhorn, Aaron Held, and Christof Wetterich. Quantum-gravity predictions for the fine-structure constant. *Physics Letters, Section B: Nuclear, Elementary Particle and High-Energy Physics*, 782:198–201, 2018.
- [68] Astrid Eichhorn and Fleur Versteegen. Upper bound on the Abelian gauge coupling from asymptotic safety. *Journal of High Energy Physics*, 2018(1), 2018.
- [69] Astrid Eichhorn and Aaron Held. Mass Difference for Charged Quarks from Asymptotically Safe Quantum Gravity. *Physical Review Letters*, 121(15), 2018.
- [70] Astrid Eichhorn and Aaron Held. Top mass from asymptotic safety. *Physics Letters, Section B: Nuclear, Elementary Particle and High-Energy Physics*, 777:217–221, 2018.
- [71] Astrid Eichhorn and Aaron Held. Towards implications of asymptotically safe gravity for particle physics. 2019.
- [72] Aaron Held, Roman Gold, and Astrid Eichhorn. Asymptotic safety casts its shadow. *Journal of Cosmology and Astroparticle Physics*, 2019(6), 2019.

- [73] Aaron Held and René Sondenheimer. Higgs stability-bound and fermionic dark matter. *Journal of High Energy Physics*, 2019(2), 2019.
- [74] Manuel Reichert and Juri Smirnov. Dark matter meets quantum gravity. *Physical Review D*, 101(6), oct 2020.
- [75] Reinhard Alkofer, Astrid Eichhorn, Aaron Held, Carlos M Nieto, Roberto Percacci, and Markus Schröfl. Quark masses and mixings in minimally parameterized UV completions of the Standard Model. *Annals of Physics*, 421, 2020.
- [76] Astrid Eichhorn and Martin Pauly. Safety in darkness: Higgs portal to simple Yukawa systems. 2020.
- [77] Roberto Percacci. *An introduction to covariant quantum gravity and asymptotic safety*, volume 3. World Scientific Publishing Co. Pte. Ltd., apr 2017.
- [78] Martin Reuter and Frank Saueressig. *Quantum Gravity and the Functional Renormalization Group*. Cambridge University Press, 2019.
- [79] Max Niedermaier and Martin Reuter. The asymptotic safety scenario in quantum gravity, dec 2006.
- [80] Daniel F. Litim. Renormalization group and the Planck scale, feb 2011.
- [81] Martin Reuter and Frank Saueressig. Quantum Einstein gravity. *New Journal of Physics*, 14, feb 2012.
- [82] Abhay Ashtekar, Martin Reuter, and Carlo Rovelli. From general relativity to quantum gravity. In *General Relativity and Gravitation: A Centennial Perspective*, pages 553–611. Cambridge University Press, aug 2015.
- [83] Alfio Bonanno and Frank Saueressig. La cosmologie asymptotiquement sûre : un rapport d'étape, feb 2017.
- [84] Astrid Eichhorn. An Asymptotically Safe Guide to Quantum Gravity and Matter, jan 2019.
- [85] Manuel Reichert. Lecture notes: Functional renormalisation group and asymptotically safe quantum gravity. In *Proceedings of Science*, volume 384, page 005. Sissa Medialab Srl, apr 2019.
- [86] Antonio D. Pereira. Quantum Spacetime and the Renormalization Group: Progress and Visions. In *Progress and Visions in Quantum Theory in View of Gravity*, pages 93–117. Springer International Publishing, apr 2020.
- [87] Astrid Eichhorn. Asymptotically safe gravity. feb 2020.

- [88] Jan M. Pawłowski and Manuel Reichert. Quantum gravity: a fluctuating point of view. jul 2020.
- [89] J. Ambjørn, B. Durhuus, and J. Fröhlich. Diseases of triangulated random surface models, and possible cures. *Nuclear Physics, Section B*, 257(C):433–449, jan 1985.
- [90] V. A. Kazakov, I. K. Kostov, and A. A. Migdal. Critical properties of randomly triangulated planar random surfaces. *Physics Letters B*, 157(4):295–300, jul 1985.
- [91] F. David. Planar diagrams, two-dimensional lattice gravity and surface models. *Nuclear Physics, Section B*, 257(C):45–58, sep 1985.
- [92] D. V. Boulatov, V. A. Kazakov, I. K. Kostov, and A. A. Migdal. Analytical and numerical study of a model of dynamically triangulated random surfaces. *Nuclear Physics, Section B*, 275(4):641–686, dec 1986.
- [93] J. Ambjørn, B. Durhuus, J. Fröhlich, and P. Orland. The appearance of critical dimensions in regulated string theories. *Nuclear Physics, Section B*, 270(C):457–482, jan 1986.
- [94] A. Billoire and F. David. Microcanonical simulations of randomly triangulated planar random surfaces. *Physics Letters B*, 168(3):279–283, mar 1986.
- [95] T. Regge. General relativity without coordinates. *Il Nuovo Cimento Series 10*, 19(3):558–571, feb 1961.
- [96] RUTH M. WILLIAMS. DISCRETE QUANTUM GRAVITY: THE REGGE CALCULUS APPROACH. *International Journal of Modern Physics B*, 06(11n12):2097–2108, 1992.
- [97] John W. Barrett, Daniele Oriti, and Ruth M. Williams. Tullio Regge’s legacy: Regge calculus and discrete gravity. dec 2018.
- [98] Jeff Cheeger, Werner Müller, and Robert Schrader. On the curvature of piecewise flat spaces. *Communications in Mathematical Physics*, 92(3):405–454, sep 1984.
- [99] M.E. Agishtein and A.A. Migdal. Simulations of four-dimensional simplicial quantum gravity as dynamical triangulation. *Modern Physics Letters A*, 07(12):1039–1061, apr 1992.
- [100] M.E. Aghisthein and A.A. Migdal. Simulations of four-dimensional simplicial quantum gravity as dynamical triangulation. *Modern Physics Letters A*, 07(12):1039–1061, apr 1992.

- [101] S. Catterall, J. Kogut, and R. Renken. Phase structure of four dimensional simplicial quantum gravity. *Physics Letters B*, 328(3-4):277–283, jan 1994.
- [102] Jan Ambjørn and Jerzy Jurkiewicz. Four-dimensional simplicial quantum gravity. *Physics Letters B*, 278(1-2):42–50, mar 1992.
- [103] S. Catterall, J. Kogut, and R. Renken. Phase structure of four dimensional simplicial quantum gravity. *Physics Letters B*, 328(3-4):277–283, jun 1994.
- [104] Bas V. de Bakker and Jan Smit. Curvature and scaling in 4D dynamical triangulation. *Nuclear Physics, Section B*, 439(1-2):239–258, jul 1995.
- [105] J. Ambjørn and Jerzy Jurkiewicz. Scaling in four-dimensional quantum gravity. *Nuclear Physics, Section B*, 451(3):643–676, mar 1995.
- [106] P. Bialas, Z. Burda, A. Krzywicki, and B. Petersson. Focusing on the fixed point of 4D simplicial gravity. *Nuclear Physics B*, 472(1-2):293–308, jan 1996.
- [107] Bas V. De Bakker. Further evidence that the transition of 4D dynamical triangulation is 1st order. *Physics Letters, Section B: Nuclear, Elementary Particle and High-Energy Physics*, 389(2):238–242, dec 1996.
- [108] J. Laiho and D. Coumbe. Evidence for asymptotic safety from lattice quantum gravity. *Physical Review Letters*, 107(16), apr 2011.
- [109] Raghav G. Jha, Jack Laiho, and Judah Unmuth-Yockey. Lattice quantum gravity with scalar fields. In *Proceedings of Science*, volume 334, 2018.
- [110] J Laiho, S Bassler, D Coumbe, D Du, and J T Neelakanta. Lattice quantum gravity and asymptotic safety. *Physical Review D*, 96(6), 2017.
- [111] Raghav G Jha, Jack Laiho, and Judah Unmuth-Yockey. Lattice quantum gravity with scalar fields. Technical report.
- [112] J. Ambjørn and R. Loll. Non-perturbative Lorentzian quantum gravity, causality and topology change. *Nuclear Physics B*, 536(1-2):407–434, may 1998.
- [113] J. Ambjørn, J. Jurkiewicz, and R. Loll. Dynamically triangulating Lorentzian quantum gravity. *Nuclear Physics B*, 610(1-2):347–382, may 2001.
- [114] R. Loll. Nonperturbative 3D Lorentzian quantum gravity. *Physical Review D - Particles, Fields, Gravitation and Cosmology*, 64(4):17, nov 2001.
- [115] J. Ambjørn, J. Jurkiewicz, and R. Loll. Nonperturbative Lorentzian path integral for gravity. *Physical Review Letters*, 85(5):924–927, feb 2000.
- [116] J. Ambjørn, J. Jurkiewicz, and R. Loll. Emergence of a 4D world from causal quantum gravity. *Physical Review Letters*, 93(13), apr 2004.

- [117] J. Ambjørn, J. Jurkiewicz, and R. Loll. Reconstructing the universe. *Physical Review D - Particles, Fields, Gravitation and Cosmology*, 72(6), may 2005.
- [118] J. Ambjørn, A. Görlich, J. Jurkiewicz, and R. Loll. Nonperturbative quantum gravity, mar 2012.
- [119] R. Loll. Quantum gravity from causal dynamical triangulations: A review, may 2020.
- [120] Jan Ambjorn, Jakub Gizbert-Studnicki, Andrzej Görlich, Jerzy Jurkiewicz, and Renate Loll. Renormalization in Quantum Theories of Geometry. *Frontiers in Physics*, 8, 2020.
- [121] J. Ambjørn, J. Jurkiewicz, and R. Loll. The spectral dimension of the universe is scale dependent. *Physical Review Letters*, 95(17), oct 2005.
- [122] J Ambjørn, A Görlich, J Jurkiewicz, and R Loll. Planckian birth of a quantum de sitter universe. *Physical Review Letters*, 100(9), 2008.
- [123] J. Ambjørn, A. Görlich, J. Jurkiewicz, and R. Loll. Nonperturbative quantum de Sitter universe. *Physical Review D - Particles, Fields, Gravitation and Cosmology*, 78(6), jul 2008.
- [124] Jan Ambjørn, S. Jordan, J. Jurkiewicz, and R. Loll. Second-order phase transition in causal dynamical triangulations. *Physical Review Letters*, 107(21), aug 2011.
- [125] J Ambjørn, J Gizbert-Studnicki, A Görlich, J Jurkiewicz, N Klitgaard, and R Loll. Characteristics of the new phase in CDT. *European Physical Journal C*, 77(3), 2017.
- [126] Jan Ambjorn, Jakub Gizbert-Studnicki, Andrzej Görlich, Jerzy Jurkiewicz, and Renate Loll. Renormalization in Quantum Theories of Geometry. *Frontiers in Physics*, 8, feb 2020.
- [127] Jan Ambjørn, Daniel N. Coumbe, Jakub Gizbert-Studnicki, and Jerzy Jurkiewicz. Signature change of the metric in CDT quantum gravity? *Journal of High Energy Physics*, 2015(8), mar 2015.
- [128] D. N. Coumbe, J. Gizbert-Studnicki, and J. Jurkiewicz. Exploring the new phase transition of CDT. *Journal of High Energy Physics*, 2016(2):1–11, oct 2016.
- [129] Jan Ambjørn, S. Jordan, J. Jurkiewicz, and R. Loll. Second- and first-order phase transitions in causal dynamical triangulations. *Physical Review D - Particles, Fields, Gravitation and Cosmology*, 85(12), jun 2012.

- [130] J Ambjørn, D Coumbe, J Gizbert-Studnicki, A Görlich, and J Jurkiewicz. Critical phenomena in causal dynamical triangulations. *Classical and Quantum Gravity*, 36(22), 2019.
- [131] Vincent Rivasseau. Quantum gravity and renormalization: The tensor track. In *AIP Conference Proceedings*, volume 1444, pages 18–29, dec 2012.
- [132] Vincent Rivasseau. The Tensor Track: An update. In *Symmetries and Groups in Contemporary Physics*, pages 63–74. sep 2013.
- [133] Vincent Rivasseau. The Tensor Track, III. *Fortschritte der Physik*, 62(2):81–107, nov 2014.
- [134] Vincent Rivasseau. Random tensors and quantum gravity. *Symmetry, Integrability and Geometry: Methods and Applications (SIGMA)*, 12:17, 2016.
- [135] Edouard Brézin and Jean Zinn-Justin. Renormalization group approach to matrix models. *Physics Letters B*, 288(1-2):54–58, jun 1992.
- [136] Luca Bombelli, Joochan Lee, David Meyer, and Rafael D. Sorkin. Space-time as a causal set. *Physical Review Letters*, 59(5):521–524, aug 1987.
- [137] Fay Dowker. Causal sets and the deep structure of spacetime. In *100 Years of Relativity: Space-Time Structure: Einstein and Beyond*, pages 445–464. World Scientific Publishing Co., aug 2005.
- [138] Joe Henson. The causal set approach to Quantum Gravity. In *Approaches to Quantum Gravity: Toward a New Understanding of Space, Time and Matter*, volume 9780521860, pages 393–413. Cambridge University Press, jan 2009.
- [139] Joe Henson. Discovering the Discrete Universe. mar 2010.
- [140] Sumati Surya. Directions in Causal Set Quantum Gravity. mar 2011.
- [141] Fay Dowker. Introduction to causal sets and their phenomenology. *General Relativity and Gravitation*, 45(9):1651–1667, sep 2013.
- [142] Sumati Surya. The causal set approach to quantum gravity, mar 2019.
- [143] Astrid Eichhorn. Steps towards Lorentzian quantum gravity with causal sets. In *Journal of Physics: Conference Series*, volume 1275, 2019.
- [144] John C. Baez. An Introduction to Spin Foam Models of BF Theory and Quantum Gravity. pages 25–93. Springer, Berlin, Heidelberg, 2000.
- [145] Alejandro Perez. Introduction to Loop Quantum Gravity and Spin Foams. sep 2004.

- [146] Carlo Rovelli. Zakopane lectures on loop gravity. In *Proceedings of Science*, volume 140. Sissa Medialab Srl, feb 2011.
- [147] Bianca Dittrich. From the discrete to the continuous: Towards a cylindrically consistent dynamics. *New Journal of Physics*, 14(27pp):123004, dec 2012.
- [148] Bianca Dittrich and Sebastian Steinhaus. Time evolution as refining, coarse graining and entangling. *New Journal of Physics*, 16, nov 2014.
- [149] Bianca Dittrich. The continuum limit of loop quantum gravity: A framework for solving the theory. In *Loop Quantum Gravity: The First 30 Years*, pages 153–179. World Scientific Publishing Co. Pte. Ltd., sep 2017.
- [150] Etera R. Livine. Deformation operators of spin networks and coarse-graining. *Classical and Quantum Gravity*, 31(7), oct 2014.
- [151] Benjamin Bahr and Sebastian Steinhaus. Numerical Evidence for a Phase Transition in 4D Spin-Foam Quantum Gravity. *Physical Review Letters*, 117(14), may 2016.
- [152] Sebastian Steinhaus. Coarse Graining Spin Foam Quantum Gravity—A Review. *Frontiers in Physics*, 8, 2020.
- [153] Steffen Gielen, Daniele Oriti, and Lorenzo Sindoni. Cosmology from group field theory formalism for quantum gravity. *Physical Review Letters*, 111(3), mar 2013.
- [154] Daniele Oriti, Lorenzo Sindoni, and Edward Wilson-Ewing. Emergent Friedmann dynamics with a quantum bounce from quantum gravity condensates. *Classical and Quantum Gravity*, 33(22), feb 2016.
- [155] Daniele Oriti. The microscopic dynamics of quantum space as a group field theory. *Foundations of Space and Time: Reflections on Quantum Gravity*, 97805211114:257–320, oct 2011.
- [156] Daniele Oriti. Group field theory as the microscopic description of the quantum spacetime fluid: A new perspective on the continuum in quantum gravity. In *Proceedings of Science*, 2007.
- [157] F David. *Simplicial Quantum Gravity and Random Lattices*. 1993.
- [158] V. A. Kazakov. Ising model on a dynamical planar random lattice: Exact solution. *Physics Letters A*, 119(3):140–144, dec 1986.
- [159] D. V. Boulatov and V. A. Kazakov. The ising model on a random planar lattice: The structure of the phase transition and the exact critical exponents. *Physics Letters B*, 186(3-4):379–384, mar 1987.

- [160] V.A. Kazakov. The appearance of matter fields from quantum fluctuations of 2d-gravity. *Modern Physics Letters A*, 04(22):2125–2139, oct 1989.
- [161] J. Ambjørn, J. Jurkiewicz, and Yu M. Makeenko. Multiloop correlators for two-dimensional quantum gravity. *Physics Letters B*, 251(4):517–524, nov 1990.
- [162] Edouard Brézin, Michael R. Douglas, Vladimir Kazakov, and Stephen H. Shenker. The ising model coupled to 2D gravity. A nonperturbative analysis. *Physics Letters B*, 237(1):43–46, mar 1990.
- [163] F. David. Conformal Field Theories coupled to 2D gravity in the conformal gauge. *Modern Physics Letters A*, 03(17):1651–1656, dec 1988.
- [164] Yu. Makeenko. Loop Equations and Virasoro Constraints in Matrix Models. dec 1991.
- [165] Robbert Dijkgraaf, Herman Verlinde, and Erik Verlinde. Loop equations and Virasoro constraints in non-perturbative two-dimensional quantum gravity. *Nuclear Physics, Section B*, 348(3):435–456, jan 1991.
- [166] Jacques Distler and Hikaru Kawai. Conformal field theory and 2D quantum gravity. *Nuclear Physics, Section B*, 321(2):509–527, jul 1989.
- [167] MASAFUMI Fukuma, HIKARU Kawai, and RYUICHI Nakayama. Continuum Schwinger-Dyson equations and universeal structures in two-dimensional quantum gravity. *International Journal of Modern Physics A*, 06(08):1385–1406, mar 1991.
- [168] Bertrand Duplantier. Conformal Random Geometry. aug 2006.
- [169] V.G. Knizhnik, A.M. Polyakov, and A.B. Zamolodchikov. Fractal Structure of 2d quantum gravity. *Modern Physics Letters A*, 03(08):819–826, jul 1988.
- [170] Petr Šeba. Parking and the visual perception of space. *Journal of Statistical Mechanics: Theory and Experiment*, 2009(10), jul 2009.
- [171] Giacomo Livan, Marcel Novaes, and Pierpaolo Vivo. Introduction to Random Matrices - Theory and Practice. 2017.
- [172] P. Di Francesco, P. Ginsparg, and J. Zinn-Justin. 2D gravity and random matrices, jun 1995.
- [173] J Ambjørn, M Carfora, and A Marzuoli. *The Geometry of Dynamical Triangulations*. 1997.
- [174] Margaret M Bayer and Louis J Billera. Generalized Dehn-Sommerville relations for polytopes, spheres and Eulerian partially ordered sets. *Inventiones Mathematicae*, 79(1):143–157, 1985.

- [175] Jan Ambjørn, Jerzy Jurkiewicz, and Charlotte F Kristjansen. Quantum gravity, dynamical triangulations and higher-derivative regularization. Technical report, 1993.
- [176] Herbert W. Hamber and Ruth M. Williams. HIGHER DERIVATIVE QUANTUM GRAVITY ON A SIMPLICIAL LATTICE. *Nucl. Phys. B*, 248:392–414, 1984. [Erratum: *Nucl.Phys.B* 260, 747–747 (1985)].
- [177] Yann Ollivier. Ricci curvature of Markov chains on metric spaces. *Journal of Functional Analysis*, 256(3):810–864, feb 2009.
- [178] N. Klitgaard and R. Loll. Introducing quantum Ricci curvature. *Physical Review D*, 97(4), dec 2018.
- [179] N Klitgaard and R Loll. Implementing quantum Ricci curvature. *Physical Review D*, 97(10), 2018.
- [180] Jan Ambjorn, Bergfinnur Durhuus, and Thordur Jonsson. Three-dimensional simplicial quantum gravity and generalized matrix models. *Mod. Phys. Lett.*, A6:1133–1146, 1991.
- [181] Naoki Sasakura. Tensor model for gravity and orientability of manifold. *Mod. Phys. Lett.*, A6:2613–2624, 1991.
- [182] Neil Godfrey and Mark Gross. Simplicial quantum gravity in more than two-dimensions. *Phys. Rev.*, D43:1749–1753, 1991.
- [183] Mark Gross. Tensor models and simplicial quantum gravity in > 2 -D. *Nucl. Phys. Proc. Suppl.*, 25A:144–149, 1992.
- [184] Razvan Gurau. Colored Group Field Theory. *Communications in Mathematical Physics*, 304(1):69–93, jul 2011.
- [185] Razvan Gurau and James P. Ryan. Colored tensor models - A review. *Symmetry, Integrability and Geometry: Methods and Applications (SIGMA)*, 8:78, sep 2012.
- [186] Valentin Bonzom, Razvan Gurau, Aldo Riello, and Vincent Rivasseau. Critical behavior of colored tensor models in the large N limit. *Nuclear Physics B*, 853(1):174–195, may 2011.
- [187] Valentin Bonzom, Razvan Gurau, and Vincent Rivasseau. Random tensor models in the large N limit: Uncoloring the colored tensor models. *Physical Review D - Particles, Fields, Gravitation and Cosmology*, 85(8), feb 2012.
- [188] Razvan Gurau. The $1/N$ Expansion of Colored Tensor Models. *Annales Henri Poincare*, 12(5):829–847, nov 2011.

- [189] R. Gurau and V. Rivasseau. The $1/N$ expansion of colored tensor models in arbitrary dimension. *EPL*, 95(5), sep 2011.
- [190] Razvan Gurau. The Complete $1/N$ Expansion of Colored Tensor Models in Arbitrary Dimension. *Annales Henri Poincare*, 13(3):399–423, feb 2012.
- [191] Pablo Diaz. Backgrounds from Tensor Models: A Proposal. 2020.
- [192] Subir Sachdev and Jinwu Ye. Gapless spin-fluid ground state in a random quantum Heisenberg magnet. *Physical Review Letters*, 70(21):3339–3342, dec 1993.
- [193] Joseph Polchinski and Vladimir Rosenhaus. The spectrum in the Sachdev-Ye-Kitaev model. *Journal of High Energy Physics*, 2016(4), jan 2016.
- [194] Edward Witten. An SYK-like model without disorder. *Journal of Physics A: Mathematical and Theoretical*, 52(47), oct 2019.
- [195] Igor R. Klebanov and Grigory Tarnopolsky. Uncolored random tensors, melon diagrams, and the Sachdev-Ye-Kitaev models. *Physical Review D*, 95(4), nov 2017.
- [196] Razvan Gurau. The complete $1/N$ expansion of a SYK-like tensor model. *Nuclear Physics B*, 916:386–401, mar 2017.
- [197] Razvan Gurau. Quenched equals annealed at leading order in the colored SYK model. *EPL*, 119(3), 2017.
- [198] Valentin Bonzom, Luca Lionni, and Adrian Tanasa. Diagrammatics of a colored SYK model and of an SYK-like tensor model, leading and next-to-leading orders. *Journal of Mathematical Physics*, 58(5), feb 2017.
- [199] Matteo Beccaria and Arkady A. Tseytlin. Partition function of free conformal fields in 3-plet representation. *Journal of High Energy Physics*, 2017(5), mar 2017.
- [200] Steven S. Gubser, Matthew Heydeman, Christian Jepsen, Sarthak Parikh, Ingmar Saberi, Bogdan Stoica, and Brian Trundy. Melonic theories over diverse number systems. *Physical Review D*, 98(12), jul 2018.
- [201] Simone Giombi, Igor R. Klebanov, and Grigory Tarnopolsky. Bosonic tensor models at large N and small ϵ . *Physical Review D*, 96(10), jul 2017.
- [202] Ksenia Bulycheva, Igor R. Klebanov, Alexey Milekhin, and Grigory Tarnopolsky. Spectra of operators in large N tensor models. *Physical Review D*, 97(2), jul 2018.

- [203] Sayantan Choudhury, Anshuman Dey, Indranil Halder, Lavneet Janagal, Shiraz Minwalla, and Rohan Poojary. Notes on Melonic $O(N)^{q-1}$ Tensor Models. *Journal of High Energy Physics*, 2018(6), jul 2017.
- [204] Chethan Krishnan, K. V. Pavan Kumar, and Dario Rosa. Contrasting SYK-like models. *Journal of High Energy Physics*, 2018(1), sep 2018.
- [205] Shiroman Prakash and Ritam Sinha. A complex fermionic tensor model in d dimensions. *Journal of High Energy Physics*, 2018(2), oct 2018.
- [206] Chi-Ming Chang, Sean Colin-Ellerin, and Mukund Rangamani. On Melonic Supertensor Models. *Journal of High Energy Physics*, 2018(10), jun 2018.
- [207] Simone Giombi, Igor R. Klebanov, Fedor Popov, Shiroman Prakash, and Grigory Tarnopolsky. Prismatic large N models for bosonic tensors. *Physical Review D*, 98(10), aug 2018.
- [208] Dario Benedetti and Nicolas Delporte. Phase diagram and fixed points of tensorial Gross-Neveu models in three dimensions. *Journal of High Energy Physics*, 2019(1), oct 2019.
- [209] Jaewon Kim, Igor R. Klebanov, Grigory Tarnopolsky, and Wenli Zhao. Symmetry Breaking in Coupled SYK or Tensor Models. *Physical Review X*, 9(2), feb 2019.
- [210] Dario Benedetti, Razvan Gurau, and Sabine Harribey. Line of fixed points in a bosonic tensor model. *Journal of High Energy Physics*, 2019(6), mar 2019.
- [211] Igor R. Klebanov, Preethi N. Pallegar, and Fedor K. Popov. Majorana fermion quantum mechanics for higher rank tensors. *Physical Review D*, 100(8), may 2019.
- [212] Fedor K. Popov. Supersymmetric tensor model at large N and small e . *Physical Review D*, 101(2), jul 2020.
- [213] Dario Benedetti, Razvan Gurau, Sabine Harribey, and Kenta Suzuki. Hints of unitarity at large N in the $O(N)^3$ tensor field theory. *Journal of High Energy Physics*, 2020(2), sep 2019.
- [214] Dario Benedetti, Nicolas Delporte, Sabine Harribey, and Ritam Sinha. Sextic tensor field theories in rank 3 and 5 . *Journal of High Energy Physics*, 2020(6), dec 2019.
- [215] Dario Benedetti, Razvan Gurau, and Kenta Suzuki. Conformal symmetry and composite operators in the $O(N)^3$ tensor field theory. *Journal of High Energy Physics*, 2020(6), jun 2020.
- [216] Dario Benedetti. Melonic CFTs. page 168, 2020.

- [217] Harold Erbin, Vincent Lahoche, and Mohamed Tamaazousti. Constructive expansion for quartic vector fields theories. I. Low dimensions. 2019.
- [218] Vincent Lahoche, Dine Ousmane Samary, and Mohamed Tamaazousti. Generalized scale behavior and renormalization group for principal component analysis. 2020.
- [219] Sylvain Carrozza and Adrian Tanasa. $O(N)$ Random Tensor Models. *Letters in Mathematical Physics*, 106(11):1531–1559, dec 2016.
- [220] Adrian Tanasa. Multi-orientable group field theory. *Journal of Physics A: Mathematical and Theoretical*, 45(16), 2012.
- [221] Stéphane Dartois, Vincent Rivasseau, and Adrian Tanasa. The $1/N$ expansion of multi-orientable random tensor models. 2013.
- [222] Eric Fusy and Adrian Tanasa. Asymptotic expansion of the multi-orientable random tensor model. *Electronic Journal of Combinatorics*, 22(1), 2015.
- [223] Razvan Gurau, Adrian Tanasa, and Donald R Youmans. The double scaling limit of the multi-orientable tensor model. *EPL*, 111(2), 2015.
- [224] Adrian Tanasa. The multi-orientable random tensor model, a review, 2016.
- [225] Astrid Eichhorn and Tim Koslowski. Continuum limit in matrix models for quantum gravity from the functional renormalization group. *Physical Review D - Particles, Fields, Gravitation and Cosmology*, 88(8), sep 2013.
- [226] Astrid Eichhorn and Tim Koslowski. Flowing to the continuum in discrete tensor models for quantum gravity. *Ann. Inst. H. Poincaré Comb. Phys. Interact.*, 5(2):173–210, 2018.
- [227] Valentin Bonzom, Thibault Delepouve, and Vincent Rivasseau. Enhancing non-melonic triangulations: A tensor model mixing melonic and planar maps. *Nuclear Physics B*, 895:161–191, feb 2015.
- [228] Valentin Bonzom. Large N limits in tensor models: Towards more universality classes of colored triangulations in dimension $d > 2$, mar 2016.
- [229] Luca Lionni and Johannes Thürigen. Multi-critical behaviour of 4-dimensional tensor models up to order 6. *Nuclear Physics B*, 941:600–635, jul 2019.
- [230] Valentin Bonzom, Luca Lionni, and Vincent Rivasseau. Colored triangulations of arbitrary dimensions are stuffed Walsh maps. aug 2015.
- [231] Valentin Bonzom and Luca Lionni. Counting gluings of octahedra. *Electronic Journal of Combinatorics*, 24(3), aug 2017.

- [232] Astrid Eichhorn and Tim Koslowski. Towards phase transitions between discrete and continuum quantum spacetime from the Renormalization Group. *Phys. Rev.*, D90(10):104039, 2014.
- [233] Dario Benedetti, Joseph Ben Geloun, and Daniele Oriti. Functional renormalisation group approach for tensorial group field theory: a rank-3 model. *Journal of High Energy Physics*, 2015(3), nov 2015.
- [234] Dario Benedetti and Vincent Lahoche. Functional renormalization group approach for tensorial group field theory: A rank-6 model with closure constraint. *Classical and Quantum Gravity*, 33(9), apr 2016.
- [235] Joseph Ben Geloun, Riccardo Martini, and Daniele Oriti. Functional Renormalization Group analysis of a Tensorial Group Field Theory on R. *EPL*, 112(3), aug 2015.
- [236] Joseph Ben Geloun, Riccardo Martini, and Daniele Oriti. Functional renormalization group analysis of tensorial group field theories on Rd. *Physical Review D*, 94(2), jan 2016.
- [237] Joseph Ben Geloun and Tim Koslowski. Nontrivial UV behavior of rank-4 tensor field models for quantum gravity. jun 2016.
- [238] Sylvain Carrozza and Vincent Lahoche. Asymptotic safety in three-dimensional SU(2) group field theory: Evidence in the local potential approximation. *Classical and Quantum Gravity*, 34(11), dec 2017.
- [239] Joseph Ben Geloun, Tim A. Koslowski, Daniele Oriti, and Antonio D. Pereira. Functional renormalization group analysis of rank-3 tensorial group field theory: The full quartic invariant truncation. *Physical Review D*, 97(12), may 2018.
- [240] Vincent Lahoche and Dine Ousmane Samary. Functional renormalization group for the U (1)- T56 tensorial group field theory with closure constraint. *Physical Review D*, 95(4), aug 2017.
- [241] Vincent Lahoche and Dine Ousmane Samary. Ward identity violation for melonic T4-truncation, sep 2019.
- [242] Vincent Lahoche and Dine Ousmane Samary. Nonperturbative renormalization group beyond the melonic sector: The effective vertex expansion method for group fields theories. *Physical Review D*, 98(12), dec 2018.
- [243] Vincent Lahoche and Dine Ousmane Samary. Unitary symmetry constraints on tensorial group field theory renormalization group flow. *Classical and Quantum Gravity*, 35(19), sep 2018.

- [244] Sylvain Carrozza, Vincent Lahoche, and Daniele Oriti. Renormalizable group field theory beyond melonic diagrams: An example in rank four. *Physical Review D*, 96(6), sep 2017.
- [245] Vincent Lahoche and Dine Ousmane Samary. Progress in solving the nonperturbative renormalization group for tensorial group field theory, mar 2019.
- [246] Vincent Lahoche and Dine Ousmane Samary. Ward-constrained melonic renormalization group flow for the rank-four ϕ^6 tensorial group field theory. *Physical Review D*, 100(8), oct 2019.
- [247] Vincent Lahoche and Dine Ousmane Samary. On the reliability of local truncations for the random tensor models renormalization group flow. 2020.
- [248] José M. Martín-García. xTensor: Fast abstract tensor computer algebra.
- [249] Remi C. Avohou, Joseph Ben Geloun, and Nicolas Dub. On the counting of $\text{SO}(N)$ tensor invariants. jul 2019.
- [250] Joseph Ben Geloun. On the counting tensor model observables as $U(N)$ and $O(N)$ classical invariants. page 175, 2020.
- [251] Joseph Ben Geloun and Sanjaye Ramgoolam. Counting tensor model observables and branched covers of the 2-sphere. *Annales de l'Institut Henri Poincaré (D) Combinatorics, Physics and their Interactions*, 1(1):77–138, 2014.
- [252] Vincent Lahoche and Dine Ousmane Samary. Ward identity violation for melonic T4-truncation, mar 2019.
- [253] Vincent Lahoche and Dine Ousmane Samary. Ward-constrained melonic renormalization group flow for the rank-four ϕ^6 tensorial group field theory. *Physical Review D*, 100(8), oct 2019.
- [254] Vincent Lahoche and Dine Ousmane Samary. Ward-constrained melonic renormalization group flow. *Physics Letters, Section B: Nuclear, Elementary Particle and High-Energy Physics*, 802:135173, mar 2020.
- [255] Vincent Lahoche and Dine Ousmane Samary. On the reliability of the local truncations for the random tensor models renormalization group flow. may 2020.
- [256] Ezinvi Baloitcha and Vincent Lahoche. Flowing in discrete gravity models and Ward identities: A review. jan 2020.
- [257] Astrid Eichhorn, Tim Koslowski, and Antonio D. Pereira. Status of background-independent coarse graining in tensor models for quantum gravity, feb 2019.

- [258] Jorn Biemans, Alessia Platania, and Frank Saueressig. Quantum gravity on foliated spacetimes: Asymptotically safe and sound. *Physical Review D*, 95(8), sep 2017.
- [259] Herbert W. Hamber, Reiko Toriumi, and Ruth M. Williams. Wheeler-DeWitt equation in 2+1 dimensions. *Physical Review D - Particles, Fields, Gravitation and Cosmology*, 86(8), jul 2012.
- [260] Atlas Collaboration, G. Aad, and Others. Observation of a new particle in the search for the Standard Model Higgs boson with the ATLAS detector at the LHC. *Physics Letters, Section B: Nuclear, Elementary Particle and High-Energy Physics*, 716(1):1–29, jul 2012.
- [261] Edward Witten. Cosmological consequences of a light Higgs boson. *Nuclear Physics, Section B*, 177(3):477–488, jan 1981.
- [262] Alan H. Guth and Erick J. Weinberg. Cosmological consequences of a first-order phase transition in the SU5 grand unified model. *Physical Review D*, 23(4):876–885, nov 1981.
- [263] Paul Joseph Steinhardt. The Weinberg-Salam model and early cosmology. *Nuclear Physics, Section B*, 179(3):492–508, mar 1981.
- [264] Paul Joseph Steinhardt. Relativistic detonation waves and bubble growth in false vacuum decay. *Physical Review D*, 25(8):2074–2085, apr 1982.
- [265] Edward Witten. Cosmic separation of phases. *Physical Review D*, 30(2):272–285, jul 1984.
- [266] C. J. Hogan. Gravitational radiation from cosmological phase transitions. *Monthly Notices of the Royal Astronomical Society*, 218(4):629–636, 1986.
- [267] Pau Amaro-Seoane and Others. Laser Interferometer Space Antenna. feb 2017.
- [268] K. Kajantie, M. Laine, K. Rummukainen, and M. Shaposhnikov. Is there a hot electroweak phase transition at $m_H > m_W$? *Physical Review Letters*, 77(14):2887–2890, may 1996.
- [269] Ankit Beniwal, Marek Lewicki, James D. Wells, Martin White, and Anthony G. Williams. Gravitational wave, collider and dark matter signals from a scalar singlet electroweak baryogenesis. *Journal of High Energy Physics*, 2017(8), Aug 2017.
- [270] Iason Baldes. Gravitational waves from the asymmetric-dark-matter generating phase transition. *Journal of Cosmology and Astroparticle Physics*, 2017(05):028–028, May 2017.

- [271] Moritz Breitbach, Joachim Kopp, Eric Madge, Toby Opferkuch, and Pedro Schwaller. Dark, cold, and noisy: constraining secluded hidden sectors with gravitational waves. *Journal of Cosmology and Astroparticle Physics*, 2019(07):007–007, Jul 2019.
- [272] S. W. Ham and S. K. Oh. Electroweak phase transition in the standard model with a dimension-six Higgs operator at the one-loop level. *Physical Review D - Particles, Fields, Gravitation and Cosmology*, 70(9), aug 2004.
- [273] Christophe Grojean, Géraldine Servant, and James D. Wells. First-order electroweak phase transition in the standard model with a low cutoff. *Physical Review D - Particles, Fields, Gravitation and Cosmology*, 71(3), jul 2005.
- [274] Qing Hong Cao, Fa Peng Huang, Ke Pan Xie, and Xinmin Zhang. Testing the electroweak phase transition in scalar extension models at lepton colliders. *Chinese Physics C*, 42(2), aug 2018.
- [275] M. E. Shaposhnikov. Baryon asymmetry of the universe in standard electroweak theory. *Nuclear Physics, Section B*, 287(C):757–775, jan 1987.
- [276] Manuel Reichert, Astrid Eichhorn, Holger Gies, Jan M. Pawłowski, Tilman Plehn, and Michael M. Scherer. Probing baryogenesis through the Higgs boson self-coupling. *Physical Review D*, 97(7), oct 2018.
- [277] K. Kajantie, M. Laine, K. Rummukainen, and M. Shaposhnikov. The electroweak phase transition: A non-perturbative analysis. *Nuclear Physics B*, 466(1-2):189–258, oct 1996.
- [278] K. Kajantie, M. Laine, K. Rummukainen, and M. Shaposhnikov. A non-perturbative analysis of the finite-T phase transition in SU(2) \times U(1) electroweak theory. *Nuclear Physics B*, 493(1-2):413–438, dec 1997.
- [279] Michela D’Onofrio and Kari Rummukainen. Standard model cross-over on the lattice. *Physical Review D*, 93(2), aug 2016.
- [280] Oliver Gould, Jonathan Kozaczuk, Lauri Niemi, Michael J. Ramsey-Musolf, Tuomas V.I. Tenkanen, and David J. Weir. Nonperturbative analysis of the gravitational waves from a first-order electroweak phase transition. *Physical Review D*, 100(11), mar 2019.
- [281] Laurent Canetti, Marco Drewes, and Mikhail Shaposhnikov. Matter and antimatter in the universe. *New Journal of Physics*, 14, 2012.
- [282] D. Sakharov. Violation of cp in variance, C asymmetry, and baryon asymmetry of the universe. *Soviet Physics - Uspekhi*, 34(5):392–393, may 1991.
- [283] M. E. Shaposhnikov. Standard model solution of the baryogenesis problem. *Physics Letters B*, 277(3):324–330, mar 1992.

- [284] Astrid Eichhorn, Holger Gies, Joerg Jaeckel, Tilman Plehn, Michael M Scherer, and René Sondenheimer. The Higgs mass and the scale of new physics. *Journal of High Energy Physics*, 2015(4), 2015.
- [285] J. Adams, N. Tetradis, J. Berges, F. Freire, C. Wetterich, and S. Bornholdt. Solving nonperturbative flow equations. *Modern Physics Letters A*, 10(31):2367–2379, oct 1995.
- [286] Jan M Pawłowski and Fabian Rennecke. Higher order quark-mesonic scattering processes and the phase structure of QCD. *Physical Review D - Particles, Fields, Gravitation and Cosmology*, 90(7), 2014.
- [287] Daniel D Scherer, Jens Braun, and Holger Gies. Many-flavor phase diagram of the $(2 + 1)$ d Gross-Neveu model at finite temperature. *Journal of Physics A: Mathematical and Theoretical*, 46(28), 2013.
- [288] A. D. Linde. Fate of the false vacuum at finite temperature: Theory and applications. *Physics Letters B*, 100(1):37–40, mar 1981.
- [289] A. D. Linde. Decay of the false vacuum at finite temperature. *Nuclear Physics, Section B*, 216(2):421–445, may 1983.
- [290] M. D. Rintoul and S. Torquato. Precise determination of the critical threshold and exponents in a three-dimensional continuum percolation model. *Journal of Physics A: Mathematical and General*, 30(16):84280–84281, aug 1997.
- [291] James M. Cline and Kimmo Kainulainen. Electroweak baryogenesis at high bubble wall velocities. *Physical Review D*, 101(6):063525, mar 2020.
- [292] K. Enqvist, J. Ignatius, K. Kajantie, and K. Rummukainen. Nucleation and bubble growth in a first-order cosmological electroweak phase transition. *Physical Review D*, 45(10):3415–3428, aug 1992.
- [293] Michael S. Turner, Erick J. Weinberg, and Lawrence M. Widrow. Bubble nucleation in first-order inflation and other cosmological phase transitions. *Physical Review D*, 46(6):2384–2403, sep 1992.
- [294] Felix Giese, Thomas Konstandin, and Jorinde Van De Vis. Model-independent energy budget of cosmological first-order phase transitions - A sound argument to go beyond the bag model. *Journal of Cosmology and Astroparticle Physics*, 2020(7):057, jul 2020.
- [295] Jose R. Espinosa, Thomas Konstandin, Jose M. No, and Geraldine Servant. Energy budget of cosmological first-order phase transitions. *Journal of Cosmology and Astroparticle Physics*, 2010(6), apr 2010.

- [296] Ariel Mégevand and Santiago Ramírez. Bubble nucleation and growth in very strong cosmological phase transitions. *Nuclear Physics B*, 919:74–109, nov 2017.
- [297] Ryusuke Jinno, Sangjun Lee, Hyeonseok Seong, and Masahiro Takimoto. Gravitational waves from first-order phase transitions: Towards model separation by bubble nucleation rate. *Journal of Cosmology and Astroparticle Physics*, 2017(11), aug 2017.
- [298] Daniel Cutting, Mark Hindmarsh, and David J. Weir. Gravitational waves from vacuum first-order phase transitions: From the envelope to the lattice. *Physical Review D*, 97(12), feb 2018.
- [299] Ryusuke Jinno, Sangjun Lee, Hyeonseok Seong, and Masahiro Takimoto. Gravitational waves from first-order phase transitions: Towards model separation by bubble nucleation rate. *Journal of Cosmology and Astroparticle Physics*, 2017(11), 2017.
- [300] Marc Kamionkowski, Arthur Kosowsky, and Michael S. Turner. Gravitational radiation from first-order phase transitions. *Physical Review D*, 49(6):2837–2851, oct 1994.
- [301] Ryusuke Jinno. Private Correspondence.
- [302] Chiara Caprini, Mark Hindmarsh, Stephan Huber, Thomas Konstandin, Jonathan Kozaczuk, Germano Nardini, Jose Miguel No, Antoine Petiteau, Pedro Schwaller, Géraldine Servant, and David J. Weir. Science with the space-based interferometer eLISA. II: Gravitational waves from cosmological phase transitions. *Journal of Cosmology and Astroparticle Physics*, 2016(4), dec 2016.
- [303] Chiara Caprini, Mikael Chala, Glauber C. Dorsch, Mark Hindmarsh, Stephan J. Huber, Thomas Konstandin, Jonathan Kozaczuk, Germano Nardini, Jose Miguel No, Kari Rummukainen, Pedro Schwaller, Geraldine Servant, Anders Tranberg, and David J. Weir. Detecting gravitational waves from cosmological phase transitions with LISA: An update. *Journal of Cosmology and Astroparticle Physics*, 2020(3), oct 2020.
- [304] Xiao Wang, Fa Peng Huang, and Xinmin Zhang. Phase transition dynamics and gravitational wave spectra of strong first-order phase transition in supercooled universe. *Journal of Cosmology and Astroparticle Physics*, 2020(5), mar 2020.
- [305] David J. Weir. Revisiting the envelope approximation: Gravitational waves from bubble collisions. *Physical Review D*, 93(12):124037, jun 2016.

- [306] Ryusuke Jinno and Masahiro Takimoto. Gravitational waves from bubble collisions: An analytic derivation. *Physical Review D*, 95(2), may 2017.
- [307] L. Badurina and And Others. AION: An atom interferometer observatory and network. *Journal of Cosmology and Astroparticle Physics*, 2020(5), nov 2020.
- [308] Leonardo Leitao and Ariel Mégevand. Gravitational waves from a very strong electroweak phase transition. *Journal of Cosmology and Astroparticle Physics*, 2016(5), dec 2016.
- [309] Bruce Allen and Joseph D. Romano. Detecting a stochastic background of gravitational radiation: Signal processing strategies and sensitivities. *Physical Review D - Particles, Fields, Gravitation and Cosmology*, 59(10), oct 1999.
- [310] Michele Maggiore. Gravitational wave experiments and early universe cosmology, aug 2000.
- [311] Eric Thrane and Joseph D Romano. Sensitivity curves for searches for gravitational-wave backgrounds. *Physical Review D - Particles, Fields, Gravitation and Cosmology*, 88(12), oct 2013.
- [312] Matthew R. Adams and Neil J. Cornish. Discriminating between a stochastic gravitational wave background and instrument noise. *Physical Review D - Particles, Fields, Gravitation and Cosmology*, 82(2), feb 2010.
- [313] Matthew R. Adams and Neil J. Cornish. Detecting a stochastic gravitational wave background in the presence of a galactic foreground and instrument noise. *Physical Review D - Particles, Fields, Gravitation and Cosmology*, 89(2), jul 2014.
- [314] Carlo Pagani. Note on scaling arguments in the effective average action formalism. *Physical Review D*, 94(4), 2016.
- [315] Carlo Pagani and Martin Reuter. Composite operators in asymptotic safety. *Physical Review D*, 95(6), 2017.
- [316] Maximilian Becker and Carlo Pagani. Geometric operators in the Einstein-Hilbert truncation, 2019.
- [317] Maximilian Becker, Carlo Pagani, and Omar Zanusso. Fractal geometry of higher derivative gravity. 2019.
- [318] Razvan Gurau and James P Ryan. Melons are Branched Polymers. *Annales Henri Poincaré*, 15(11):2085–2131, 2014.
- [319] Z Burda, A Jarosz, G Livan, M A Nowak, and A Swiech. Eigenvalues and singular values of products of rectangular Gaussian random matrices. *Physical Review E - Statistical, Nonlinear, and Soft Matter Physics*, 82(6), 2010.

- [320] Paul J Kelly. A congruence theorem for trees. *Pacific Journal of Mathematics*, 7(1):961–968, 1957.
- [321] Stanislaw Ulam. A collection of mathematical problems. *New York*, 1960.
- [322] B. P. Abbott, , and Others. GW170817: Observation of Gravitational Waves from a Binary Neutron Star Inspiral. *Physical Review Letters*, 119(16):161101, oct 2017.
- [323] Astrid Eichhorn, Yuta Hamada, Johannes Lumma, and Masatoshi Yamada. Quantum gravity fluctuations flatten the Planck-scale Higgs potential. *Physical Review D*, 97(8), apr 2018.
- [324] Dietrich Bödeker and Guy D. Moore. Can electroweak bubble walls run away? *Journal of Cosmology and Astroparticle Physics*, 2009(5), mar 2009.
- [325] Mark Hindmarsh, Stephan J Huber, Kari Rummukainen, and David J Weir. Numerical simulations of acoustically generated gravitational waves at a first order phase transition. *Physical Review D - Particles, Fields, Gravitation and Cosmology*, 92(12), 2015.
- [326] Mark Hindmarsh, Stephan J Huber, Kari Rummukainen, and David J Weir. Shape of the acoustic gravitational wave power spectrum from a first order phase transition. *Physical Review D*, 96(10), 2017.
- [327] Bernard Schutz. A First Course in General Relativity (Second Edition). *Classical and Quantum Gravity*, 27(10):109001, 2010.
- [328] Dietrich Bödeker and Guy D. Moore. Can electroweak bubble walls run away? *Journal of Cosmology and Astroparticle Physics*, 2009(5), mar 2009.

Erklärung:

Ich versichere, dass ich diese Arbeit selbstständig verfasst habe und keine anderen als die angegebenen Quellen und Hilfsmittel benutzt habe.

Heidelberg, den (Datum)

Acknowledgements

First and foremost, I am deeply grateful to my supervisor Astrid Eichhorn. Not only have I greatly benefited from her physics knowledge and intuition, but she has also been a source of inspiration for me. I feel like I have benefited a lot on a personal level from her and the environment she has created for the group. Thank you, Astrid!

I would like to thank Prof. Björn Malte Schäfer for agreeing to referee this thesis.

I would like to thank Aaron Held, Martin Pauly, Marc Schiffer, Fleur Versteegen, Antonio D. Pereira, Andreas Pithis, Alessia Platania, Gustavo Pazzini Brito, Masatoshi Yamada and Manuel Reichert for the amazing times. The usual struggles of a PhD become more bearable when shared with great people. I also thank them for proof-reading this thesis!

Many thanks also go to my collaborators Astrid Eichhorn, Tim Koslowski, Yuta Hamada, Mark Hindmarsh, Marvin Lüben, Martin Pauly, Jan M. Pawłowski, Manuel Reichert and Arslan Sikandar for accompanying me on this journey into the fundamental nature of space-time and the wonders of the early universe.

I would also like to express my deepest gratitude to Joseph Ben Geloun, Dario Benedetti, Valentin Bonzom, Vincent Rivasseau, and Razvan Gurau for their hospitality during my stay in Paris and welcoming me to tensor model community.

I also thank Debtosh Chowdhury, Nicolas Delporte, Sabine Harribey, Vincent LaHoche and Dine Ousmane Samary as well as all the people at CPHT who made my stay there very enjoyable.

I would also like to thank the people at CP³-Origins in Odense for welcoming me so kindly and it is really a pity that my stay there was cut short by a pandemic.

Finally, I would like to thank my family and friends for their constant support during these last years. Thank you Isabel, Klaus, Konrad, Lukas, Marlene, Moritz, Simon, Stephan, Valentina, Viktor, Viktoria for sharing many great, fun moments with me and also being there in the tough times!